Ionization and fragmentation dynamics of singly and multiply charged ions



Weiwei Zhou

Exeter College

University of Oxford

A thesis submitted for the degree of

Doctor of Philosophy

Michaelmas 2018

© Copyright 2018 **Weiwei Zhou**
Ionization and fragmentation dynamics of singly and multiply charged ions

DPhil thesis, Michaelmas Term 2018
Supervisor: Professor Claire Vallance
Examiners: Professor Grant Ritchie and Professor Stephen Price

University of Oxford
Chemistry Research Laboratory
12 Mansfiled Road, Oxford, United Kingdom, OX1 3TA

Abstract

This thesis investigates the ionization and fragmentation dynamics of gas-phase molecules, particularly those relevant to astrochemistry and of interest in velocity-map imaging experiments into the dynamics of Coulomb explosions. These two topics are covered in Part I and Part II, respectively.

Part I focuses on the redesign of a total electron ionization cross-section measurement apparatus. The aim was to satisfy a number of key experimental criteria, such as achieving full collection efficiency for the ions and electrons generated in the experiment, and obtaining accurate absolute pressure and temperature measurements. A combination of SIMION ion and electron trajectory simulations and experimental optimisation led to the final version of the instrument. The absolute total cross-section data obtained using the apparatus (including nine interstellar molecules measured) are considered to be highly reliable without significant sources of systematic errors, and the results show good agreement with cross-sections predicted using the binary-encounter Bethe (BEB) model, especially at low incident electron energy. In common with previous studies, the maximum in the experimentally measured cross-section correlates linearly with the molecular polarizability volume.

The instrument developed in this thesis will be used to perform further measurements on many more molecules, and the absolute total cross-section data will be combined with relative partial ionization cross-section data measured on an electron-molecule crossed-beam velocity-map imaging apparatus in the same laboratory to determine absolute partial ionization cross-sections for each fragment ion. A larger project to establish a comprehensive database which contains both total and partial ionization cross-sections of molecules relevant to astrochemistry and plasma science is proposed, and is currently under development.

Part II of the thesis is devoted to the ionization and fragmentation dynamics of multiply charged ions, for which Coulomb explosion plays an important role as a dissociation mechanism. While femtosecond-laser-pulse-induced Coulomb explosion experiments have been performed extensively, the corresponding simulation work has relied on simple Coulomb-only models. In the present work, we develop a new trajectory simulation

code in which the forces on each atom are calculated via electronic structure methods at each trajectory time step. The electronic structure calculations and classical trajectory calculations are performed within Gaussian and Matlab, respectively, packaged within a single executable Linux shell script. All Gaussian and Matlab parameters may be set and adjusted to calculate outcomes such as evolution of atomic charges, bond orders, bond lengths, atomic velocities, atomic forces, and SCF energies of the molecular system. In addition to providing additional insight into the product scattering distributions observed in Coulomb-explosion imaging experiments, the simulations also allow a number of experimentally inaccessible features to be investigated, including details of the fragmentation mechanism and the extensive charge redistribution that occurs in the early stages of the Coulomb explosion process.

The new simulation program is the good starting point towards full simulation as per experimental conditions to re-produce measured velocity-map images. Future work will develop multi-trajectory simulations based on a range of initial conditions sampled statistically. With ever-increasing CPU power and proper technical considerations, this perspective is no longer out of reach.

To my family

Acknowledgements

I would like to sincerely thank my supervisor, Professor Claire Vallance, for her guidance, inspiration, and patience throughout my DPhil life. Her determination and professionalism constantly motivated me whenever I was surrounded by confusion and disappointment. She encouraged me to attend conferences, give talks, and build collaboration, through which I have developed in many ways as a person. I also want to particularly thank her for all the meetings and discussions during my thesis writing, and the time and effort that she has dedicated.

I felt very fortunate to have met and made many friends in the Vallance group lab during the past years. I would like to thank Cécilia, Simon, James, Alfredo, Sara, and Dean for their help, advices, and companion.

As a reaction dynamics experimentalist, I am greatly indebted to the PTCL Mechanical Engineering Workshop and Electronics Workshop. I would like to thank Les, Andy, Samuel, and Dennis for their help whenever I rushed to the mechanical workshop. I want to thank Charlie Jones for making the collision cell assembly, and for teaching me to use machines at the student workshop course. I want to thank Howard for making countless number of tubings for me. I also want to thank Peter for making the excellent cold finger trap. I would like to thank Kevin, Tim, Phil, John, and Neville for helping with many issues that I had with my electronics units. Particularly, I want to thank Phil for lending me the book *The Art of Electronics*, and thank Tim for often drawing circuit diagram to explain problems to me. I have always wanted to learn more electronics and luckily I did.

Also as a reaction dynamics experimentalist who often deals with gas cylinders and vacuum pumps, I would like to thank CRL Facilities Team, Martin, Ron, and Jude, for their help and advices. I also want to thank Steve Orton from Pfeiffer Vacuum Ltd who helped me with changing turbo pump oil wick and repaired my poor HiPace 700.

And as a reaction dynamics experimentalist who decided to do some simulation work, I would like to thank Pete Biggs for patiently solving my Linux issues and detailedly explaining the various functionalities of clusters. I would like to thank Dr Alexandra Simperler from NSCCS and Dr Douglas J. Fox from Gaussian, Inc. for helping me

overcome challenging Gaussian issues. I also would like to thank Mihai Duta and Matthew Lowy from IT services for guiding me through using the Oxford Advanced Research Computing facilities.

And as a reaction dynamics experimentalist who is passionate about teaching, I would like to thank Dr Martin Galpin for giving me opportunity to teach *Physics for Chemists* problem classes to undergraduate students, from which I have benefited greatly.

I would like to thank Professor Grant Ritchie and Professor Stephen Price for agreeing to examine my thesis.

For such a long journey, I wouldn't be able to cope with all the difficulties and discouragements without the support and inspiration from my family and friends. Dad and Mum, thank you for everything. Thank you for always being there for me.

Huni, my dear wife, thank you for your patience, encouragement, and companion. Thank you for your cute drawings on my diary, notebook, and printed journal articles. Thank you for always bringing the bright side of life to me.

Tofu and Puff, my prickly Erinaceidae fencers, thank you for running on the wheel everyday (6am) and keeping the writing room noisy.

Tanggao and Taosu, my hoarding Cricetidae gymnasts, thank you for biting my finger and pretending it wasn't you.

Moomin, my little lion, thank you for brightening me up when I was in the most difficult time. Thank you for sitting on my keyboard to proofread my chapters and providing constructive comments such as "hhhhhh77777778888888888888888888888888".

Pippi, my little kitty, thank you for coming and living with us. Thank you for napping on my desk and scratching my sleeve. Thank you for being so strong and positive when we couldn't do anything more for you. How is everything on the other side of the Rainbow Bridge, my sweet girl? I miss you.

Contents

List of Figures xvii

List of Tables xxv

List of Abbreviations xxix

1 Introduction 1

1.1 Motivations . . . 1

1.2 Chapter summary . . . 3

References . . . 5

2 Electron ionization phenomena 7

2.1 Introduction . . . 8

2.2 Ionization mechanism . . . 8

2.2.1 Ionization processes . . . 8

2.2.2 Frank-Condon principle . . . 10

2.3 Types and properties of ions produced . . . 11

2.3.1 Molecular ions . . . 11

2.3.2 Fragment ions . . . 13

2.3.3 Multiply charged ions . . . 15

2.3.4 Metastable ions, stable ions, and unstable ions . . . 16

2.3.5 Rearrangement ions . . . 16

2.4 Total ionization cross-sections . . . 17

2.4.1 Introduction . . . 17

2.4.2 Principles of an ionization cross-section measurement . . . 18

2.4.3 Experimental considerations . . . 20

2.4.3.1 Electron current I^- and ion current I^+ . . . 20

2.4.3.2 Number density n . . . 21

2.4.3.3 Pathlength l . . . 22
2.4.3.4 Electron energy . . . 23
2.4.4 Experimental techniques for measuring total ionization cross-section 24
2.4.4.1 Condenser-plate method . . . 24
2.4.4.2 Lozier tube . . . 27
2.4.4.3 Bell and Nottingham method . . . 28
2.4.4.4 Crossed-beam methods . . . 28
2.4.4.5 Summation method . . . 31
2.4.4.6 Gas-filled counters . . . 31
2.5 Application of electron ionization cross-section data . . . 33
2.5.1 Plasma modelling . . . 33
2.5.2 Biological processes . . . 34
2.5.3 Astrochemistry and astrophysics . . . 35
2.5.4 Other . . . 35
References . . . 36

3 Semi-classical and semi-empirical methods for calculating electron ionization cross-sections 43
3.1 Introduction . . . 44
3.2 Semi-classical formulae . . . 44
3.2.1 The Deutsch-Märk (DM) method . . . 46
3.2.2 The binary-encounter Bethe (BEB) method . . . 48
3.2.2.1 Mott cross-section . . . 48
3.2.2.2 Binary-encounter cross-section . . . 49
3.2.2.3 Binary-encounter dipole (BED) model . . . 51
3.2.2.4 Binary-encounter Bethe (BEB) model . . . 52
3.3 Empirical and semi-empirical formulae . . . 53
3.3.1 The Lotz method . . . 54
3.3.2 The Jain-Khare method . . . 55
3.3.3 The Bell method . . . 57
3.3.4 Kistemaker's modified additivity rule . . . 58
3.3.5 The polarizability model . . . 60
3.4 Discussion . . . 62

3.5 Current work . . . 63
3.5.1 Total ionization cross-section calculation of molecules relevant to astrochemistry by using BEB model . . . 63
3.5.2 Total ionization cross-section calculation of molecules relevant to astrochemistry by using polarizability model . . . 64
References . . . 66

4 Experimental design **71**
4.1 Overall set-up . . . 72
4.2 Optimisation of cell design . . . 74
4.2.1 Optimisation of electron beam emitter . . . 76
4.2.1.1 Filament shape and material . . . 77
4.2.1.2 Filament saturation and operating current . . . 78
4.2.2 Optimisation of ion optics . . . 78
4.2.3 Experimental optimisation of static potentials . . . 81
4.2.4 Optimisation of sample pressure . . . 85
4.2.5 Optimisation of gas tubing and feedthroughs . . . 87
4.3 Summary of optimised cell design . . . 88
4.3.1 Electron source . . . 88
4.3.2 First Einzel lens . . . 88
4.3.3 Collision cell . . . 89
4.3.4 Lens elements L4 and L5, and Faraday cup . . . 90
4.4 Electronics . . . 91
4.4.1 Filament power supply . . . 91
4.4.2 Electrostatic Lens Power supply . . . 91
4.4.3 Electron and ion detection . . . 91
4.4.4 Capacitance manometer and absolute pressure measurement . . . 93
4.4.5 Thermocouple . . . 95
4.4.6 Instrument control and data acquisition . . . 95
4.5 Vacuum system . . . 95
4.6 Sample preparation and sample line set-up . . . 96
4.7 Calibration of the new cell design . . . 98
4.7.1 Calibration factors to be considered . . . 98

4.7.2 Testing and optimisation with N_2 . . . 100
4.7.3 Comparison with other common permanent gas molecules . . . 101
4.8 Common issues . . . 103
4.8.1 Cell and ion optics contamination . . . 103
4.8.2 Stability and hysteresis of gas pressure reading . . . 107
4.9 Standard operating procedures . . . 108
References . . . 109

5 Absolute total ionization cross-section of interstellar molecules 113
5.1 Molecules discovered in the interstellar medium . . . 114
5.1.1 The interstellar medium . . . 114
5.1.2 Molecules in the ISM . . . 114
5.1.3 Ionization processes in the ISM . . . 114
5.2 Results . . . 117
5.2.1 Acrolein . . . 119
5.2.2 Acrylonitrile . . . 120
5.2.3 Methyl cyanide . . . 120
5.2.4 Ethyl cyanide . . . 121
5.2.5 Propyl cyanide . . . 122
5.2.6 Isopropyl cyanide . . . 122
5.2.7 Ethanethiol . . . 124
5.2.8 Methyl oxirane . . . 124
5.2.9 Benzene . . . 126
5.3 Discussion . . . 126
5.3.1 General features . . . 126
5.3.2 Comparison of experimental maximum cross-section and maximum cross-section calculated using the polarizability volume method . . . 127
5.4 New database of partial and total ionization cross-section of ISM molecules 131
References . . . 133

6 Simulating Coulomb explosion imaging from first principles 137
6.1 Introduction . . . 137
6.2 Coulomb explosion imaging experiments . . . 138
6.3 Review of simulating Coulomb explosion imaging . . . 140

6.3.1 Classical molecular dynamics simulation 142
6.3.2 *Ab initio* molecular dynamics simulation 143
6.3.3 *Ab initio* classical trajectory calculation 144
6.3.4 Simulating velocity-map images for Coulomb explosion products 145
6.4 Novel approach of simulating Coulomb explosion from first principles . . . 147
6.4.1 Aims and algorithm 147
6.4.2 Adjustment, benchmarking and testing 153
6.4.2.1 General considerations 153
6.4.2.2 Effect of level of theories 155
6.4.2.3 Effect of initial vibrational excitation energy 168
6.4.2.4 Effect of classical trajectory parameters 170
6.4.2.5 Effect of system setup 172
6.4.3 Limitation and technique issues 173
6.5 Summary 174
References 175

7 Coulomb explosion simulation of small organic molecules 181
7.1 Introduction 181
7.2 Simulated outcome as a function of initial parent ion charge states 182
7.2.1 Formyl chloride (HClCO) 183
7.2.1.1 Partial charge and Wiberg bond index evolution 183
7.2.1.2 Velocity evolution 186
7.2.1.3 Terminal velocity 187
7.2.2 *cis*-1,2-dichloroethene ($C_2H_2Cl_2$) 188
7.2.2.1 Fragment charge and Wiberg bond index evolution 191
7.2.2.2 Velocity evolution 193
7.2.2.3 Terminal velocity 193
7.2.3 Fluoromethane (CH_3F) 199
7.2.3.1 Partial charge and Wiberg bond index evolution 199
7.2.3.2 Velocity evolution 202
7.2.3.3 Terminal velocity 202
7.2.4 Chloroiodomethane (CH_2ICl) 207
7.2.4.1 Partial charge and Wiberg bond index evolution 207

7.2.4.2 Velocity evolution . . . 210
7.2.4.3 Terminal velocity . . . 214
7.3 Simulation of Velocity-Map Imaging experimental data . . . 215
7.3.1 3,5-dibromo-3',5'-difluoro-4'-cyanobiphenyl (DBrDFCNBph) . . . 215
7.3.1.1 Trajectory and fate of each atom . . . 216
7.3.1.2 Ion images . . . 218
7.3.1.3 Covariance-map imaging . . . 223
7.4 Conclusion and future work . . . 229
References . . . 236

8 Summary and Perspectives **237**
References . . . 240

Appendices

A Derivation of Beer-Lambert law for describing electron ionization **243**

B Standard operating procedures of total ionization cross-section measurement **247**
B.1 Procedures of starting and terminating a measurement . . . 247
B.2 Maintenance considerations . . . 249

C Deconvolution method of cross-section data **251**

D Absolute total ionization cross-section data **257**
D.1 Interstellar molecules . . . 258
D.1.1 Acrolein (CH_2CHCHO) . . . 258
D.1.2 Acrylonitrile (CH_2CHCN) . . . 259
D.1.3 Methyl cyanide (CH_3CN) . . . 260
D.1.4 Ethyl cyanide (CH_3CH_2CN) . . . 261
D.1.5 Propyl cyanide ($CH_3CH_2CH_2CN$) . . . 262
D.1.6 Isopropyl cyanide ($(CH_3)_2CHCN$) . . . 263
D.1.7 Ethanethiol (CH_3CH_2SH) . . . 264
D.1.8 Methyl oxirane (C_3H_6O) . . . 265
D.1.9 Benzene (C_6H_6) . . . 266
D.2 Common permanent gas molecules . . . 267

D.2.1 Nitrogen (N_2) . . . 267
D.2.2 Carbon dioxide (CO_2) . . . 268
D.2.3 Ethylene (C_2H_4) . . . 269
D.2.4 Propene (C_3H_6) . . . 270
D.2.5 Nitrous oxide (N_2O) . . . 271
D.2.6 Tetrafluoromethane (CF_4) . . . 272
D.2.7 Sulfur hexafluoride (SF_6) . . . 273

E Coulomb explosion simulation program and standard operating procedures 275

E.1 Standard operating procedures . . . 275

E.2 Sample Matlab simulation program (*cis*-1,2-dichloroethene) . . . 276

E.2.1 CES_dichloroethene.m . . . 277
E.2.2 dichloroethene.inp . . . 291
E.2.3 g09commands . . . 291
E.2.4 g09commandf . . . 292
E.2.5 runces . . . 293

List of Figures

2.1 Schematic Franck–Condon principle potential energy diagram of a diatomic molecule. . . . 11
2.2 Schematic mass spectrum of triacontane at 70 eV electron energy at temperature of 538 K and 343 K. . . . 13
2.3 Fraction of different types of ions termed in mass spectrometry as a function of rate constants of ion dissociations. . . . 17
2.4 Schematic conceptual design of experiment for determining total ionization cross-section. . . . 19
2.5 Schematic diagram of (a) Compton and Van Voorhis' total ionization apparatus and (b) equipotential surfaces of ionization chamber. . . . 25
2.6 Schematic diagram of Tate and co-workers' total ionization apparatus. . . . 26
2.7 Schematic diagram of Lozier tube. . . . 28

2.8 The schematic diagram of the top view of the experimental tube of Bell and Nottingham method. 29

2.9 Schematic block diagram of crossed-beam apparatus used in Fite and Brackmann's experiment. 30

2.10 Schematic diagram of gas-filled counters apparatus used in Rieke and Prepejchal's experiment. 32

4.1 Schematic diagram of current instrument used to measure absolute total electron ionization cross-sections. 72

4.2 Schematic cross-sectional view of original Canterbury cell and SIMION simulated equipotential lines. 75

4.3 Schematic cross-sectional view of original Canterbury cell and SIMION simulated (a) primary electron beam trajectories and (b) molecular nitrogen ion trajectories. 75

4.4 Schematic diagram (left) and picture (right) of Agar Scientific AGA054 tungsten-rhenium filament. 77

4.5 Schematic cross-sectional view of new cell and SIMION simulated equipotential lines. 80

4.6 Schematic cross-sectional view of new cell and SIMION simulated (a) primary electron beam trajectories and (b) molecular nitrogen ions trajectories. 80

4.7 (a) Currents on L4 by varying incident electron energies from 0 to 200 eV; (b) Percentage of currents on L4 among total currents on both L4 and Trap; (c) Same as top-left figure but only shows close-up area when trap potential $\geq$ 50 V; (d) Same as Top-right figure but only shows close-up area when trap potential $\geq$ 50 V (to test goal 1 in Section 4.2.2). 82

4.8 Collection efficiency of (a) ion and (b) electron detectors (to test optimisation criteria 2 and 3 in Section 4.2.2). 83

4.9 Effects of varying Faraday cup potential on ion detector collection efficiency (To test goal 4 in Section 4.2.2). 84

4.10 SIMION simulated electron beam spot distribution on the bottom of Faraday cup at 7 representative electron energies. Red circles have diameters of 4 mm. Total number of trajectories for each simulation: 5000. Number of trajectories reaching the bottom of the Faraday cup are 18, 87, 154, 189, 232, 251, and 256 at EE = 10 eV, 50 eV, 100 eV, 150 eV, 200 eV, 250 eV, and 290 eV, respectively. 85

4.11 SIMION simulated cross-sectional electron beam distribution when passing through lens elements (a) L4 and (b) L5 at EE = 290 eV. 86

4.12 (a) Effects of gas pressure on apparent ionization cross-section and (b) standard deviation of each pressure measurement vs apparent pressure values. 87

4.13 Cross-sectional view of electron source. 89

4.14 Cross-sectional view of internal structure of MKS Baratron® Capacitance Manometer. 94

4.15 A schematic diagram of vacuum system with collision cell assembly and external electronics. 96

4.16 Schematic diagram of cold finger trap utilising freeze-pump-thaw cycle technique. 97

4.17 SIMION simulated percentage of ions collected by the cell as a function of distance from the middle of L4 towards L5. 99

4.18 (a) Absolute total ionization cross-section of N_2 recorded in the current work, Rapp and Englander-Golden's experiment, BEB calculation, and other literature values; (b) Data from current work, Rapp and Englander-Golden's, and Straub *et al.*'s near threshold region. 100

4.19 Absolute total ionization cross-section of common permanent gas molecules of current work, BEB calculation, and other literature values. (a) Carbon dioxide; (b) Ethylene; (c) Propene; (d) Nitrous oxide; (e) Tetrafluoromethane; (f) Sulfur hexafluoride. 102

4.20 Comparison of total ionization cross-section data of acrolein, measured on 31 Oct 2016 (normal) and 1 Nov 2016 (uneven "spikes" at several electron energies). 104

4.21 Uneven "spikes" feature developed on the total ionization cross-section curve from Nelson's work, at around 70 eV. 105

4.22 Uneven "spikes" feature developed on total ionization cross-section curve from Bart's work, at around 30 eV. 105

4.23 Before (a) and after (b) cleaning the inside of the shield, when Aquadag was not coated beforehand. 106

4.24 (a) An extreme example of contamination layer on lens element L1 after long running hours, note the filament being used was a hairpin shape, i.e. point source. (b) The same lens element L1 (coated with Aquadag) after long running hours when using a line filament. 106

5.1 Total ionization cross-section of acrolein from current experimental measurement, BEB calculation, and calculation using the polarizability volume method described in Chapter 3. 119

5.2 Total ionization cross-section of acrylonitrile from current experimental measurement, BEB calculation, and calculation using the polarizability volume method described in Chapter 3. 120

5.3 Total ionization cross-section of methyl cyanide from current experimental measurement, BEB calculation, and calculation using the polarizability volume method described in Chapter 3. 121

5.4 Total ionization cross-section of ethyl cyanide from current experimental measurement, BEB calculation, and calculation using the polarizability volume method described in Chapter 3. 122

5.5 Total ionization cross-section of propyl cyanide from current experimental measurement, BEB calculation, and calculation using the polarizability volume method described in Chapter 3. 123

5.6 Total ionization cross-section of isopropyl cyanide from current experimental measurement, BEB calculation, and calculation using the polarizability volume method described in Chapter 3. 123

5.7 Total ionization cross-section of ethanethiol from current experimental measurement, BEB calculation, and calculation using the polarizability volume method described in Chapter 3. 125

5.8 Total ionization cross-section of methyl oxirane from current experimental measurement, BEB calculation, and calculation using the polarizability volume method described in Chapter 3. 125

5.9 Total ionization cross-section of Benzene from current experimental measurement, BEB calculation, and calculation using the polarizability volume method described in Chapter 3. 126

5.10 Total ionization cross-section of the 4 organic cyanides. 128

5.11 Empirical correlation between experimental σ_{max} and calculated polarizability volume for 63 medium size organic and halocarbon species studied Bull *et al.*. R^2 = 0.979 and slope = 1.478. 129

5.12 Empirical correlation between experimental σ_{max} and calculated polarizability volume for 9 astrochemistry molecules in current work. 129

5.13 Empirical correlation between experimental σ_{max} and calculated polarizability volume for 5 organic nitrile molecules in the current work; R^2 = 0.9954 and slope = 1.405. 130

5.14 Empirical correlation between experimental σ_{max} and calculated polarizability volume for 9 astrochemistry molecules in the current work with 63 medium size organic and halocarbon species in Bull *et al.* 2012's work; R^2 = 0.9978 and slope = 1.479. 131

6.1 A schematic representation of the original Coulomb explosion experiment carried out by Vager and co-workers. 140

6.2 The 3,5-dibromo-3',5'-difluoro-4'-cyanobiphenyl (DBrDFCNBph) molecule in skeletal formula, as used in Slater *et al.*'s work. 140

6.3 Steps of generating recoild frame covariance image as described in Slater *et al.*'s work. 141

6.4 Laboratory-frame image of H^+ (left) and covariance image of H^+ with respect to N^+ of DBrDFCNBph in parallel alignment (middle) as shown in the skeleton representation (right). 141

6.5 Plots of simulated ion trajectories following Coulomb explosion of DBrDFCNBph with a single positive charge on each atom, (a) in three dimensions and (b) plotted onto *xz*-plane, as described in Slater *et al.*'s work. Trajectories time = 70 fs after onset of simulation. 146

6.6 Covariance images of DBrDFCNBph recorded in (left column) experiment and (right column) simulation in (top row) perpendicular and (bottom row) parallel alignment, as described in Slater *et al.*'s work. 148

6.7 Flow chart of the algorithm of the current *ab initio* classical trajectories simulation program. 150

6.8 Ball and stick representation of the (*R*,*R*)-trans-2,3-dideuterooxirane moleule. 158

6.9 Evolution of the atomic charge states during Coulomb explosion of trans-2,3-dideuterooxirane (*R*,*R*) at $z = +10$ using the MP2 and B3LYP method, with 6-311G(d,p) basis set. Note that atoms are numbered in the same way as in the picture of the molecule in Figure 6.8. 159

6.10 Evolution of atomic velocities during Coulomb explosion of trans-2,3-dideuterooxirane (*R*,*R*) at $z = +10$ using the MP2 and B3LYP method, with 6-311G(d,p) basis set. Note that atoms are numbered in the same way as in the picture of the molecule in Figure 6.8. 160

6.11 Evolution of Interatomic forces during Coulomb explosion of trans-2,3-dideuterooxirane (*R*,*R*) at $z = +10$ using the MP2 and B3LYP method, with 6-311G(d,p) basis set. Note that atoms are numbered in the same way as in the picture of the molecule in Figure 6.8. 161

6.12 Velocitiy-map image of trans-2,3-dideuterooxirane (*R*,*R*) on *xz*-plane. . . 163

6.13 Comparison of velocities of D atom in trans-2,3-dideuterooxirane (*R*,*R*) in *xz*-plane between experimental measurement by Herwig *et al.* and current simulation. 163

6.14 Ball and stick representation of the chloroiodomethane moleule. 164

6.15 Trajectories of atoms of CH_2ICl during Coulomb explosion at z = +4 simulated using (a) MP2 and (b) B3LYP method, with Def2-TZVP basis set. 165

6.16 Evolution of (a,b) partial charge states and (c,d) Wiberg bond indices of atoms and molecular fragments during Coulomb explosion of CH_2ICl at z = +4 simulated using (a,c) MP2/Def2-TZVP and (b,d) B3LYP/Def2-TZVP. 166

6.17 Ball and stick representation of the methyl iodide moleule. 169

6.18 Trajectory plots, evolution of partial charge states, and evolution of SCF energy during Coulomb explosion of methyl iodide at z = +2 simulated (a,c,e) without initial vibrational excitation and (b,d,f) with initial vibrational excitation. I, C, and H are respectively colored magenta, black, and cyan in trajectory plots. 171

7.1 Ball and stick representation of the formyl chloride moleule. 183

7.2 Trajectories of atoms of HClCO during Coulomb explosion at z = +2 and (b) z = +22. 184

7.3 Evolution of bond lengths during Coulomb explosion of HClCO at z = +2 to z = +22 for (a) C-Cl bond, (b) C-O bond, and (c) C-H bond. 184

7.4 Evolution of atomic charges during Coulomb explosion of HClCO at z = +2 to z = +22 for (a) Cl, (b) O, (c) C, and (d) H. 186

7.5 Evolution of Wiberg bond index during Coulomb explosion of HClCO at z = +2 to z = +22 for (a) C-Cl bond, (b) C-O bond, and (c) C-H bond. . . . 187

7.6 Evolution of partial charges (top) and Wiberg bond indices (bottom) of atoms and molecular fragments during Coulomb explosion of HClCO at (a) z = +3, (b) z = +4, and (c) z = +5. 188

7.7 Evolution of atomic velocities during Coulomb explosion of HClCO at z = +2 to z = +22 for (a) Cl, (b) O, (c) C, and (d) H. 189

7.8 Evolution of velocities of atoms and molecular fragments during Coulomb explosion of HClCO at z = +4. (a) Individual atoms. (b) Cl and H atoms with CO^+ treated as a molecular fragment rather than individual atoms. . 189

7.9 Atomic terminal velocity as a function of initial charge state of parent ion of HClCO. 190

7.10 Relationship between Coulomb explosion time (defined as the time at which the fragment is within 1% of its asymptotic velocity) and initial charge state of parent ion of HClCO. 190

7.11 Ball and stick representation of the *cis*-1,2-dichloroethene molecule. . . . 191

7.12 Schematic diagram of fragmentation channels of *cis*-1,2-dichloroethene during Coulomb explosion at z = +2 to z = +22. 192

7.13 Trajectory of atoms of *cis*-1,2-dichloroethene during Coulomb explosion at (a) $z = +4$, (b) $z = +5$, (c) $z = +6$, (d) $z = +7$, (e) $z = +8$, and (f) $z = +9$. . 195

7.14 Trajectory of atoms of *cis*-1,2-dichloroethene on *yz*-plane during Coulomb explosion at (a) $z = +8$, (b) $z = +9$, (c) $z = +10$, (d) $z = +11$, (e) $z = +12$, and (f) $z = +13$. 196

7.15 Evolution of atomic velocities during Coulomb explosion of *cis*-1,2-dichloroethene at $z = +2$ to $z = +22$ for (a) Cl1, (b) Cl2, (c) C1, (d) C2, (e) H1, and (f) H2. 197

7.16 Atomic terminal velocity as a function of initial charge state of parent ion of *cis*-1,2-dichloroethene. 198

7.17 Relationship between Coulomb explosion time (defined as the time at which the fragment is within 1% of its asymptotic velocity) and initial charge state of parent ion of *cis*-1,2-dichloroethene. 198

7.18 Ball and stick representation of the fluoromethane molecule. 199

7.19 Schematic diagram of fragmentation channels of fluoromethane during Coulomb explosion at $z = +2$ to $z = +14$. 200

7.20 Trajectory of atoms of fluoromethane during Coulomb explosion at (a) $z = +2$, (b) $z = +3$, (c) $z = +4$, (d) $z = +5$, (e) $z = +6$, and (f) $z = +7$. 203

7.21 Evolution of C-F bond length of fragments (a) $CFH2H3^{+}$, (b) CF^{+}, (c) CF^{+}, (d) CF^{2+}, and (e) CF^{3+} formed during Coulomb explosion of fluoromethane at (a) $z = +2$, (b) $z = +3$, (c) $z = +4$, (d) $z = +5$, and (e) $z = +6$, respectively. 204

7.22 Evolution of atomic velocities of fluoromethane during Coulomb explosion at $z = +2$ to $z = +14$ for (a) F, (b) C, (c) H1, (d) H2, and (e) H3. 205

7.23 Atomic terminal velocity as a function of initial charge state of parent ion of fluoromethane. 206

7.24 Relationship between Coulomb explosion time (defined as the time at which the fragment is within 1% of its asymptotic velocity) and initial charge state of parent ion of fluoromethane. 206

7.25 Ball and stick representation of the chloroiodomethane moleule. 207

7.26 Schematic diagram of fragmentation channels of chloroiodomethane during Coulomb explosion at $z = +2$ to $z = +30$. 209

7.27 Trajectory of atoms of chloroiodomethane during Coulomb explosion at (a) $z = +2$, (b) $z = +3$, (c) $z = +4$, (d) $z = +5$, (e) $z = +6$, (f) $z = +10$, (g) $z = +20$, (h) $z = +30$. 211

7.28 Evolution of bond lengths of chloroiodomethane during Coulomb explosion at $z = +5$ for (a) C-I bond, (b) C-Cl bond, (c) C-H1 bond, and (d) C-H2 bond.212

7.29 Evolution of atomic velocities of chloroiodomethane during Coulomb explosion at z = +2 to z = +30 for (a) I, (b) Cl, (c) C, (d) H1, and (e) H2. . 213

7.30 Atomic terminal velocity as a function of initial charge state of parent ion of chloroiodomethane. 214

7.31 Relationship between Coulomb explosion time (defined as the time at which the fragment is within 1% of its asymptotic velocity) and initial charge state of parent ion of chloroiodomethane. 214

7.32 Ball and stick representation of the 3,5-dibromo-3,5-difluoro-4-cyanobiphenyl (DBrDFCNBph) molecule. 216

7.33 Trajectories of atoms of DBrDFCNBph during Coulomb explosion at z = +23. (a) Seen within a cubic space of 60 Å side. (b) Seen within a cubic space of 16 Å side. 217

7.34 Location of C5, C6, C8, C9, C10, and C13 of DBrDFCNBph at t = 2 ps during Coulomb explosion at z = +23 on (a) *xy*-plane, (b) *xz*-plane, and (c) *yz*-plane. 219

7.35 Ion images of DBrDFCNBph at t = 2 ps during Coulomb explosion at z = +23 on *xz*-plane generated from original method (open markers) and current method (filled makers) where identical fragment ions are generated from the same atoms between the two methods. In both original and current methods, the fragment ions are (a) N^+ from N1, (b) C^+ from C1, C2, C4, C11, and C12, and (c) H^+ from H1, H2, H3, H4, and H5. 221

7.36 Ion images of DBrDFCNBph at t = 2 ps during Coulomb explosion at z = +23 on *xz*-plane generated from original method (open markers) and current method (filled markers) where different fragment ions are generated from the same atoms between the two methods. In original method, the fragment ions are (a) Br^+ from Br1 and Br2, (c) C^+ from C5, C6, C8, C9, C10, and C13, and (e) C^+ and F^+ from C3, C7, F1, and F2. In current method, the fragment ions are (b) Br^{2+} from Br1 and Br2, (d) ${C_6}^{3+}$ from C5, C6, C8, C9, C10, and C13, and (f) CF^+ from C3, C7, F1, and F2. 222

7.37 Recoil-frame covariance images in parallel alignment from (a) original simulation method and (b) experimental measurement. 225

7.38 Recoil-frame covariance images in parallel alignment from (a) current simulation method at MP2/6-311G(d,p) and (b) experimental measurement. 226

7.39 Recoil-frame covariance images in perpendicular alignment from (a) original simulation method and (b) experimental measurement. 227

7.40 Recoil-frame covariance images in perpendicular alignment from (a) current simulation method at MP2/6-311G(d,p) and (b) experimental measurement. 228

7.41 Recoil-frame covariance images in parallel alignment from (a) current simulation method at MP2/6-31G(d,p) and (b) experimental measurement. 230

7.42 Recoil-frame covariance images in parallel alignment from (a) current simulation method at cc-pVTZ and (b) experimental measurement. 231

7.43 Recoil-frame covariance images in perpendicular alignment from (a) current simulation method at MP2/6-31G(d,p) and (b) experimental measurement. 232

7.44 Recoil-frame covariance images in perpendicular alignment from (a) current simulation method at cc-pVTZ and (b) experimental measurement. . 233

A.1 Schematic conceptual diagram of electron ionization cross-section experiment with terms used in Beer-Lambert law derivation. 244

C.1 Potential along the axis of the cell when EE = 100 eV. 252

C.2 Raw and deconvoluted data of total ionization cross-section of N_2. 255

E.1 Functional block diagram showing relationships between the six simulation files. Use *cis*-dichloroethene as a working example. 276

List of Tables

2.1 Necessary conditions for each quantity in order to accurately measure ionization cross-sections. 22

4.1 Static potentials on various elements in the electron ionization cross-section instrument after experimental optimisation. 86

4.2 Details of multichannel power supply. 92

4.3 Experimental parameters of current work. 103

5.1 List of detected ISM molecules, ordered by number of constitute atoms. . 115

5.2 Basic physical properties of molecules measured in current project. . . . 118

6.1 Initial parameters of simulation before characterization. 154

6.2 Terminal atomic partial charge states of trans-2,3-dideuterooxirane (z = +10) simulated using MP2 method with different basis sets. 167

6.3 Terminal atomic velocities (in m s^{-1}) of trans-2,3-dideuterooxirane (z = +10) simulated using MP2 method with different basis sets. 168

6.4 Terminal atomic forces (in Hartrees $Bohr^{-1}$) of trans-2,3-dideuterooxirane (z = +10) simulated using MP2 method with different basis sets. 168

6.5 Terminal SCF energies (in Hartrees) of trans-2,3-dideuterooxirane (z = +10) simulated using MP2 method with different basis sets. 168

6.6 Total computational time (in hh:mm:ss) of simulating of trans-2,3-dideuterooxirane (z = +10) using MP2 method with different basis sets. 168

6.7 Summary of ODE solvers in Matlab. 172

6.8 Typical values of parameters for current simulation program. 173

7.1 Atomic separations in *cis*-1,2-dichloroethene at t = 0 fs and t = 500 fs during Coulomb explosion at z = +2 to z = +22. Unit: Å. 192

7.2 Atomic partial charges of *cis*-1,2-dichloroethene at t = 0 fs and t = 500 fs during Coulomb explosion at z = +2 to z = +22. Charges differ from nearest integer value under 0.001 are displayed as integer number with no decimal places. 194

7.3 Wiberg bond index of *cis*-1,2-dichloroethene at t = 0 fs and t = 500 fs during Coulomb explosion at z = +2 to z = +22. 194

7.4 Bond lengths of fluoromethane at t = 0 fs and t = 500 fs during Coulomb explosion at z = +2 to z = +14. Unit: Å. 200

7.5 Atomic partial charges of fluoromethane at t = 0 fs and t = 500 fs during Coulomb explosion at z = +2 to z = +14. Charges differ from nearest integer value under 0.001 are displayed as integer number with no decimal places. 201

7.6 Wiberg bond index of fluoromethane at t = 0 fs and t = 500 fs during Coulomb explosion at z = +2 to z = +14. 201

7.7 Bond lengths of chloroiodomethane at t = 0 fs and t = 500 fs during Coulomb explosion at z = +2 to z = +30. Unit: Å. 208

7.8 Atomic partial charges of chloroiodomethane at t = 0 fs and t = 500 fs during Coulomb explosion at z = +2 to z = +30. Charges differ from nearest integer value under 0.001 are displayed as integer number with no decimal places. 209

7.9 Wiberg bond index of chloroiodomethane at t = 0 fs and t = 500 fs during Coulomb explosion at z = +2 to z = +30. 210

7.10 Wiberg bond index of DBrDFCNBph during Coulomb explosion at z = +23 for original bonds and possible bonds on the Br-substituted ring at t = 0 ps and t = 2 ps. 218

7.11 Initial and final atomic partial charges of DBrDFCNBph during Coulomb explosion at z = +23 calculated at three different level of theories. Non-integer final partial charges of carbon ions, except for those formed CF molecular fragments, are coloured in red. 220

D.1 Absolute total ionization cross-section data of acrolein. 258

D.2 Absolute total ionization cross-section data of acrylonitrile. 259

D.3 Absolute total ionization cross-section data of methyl cyanide. 260

D.4 Absolute total ionization cross-section data of ethyl cyanide. 261

D.5 Absolute total ionization cross-section data of propyl cyanide. 262

D.6 Absolute total ionization cross-section data of isopropyl cyanide. 263

D.7 Absolute total ionization cross-section data of ethanethiol. 264

D.8 Absolute total ionization cross-section data of methyl oxirane. 265

D.9 Absolute total ionization cross-section data of benzene. 266

D.10 Absolute total ionization cross-section data of nitrogen. 267

D.11 Absolute total ionization cross-section data of carbon dioxide. 268

D.12 Absolute total ionization cross-section data of ethylene. 269

D.13 Absolute total ionization cross-section data of propene. 270

D.14 Absolute total ionization cross-section data of nitrous oxide. 271

D.15 Absolute total ionization cross-section data of tetrafluoromethane. 272

D.16 Absolute total ionization cross-section data of sulfur hexafluoride. 273

E.1 Description of all six files of current Coulomb explosion simulation. Use *cis*-dichloroethene as a working example. 277

List of Abbreviations

A . . . . . ampere

Å . . . . . Ångström

B3LYP . . . . . Becke, three-parameter, Lee-Yang-Parr

BEB . . . . . binary-encounter-Bethe model

BED . . . . . binary-encounter dipole model

BSE . . . . . Basis Set Exchange

CC . . . . . coupled cluster

CDMS . . . . . Cologne Database for Molecular Spectroscopy

CPU . . . . . central processing unit

CRL . . . . . Chemistry Research Laboratory (Department of Chemistry, University of Oxford)

DAQ . . . . . data acquisition

DBrDFCNBph . 3,5-dibromo-3',5'-difluoro-4'-cyanobiphenyl

DC . . . . . direct current

DFT . . . . . density functional theory

DM . . . . . Deutsch-Märk

EE . . . . . electron energy

eV . . . . . electronvolt

fs . . . . . femtosecond

G . . . . . gauss

GUI . . . . . graphical user interface

HCFCs . . . . . hydrochlorofluorocarbons

HF . . . . . Hartree-Fock

ISM . . . . . interstellar medium

JILA . . . . . Joint Institute for Laboratory Astrophysics

K . . . . . kelvin

keV . . . . . kiloelectronvolt

kV . . . . . kilovolt

LJTIA . . . . . LabJack LJTick-InAmp

m . . . . . meter

mA . . . . . microampere

MeV . . . . . megaelectronvolt

MP*n* . . . . . *n*th order Møller-Plesset perturbation theory

nA . . . . . nanoampere

NBO . . . . . natural bond orbital

NIST . . . . . National Institute of Standards and Technology

NSCCS . . . . . EPSRC National Service for Computational Chemistry Software

ODE . . . . . ordinary differential equation

PACS . . . . . Physics and Astronomy Classification Scheme

PImMS . . . . . Pixel-Imaging Mass-Spectrometry

ps . . . . . picosecond

PTCL . . . . . Physical and Theoretical Chemistry (Department of Chemistry, University of Oxford)

QCI . . . . . quadratic configuration interaction

RHS . . . . . right-hand side

s . . . . . second

SCF . . . . . self-consistent field

SD . . . . . standard deviation

σ . . . . . ionization cross-section

TDDFT . . . . . time-dependent density functional theory

u . . . . . unified atomic mass unit

VMI . . . . . velocity-map imaging

w.r.t. . . . . . with respect to

z . . . . . total charge states of parent ion

1 Introduction

Contents

1.1 Motivations **1**
1.2 Chapter summary **3**
References **5**

1.1 Motivations

This thesis is centred on investigations into molecular ionization and subsequent fragmentation processes. These are presented in two parts. Part I, comprised of Chapters 2 to 5, describes electron ionization cross-section measurements and modelling. Part II, comprised of Chapters 6 and 7, introduces a novel simulation package developed to explore Coulomb explosion processes induced by femtosecond laser pulses. Accordingly, electron ionization and photo ionization are the underlying ionization methods relevant to the two parts, respectively.

Electron ionization has been the subject of a wide range of research activities for more than a century, especially since the 1930s, and plays an important role in many areas of

science, including plasma modelling, stellar atmospheres, radiation physics, instrument developments in vacuum technology, and particularly mass spectrometry [1–4]. It is one of the most fundamental collision processes studied within the atomic and molecular physics community. Advances in experimental methods have made it possible to probe the ionization process in detail, with total ionization cross-sections being one of the parameters that can now be measured routinely [5–12]. In the meantime, theorists, enjoying the ever-increasing power of computational resources, have pushed the limits in calculating accurate quantitative ionization cross-sections [13]. A significant number of published measurements of electron ionization cross-sections have, by necessity, relied on normalisation of measured relative cross-sections to established benchmark data, or have suffered from significant uncertainties associated with the measurement of ion and electron currents, resulting in considerable disagreement between published measurements for a variety of molecules [13–15]. The technology available for measuring currents at the nA level have been greatly improved since many of the original measurements were made, and it is therefore a good point in time to redesign an instrument for measuring absolute total electron ionization cross-sections to the best standard possible today.

The aim of the redesign was to examine every aspect of instrument development and to construct an advanced and robust apparatus capable of measuring accurate total ionization cross-section data for molecules relevant to astrochemistry and other areas. In addition to being useful data in their own right, the total ionization cross-sections will be used to normalize relative partial ionization cross-section data collected from a cross-beam experiment in the same laboratory to obtain absolute values of partial ionization cross-section of each fragment ions produced. In addition, two theoretical methods using BEB model [16] and polarizability model [17], will be used to perform calculations of the total ionization cross-section, for comparison with the experimental data. Electron ionization in the energy range accessible to our instrument (0-300 eV) primarily leads to single ionization of the sample molecule. In contrast, photoionization with an ultra-short

laser pulse often yields a variety of multiply charged ions, which go on to fragment via a variety of different mechanisms. Of these, Coulomb explosion is a key dissociation mechanism. "Coulomb explosion" refers to the violent fragmentation processes that occur due to massive Coulomb repulsion between positively charged ions when multiple valence electrons of a molecule are stripped off [18]. As well as being interesting from a fundamental perspective, experiments in which the products of a Coulomb explosion are velocity-map imaged hold great promise for studying molecular structure and dynamics [19–23]. Simulation of the Coulomb explosion dynamics provides the link between the molecular structure and the observed velocity-map images of the Coulomb explosion products. This motivated the work carried out in the second part of this thesis [23].

The simulation method uses the electronic structure calculations within the Gaussian software package to calculate the forces acting on each atom at each timestep in the Coulomb explosion, while the trajectories themselves are propagated by separate code within Matlab. Determining the optimal simulation parameters formed a significant part of the development work.

1.2 Chapter summary

In Chapter 2, general principles of the electron ionization mechanism and types of product ions are introduced, followed by a discussion of experimental considerations involved in measuring absolute total ionization cross-sections. Data analysis procedures are also discussed. Historical and recent instrumental development are then introduced in chronological order, and application areas are discussed. In Chapter 3, popular semi-classical and semi-empirical methods of calculating total ionization cross-sections are reviewed and discussed. Technical aspects of implementing a semi-classical method, the binary-encounter Bethe (BEB) method, and a semi-empirical method known as the polarizability model method, are explicitly elaborated. In Chapter 4, the development of the instrument used in the current work is described, including a discussion of the

collision cell design and optimisation, electronics, vacuum system, sample preparation, and calibration. The results of total ionization cross-section measurements on a number of molecules that have been identified in the interstellar medium are then presented in Chapter 5 and compared with the predictions of theoretical models.

In Part II of the thesis, Chapter 6 introduces the principle of Coulomb explosion imaging experiments, and surveys previous work on simulation of Coulomb explosions. A major part of this chapter focuses on presenting the current method of simulating Coulomb explosion from first principles, with an emphasis on benchmarking and testing of the approach to characterise its functionality and applicability. In Chapter 7, Coulomb explosions of a number of representative molecules are simulated, and the results presented.

Chapter 8 provides a concise summary of all the work performed in this thesis, and considers future directions for the research.

References

[1] National Research Council. *Database Needs for Modeling and Simulation of Plasma Processing*. Washington, DC: The National Academies Press, 1996, p. 74.

[2] W. Lindinger, F. Howorka, J. M. Shull, A. V. Phelps, E. C. Zipf, Y.-K. Kim, and J. H. Futrell. "Applications". In: *Electron Impact Ionization*. Ed. by T. D. Märk and G. H. Dunn. Vienna: Springer, 1985.

[3] T. D. Märk. "Ionization of Molecules by Electron Impact". In: *Electron-Molecule Interactions and Their Applications*. Ed. by L. G. Christophorou. Vol. 1. Orlando, FL: Academic Press, 1984. Chap. 3, pp. 251–334.

[4] F. H. Field and J. L. Franklin. *Electron Impact Phenomena and the Properties of Gaseous Ions*. New York: Academic Press, 1970, p. 185.

[5] D. Rapp and P. Englander-Golden. "Total Cross Sections for Ionization and Attachment in Gases by Electron Impact. I. Positive Ionization". In: *The Journal of Chemical Physics* 43.5 (1965), pp. 1464–1479.

[6] C. Vallance, S. A. Harris, J. E. Hudson, and P. W. Harland. "Absolute electron impact ionization cross sections for CH_3X, where X=H, F, Cl, Br, and I". In: *Journal of Physics B: Atomic, Molecular and Optical Physics* 30.10 (1997), pp. 2465–2475.

[7] M. Bart, P. W. Harland, J. E. Hudson, and C. Vallance. "Absolute total electron impact ionization cross-sections for perfluorinated hydrocarbons and small halocarbons". In: *Physical Chemistry Chemical Physics* 3.5 (2001), pp. 800–806.

[8] J. E. Hudson, C. Vallance, M. Bart, and P. W. Harland. "Absolute electron-impact ionization cross sections for a range of C1 to C5 chlorocarbons". In: *Journal of Physics B: Atomic, Molecular and Optical Physics* 34.15 (2001), pp. 3025–3039.

[9] J. E. Hudson, M. L. Hamilton, C. Vallance, and P. W. Harland. "Absolute electron impact ionization cross-sections for the C1 to C4 alcohols". In: *Physical Chemistry Chemical Physics* 5.15 (2003), pp. 3162–3168.

[10] J. E. Hudson, C. Vallance, and P. W. Harland. "Absolute electron impact ionization cross-sections for CO, CO_2, OCS and CS_2". In: *Journal of Physics B: Atomic, Molecular and Optical Physics* 37.2 (2004), pp. 445–455.

[11] J. E. Hudson, Z. F. Weng, C. Vallance, and P. W. Harland. "Absolute electron impact ionization cross-sections and polarizability volumes for the C2 to C6 methanoates and C3 to C7 ethanoates". In: *International Journal of Mass Spectrometry* 248.1-2 (2006), pp. 42–46.

[12] J. N. Bull and P. W. Harland. "Absolute electron impact ionization cross-sections and polarisability volumes for C2 to C4 aldehydes, C4 and C6 symmetric ethers and C3 to C6 ketones". In: *International Journal of Mass Spectrometry* 273.1-2 (2008), pp. 53–57.

[13] K. H. Becker and V. Tarnovsky. "Electron-Impact Ionization of Atoms, Molecules, Ions and Transient Species". In: *Plasma Sources Science and Technology* 4.2 (1995), pp. 307–315.

[14] L. J. Kieffer and G. H. Dunn. "Electron Impact Ionization Cross-Section Data for Atoms, Atomic Ions, and Diatomic Molecules: I. Experimental Data". In: *Reviews of Modern Physics* 38.1 (1966), pp. 1–35.

[15] M. A. Lennon, K. L. Bell, H. B. Gilbody, J. G. Hughes, A. E. Kingston, M. J. Murray, and F. J. Smith. “Recommended Data on the Electron Impact Ionization of Atoms and Ions: Fluorine to Nickel”. In: *Journal of Physical and Chemical Reference Data* 17.3 (1988), pp. 1285–1363.

[16] W. Hwang, Y.-K. Kim, and M. E. Rudd. “New model for electron-impact ionization cross sections of molecules”. In: *Journal of Chemical Physics* 104.8 (1996), pp. 2956–2966.

[17] P. W. Harland and C. Vallance. “Ionization cross-sections and ionization efficiency curves from polarizability volumes and ionization potentials”. In: *International Journal of Mass Spectrometry* 171.1-3 (1997), pp. 173–181.

[18] T. A. Carlson and R. M. White. “Measurement of the Relative Abundances and Recoil-Energy Spectra of Fragment Ions Produced as the Initial Consequences of X-Ray Interaction with CH_3I, HI, and DI”. In: *The Journal of Chemical Physics* 44.12 (1966), pp. 4510–4520.

[19] Z. Vager, R. Naaman, and E. P. Kanter. “Coulomb Explosion Imaging of Small Molecules”. In: *Science* 244.4903 (1989), pp. 426–431.

[20] P. Herwig, K. Zawatzky, M. Grieser, O. Heber, B. Jordon-Thaden, C. Krantz, O. Novotný, R. Repnow, V. Schurig, D. Schwalm, Z. Vager, A. Wolf, O. Trapp, and H. Kreckel. “Imaging the Absolute Configuration of a Chiral Epoxide in the Gas Phase”. In: *Science* 342.6162 (2013), pp. 1084–1086.

[21] M. Pitzer, M. Kunitski, A. S. Johnson, T. Jahnke, H. Sann, F. Sturm, L. P. H. Schmidt, H. Schmidt-Böcking, R. Dörner, J. Stohner, J. Kiedrowski, M. Reggelin, S. Marquardt, A. Schießer, R. Berger, and M. S. Schöffler. “Direct Determination of Absolute Molecular Stereochemistry in Gas Phase by Coulomb Explosion Imaging”. In: *Science* 341.6150 (2013), pp. 1096–1100.

[22] C. S. Slater, S. Blake, M. Brouard, A. Lauer, C. Vallance, J. J. John, R. Turchetta, A. Nomerotski, L. Christensen, J. H. Nielsen, M. P. Johansson, and H. Stapelfeldt. “Covariance imaging experiments using a pixel-imaging mass-spectrometry camera”. In: *Physical Review A* 89.1 (2014), p. 011401.

[23] C. S. Slater, S. Blake, M. Brouard, A. Lauer, C. Vallance, C. S. Bohun, L. Christensen, J. H. Nielsen, M. P. Johansson, and H. Stapelfeldt. “Coulomb-explosion imaging using a pixel-imaging mass-spectrometry camera”. In: *Physical Review A* 91.5 (2015), p. 053424.

2

Electron ionization phenomena

Contents

2.1 Introduction **8**
2.2 Ionization mechanism **8**
2.2.1 Ionization processes 8
2.2.2 Frank-Condon principle 10
2.3 Types and properties of ions produced **11**
2.3.1 Molecular ions 11
2.3.2 Fragment ions 13
2.3.3 Multiply charged ions 15
2.3.4 Metastable ions, stable ions, and unstable ions 16
2.3.5 Rearrangement ions 16
2.4 Total ionization cross-sections **17**
2.4.1 Introduction 17
2.4.2 Principles of an ionization cross-section measurement 18
2.4.3 Experimental considerations 20
2.4.4 Experimental techniques for measuring total ionization cross-section 24
2.5 Application of electron ionization cross-section data **33**
2.5.1 Plasma modelling 33
2.5.2 Biological processes 34
2.5.3 Astrochemistry and astrophysics 35
2.5.4 Other 35
References **36**

2.1 Introduction

Electron ionization is a collision process between an electron and a target atom or molecule, which leads to formation of an ion and an ejected electron or electrons [1]. One of the earliest observations of electron ionization and its dependence on incident energy was documented at the very dawn of 20^{th} century by Lenard, who experimented in bombarding atoms with low energy electrons [2]. Some ten years later, electron ionization was first used in mass spectrometry by Dempster [3], who improved on the achievable resolution and signal intensity of the original mass spectrometry method proposed by J. J. Thomson in 1913 [4, 5]. Electron ionization has then been studied experimentally and theoretically to a great extent, not only because of its fundamental interest, but also the wide range of applications in areas such as plasma modelling, radiation physics, mass spectrometry, and astrochemistry [6].

2.2 Ionization mechanism

2.2.1 Ionization processes

In an electron-atom or electron-molecule collision event, if the energy of the incident electron is greater than a critical value, known as the ionization energy, some of the target atoms or molecules will be ionized. If the energy of the incident electron beam is further increased, the number of energetically accessible ionization and fragmentation channels increases, which results in an increase in the abundance and variety of the products observed. For molecular targets, the available fragmentation channels following electron ionization will generate characteristic ionic and neutral products. As a simple example, some of the ionization channels available to a diatomic molecule AB are shown below [1, 7]:

$$\mathrm{AB} + \mathrm{e} \rightarrow \mathrm{AB}^{+} + \mathrm{e_s} + \mathrm{e_e} \quad \text{single ionization} \tag{2.1}$$

$$\rightarrow \mathrm{AB}^{2+} + \mathrm{e_s} + 2\mathrm{e_e} \quad \text{double ionization} \tag{2.2}$$

$$\rightarrow \mathrm{AB}^{z+} + \mathrm{e_s} + z\mathrm{e_e} \quad z\text{-fold multiple ionization} \tag{2.3}$$

$$\rightarrow \mathrm{AB}^{\mathrm{K}+} + \mathrm{e_s} + \mathrm{e_e} \quad \text{K shell ionization} \tag{2.4}$$

$$\rightarrow \mathrm{A}^{+} + \mathrm{B} + \mathrm{e_s} + \mathrm{e_e} \quad \text{dissociative ionization} \tag{2.5}$$

$$\rightarrow \mathrm{A}^{+} + \mathrm{B}^{-} + \mathrm{e_s} \quad \text{ion pair formation} \tag{2.6}$$

$$\rightarrow \mathrm{AB}^{+*} + \mathrm{e_s} + \mathrm{e_e} \rightarrow \mathrm{A}^{+} + \mathrm{B} + \mathrm{e_s} + \mathrm{e_e} \quad \text{fragmentation} \tag{2.7}$$

$$\rightarrow \mathrm{AB}^{2+} + \mathrm{e_s} + 2\mathrm{e_e} \quad \text{autoionization} \tag{2.8}$$

$$\rightarrow \mathrm{AB}^{**} + \mathrm{e_s} \rightarrow \mathrm{AB}^{+} + \mathrm{e_s} + \mathrm{e_e} \quad \text{autoionization} \tag{2.9}$$

where $\mathrm{e_s}$ and $\mathrm{e_e}$ denote the scattered electron and the ejected electron, respectively.

Processes (2.1) to (2.6) are classified as direct ionization processes, as the ejected electron and scattered electron leave the molecular ion simultaneously or within 10^{-16} s of each other [8]. Conversely, the autoionization processes (2.7) to (2.9) are sequential processes in which electrons are ejected one after another. As can be seen from processes (2.7) to (2.9), autoionization typically involves a two-step process. A molecule AB is first raised into a metastable superexcited bound state (AB**), from which it couples radiationlessly to the continuum and proceeds to ionization.

For direct ionization processes, the electron being removed is usually considered to be a valence-shell electron, as shown in processes (2.1) to (2.3), (2.5) and (2.6). However, if the energy of the incident electron is high enough, an inner-shell or core electron may be removed. This process is referred to as inner-shell ionization (2.4), and can technically be verified by the observation of subsequent emitted characteristic X-rays and/or Auger electrons, or by electron energy loss spectroscopy.

In the following sections, factors that determine the probability of a particular process

occurring will be investigated, which include innate properties of the molecular potential energy surfaces, via Franck-Condon factors, as well as the energy of the incident electron.

2.2.2 Frank-Condon principle

Electron ionization of a target molecular species involves the transition between two well-defined electronic states. The changes of vibrational quantum states within the system following the ionization are described within the framework of the Franck-Condon principle [9]. Qualitatively, the principle can be understood in terms of the following description: since nuclei are so much more massive than electrons, during an electronic transition, no (or negligible) changes in the geometric positions and velocities of the nuclei of a molecule occur. The system therefore has the same nuclear configuration immediately before and after the transition. This implies that the location on the potential energy surface of the nascent molecular ion, i.e. the geometric configuration of the molecule after the transition, lies directly above the point on the potential energy surface corresponding to the neutral geometry of the ground state molecule (as illustrated in Figure 2.1). Hence, these transitions are referred to as "vertical" transitions. In the context of electron ionization, the validity of the Franck-Condon approximation can be easily appreciated by the fact that the ratio of nuclear to electronic mass is so great that the amount of momentum that incident electrons can transfer to the nuclei is negligibly small.

For a diatomic molecule, the quantum mechanical interpretation of the Franck-Condon principle is formulated in the following equation:

$$P_{a,b} \propto \left[\int \Psi_a^* \Psi_b \mathrm{d}r \right]^2 \tag{2.10}$$

where $P_{a,b}$ is the probability that the transition involves the vibrational level a in the lower electronic state and b in the upper molecular ion state. Ψ_a and Ψ_b are the corresponding vibrational wave functions. r is the internuclear distance. This probability depends on the relative positions of the potential energy curves (for a diatomic molecule) or

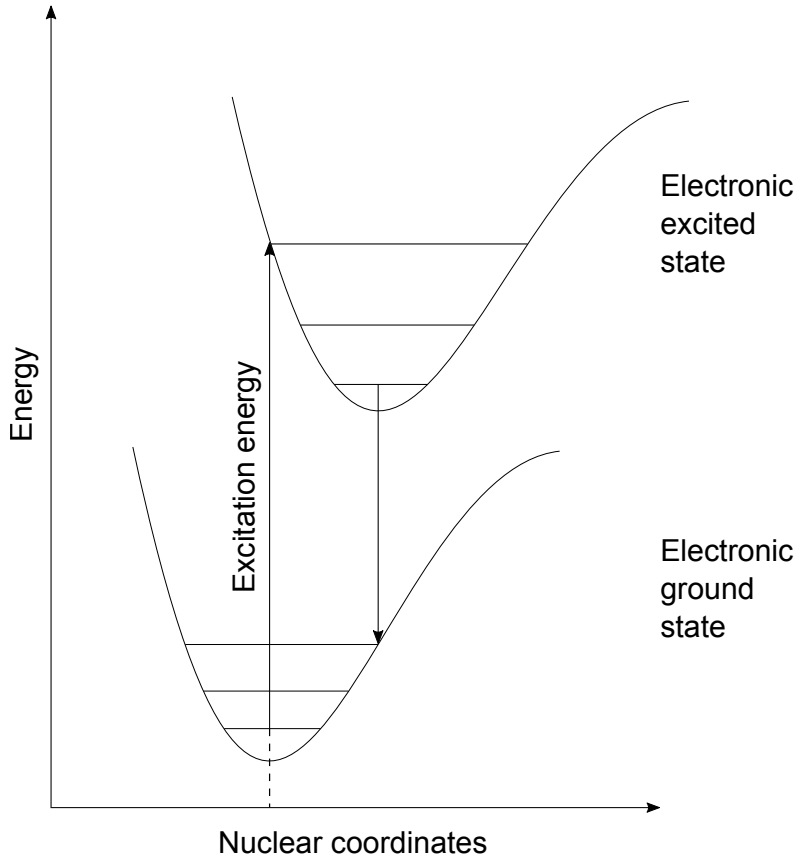


Figure 2.1: Schematic Franck–Condon principle potential energy diagram of a diatomic molecule. Note that the geometric configuration of the molecule in the electronic excited state lies directly above the point on the potential energy surface corresponding to the neutral geometry of the electronic ground state molecule.

high-dimensional potential energy surfaces (for molecule consists of N atoms, where $N \geq 3$) of the two states.

2.3 Types and properties of ions produced

2.3.1 Molecular ions

A molecular ion is defined as the positively charged ion produced by ejection of one electron from a neutral molecule. As mentioned above in Section 2.2.1, no ions are formed when energy of incident electron is below ionization potential, which is between 7 and 15 eV for most molecules. At energies just above the ionization potential, singly charged molecular ions are produced. As the incident energy is increased well above

the ionization potential, fragment ions and multiply charged ions become observable as higher vibronic levels of the ion become accessible.

The relationship between the size of the molecule and the stability of its molecular ion has been studied and summarised [7]. For small diatomic, triatomic, and some tetratomic molecules, with a few exceptions the molecular ion is abundant in the electron ionization mass spectrum across all electron energies [10]. However, for larger molecules, the molecular ion generally becomes less abundant as either the electron energy [11] or the molecular size increases [12], again with some exceptions [13]. Some molecular ions are too transient to be detected in the majority of mass spectrometry experiments, with lifetimes of less than 10^{-5} s.

Electron ionization mass spectra are normally recorded with electron energies in the range 50-100 eV. Within this range, fragmentation patterns tend to be less variable than in other energetic regions, and the ionization cross-section (and therefore the ion signal) usually reaches its maximum within such energy range. Since these energies are well above the ionization threshold, multiple fragment ions are expected to be seen. As a result of this fragmentation, electron ionization is therefore termed a “non-soft” or “hard” ionization technique. Photoionization, on the other hand, usually invokes much less fragmentation (depending on the photon energy employed), and is termed a “soft ionization” technique.

Another factor that can affect the production and stability of the molecular ion is the temperature of the neutral molecules. As shown in Figure 2.2, the relative intensities of triacontane parent ion decrease considerably with increasing fragmentation rate when being raised from 343 K to 538 K [11]. This is due to the increase in vibrational energy of the molecular ion at higher temperature.

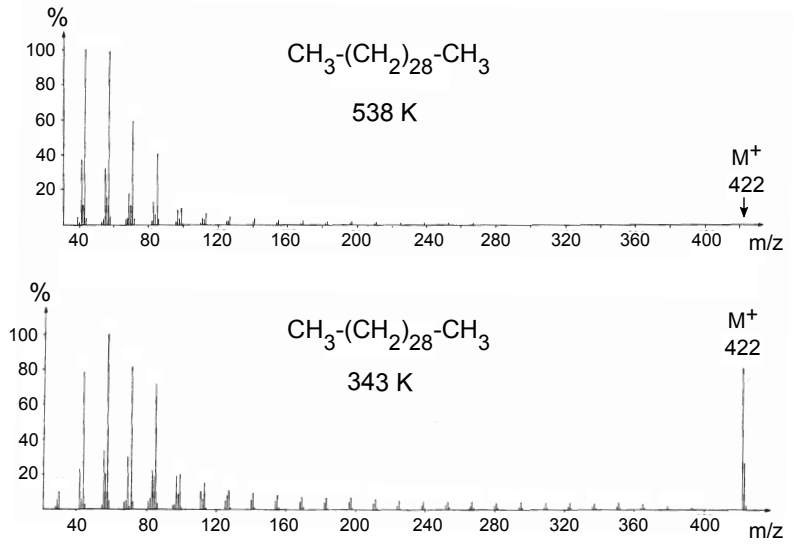


Figure 2.2: Schematic mass spectrum of triacontane at 70 eV electron energy at temperature of 538 K and 343 K [11].

2.3.2 Fragment ions

Fragment ions, as the name suggests, are the dissociation products of ionization process (Equation (2.5)). Nearly all electrically neutral organic molecules have an even number of electrons. When an electron is removed during an ionization process, the resultant molecular ion $M^{+\bullet}$ has an odd number of electrons, which can then dissociate into an even-electron fragment ion and a neutral radical:

$$M^{+\bullet} \rightarrow F_i^{+} + N_j^{\bullet} \tag{2.11}$$

$M^{+\bullet}$ can also dissociate into an odd-number-electron fragment ion and a neutral atom (or molecule):

$$M^{+\bullet} \rightarrow F_i^{+\bullet} + N_j \tag{2.12}$$

Fragment ion F_i^{+} is referred to as a primary fragment ion, and may undergo further dissociation to form secondary or even further fragment ions with lower formula weight.

For a triatomic molecule ABC, five primary fragment ions may be obtained via a series of possible fragmentation pathways as shown below:

$$ABC + e^- \rightarrow ABC^+ + 2e^- \tag{2.13}$$

$$ABC^+ \rightarrow A^+ + BC \rightarrow A^+ + B + C \tag{2.14}$$

$$ABC^+ \rightarrow AB^+ + C \rightarrow A^+ + B + C \tag{2.15}$$

$$\rightarrow A + B^+ + C \tag{2.16}$$

$$ABC^+ \rightarrow A + BC^+ \rightarrow A + B + C^+ \tag{2.17}$$

$$\rightarrow A + B^+ + C \tag{2.18}$$

$$ABC^+ \rightarrow AB + C^+ \rightarrow A + B + C^+ \tag{2.19}$$

Fragment ions generally bear the chemical and physical characteristics of their respective parent molecular ions, such as the bond strength of the ions. Mass spectrometry can be used as a structural technique to work out how fragments fit together to form the original parent molecule. Nonetheless, this is a demanding task, particularly for large molecules with many possible fragmentation channels.

Fragment ion formation can be investigated theoretically with the help of the Franck-Condon principle, and the results compared with experimental data. Advances in *ab initio* electronic structure methods [14] have made possible the calculation of electronic states and their crossings on potential energy surface for small polyatomics, which are the focus of this thesis, will be discussed in detail in Chapter 3. However, it remains challenging to use the abovementioned approaches or even quasi-equilibrium theory to consider large polyatomic molecules, due to the vastly increased complexity and number of parameters such as frequencies, moment of inertia, and activation energies [15].

The overall rate of production of fragment ions is the combined result of their rate of formation and rate of decomposition. These depend on factors such as ionization potential, electron configuration, bond dissociation energies, and rearrangement and elimination channels.

2.3.3 Multiply charged ions

Multiply charged ions, though generally formed in low abundance compared to singly charged ions, may be produced via reactions (2.2) and (2.3) listed above in Section 2.2.1. The first doubly charged molecular ions were observed almost a century ago by J. J. Thomson [16], and later by Conrad [17] and by Vaughan [18]. Ever since then, a wealth of doubly charged polyatomic and even triply charged molecular ions have been observed. While certain types of molecules fail to produce any doubly charged ion, others may produce only doubly charged parent molecular ion (e.g. NH_3) [19], or both doubly charged parent molecular ions and fragment ions (e.g. PH_3) [20].

The observation, or not, of doubly charged ions largely depends on the specific types of molecules being considered. Molecules containing relatively strong bonds, such as aromatic or heteroaromatic species [21], as well as some aminoboranes [22], polyfluor compounds [21], and organometallic compounds [23], yield doubly charged ions with reasonable efficiency. In some cases, the abundance of doubly charged ions is even higher than those of the corresponding singly charged ions [24, 25]. In contrast, saturated aliphatic hydrocarbons are easily fragmented and yield virtually no doubly charged ions [21]. However, if double bonds are constituent parts of the molecules, fragmentation becomes less likely due to strong π-bonding, thus increasing the stability of doubly charged ions [26]. Readers are directed to more detailed review in this matter [27].

In the event of decomposition of doubly charged molecular ions, two different channels are possible, in a way similar to the singly charged molecular ion analogs. Now the two charges can either be shared between the two products, or reside on only one fragment.

$$AB^{2+} \rightarrow A^{+} + B^{+} \tag{2.20}$$

$$AB^{2+} \rightarrow A^{2+} + B \tag{2.21}$$

It has been noted that the charge separation channel (2.20) generally dominates [28]. Such channels often involve Coulomb-explosion type mechanisms as a result of the strong Coulomb repulsion between the two charges. Studies of Coulomb explosions, and more recently, use of Coulomb explosion imaging techniques as a probe of molecular structure, have attracted a great deal of interest during the past few decades [29–33]. Coulomb explosions are treated in detail in Chapters 6 and 7.

Decomposition channels of the type shown in Equation (2.21) have been observed in several experimental studies, with mechanisms including loss of CO [34], C_2H_2 and C_2H_4 for even mass number ions [35] and other neutral molecules. Triply charged fragment ions are also evident in some systems, which strongly suggests the formation of triply charged molecular ions in the initial ionization process [35].

2.3.4 Metastable ions, stable ions, and unstable ions

Metastable ions are ions produced with sufficient internal energy to enable them to dissociate *en route* from the ion source to the detector, usually within a time scale a of $<10^{-5}$ s. They are defined as metastable in contrast to stable ions which reach the detector without decomposition, and unstable ions which possess enough internal energy to dissociate immediately before leaving the ion source. They can also be classified in terms of the time scale over which ions traverse a mass spectrometer: ions that dissociate at rates above 10^6 s^{-1} are termed unstable; those that dissociate at rates below 10^5 s^{-1} or remain undissociated are termed stable; and those dissociating at rates in between (i.e. $10^5 \sim 10^6$ s^{-1}) are the so-called metastable ions [36]. Fraction of different types of ions as a function of rate constants of ion dissociations is illustrated in Figure 2.3.

2.3.5 Rearrangement ions

Rearrangement ions are considered to be those containing bonds that do not exist in their respective precursor molecule.

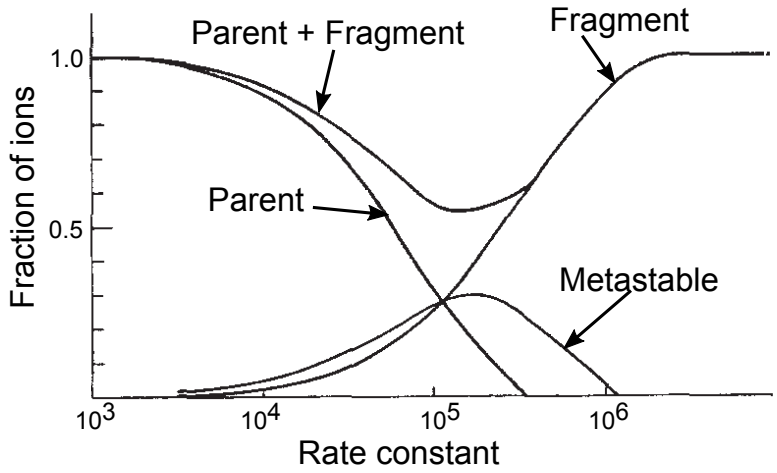


Figure 2.3: Fraction of different types of ions termed in mass spectrometry as a function of rate constants of ion dissociations [37].

$$\mathrm{ABCD} + \mathrm{e} \rightarrow \mathrm{ABCD}^+ + 2\mathrm{e} \rightarrow \mathrm{AD}^+ + \mathrm{BC} + 2\mathrm{e} \tag{2.22}$$

Observable rearrangements need to take place at some time in between formation of the precursor ABCD^+ and detection of the fragment. The relevant timescales over which this can occur and still be observed will depend on the type of mass spectrometer and mass selection approach being employed.

Common rearrangements include transfer of hydrogen, fluorine, and larger functional groups such as CH_3 or C_6H_5. Classification of structure determination in molecular rearrangement and respective mechanisms were proposed by McLafferty [38]. Review is available for further details on this topic [39].

2.4 Total ionization cross-sections

2.4.1 Introduction

The total ionization cross-section, σ, quantifies the probability of forming an ion during a collision between an electron and a molecule. It gives no information on the identity of the ion (or ions); this information is given by the partial ionization cross-section, σ_i, for

formation of the ion i of interest. The total cross-section is equal to the sum of the partial cross-sections for all ions that can be formed during the collision, and can be expressed as:

$$\sigma = \sum_i z_i \sigma_i \tag{2.23}$$

where z is the charge state of ion i.

The total ionization cross-sections mentioned above is also termed gross ionization cross-section, as opposed to another type of total cross-section called counting ionization cross-section:

$$\sigma_c = \sum_i \sigma_i \tag{2.24}$$

Within this work, only gross ionization cross-section will be measured and discussed.

Studies aimed at determining total electron ionization cross-sections via both experimental and theoretical means have been conducted extensively since the 1930s. As one of the most fundamental measurements in the field of electron ionization, cross-section data are of great interests in many areas such as astrochemistry, astrophysics, stellar atmospheres, and radiation chemistry, and are needed for modelling and quantitative data analysis in fields such as plasma physics, mass spectrometry, vacuum technology, and so on [6, 7, 40, 41]. In the following, we will outline principles of measurement and calculation of total ionization cross-sections, and review previous work in the area.

Absolute cross-sections are given in units of area, usually Å^2. We note that some experimental techniques are not able to determine absolute cross-sections, only relative cross-sections, usually normalized to an arbitrary value.

2.4.2 Principles of an ionization cross-section measurement

The most straightforward way to measure a total ionization cross-section is via a beam-gas experiment, in which a well collimated and homogeneous electron beam with well-

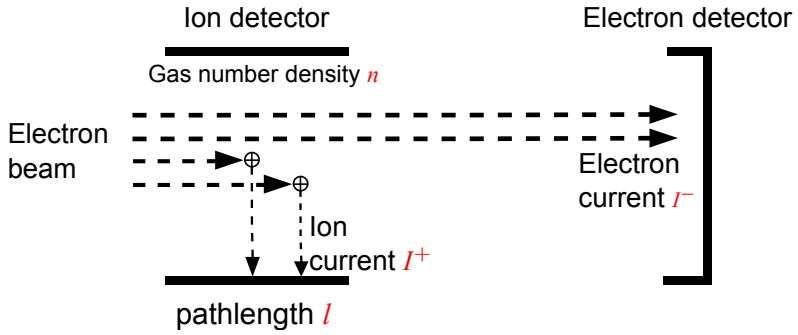


Figure 2.4: Schematic conceptual design of experiment for determining total ionization cross-section. Quantities appearing in the simplified Beer-Lamber law (Equation (2.26)) are colored red.

defined energy passes through a static gas sample. Ions generated within the collision cell are recorded as an ion current, I^+, at an ion detector, and the transmitted electron beam is measured as an electron current, I^-, at an electron detector positioned after the collision cell (see Figure 2.4). The relationship between the incident and transmitted electron currents, I_0^- and I^-, respectively, the number density of the gas molecules n, and the pathlength over which electron beam collides with gas molecules l, can be described by the Beer-Lambert law

$$\frac{I^-}{I_0^-} = \mathrm{e}^{-\sigma n l} \tag{2.25}$$

For an ideal gas, the number density can be calculated from $n = p/k_\mathrm{B}T$, where p and T are the pressure and temperature of the gas sample, respectively, both of which can easily be measured during an experiment.

As noted above, in an experiment, one typically records the transmitted electron current, I^-, and the ion current I^+, rather than measuring the incident electron current I_0^-. By ensuring that measurements are made under conditions such that attenuation of the incident electron beam is small, i.e. $I_0^- \approx I^-$, and using the Taylor expansion $\mathrm{e}^x \approx 1 + x + \cdots$, the Beer-Lambert law can be simplified to:

$$\frac{I^+}{I^-} = \sigma n l \tag{2.26}$$

Therefore, determination of the total ionization cross-section σ, simply requires the accurate measurement of I^+, I^-, n (i.e. p and T) and l . A detailed derivation of both Equations (2.25) and (2.26) can be found in Appendix A.

2.4.3 Experimental considerations

According to Equations (2.23) and (2.26), the only difference between determining total ionization cross-sections and partial ionization cross-sections from an experimental point of view is whether it is necessary to separate the ions according to their identity before recording the ion current. For total ionization cross-sections measurements, a device capable of collecting the total signal from all ions is sufficient. For partial ionization cross-section measurements, a mass analyser is usually incorporated into the experiment in order to sort the ions according to their mass-to-charge ratio before recording the ion current for each ion type. In practice, this is achieved by recording the mass spectrum of ions produced in the electron-molecule collisions as a function of the collision energy. In such an experiment it is usually only possible to record the relative amounts of each ion formed. To convert the mass spectrum into a set of absolute partial cross-sections, the charge-weighted sum (Equation (2.23)) is normalized to a known absolute total ionization cross-section. Kieffer and Dunn have presented a through review of partial ionization cross-section measurements, with a detailed discussion of experimental conditions and challenges [42]. Some of the key issues, with particular relevance to modern instrument set-up, will be summarised below.

2.4.3.1 Electron current I^- and ion current I^+

Despite the relatively simple theory behind total ionization cross-section measurements, as formulated in Equation (2.26), the practical issues of measuring each of the quantities are critical to the accuracy of measurement and can severely affect the accuracy of the total ionization cross-section data obtained. For an accurate measurement, a known

fraction (or all) of the product ions must be detected along a known pathlength over which those ions were formed, together with the total transmitted electron beam current and the number density of the gas molecules in the region where ionization events happen. The ion and electron collection efficiencies should be as high as possible. Table 2.1 summarises some of the experimental considerations in ensuring that these measurements are made as accurately as possible.

The ability to achieve high ion and electron detection efficiencies is determined primarily by the design of the cross-section measurement apparatus. Detection of secondary electrons should be minimised, as should scattering of electrons or ions from their respective detectors. The first of these requirements can often be satisfied through the geometrical design of the instrument, so that secondary electrons generated in the electron-molecule collisions or by surface scattering are unlikely to reach either detector. The second is achieved by coating the detector surfaces with a layer of a high conductance material such as colloidal graphite, which greatly reduces the number of secondary electrons and scattered particles from the surfaces. Most importantly, the detectors and ion optics need to be designed in such a way that the generated electric field effectively directs all nascent ions to the ion detector and all transmitted electrons to the electron detector, with little or no scattering of either type of particle from electrostatic lens elements within the system.

2.4.3.2 Number density n

The number density n of the gas sample is obtained indirectly from the measured pressure p and temperature T using the ideal gas law:

$$p = nk_{\mathrm{B}}T \tag{2.27}$$

In principle, more accurate gas laws could be used, but at the low sample gas pressures (10^{-4} Torr) employed in the experiments, treating the gas as ideal is usually sufficient.

Table 2.1: Necessary conditions for each quantity in order to accurately measure ionization cross-sections.

Quantities	Conditions
Ion current I^+	Maximise the ion collection efficiency. Ensure that no secondary electrons are detected at the ion collector, and that ions are not scattered from the ion collector rather than being detected.
Electron current I^-	Maximise the electron collection efficiency. Ensure that electrons from other sources are not be collected by Faraday cup.
Temperature T	Measure temperature both inside the collision cell and the pressure gauge simultaneously and accurately.
Pressure p	Maintain the pressure inside the collision cell at a sufficiently stable value that averaging over a number of measurements is possible.
Pathlength l	Determine an accurate pathlength, including accounting for effects from any magnetic field used to collimate the electron beam.

While temperature is straightforward to measure, and introduces only very small experimental uncertainties, accurate pressure measurements at low pressures present more of a challenge. A typical issue is related to maintaining a constant pressure inside the cell. It requires a careful balance between the rate of gas entering the cell, which depends on the pressure in the gas line and the operation of the needle valve used to admit the gas to the cell, as well as the pumping speed of gas out of the cell. While this is straightforward in principle, in practice it is quite difficult to keep the pressure highly stable at the relatively low pressures of approximately 10^{-4} Torr required to do the experiments, and some pressure fluctuations during the experiment are inevitable. The easiest and usually working solution is to take the average value of many readings (e.g. 30 or more).

2.4.3.3 Pathlength l

The pathlength is determined primarily by the geometrical distance along the axis of the ionization cell, l, over which gas molecules are ionized by electrons. However, since most instruments use a magnetic field to help collimate the electron beam, the

actual trajectory of electrons, L, includes a cyclotron or helical component which slightly increases the effective pathlength. In practice this is a small effect [43]. If the helical radius of the electron path is determined by the angle at which the electron beam enters the magnetic field, the maximum pathlength is

$$L = l\left(1 + \frac{1.10 \times 10^{-4} d^2 H^2}{V}\right) \tag{2.28}$$

where d is the diameter of the entrance aperture to the collision cell in mm, H is the strength of the magnetic field in Gauss, and V is the energy of the electrons in electron volts [44]. This expression can also be written as the ratio between transverse electron velocity $v_\perp$ and total velocity v as below [45]:

$$L = l\left[1 - \left(\frac{{v_\perp}^2}{v^2}\right)\right]^{-\frac{1}{2}} \tag{2.29}$$

Asundi [46] showed that the pathlength is primarily governed by the energy available to electrons normal to the magnetic field direction, and concluded that $\left({v_\perp}^2/v^2\right)$ is as small as 0.001 for one of the early instruments used by Tate and Smith to record total ionization cross-sections. This was assessed as being safely negligible [47]. Craggs and co-workers also found out that scattering of electrons by gas molecules is a possible contribution to the transverse component of the electron energy [48]. Other studies exploring various factors affecting pathlength showed that these were all insignificant [49].

2.4.3.4 Electron energy

Electron energy is usually determined by the potential difference between the electron source such as a filament, and the collision region, which needs to be uniform and well-defined across the whole region. Historically, most total ionization cross-sections apparatus utilised a pair of parallel plates (condenser-plate method) as the collision region which created a non-uniformed electric field as well as a voltage drop across the electron-beam width. The electron energy along the beam between the condenser

plates are therefore not precisely zero, which invalidated the definition of electron energy as per filament voltage. A pair of grounded guarding plates are commonly applied to ascertain uniform electric field within the ion collector region [47, 50–53]. Another practical method is to employ of a pulsed electron beam followed by a delayed pulsed ion collector voltage, such that the fast electron beam wouldn't be experiencing the ion collector field at the time of colliding with target gas [54, 55].

Potential drop across the filament of electron gun is another critical consideration in determining electron energy, especially those near the threshold region. Thermal velocities of electrons that leave the filament introduce uncertainly to the definition of electron energy, which will need to be taken in account when reporting final results. In addition, contact potential difference between filament and ion collector may cause deviation of electron energy from nominal voltage values on filament. Further discussion about how to consider and correct electron energy of current experimental set-up will be presented in Chapter 4.

2.4.4 Experimental techniques for measuring total ionization cross-section

2.4.4.1 Condenser-plate method

Historically, the condenser-plate method has been the most commonly used method for measuring total ionization cross-sections. A typical setup is shown schematically in Figure 2.5. Based on the principle described in Section 2.4.1, the key feature is the two parallel plates that act as ion collecting electrodes. The setup shown in the diagram is from one of the very early pioneering experiments performed by Compton and Van Voorhis, who measured the probability of ionization for a series of diatomic and noble gas molecules [56]. The basic procedure was to bombard static gas samples with the electron beam, and use the ion collecting electrodes to collect product ions formed in the electron-molecule or electron-atom collisions. The reliability of the measured data was

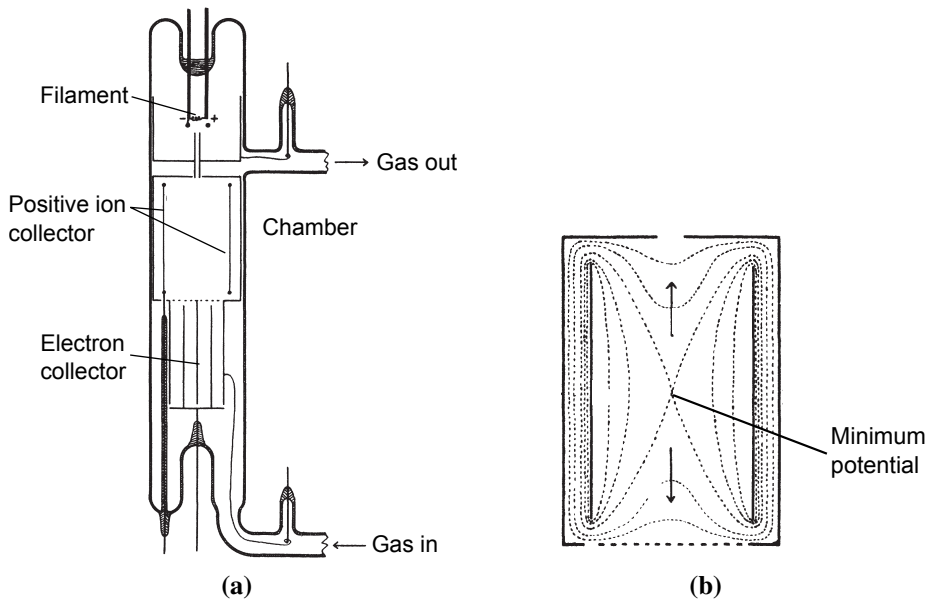


Figure 2.5: Schematic diagram of (a) Compton and Van Voorhis' total ionization apparatus and (b) equipotential surfaces of ionization chamber (adapted from [56]).

limited by the fact that a large non-zero electric field was applied in the ion collection region (Figure 2.5(b)) in order to prevent collection of scattered electrons from the primary beam, which led to an inaccurate definition of the electron energy (see Section 2.4.3.4 for discussion of factors affecting the electron energy).

To overcome this difficulty, Tate and co-workers [47, 52, 57] introduced a solenoid to surround the collision cell in their experiment so that a magnetic field of 250 G could facilitate the separation of ions from electrons, as well as better define the electron beam. This greatly reduced the potential difference that needed to be applied across the ion collecting plates, allowing a more accurate knowledge of the electron energy.

In the apparatus used by Tate and co-workers, shown in Figure 2.6, electrons were generated by heating a tungsten wire filament, and collimated by a set of lenses before entering the collision region containing sample gas in the region between two parallel plates. Product ions were collected on the top plate as a result of the electric field applied between the two plates. The top plate was connected to a guard-ring to ensure the homogeneity of the electric field. The unscattered portion of the primary electron

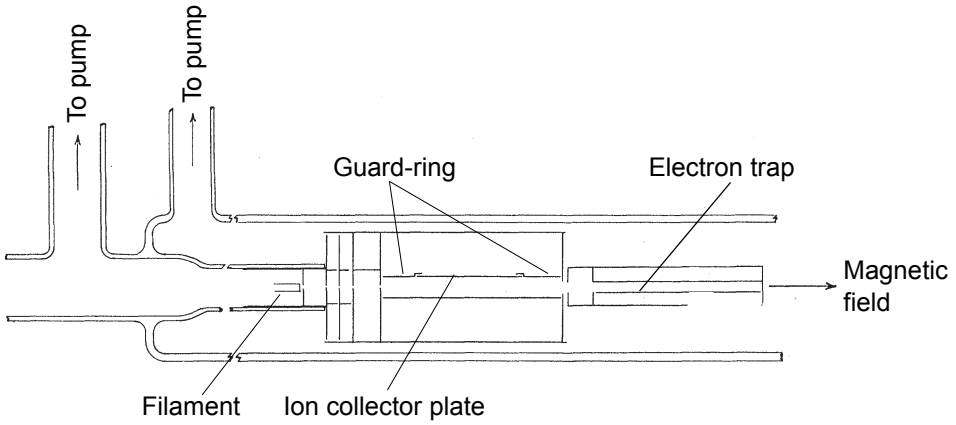


Figure 2.6: Schematic diagram of Tate and co-workers' total ionization apparatus (adapted from [47]).

beam was recorded as an electron current at the electron trap. The number density of gas molecules was calculated from the ideal gas law (Equation (2.27)) after measurement of the gas pressure and temperature. The absolute total ionization cross-section was then obtained from the Beer-Lambert law (Equation (2.26)) given in Section 2.4.1. Tate and co-workers' apparatus has been used and modified in many later experiments, due to its excellence of design.

Later in 1960s, Rapp and Englander-Golden [58] improved on the experiments of Tate and Smith, and measured absolute total cross-sections on a batch of common atoms and small molecules which are now considered to be benchmark data. Their improvements can be attributed to their careful consideration of many aspects of the instrumentation and procedures. A McLeod gauge was a popular choice for measuring the low samples pressure within collision chamber, but gave rise to a source of error due to a steady mercury stream diffused from the mercury reservoir to the cold trap, and causes incorrect readings of pressure, as revealed by Ishii and Nakayama in 1961 [59]. To overcome this, Rapp and Englander-Golden only used a McLeod gauge for measuring the pressure of $H_{2,}$ and devised a new method for measuring the sample pressure based on characterising the relationship between the collision chamber pressure and the reservoir pressure, which moderately improved the accuracy of the results. Consistency checks on the

ion and electron collection efficiencies were also made to assure complete collection of electrons and ion currents.

A further improvement to the pressure measurement was made by Djurić and co-workers, who used a capacitance manometer for determining the collision cell pressure [60, 61]. A capacitance manometer provides an absolute pressure measurement, independent of the identity of the sample gas, and can record accurate pressures down to around 10^{-6} Torr.

2.4.4.2 Lozier tube

Another group of total ionization cross-section data was measured using a Lozier tube apparatus, which was first described and then later improved by Lozier [51, 62–64]. The design and modified versions thereof have since been used for a number of other measurements [46, 48, 65]. A schematic diagram of the Lozier tube is shown in Figure 2.7. The main difference compared to the condenser-plate apparatus can be seen inside the collision chamber, where a set of inner vanes are placed concentrically about the axis of the electron beam and are grounded with the two plates at each end of the chamber. Another set of outer vanes are set to either a negative or positive voltage, depending on whether one wishes to detect positive or negative ions formed in the electron-molecule collisions. A cylinder and a further guard electrode encompass the vanes. By applying a suitable electric field in the intervals between the cylinder and the outer vanes, and between the outer vanes and the inner vanes, the kinetic energy of either positive or negative ions can be measured. An external solenoid is used to generate a magnetic field along the electron beam axis in order to confine the beam to this axis. Since only ion currents (and corresponding electron currents) are measured, and not the pressure and temperature of the sample gas, the obtained total ionization cross-sections are relative quantities as a function of electron energy and must be normalized to known absolute total ionization cross-sections.

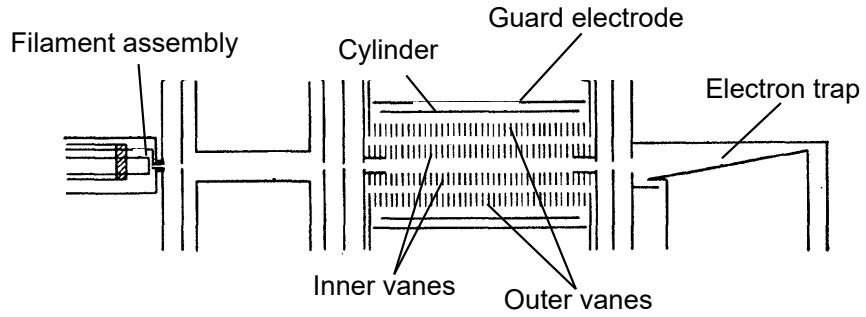


Figure 2.7: Schematic diagram of Lozier tube (adapted from [63]).

Because of the fact that the collision chamber is designed to selectively collect ions at right angles to the electron beam, anisotropies in the angular distribution of dissociation products are not considered. This can cause significant errors in the data measured [66], especially for polyatomic gas molecules at high electron energy [67].

2.4.4.3 Bell and Nottingham method

Bell and Nottingham [68, 69] measured the electron ionization cross-section of mercury vapor with an apparatus capable of accurately determining the electron energy based on a known magnetic field and known dimensions of the ion chamber. The basic design of their apparatus are shown in Figure 2.8. Electrons were generated from the filament and accelerated into the analyser, and only those with desired energy could pass the the exit slit. They were then accelerated into ion chamber, and the increased radius of the electron path enable them to pass out via exit slit and to be collected by electron cage. Positive ion collector with inner and outer grids are located in the centre of ion chamber. With certain similarities to the condenser-plate method, the novelty of their design is a semi-circular channel after the filament which only selected electrons with desired energy.

2.4.4.4 Crossed-beam methods

In contrast to the abovementioned techniques, the crossed-beam method is designed to allow measurements on species that are not necessarily stable at normal temperature,

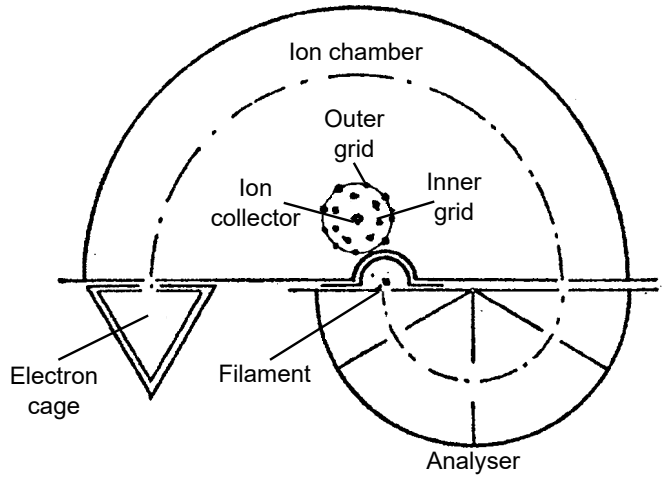


Figure 2.8: The schematic diagram of the top view of the experimental tube of Bell and Nottingham method (adapted from [68, 69]).

such as atomic hydrogen, helium, and oxygen. The method was first used by Boyd and Green [70] and Fite and Brackmann [71] for studying ionization cross-sections of atomic hydrogen on electron impact. The schematic design of a general crossed-beam apparatus is shown by Figure 2.9. A collimated beam of electrons is accelerated to intersect at right angles with a beam of neutral atomic species, and the ions produced in the resulting collisions, as well as the electron beam current, are detected. Though the experiment is performed within a high-vacuum system, the collected ion signal inevitably includes some contribution from ionization of background gas by the electron beam. Often, this contribution is large (in Fite and Brackmann's study, the background signal was 40 times higher than the crossed-beam signal [71]). Solutions to separate the two signals often involved introducing modulation to the source beam and/or electron beam by means of a chopper wheel, and detecting only the modulating part of the resulting ion signals [70–72].

Due to the dynamic nature of the source beam, the equation for determining ionization cross-sections from a crossed-beam experiment is modified as follows [73]:

$$\sigma(E) = \frac{I_{\mathrm{i}}(E)\, v_{\mathrm{e}} v_{\mathrm{n}}}{I_{\mathrm{e}}(E)\, RF\, (v_{\mathrm{e}}^2 + v_{\mathrm{n}}^2)^{\frac{1}{2}}} \tag{2.30}$$

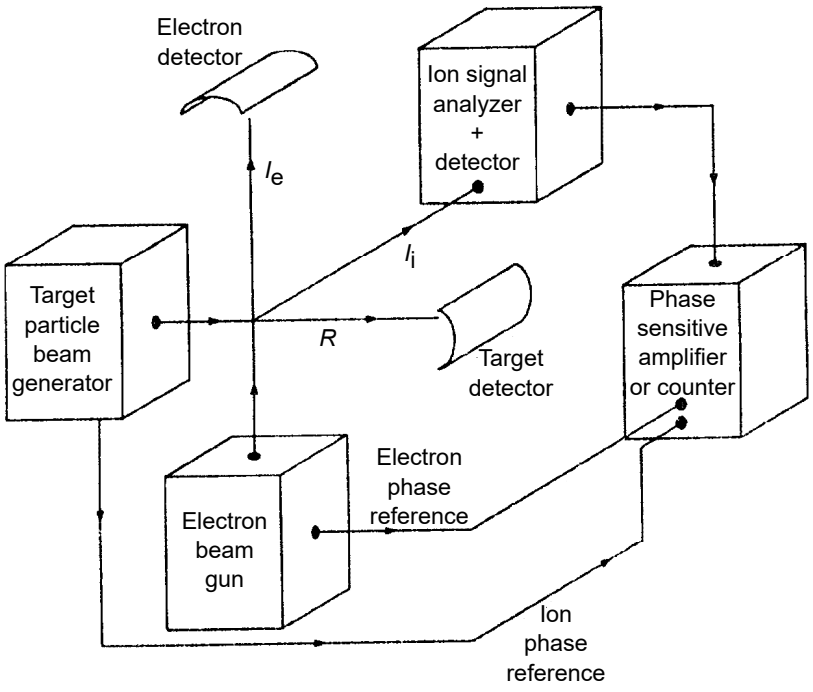


Figure 2.9: Schematic block diagram of crossed-beam apparatus used in Fite and Brackmann's experiment (adapted from [42]).

where I_i and I_e are the ion current and electron current, respectively. v_e and v_n are the electron beam and neutral beam velocities, respectively. R is the number of target atoms/molecules arriving at the collector per second. E is the relative energy of the target particles and electrons, and F is a measure of the overlap of the two beams, which is mathematically given by:

$$F = \frac{\int j_n(z)\, j_e(z)\, dz}{\int j_n(z) dz \int j_e(z)\, dz} \tag{2.31}$$

where j_n and j_e are the source and electron beam profiles measured as a distribution of distance from the centre of the beams. Depending on whether it is feasible to measure R or not, absolute or normalized relative cross-section data can be obtained, respectively [73].

Based on the crossed-beam approach, the orientation dependence of electron ionization cross-sections has been studied using a beam of spatially oriented symmetric top

molecules prepared using a combination of an inhomogeneous hexapole electric field and a uniform orienting field [74]. It was demonstrated that, for CH_3Cl as an example, ionization cross-section is larger when electron approaches the partially positively charged CH_3 end of the molecule than the negatively charged chlorine end.

2.4.4.5 Summation method

In mid 1970s, Märk and Egger [75, 76] introduced a method which essentially consisted of a double-focussing-type mass spectrometer to measure relative partial ionization cross-sections as a function of electron energy. The relative partial ionization cross-sections of various ions were then summed as per Equation (2.23) to yield the relative total ionization cross-section, which were then normalized by a factor which is the ratio of a known absolute total ionization cross-section value at a particular electron energy to the relative total ionization cross-section at the same electron energy. Assuming the ion and electron collection efficiencies are constant, the normalisation factor is assumed to be, and should be, independent of the electron energy. For molecules for which no absolute total ionization cross-section data was available, the normalisation factor was assumed to be the same as that for a noble gas, such as Ar, for which the absolute total ionization cross-section is known [20]. Consistency checks were performed for the summation method, and the dependence of the total ionization cross-section on electron energy was found to be in good agreement with those reported by Rapp and Englander-Golden [58].

2.4.4.6 Gas-filled counters

The use of gas-filled counters to study electron ionization at high collision energies was first explored by Graf [77] and followed by McClure [78]. More extensive studies were performed by Rieke and Prepejchal on 40 gases for electrons with incident energies in the range from 0.1 to 2.7 MeV [79]. The high incident energies used in these measurements are particularly beneficial for comparing results with Bethe theory [80, 81].

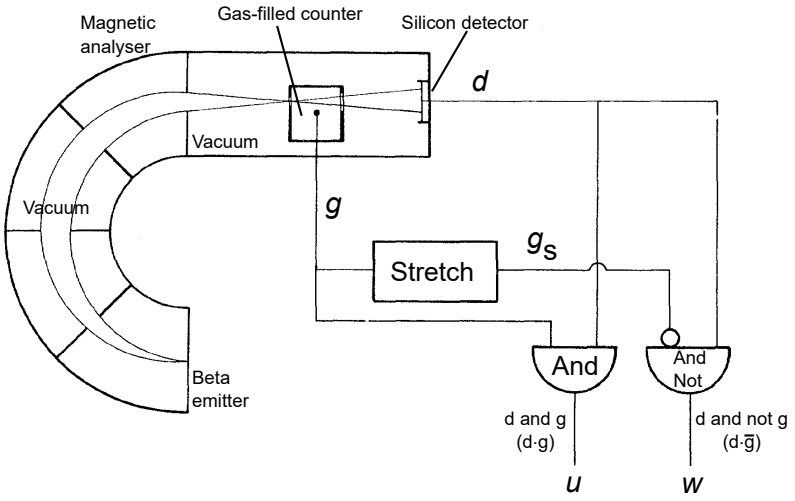


Figure 2.10: Schematic diagram of gas-filled counters apparatus used in Rieke and Prepejchal's experiment (adapted from [79]).

The principle underlying the gas-filled counter method is still based on the basic principles outlined in Section 2.4.1. If an electron travels across a pathlength of L through a static gas with number density n, the relationship between ionization cross-section σ and average number of ionization events, z, per electron is given by:

$$z = nL\sigma \tag{2.32}$$

and the probability θ that no ionization takes place, and therefore that the electron is transmitted, can be described by:

$$\theta = \mathrm{e}^{-z} \tag{2.33}$$

Therefore, the ionization cross-section σ can be determined if θ, n, and L are measurable in the experiment.

The apparatus that was used in Rieke and Prepejchal's work is illustrated schematically in Figure 2.10. Electrons are generated from a beta emitter, are then energy selected by the magnetic analyser, enter the gas-filled counter via a thin-window, and eventually reach the silicon barrier-layer detector. Depending on whether ionization events occur or

not, two channels of pulse are observed. Channel d•g records an ionization by electron impact, where channel d•$\overline{g}_s$ records no ionization when primary electron passes through the gas sample without producing any ions. The "stretch" unit acts to exclude d•$\overline{g}_s$ pulses that originated from detector when gas-filled counter is not yet recovered from its full sensitivity after responding to an ionization event. During an experiment, if there are u counts in channel d•g, and w counts in channel d•$\overline{g}_s$, the probability that the incident electron gives rise to no ionization event, Φ, is:

$$\Phi = \frac{w}{u+w} \tag{2.34}$$

Φ may or may not be equated to θ, depending on whether wall effects can be excluded or not.

2.5 Application of electron ionization cross-section data

With the improvement in experimental measurements as introduced in preceding sections, it is perhaps not surprising that ionization cross-section data are of great practical interests in diverse fields such as plasma modelling, stellar atmospheres, mass spectrometry, biological processes, and may also be used for testing theoretical predictions and approximations. A general discussion of ionization cross-section data in some of the most representative application areas is given in this section.

2.5.1 Plasma modelling

Plasma, the fourth state of matter, is gas that contains sufficient energy that ionized species are formed within it. Plasma processing is a plasma-based technique for material processing where new materials with superior properties are produced and existing materials and surfaces are altered and refined. Typical activities include manufacturing of electronic materials, techniques of deposition and coating, production of powders of uniform size, and melting and refining of engineering materials [82]. Ions and radicals

are formed through collisions of electrons with a feed gas, leading to various chemical reactions at the material surface that result in processes such as etching, cleaning, and deposition. Electron collision data are critical in understanding the nature of those processes [83], and therefore for modelling such processes. This is particularly important for microelectronics fabrication industry, where accurate simulations are needed in order to improve on plasma equipment and to develop novel processes [40, 84, 85].

Another important plasma process is the plasma-wall interaction processes in fusion experiments such as the tokamak nuclear fusion reactor [86]. Inside the tokomak, fusion occurs in a plasma contained within a torus-shaped vacuum chamber. Due to their low radiative capacity and high heat resistivity, carbon-based wall materials are commonly used in tokamaks to contain the plasma [87]. As a result of interactions of the hydrogenic plasma with these carbon-based wall materials, a variety of hydrocarbon molecules and ions are produced near the edge of the fusion plasma. In order to model the fusion plasma properly, accurate and detailed knowledge of the total and partial electron ionization cross-section of those molecules are needed [88]. Additionally, ionization cross-sections data may be used to assist the modelling of turbulent transport of trace impurities in the edge of tokamaks [89].

2.5.2 Biological processes

Electron ionization cross-sections are of great importance in modelling radiobiological damage induced by ionizing particles [90, 91]. Collisional dynamics between slow electrons and biomolecules has been studied to demonstrate that the majority of radiation damage to DNA is due to interactions with secondary low energy electron [92]. Understanding of such processes and developing radiation models requires accurately measured ionization cross-sections data [93–96].

2.5.3 Astrochemistry and astrophysics

Hydrogen and Helium are the most common species in the universe, and they are predominantly ionized due to radiative or collisional ionization. Low-energy electrons are generated through ionization of hydrogen and helium, and can go on to partially ionize other heavier atoms and molecules [6]. In particular, molecules in the interstellar medium (ISM) and their ionization processes are of great interest within the astrochemistry community [97], and are the main focuses of current project. Further details about ionization cross-sections of ISM molecules will be covered in Chapter 5.

2.5.4 Other

Other applications of ionization cross-section data include normalization of relative ionization cross-section data to obtain absolute values, mass spectrometer calibration, atmospheric modelling [98], and determination of key parameters in analytical electron microscopy [99].

References

[1] T. D. Märk. “Fundamental Aspects of Electron-Impact Ionization”. In: *International Journal of Mass Spectrometry and Ion Processes* 45 (1982), pp. 125–145.

[2] P. Lenard. “Ueber die lichtelektrische Wirkung”. In: *Annalen der Physik* 8 (1902), pp. 149–199.

[3] A. J. Dempster. “A new Method of Positive Ray Analysis”. In: *Physical Review* 11.4 (1918), pp. 316–325.

[4] J. J. Thomson. “XLII. Ionization by moving electrified particles”. In: *The London, Edinburgh, and Dublin Philosophical Magazine and Journal of Science* 23.136 (1912), pp. 449–457.

[5] J. J. Thomson. *Rays of Positive Electricity and Their Application to Chemical Analyses*. London: Longmans, Green and Co., 1913.

[6] W. Lindinger, F. Howorka, J. M. Shull, A. V. Phelps, E. C. Zipf, Y.-K. Kim, and J. H. Futrell. “Applications”. In: *Electron Impact Ionization*. Ed. by T. D. Märk and G. H. Dunn. Vienna: Springer, 1985.

[7] T. D. Märk. “Ionization of Molecules by Electron Impact”. In: *Electron-Molecule Interactions and Their Applications*. Ed. by L. G. Christophorou. Vol. 1. Orlando, FL: Academic Press, 1984. Chap. 3, pp. 251–334.

[8] L. P. Johnson and J. D. Morrison. “Double ionization to low-lying states of the doubly-charged rare gases”. In: *International Journal of Mass Spectrometry and Ion Physics* 18.4 (1975), pp. 355–366.

[9] J. Franck. “Elementary processes of photochemical reactions”. In: *Transactions of the Faraday Society* 21 (1926), pp. 536–542.

[10] C. J. Schack, D. Pilipovich, S. N. Cohz, and D. F. Sheehan. “Mass spectra and sublimation pressures of IF_7 and IOF_5”. In: *The Journal of Physical Chemistry* 72.13 (1968), pp. 4697–4698.

[11] G. Remberg, E. Remberg, M. Spiteller-Friedmann, and G. Spiteller. “Massenspektren Schwach Angeregter Moleküle. 4.Mitteilung”. In: *Organic Mass Spectrometry* 1.1 (1968), pp. 87–113.

[12] C. Brunnée and H. Voshage. *Massenspektrometrie*. München: Karl Thiemig, 1964.

[13] F. McLafferty. *Interpretation of mass spectra: an introduction*. New York: W. A. Benjamin, 1966.

[14] J. A. Pople. “Molecular orbital studies of the energies and structure of polyatomic cations”. In: *International Journal of Mass Spectrometry and Ion Physics* 19.1 (1976), pp. 89–106.

[15] H. M. Rosenstock, M. B. Wallenstein, A. L. Wahrhaftig, and H. Eyring. “Absolute Rate Theory for Isolated Systems and the Mass Spectra of Polyatomic Molecules”. In: *Proceedings of the National Academy of Sciences of the United States of America* 38.8 (1952), pp. 667–678.

[16] J. J. Thomson. *Rays of Positive Electricity and Their Application to Chemical Analyses*. 2nd. London: Longmans, Green and Company, 1921.

[17] R. Conrad. In: *Physikalische Zeitschrift* 31 (1930), pp. 888–892.

[18] A. L. Vaughan. “Mass Spectrograph Analyses, and Critical Potentials for the Production of Ions by Electron Impact, in Nitrogen and Carbon Monoxide”. In: *Physical Review* 38.9 (1931), pp. 1687–1695.

[19] T. D. Märk, F. Egger, and M. Cheret. “Ionization of ammonia and deuterated ammonia by electron impact from threshold up to 180 eV”. In: *The Journal of Chemical Physics* 67.8 (1977), pp. 3795–3802.

[20] T. D. Märk and F. Egger. “Ionization of phosphine and deuterated phosphine by electron impact from threshold up to 180 eV”. In: *The Journal of Chemical Physics* 67.6 (1977), pp. 2629–2635.

[21] H. Kienitz and F. Aulinger. *Massenspektrometrie*. Weinheim: Verlag Chemie, 1968.

[22] M. J. S. Dewar and P. Rona. “Doubly Charged Ions in the Mass Spectra of Some Organoboron Derivatives”. In: *Journal of the American Chemical Society* 87.23 (1965), pp. 5510–5510.

[23] R. B. King. “Mass spectra of organometallic compounds. VI. Some indenylmetal derivatives and related compounds”. In: *Canadian Journal of Chemistry* 47.4 (1969), pp. 559–568.

[24] M. Solomon and A. Mandelbaum. “Studies in mass spectrometry. Singly- and doubly-charged molecular ions; stability and abundance”. In: *Journal of the Chemical Society D: Chemical Communications* 15 (1969), pp. 890–890.

[25] E. S. Waight. “Studies in mass spectrometry. Singly- and doubly-charged molecular ions; stability and abundance”. In: *Journal of the Chemical Society D: Chemical Communications* 21 (1969), 1258a–1258a.

[26] P. Vouros and K. Biemann. “The structural significance of doubly charged ion spectra. Phenylenediamine derivatives”. In: *Organic Mass Spectrometry* 2.4 (1969), pp. 375–386.

[27] K. Vékey. “Multiply charged ions”. In: *Mass Spectrometry Reviews* 14.3 (1995), pp. 195–225.

[28] B. Brehm and G. de Frênes. “Investigation of ion pairs from fast decay processes of doubly-charged molecular ions”. In: *International Journal of Mass Spectrometry and Ion Physics* 26.3 (1978), pp. 251–266.

[29] D. S. Gemmell. “Determining the stereochemical structures of molecular ions by "Coulomb-explosion" techniques with fast (MeV) molecular ion beams”. In: *Chemical Reviews* 80.4 (1980), pp. 301–311.

[30] Z. Vager, R. Naaman, and E. P. Kanter. “Coulomb Explosion Imaging of Small Molecules”. In: *Science* 244.4903 (1989), pp. 426–431.

[31] H. Stapelfeldt, E. Constant, and P. B. Corkum. “Wave Packet Structure and Dynamics Measured by Coulomb Explosion”. In: *Physical Review Letters* 74.19 (1995), pp. 3780–3783.

[32] T. Ergler, A. Rudenko, B. Feuerstein, K. Zrost, C. D. Schröter, R. Moshammer, and J. Ullrich. “Spatiotemporal Imaging of Ultrafast Molecular Motion: Collapse and Revival of the D_2^+ Nuclear Wave Packet”. In: *Physical Review Letters* 97.19 (2006), p. 193001.

[33] J. L. Hansen, J. H. Nielsen, C. B. Madsen, A. T. Lindhardt, M. P. Johansson, T. Skrydstrup, L. B. Madsen, and H. Stapelfeldt. “Control and femtosecond time-resolved imaging of torsion in a chiral molecule”. In: *The Journal of Chemical Physics* 136.20 (2012), p. 204310.

[34] J. H. Beynon, G. R. Lester, and A. E. Williams. “Some Specific Molecular Rearrangements in the Mass Spectra of Organic Compounds”. In: *The Journal of Physical Chemistry* 63.11 (1959), pp. 1861–1868.

[35] S. Meyerson and R. W. V. Haar. “Multiply Charged Organic Ions in Mass Spectra”. In: *The Journal of Chemical Physics* 37.10 (1962), pp. 2458–2462.

[36] J. H. Gross. “Mass spectrometry: a textbook”. In: Berlin: Springer, 2004, p. 33.

[37] W. A. Chupka. “Effect of Unimolecular Decay Kinetics on the Interpretation of Appearance Potentials”. In: *The Journal of Chemical Physics* 30.1 (1959), pp. 191–211.

[38] F. W. McLafferty. “Mass Spectrometric Analysis. Molecular Rearrangements”. In: *Analytical Chemistry* 31.1 (1959), pp. 82–87.

[39] F. H. Field and J. L. Franklin. “Rearrangement”. In: *Electron Impact Phenomena and the Properties of Gaseous Ions*. New York: Academic Press, 1970. Chap. V, p. 185.

[40] National Research Council. *Database Needs for Modeling and Simulation of Plasma Processing*. Washington, DC: The National Academies Press, 1996, p. 74.

[41] F. H. Field and J. L. Franklin. *Electron Impact Phenomena and the Properties of Gaseous Ions*. New York: Academic Press, 1970, p. 185.

[42] L. J. Kieffer and G. H. Dunn. “Electron Impact Ionization Cross-Section Data for Atoms, Atomic Ions, and Diatomic Molecules: I. Experimental Data”. In: *Reviews of Modern Physics* 38.1 (1966), pp. 1–35.

[43] B. L. Schram, F. J. de Heer, M. van der Wiel, and J. Kistemak. “Ionization Cross Sections for Electrons (0.6-20 keV) in Noble and Diatomic Gases”. In: *Physica* 31.1 (1965), pp. 94–112.

[44] H. S. W. Massey and E. H. S. Burhop. “The Experimental Analysis of The Cross-Sections for Impact of Electrons with Atoms”. In: *Electronic and Ionic Impact Phenomena*. Oxford: Clarendn Press, 1952. Chap. 2, p. 34.

[45] F. J. de Heer and M. Inokuti. “Total Ionization Cross Sections”. In: *Electron Impact Ionization*. Ed. by T. D. Märk and G. H. Dunn. Vienna: Springer, 1985. Chap. 7, p. 235.

[46] R. K. Asundi. “Electron Path Length in Collision Experiments”. In: *Proceedings of the Physical Society of London* 82.527 (1963), pp. 372–374.

[47] J. T. Tate and P. T. Smith. “The Efficiencies of Ionization and Ionization Potentials of Various Gases Under Electron Impact”. In: *Physical Review* 39.2 (1932), pp. 270–277.

[48] J. D. Craggs, R. Thorburn, and B. A. Tozer. “The Attachment of Slow Electrons in Oxygen”. In: *Proceedings of the Royal Society of London. Series A. Mathematical and Physical Sciences* 240.1223 (1957), pp. 473–483.

[49] M. V. Kurepa, I. M. Čadež, and V. M. Pejčev. “Absolute measurements of the electron-argon atom total ionization cross section”. In: *Fizika* 6.4 (1974), pp. 185–209.

[50] T. J. Jones. “Probability of Ionization of Mercury Vapor by Electron Impact”. In: *Physical Review* 29.6 (1927), pp. 822–829.

[51] W. W. Lozier. “A study of the velocities of H^+ ions formed in hydrogen by dissociation following electron impact”. In: *Physical Review* 36.8 (1930), pp. 1285–1292.

[52] P. T. Smith. “The Ionization of Helium, Neon, and Argon by Electron Impact”. In: *Physical Review* 36.8 (1930), pp. 1293–1302.

[53] D. D. Briglia and D. Rapp. "Ionization of H_2 by Electron Impact Near Threshold". In: *Journal of Chemical Physics* 42.9 (1965), pp. 3201–3213.

[54] I. R. Cowling and J. Fletcher. "Electron-molecule collision ionization in hydrogen and deuterium". In: *Journal of Physics B: Atomic, Molecular and Optical Physics* 6.4 (1973), pp. 665–674.

[55] H. C. Straub, P. Renault, B. G. Lindsay, K. A. Smith, and R. F. Stebbings. "Absolute partial and total cross sections for electron-impact ionization of argon from threshold to 1000 eV". In: *Physical Review A* 52.2 (1995), pp. 1115–1124.

[56] K. T. Compton and C. C. Van Voorhis. "Probability of Ionization of Gas Molecules by Electron Impacts". In: *Physical Review* 26.4 (1925), pp. 436–453.

[57] P. T. Smith. "The Ionization of Mercury Vapor by Electron Impact". In: *Physical Review* 37.7 (1931), pp. 808–814.

[58] D. Rapp and P. Englander-Golden. "Total Cross Sections for Ionization and Attachment in Gases by Electron Impact. I. Positive Ionization". In: *The Journal of Chemical Physics* 43.5 (1965), pp. 1464–1479.

[59] H. Ishii and K. Nakayama. *Transactions of the Eighth Vacuum Symposium and Second International Congress*. New York: Pergamon Press, 1961.

[60] N. L. Djurić, I. M. Čadež, and M. V. Kurepa. "H_2O and D_2O total ionization cross-sections by electron impact". In: *International Journal of Mass Spectrometry and Ion Processes* 83.3 (1988), R7–R10.

[61] N. L. Djurić, I. M. Čadež, and M. V. Kurepa. "Electron impact total ionization cross-sections for methane, ethane and propane". In: *International Journal of Mass Spectrometry and Ion Processes* 108.1 (1991), R1–R10.

[62] J. T. Tate and W. W. Lozier. "The Dissociation of Nitrogen and Carbon Monoxide by Electron Impact". In: *Physical Review* 39.2 (1932), pp. 254–269.

[63] W. W. Lozier. "The Heats of Dissociation of Hydrogen and Nitrogen". In: *Physical Review* 44.7 (1933), pp. 575–581.

[64] W. W. Lozier. "The Heat of Dissociation of CO and the Electron Affinity of O". In: *Physical Review* 46.4 (1934), pp. 268–276.

[65] G. J. Schulz. "Cross Sections and Electron Affinity for O^- Ions From O_2, CO, and CO_2 by Electron Impact". In: *Physical Review* 128.1 (1962), pp. 178–186.

[66] G. H. Dunn. "Anisotropies in Angular Distributions of Molecular Dissociation Products". In: *Physical Review Letters* 8.2 (1962), pp. 62–64.

[67] B. A. Tozer. "Measurements of Ionization Cross Sections for Electron Impact I: Technique and Data for Methane". In: *Journal of Electronics and Control* 4.2 (1958), pp. 149–159.

[68] M. E. Bell. "The Probability of Ionization of Mercury Atoms by Collision with Low Velocity Electrons". In: *Physical Review* 55.2 (1939), pp. 201–202.

[69] W. B. Nottingham. "Ionization and Excitation in Mercury Vapor Produced by Electron Bombardment". In: *Physical Review* 55.2 (1939), pp. 203–219.

[70] R. L. F. Boyd and G. W. Green. "Electron Ionization Cross Sections using Chopped Beams". In: *Proceedings of the Physical Society* 71.3 (1958), p. 351.

[71] W. L. Fite and R. T. Brackmann. “Collisions of Electrons with Hydrogen Atoms. I. Ionization”. In: *Physical Review* 112.4 (1958), pp. 1141–1151.

[72] K. T. Dolder, M. F. A. Harrison, and P. C. Thonemann. “A Measurement of the Ionization Cross-Section of Helium Ions by Electron Impact”. In: *Proceedings of the Royal Society of London. Series A. Mathematical and Physical Sciences* 264.1318 (1961), pp. 367–378.

[73] R. C. Wetzel, F. A. Baiocchi, T. R. Hayes, and R. S. Freund. “Absolute cross sections for electron-impact ionization of the rare-gas atoms by the fast-neutral-beam method”. In: *Physical Review A* 35.2 (1987), pp. 559–577.

[74] C. G. Aitken, D. A. Blunt, and P. W. Harland. “Electron impact ionization of spatially oriented CH_3Cl and CCl_3H”. In: *International Journal of Mass Spectrometry and Ion Processes* 149-150 (1995), pp. 279–286.

[75] T. D. Märk. “Cross section for single and double ionization of N_2 and O_2 molecules by electron impact from threshold up to 170 eV”. In: *The Journal of Chemical Physics* 63.9 (1975), pp. 3731–3736.

[76] T. D. Märk and F. Egger. “Cross-section for single ionization of H_2O and D_2O by electron impact from threshold up to 170 eV”. In: *International Journal of Mass Spectrometry and Ion Physics* 20.1 (1976), pp. 89–99.

[77] T. Graf. “La méthode des coïncidences appliquée à la détermination de l’efficacité des compteurs Geiger-Müller et à la mesure de l’ionisation spécifique des rayons β de 50 a 1000 ekV”. In: *Journal de Physique et Le Radium* 10.12 (1939), pp. 513–518.

[78] G. W. McClure. “Specific Primary Ionization of H_2, He, Ne, and A by High Energy Electrons”. In: *Physical Review* 90.5 (1953), pp. 796–803.

[79] F. F. Rieke and W. Prepejchal. “Ionization Cross Sections of Gaseous Atoms and Molecules for High-Energy Electrons and Positrons”. In: *Physical Review A* 6.4 (1972), pp. 1507–1519.

[80] H. Bethe. “Zur Theorie des Durchgangs schneller Korpuskularstrahlen durch Materie”. In: *Annalen der Physik* 397.3 (1930), pp. 325–400.

[81] H. Bethe. “Bremsformel für Elektronen relativistischer Geschwindigkeit”. In: *Zeitschrift für Physik* 76.5 (1932), pp. 293–299.

[82] *Plasma Processing of Materials*. Washington, DC: The National Academies Press, 1985, p. 180.

[83] W. M. Huo and Y.-K. Kim. “Electron collision cross-section data for plasma modeling”. In: *IEEE Transactions on Plasma Science* 27.5 (1999), pp. 1225–1240.

[84] *Plasma Processing and Processing Science*. Washington, DC: The National Academies Press, 1995, p. 47.

[85] H. Deutsch and M. Schmidt. “Ionization Cross Sections of Gas Molecules for Plasma Chemistry”. In: *Beiträge aus der Plasmaphysik* 25.5 (1985), pp. 475–484.

[86] J. Roth, E. Tsitrone, A. Loarte, T. Loarer, G. Counsell, R. Neu, V. Philipps, S. Brezinsek, M. Lehnen, P. Coad, C. Grisolia, K. Schmid, K. Krieger, A. Kallenbach, B. Lipschultz, R. Doerner, R. Causey, V. Alimov, W. Shu, O. Ogorodnikova, A. Kirschner, G. Federici, and A. Kukushkin. “Recent analysis of key plasma wall interactions issues for ITER”. In: *Journal of Nuclear Materials* 390-391 (2009), pp. 1–9.

[87] G. Gluch, S. Feil, P. Scheier, W. Schustereder, T. Tepnual, L. Feketeova, C. Mair, S. Matt-Leubner, A. Stamatovic, and T. D. Märk. "Partial and Differential Electron Impact Ionization Cross-Sections for Small Hydrocarbon Molecules". In: *Nuclear Fusion Research Understanding Plasma-Surface Interactions*. Ed. by R. Clark and D. Reiter. Berlin: Springer, 2005. Chap. 20, pp. 437–456.

[88] S. Matt, D. Muigg, G. Denifl, M. Sonderegger, T. Fiegele, R. David, V. Grill, P. Scheier, T. D. Märk, H. Deutsch, K. H. Becker, and A. Stamatovic. "Experimental and theoretical determination of electron ionization cross sections for atoms, molecules and molecular ions relevant to fusion edge plasmas". In: *Czechoslovak Journal of Physics* 48.2 (1998), pp. 333–338.

[89] A. Kendl. "Modelling of turbulent impurity transport in fusion edge plasmas using measured and calculated ionization cross sections". In: *International Journal of Mass Spectrometry* 365-366 (2014), pp. 106–113.

[90] M. A. Quinto, J. M. Monti, P. D. Montenegro, O. A. Fojón, C. Champion, and R. D. Rivarola. "Single ionization and capture cross sections from biological molecules by bare projectile impact". In: *The European Physical Journal D* 71.2 (2017), p. 35.

[91] M. Vinodkumar, C. Limbachiya, M. Barot, M. Swadia, and A. Barot. "Electron impact total ionization cross sections for all the components of DNA and RNA molecule". In: *International Journal of Mass Spectrometry* 339-340 (2013), pp. 16–23.

[92] B. Boudaïffa, P. Cloutier, D. Hunting, M. A. Huels, and L. Sanche. "Resonant Formation of DNA Strand Breaks by Low-Energy (3 to 20 eV) Electrons". In: *Science* 287.5458 (2000), p. 1658.

[93] I. Baccarelli, F. A. Gianturco, E. Scifoni, A. V. Solov'yov, and E. Surdutovich. "Molecular level assessments of radiation biodamage". In: *European Physical Journal D* 60.1 (2010), pp. 1–10.

[94] J. N. Bull, J. W. L. Lee, and C. Vallance. "Absolute electron total ionization cross-sections: molecular analogues of DNA and RNA nucleobase and sugar constituents". In: *Physical Chemistry Chemical Physics* 16.22 (2014), pp. 10743–10752.

[95] P. Pater, J. Seuntjens, and I. El Naqa. "WE-E-BRE-11: New Method to Simulate DNA Damage Using Ionization Cross-Sections and a Geometrical Nucleosome Model". In: *Medical Physics* 41.6 (2016), pp. 506–506.

[96] I. Plante and F. A. Cucinotta. "Binary-Encounter-Bethe ionisation cross sections for simulation of DNA damage by the direct effect of ionising radiation". In: *Radiation Protection Dosimetry* 166.1-4 (2015), pp. 19–23.

[97] J. Lequeux, E. Falgarone, and C. Ryter. *The Interstellar Medium*. Springer Berlin Heidelberg, 2006.

[98] C. Ciccarino and D. W. Savin. "Electron-impact Ionization of Atomic Nitrogen". In: *2018 AIAA Aerospace Sciences Meeting*. AIAA SciTech Forum. American Institute of Aeronautics and Astronautics, 2018.

[99] D. B. Williams, D. E. Newbury, J. I. Goldstein, and C. E. Fiori. "On the use of ionization cross sections in analytical electron microscopy". In: *Journal of Microscopy* 136.2 (1984), pp. 209–218.

3

Semi-classical and semi-empirical methods for calculating electron ionization cross-sections

Contents

3.1 Introduction **44**
3.2 Semi-classical formulae **44**
3.2.1 The Deutsch-Märk (DM) method 46
3.2.2 The binary-encounter Bethe (BEB) method 48
3.3 Empirical and semi-empirical formulae **53**
3.3.1 The Lotz method 54
3.3.2 The Jain-Khare method 55
3.3.3 The Bell method 57
3.3.4 Kistemaker's modified additivity rule 58
3.3.5 The polarizability model 60
3.4 Discussion **62**
3.5 Current work **63**
3.5.1 Total ionization cross-section calculation of molecules relevant to astrochemistry by using BEB model 63
3.5.2 Total ionization cross-section calculation of molecules relevant to astrochemistry by using polarizability model 64
References **66**

3.1 Introduction

One of the fundamental difficulties associated with employing a full quantum mechanical treatment of electron ionization, in addition to general complexities associated with electron-atom scattering, is the quantum many-body problem which arises from the two free electrons in the field of the ionized atom in the exit channel [1]. Hence, efforts have been devoted to developing approximate methods that may be implemented practically with modern computational resources.

The difficulty of using a full quantum-mechanical treatment to calculate electron ionization cross-section is inconveniently paralleled with the equally formidable experimental challenge, as discussed in Chapter 2. To fill the gap between the two approaches, a significant amount of effort has been devoted to developing semi-classical and semi-empirical formulae, each introducing different levels of approximation. The primary goal has been to reproduce experimental ionization cross-section data for a wide range of target atoms and molecules within a specified electron energy range. The most successful methods developed in this way have then been extended to atoms or molecules that are less amenable to experimental study. In this chapter, a range of representative and significant semi-classical and semi-empirical methods have been selected, and are introduced in chronological order of their original publication. The originality and applicability of each method will be discussed.

3.2 Semi-classical formulae

Semi-classical methods attempt to address the complexities implicit within the quantum scattering problem by making classical approximations. Adjustable parameters determined by comparing with reliable experimental results are often introduced into semi-classical methods in order to achieve more reliable results. When using classical

mechanics to describe ionization processes, three basic approximations are necessary, as summarised by Rudge [2]:

1) Prior to collision with the free electron, a classical treatment must be used for describing the initial state of the bound atomic electron. Depending on the methods being introduced, it is assumed either that it might be at rest, or that it might possess a fixed velocity or certain velocity distribution.
2) The collision process is described by the framework of classical laws of motion.
3) Due to the difficulties associated with the three-body problem for even the simplest case, such as e-H ionization, a two-body approximation is implemented.

Approximation 1) and 3) may vary depending on the classical methods considered. If approximation 2) is only partially fulfilled, then the method is accordingly termed semi-classical. The approach was pioneered by J. J. Thomson [3], who first proposed the classical treatment with binary-encounter approximation, which assumed the electron of target atom or molecule is at rest.

The choice of a particular approximation depends on the collision energy. Collisions can be classified as "fast" or "slow" by comparing the velocity of the incident electron with that of the target electrons. Collision of the molecule with a fast electron can be considered as a sudden and external perturbation to the target electron, in which case the Born approximation is employed [4, 5]. For slow collisions, classical scattering theory, including the binary encounter approximation [3], is employed, with the system in question considered as being comprised of both incident and target electrons.

More details of two prominent semi-classical methods, the Deutsch-Märk method and the binary-encounter Bethe method, will be introduced below.

3.2.1 The Deutsch-Märk (DM) method

Along with the discovery of the electron and many other significant achievements, J. J. Thomson [3] also first proposed a formula for the electron ionization cross-section based on a classical mechanical treatment:

$$\sigma(E) = \sum_n 4\pi a_0^2 \xi_n \left(\frac{E_i^{\mathrm{H}}}{E_{\mathrm{in}}}\right)^2 \frac{u-1}{u^2} \tag{3.1}$$

where a_0 is the Bohr radius, ξ_n is the number of electrons in the nth subshell, E_{in} is the ionization energy in the nth subshell, E_i^{H} is the ionization energy of H atom, and u is $=E/E_{\mathrm{in}}$, with E the energy of the incident electron. J. J. Thomson's approach has been modified by a number of authors, but little improvement was made to the large disagreement at both high and low incident energies present in J. J. Thomson's original treatment [3]. Later, in 1965, Gryzinski [6] put forward a proposal that the atomic electrons may possess a continuous velocity distribution, and derived an improved formula for electron ionization cross-section for single ionization as:

$$\begin{aligned}\sigma(E) = \sum_n 4\pi a_0^2 \xi_n \left(\frac{E_i^{\mathrm{H}}}{E_{\mathrm{in}}}\right)^2 \frac{1}{u} \left(\frac{u-1}{u+1}\right)^{\frac{3}{2}} \\ \times \left\{1 + \frac{2}{3}\left(1 - \frac{1}{2u}\right) \ln\left(2.7 + (u-1)^{\frac{1}{2}}\right)\right\}\end{aligned} \tag{3.2}$$

Other attempts to modify the model were suggested within the same decade by Burgess [7] and Vriens [8], in order to incorporate quantum mechanical considerations such as exchange effects into the approximation. However, the resulting expressions were still unable to describe ionization cross-sections correctly, even for fairly simple targets.

Bethe theory shows that there exists an approximate proportionality between the ionization cross-section of an electron, $\sigma_{n,l}$, and the mean square radius $\langle r_{n,l}^2 \rangle$ of the respective electron shell. Additionally, the measured maximum atomic cross-sections correlate with the sum of the mean square radii of the outer electrons. Accordingly, after comparing the classical formulae with the Bethe theory, Deutsch and Märk [9] proposed that the

classical models could be further improved by replacing the Bohr radius in the original classical expression by the radius of the respective subshell. The resulting expression for the ionization cross-section of a single electron within a subshell with quantum numbers n,l has the following form:

$$\sigma = \sum_{n,l} \sigma_{n,l} = \sum_{n,l} g_{n,l} \pi r_{n,l}^2 N_{n,l} f(u) \tag{3.3}$$

where $N_{n,l}$ is the number of target electrons within the shell with principal quantum number n,l, the parameter $r_{n,l}^2$ is the mean square radius of the n,l shell, and $g_{n,l}$ are generalised weighting factors which were determined empirically by implementing a rather sophisticated fitting procedure based on experimental data for rare gases and uranium. It was then discovered that the product of $g_{n,l}$ and the binding energy for a specific set of n,l and $N_{n,l}$ is conveniently independent of the atomic number Z [10]:

$$g_{n,l} E_{n,l} = \text{constant} \tag{3.4}$$

With the weighting factors $g_{n,l}$, inner atomic orbitals contribute less with smaller weighting factors due to large binding energies. The DM approach may also be used to study molecules as a result of the additivity rule proposed by Otvos and Stevenson [11]. A population analysis is required in order to determine the contribution of each atomic orbital to the molecular orbitals of the molecule, and one can then perform an appropriately weighted sum over the atomic orbitals in the same way as for atoms.

It has been demonstrated that, when comparing with the classical binary encounter approximation [6] and with semi-classical treatments [7, 8], the DM method on average yields more consistent agreement with experimental data [9, 10, 12]. Perhaps the most useful feature of the DM method is its simple form of an analytical formula which requires a relatively small amount of input data, mostly in the form of basic atomic properties.

3.2.2 The binary-encounter Bethe (BEB) method

The BEB model, developed by Kim and Rudd [13], is an alternative theoretical model for calculating electron ionization cross-sections for atoms and molecules. It uses no adjustable or fitted parameters, and in principle requires no input from experimental data (however, using an experimental value for the ionization potential of the outermost electron is beneficial for achieving correct threshold behaviour). The BEB model is a simplified version of the binary-encounter dipole (BED) model developed by the same authors [14].

The BED model combines two theoretical cross-sections which are intended for describing collisions at low and high incident energies, respectively: the Mott cross-section [15] modified by the binary-encounter theory [16], which describes the hard collisions between a free electron and a bound electron for low incident energies, T; and the Bethe theory [4, 5] which describes collisions at high energy, when the dipole interaction dominates.

3.2.2.1 Mott cross-section

A low-energy collision between two electrons is described by the Mott cross-section:

$$\frac{\mathrm{d}\sigma\left(W,T\right)}{\mathrm{d}W}=\frac{4\pi a_0^2R^2}{T}\left[\frac{1}{W^2}-\frac{1}{W\left(T-W\right)}+\frac{1}{\left(T-W\right)^2}\right] \tag{3.5}$$

where a_0 is the Bohr radius, R is the Rydberg energy, W is the kinetic energy of the ejected electron, T is the kinetic energy of the incident electron, and $T-W$ is therefore the kinetic energy of the scattered incident electron. Equation (3.5) is presented as a singly differential cross-section, which shows the energy distribution of the ejected electron.

A distinct feature of the Mott cross-section is the fact that it is symmetric in the kinetic energies of one electron, W and the other, $T-W$. This is in accordance with the experimental limitation that scattered and ejected electrons are indistinguishable on the detector. Equation (3.5) arranges the terms on the right-hand side (RHS) in such a way

that the three terms in the brackets represent the direct collision, interference between direct and exchange collision, and exchange collision, respectively. The Mott cross-section can be modified to account for the fact that the binding energy B of a bound electron needs to be overcome in order for the electron to be ejected. Hence if W is replaced by $E = W + B$, the Mott cross-section for a subshell becomes:

$$\frac{\mathrm{d}\sigma(W,T)}{\mathrm{d}W} = \frac{\mathrm{d}\sigma}{\mathrm{d}E} = \frac{4\pi a_0^2 R^2 N}{T}\left[\frac{1}{E^2} - \frac{1}{E(T-W)} + \frac{1}{(T-W)^2}\right] \tag{3.6}$$

where N is the number of bound electrons in the subshell.

3.2.2.2 Binary-encounter cross-section

For a real ionization event, one of the electrons is a bound target, rather than a free electron. The orbital motion of this bound electron can be manifested by adding a velocity or momentum distribution, which is usually derived from the wave function for the target electron. Hence the symmetric form of the Mott cross-section can be extended to include an additional term, i.e. as a binary-encounter cross-section:

$$\begin{aligned}\frac{\mathrm{d}\sigma(E,T)}{\mathrm{d}E} = &\frac{4\pi a_0^2 R^2 N}{T+U+B}\left\{\frac{1}{E^2} - \frac{1}{E(T-W)} + \frac{1}{(T-W)^2}\right. \\ &\left. + \frac{4U}{3}\left[\frac{1}{E^3} + \frac{1}{(T-W)^3}\right]\right\}\end{aligned} \tag{3.7}$$

The new quantity U appearing in this expression is the average kinetic energy, $U \equiv \langle \overrightarrow{p}^2 \rangle / 2m$, where $\overrightarrow{p}$ is the momentum operator of the electrons in a subshell. The expression can be further recast to express all energy variables in units of the binding energy B of electrons in a subshell:

$$t = T/B \tag{3.8}$$

$$w = W/B \tag{3.9}$$

$$u = U/B \tag{3.10}$$

$$S = 4\pi a_0^2 N (R/B)^2 \tag{3.11}$$

The binary-encounter cross-section (3.7) therefore becomes

$$\begin{aligned}\frac{\mathrm{d}\sigma(W,T)}{\mathrm{d}W} = \frac{S}{B(t+u+1)} \Bigg\{ & \frac{1}{(w+1)^2} + \frac{1}{(t-w)^2} \\ & - \frac{1}{(w+1)(t-w)} + \frac{4u}{3}\left[\frac{1}{(w+1)^3} + \frac{1}{(t-w)^3}\right]\Bigg\}\end{aligned} \tag{3.12}$$

The binary-encounter cross-sections for electron ionization can be written in series form:

$$\frac{\mathrm{d}\sigma(W,T)}{\mathrm{d}W} = \frac{S}{B}\sum_{n=1}^{3} F_n(t)\left[\frac{1}{(w+1)^n} + \frac{1}{(t-w)^n}\right] \tag{3.13}$$

Where the function F_n has the following form:

$$F_1 = -\frac{F_2}{t+1} \tag{3.14}$$

$$F_2 = \frac{1}{t+u+1} \tag{3.15}$$

$$F_3 = \frac{4u}{3(t+u+1)} \tag{3.16}$$

As mentioned earlier for Equation (3.5), the two terms inside the brackets represent the ejected electrons and scattered incident electron, respectively. Compared to Equation (3.5), it is clear that the $n = 1$ term represents interference between the two electrons, and the $n = 2$ term represents the close collisions. The $n = 3$ term represents the intrinsic momentum distribution that an ionized bound electron possesses.

Equation (3.13) is the singly differential cross-section, which may be integrated from $w = 0$ to $(t-1)/2$ to get the total ionization cross-section σ_i:

$$\sigma_i = \int_0^{(t-1)/2} \frac{\mathrm{d}\sigma}{\mathrm{d}w}\mathrm{d}w \tag{3.17}$$

$$\sigma_i = S\left[F_1 \ln t + F_2\left(1 - t^{-1}\right) + \frac{1}{2}F_3\left(1 - t^{-2}\right)\right] \tag{3.18}$$

3.2.2.3 Binary-encounter dipole (BED) model

There exists an asymptotic behaviour, based on the total cross-section expression (3.18) with values of F_n shown in Equations (3.14) to (3.16), that σ_i approaches t^{-1} when $t \gg 1$. This departs from the experimental results and the predictions from Bethe theory in that it decays much faster with t [14]. In the asymptotic high T region where $t \gg w$, or $(t-w) \gg 1$, the $(t-w)^{-n}$ can be safely omitted. Equation (3.13) can then be simplified to:

$$\frac{\mathrm{d}\sigma}{\mathrm{d}w} = S\sum_{n=1}^{3} F_n(t)\, f_n(w) \tag{3.19}$$

where $f_n(w) = 1/(w+1)^n$ when $n = 1,\ 2$, and $F_n(t)$ and $f_3(w)$ need to be worked out to account for the dipole interaction, which turn out to be [14]:

$$F_1 = -\frac{F_2}{t+1} \tag{3.20}$$

$$F_2 = \frac{2-(N_i/N)}{t+u+1} \tag{3.21}$$

$$F_3 = \frac{\ln t}{t+u+1} \tag{3.22}$$

$$f_3(w) = \frac{1}{N(w+1)}\frac{\mathrm{d}f(w)}{\mathrm{d}w} \tag{3.23}$$

Substituting Equations (3.20) to (3.23) into Equation (3.19) yields the BED model, combining the modified form of Mott cross-section with Bethe cross-section. For a subshell in a singly differential cross-section form, the result is:

$$\begin{aligned}\frac{\mathrm{d}\sigma(W,T)}{\mathrm{d}W} = \frac{S}{B(t+u+1)}\Bigg\{&\frac{(N_i/N)-2}{t+1}\left(\frac{1}{w+1}+\frac{1}{t-w}\right)\\ &+[2-(N_i/N)]\left[\frac{1}{(w+1)^2}+\frac{1}{(t-w)^2}\right]+\frac{\ln t}{N(w+1)}\frac{\mathrm{d}f(w)}{\mathrm{d}w}\Bigg\}\end{aligned} \tag{3.24}$$

The ratio between the electron exchange term, the hard collision term (binary-encounter) and the dipole interaction term (Bethe theory) is found based on the agreement between binary-encounter theory and Bethe theory, in terms of the asymptotic total ionization cross-section and the stopping cross-section. The stopping cross-section, obtained by

integrating the product of the energy loss cross-section and the energy loss of the primary electron, is a measurement of the stopping power of the target particles.

The corresponding integrated total ionization cross-section predicted by the BED model for an atomic orbital i is then given by:

$$\sigma_i(t) = \frac{S}{t+u+1}\left[D(t)\ln t + \left(2-\frac{N_i}{N}\right)\left(\frac{t-1}{t}-\frac{\ln t}{t+1}\right)\right] \tag{3.25}$$

where

$$D(t) \equiv N^{-1}\int_0^{(t-1)/2}\frac{1}{w+1}\frac{\mathrm{d}f(w)}{\mathrm{d}w}\mathrm{d}w \tag{3.26}$$

$$N_i \equiv \int_0^{\infty}\frac{\mathrm{d}f(w)}{\mathrm{d}w}\mathrm{d}w \tag{3.27}$$

Summing Equation (3.25) over all of the atomic or molecular orbitals yields the total ionization cross-section for the target atom or molecule.

From Equations (3.8) to (3.11) and (3.25) to (3.27), it can be seen that the quantities required for calculating total ionization cross-sections using the BED model are: the binding energy B, which can easily be calculated using common electronic structure packages, with the option of using experimental data to assure correct threshold behaviour; average orbital kinetic energy U, which is a theoretical quantity but is also obtainable from electronic structure packages; the orbital occupation number N; and the continuum dipole oscillator strength $\mathrm{d}f/\mathrm{d}w$, which poses difficulties to calculate, as both the initial- and continuum-state wave function are needed. These parameters are only available for a small range of atoms and molecules.

3.2.2.4 Binary-encounter Bethe (BEB) model

The BEB model is designed to overcome the abovementioned issue regarding calculation of the continuum dipole oscillator strength $\mathrm{d}f/\mathrm{d}w$, and assumes that it takes the following simplified form:

$$\frac{\mathrm{d}f}{\mathrm{d}w} = \frac{N}{(w+1)^2} \tag{3.28}$$

The integrated total ionization cross-section for a given orbital is then given by:

$$\sigma_{\mathrm{BEB}} = \frac{S}{t+u+1}\left[\frac{\ln t}{2}\left(1-\frac{1}{t^2}\right)+1-\frac{1}{t}-\frac{\ln t}{t+1}\right] \tag{3.29}$$

In both Equations (3.25) and (3.29), the first logarithmic term on the right hand side describes soft collisions with large impact parameters, where dipole interactions dominate. The remaining terms describe hard collisions with small impact parameters, where the binary-encounter theory modified Mott cross-section is applicable. The second logarithmic term represents the interference between the direct and exchange interaction.

It is also worth noting that, based on its theoretical definition, both the BED and BEB cross-sections are sums of cross-sections for ejecting one electron from each orbital, i.e. for generating a singly charged parent ion, or single ionization. Therefore, both models are incapable of accounting for dissociative ionization or fragmentation for larger molecules possessing various potential fragmentation channels, especially at high incident energy.

3.3 Empirical and semi-empirical formulae

Empirical and semi-empirical methods aim to represent known experimentally determined ionization cross-sections by constructing simple formulae with minimal adjustable parameters determined empirically from the data. It is also sensible to be able to use these formulae to predict ionization cross-section functions for any target atoms or molecules for which experimental data are scarce.

A number of popular empirical and semi-empirical approaches are discussed below. More comprehensive reviews are available.

3.3.1 The Lotz method

One of the most popular empirical formulae for calculating electron ionization cross-sections was presented by Lotz [17–19]. Using three free parameters, this empirical formula can approximate experimental ionization cross-sections for single ionization from the ground state to within 10% across the energy range from threshold to 10 keV, for a very wide range of atoms and ions.

The total ionization cross-section is calculated as the sum of all subshell cross-sections, σ_i, which in turn contains contributions from all electrons within each subshell:

$$\sigma = \sum_{i=1}^{N} \sigma_i; \qquad \sigma_i = q_i \sigma_{ei} \tag{3.30}$$

where N is the number of subshells, q_i is the number of equivalent electrons within a subshell i, and σ_{ei} is the cross-section contribution from an electron e within a subshell i.

Based on results from Bethe [4] and Rudge and Schwartz [20], σ_i can be expressed as:

$$\sigma_i = a_i q_i \frac{\ln(E/P_i)}{EP_i}; \qquad E \geq P_i \tag{3.31}$$

where E is the kinetic energy of the impact electron, P_i is the binding energy of the bound electrons, and a_i is a constant with values lie between 2.6×10^{-14} to 4.5×10^{-14} cm^2 eV^2 as long as $E \gg P_i$.

Based on this formula and extensive trials, a further formula with three free parameters was proposed:

$$\sigma_i = a_i q_i \frac{\ln(E/P_i)}{EP_i} \{1 - b_i \exp[-c_i (E/P_i - 1)]\} \tag{3.32}$$

where a_i, b_i, and c_i are constants. Hence, the total ionization cross-section for single ionization from the ground state is given by:

$$\sigma = \sum_{i=1}^{N} a_i q_i \frac{\ln(E/P_i)}{EP_i} \{1 - b_i \exp[-c_i (E/P_i - 1)]\}; \qquad E \geq P_i \tag{3.33}$$

where i is the index number of ith shell, starting from $i = 1$, the outermost shell, and P_1 is the ionization potential of the atom.

Depending on the incident energy, two further approximations can be made. For the near-threshold region, where $E \approx P_1$, Equation (3.33) may be reduced to:

$$\sigma \approx a_1 q_1 \frac{(E/P_1 - 1)}{P_1^2} (1 - b_1) \propto U - 1 \tag{3.34}$$

where $U = E/P_1$.

For much higher incident energy region, $E \gg P_i$, Equation (3.32) may be reduced to:

$$\sigma_i = a_i q_i \frac{\ln(E/P_i)}{EP_i} \propto \frac{\ln E}{E} \tag{3.35}$$

It is then clear that Equation (3.32) and (3.33) can reproduce the expected energy dependence for both the low and high incident energy region. Practically, for most cases, Equation (3.33) may be replaced by an even more succinct form:

$$\sigma = a\{1 - b\exp[-c(U-1)]\} \sum_{i=1}^{N} q_i \frac{\ln(E/P_i)}{EP_i}; \quad E \geq P_i \tag{3.36}$$

where $N = 2$ is considered to be sufficient to produce acceptable results for most atoms.

The Lotz method proved to be versatile, and may be used to account for other cases such as negative ions [19], autoionization effects, threshold features, and even complex ions [21, 22].

3.3.2 The Jain-Khare method

By considering the energy being transfer during ionizing collisions, Jain and Khare [23, 24] treated soft collisions, in which a small amount of energy is transferred from the incident electron to the target molecule, differently from hard collisions, in which a large amount of energy is transferred. If the incident electron energy is high and the energy transferred is small, the validity of the Born-Bethe approximation is retained, and $Q(E, \varepsilon)$,

the ionization cross-section for an ejected electron with energy ε following a collision with an incident electron of energy E, is known to be proportional to the differential optical oscillator strength. In the case of a hard collision, the ionization cross-section can by described by the Mott cross-section.

In the event of an ionizing collision between an incident electron of energy E and a target molecule which results an ejected electron of energy ε, Khare [25] proposed two semi-empirical relations for calculating $Q(E,\varepsilon)$:

$$Q(E,\varepsilon) = S(E,W) = f_1^{'}(E,\varepsilon)\, Q_{\mathrm{BB}}(E,\varepsilon) \qquad \text{for } I \le W \le W_0 \tag{3.37}$$

$$= f_2^{'}(E,\varepsilon)\, Q_{\mathrm{M}}(E,\varepsilon) \qquad \text{for } W_0 \le W \le (E+I)/2 \tag{3.38}$$

where

$$f_1^{'} = \left(1 - \frac{2W-I}{E}\right) \frac{\ln\left[1 + C(E-I)\right]}{\ln CE} \tag{3.39}$$

$$f_2^{'} = \left(1 - \frac{2W-I}{E}\right) \tag{3.40}$$

In Equations (3.37) and (3.38), the Born-Bethe and Mott cross-sections are given by the following expressions:

$$Q_{\mathrm{BB}}(E,\varepsilon) = \frac{4\pi a_0^2 R^2}{E} \frac{1}{W} \frac{\partial f(W,0)}{\partial W} \ln CE \tag{3.41}$$

$$Q_{\mathrm{M}}(E,\varepsilon) = \frac{4\pi a_0^2 R^2}{E} S \left[\frac{1}{\varepsilon^2} - \frac{1}{\varepsilon(E-\varepsilon)} + \frac{1}{(E-\varepsilon)^2}\right] \tag{3.42}$$

where C is the collisional parameter defined by Miller and Platzman [26], I is the ionization potential of the target molecule, and W_0 is a cut-off value between the energy loss for an ejected electron formed by soft and hard collision, which was suggested by Jain and Khare to be $(I+60)$ eV. The $f_1^{'}$ and $f_2^{'}$ functions act to extrapolate the cross-section in the low incident energy region where the Born-Bethe and Mott cross-sections are likely to be very high. W is the energy loss suffered by the incident electron in the ionizing collision. It is generally found that the $Q(E,\varepsilon)$ determined by the two semi-empirical

equations leads to a discontinuity at $W = W_0$. This is overcome by combining Equations (3.37) and (3.38) with appropriate weighting factors to account for the whole energy range. The resulting single expression is:

$$Q(E,\varepsilon) = S(E,W) = f_1(E,\varepsilon)\, Q_{\mathrm{BB}}(E,\varepsilon) + f_2(E,\varepsilon)\, Q_{\mathrm{M}}(E,\varepsilon) \tag{3.43}$$

where

$$f_1(E,\varepsilon) = \frac{1}{1+I/E}\left(1-\frac{\varepsilon}{E-I}\right)\frac{\ln[1+C(E-I)]}{\ln CE} \tag{3.44}$$

$$f_2(E,\varepsilon) = \frac{\varepsilon^3}{\varepsilon^3+\varepsilon_0^3}(1-I/E) \tag{3.45}$$

Similar to the original semi-empirical equations, f_1 and f_2 are functions to extrapolate the Born-Bethe and Mott cross-sections to low incident energy region, as well as to adjust the mixing ratio of the soft and hard collisions. ε_0 is a parameter determined by fitting the experimental data of Opal *et al.* when $E = 500$ eV [27].

When using this method to calculate ionization cross-section for CO_2, CO, H_2O, CH_4 and NH_3, Jain and Khare found that their results showed good agreement with experimental data except for CO. This was an encouraging achievement, considering the relative large uncertainties associated with the experimental data, and the disagreement between those data sets. Their method, however, suffers the same limitation as that of BED theory, namely that the requirement for accurate differential oscillator strengths hinders application to a wider range of systems.

3.3.3 The Bell method

In an assessment of experimental and theoretical cross-section data for electron ionization of light atoms and ions, Bell *et al.* [28] fitted the recommended cross-section to the following analytical equation:

$$\sigma(E) = \frac{1}{IE}\left\{A\ln\left(\frac{E}{I}\right) + \sum_{i=1}^{N} B_i \left(1 - \frac{I}{E}\right)^i\right\} \tag{3.46}$$

where E is the incident energy of the primary electron, I is the ionization potential, and B_i are coefficients found by least-squares fitting of available experimental data. In many instances, no more than two or three such coefficients are needed. A is a Bethe coefficient which describes the ionization cross-section curves at high incident energy. It is determined by fitting the equation:

$$\sigma(E) = \frac{1}{IE}\{A\ln(E) + B\} \tag{3.47}$$

to the high-incident-energy form of the Born approximation. Alternatively, it can be obtained from the equation:

$$A = \frac{I}{\pi\alpha}\int_I^\infty \frac{\sigma_{\text{ph}}}{\varepsilon}\mathrm{d}\varepsilon \tag{3.48}$$

where σ_{ph} is the photoionization cross-section and α is the fine structure constant.

The Bell formula predicts correct behaviour for the ionization cross-section within both the low and high incident energy region. However, difficulties arise when excitation autoionization becomes important, when a new approach is needed. Bell proposed the use of two separate fits of Equation (3.46): one fit is only effective from the ionization threshold to the autoionization threshold; the second applies to energies above the autoionization threshold.

3.3.4 Kistemaker's modified additivity rule

Otvos and Stevenson's [11] additivity rule proposed that the relative molecular total ionization cross-section is the sum of the atomic cross-sections, which are then approximated by the sum of valence electrons weighted by the mean square radii of such electrons [4, 5]. Bobeldijk and co-workers [29] examined the outcomes of this hypothesis, and found that the original 100% atomic additivity rule overestimated experimental data to a large

extent, due to the omission of several effects, one of which implies that the inner atoms of a molecule are "shielded" by the outer atoms in terms of contribution to the overall molecular ionization cross-section. To account for this shielding effect, a geometric or orientational dependence is introduced when considering ionization cross-sections of non-spherically symmetric molecules. This modified additivity approach is named the geometric additivity model, and incorporates the shielding effect. The basic strategy is to divide the molecule into sub-units rather than atoms, and sum over the cross-sections of these sub-units, which are known either experimentally or theoretically. In case where the ionization cross-sections of the desired sub-units are unattainable, further division is needed until cross-sections for the respective units are known. However, overestimation of the cross-section is known to arise if sub-units are divided into too small a size, suggesting the necessity of a weighted additivity model. The weighting factor is a realization of the geometry dependence of the ionization cross-section. If target molecules are being approximated to a cylindrical symmetry, the ionization cross-section will be different depending on the direction of the ionizing electrons with respect to the orientation of the cylindrically symmetric target molecule. For instance, for a linear hydrocarbon molecules $CH_3(CH_2)_nCH_3$, the ionization cross-section when the ionizing electron approaches parallel to the direction of the hydrocarbon chain, $\sigma_{||}(E)$, is simply the cross-section of the CH_3 unit on either end of the molecule. Conversely, the ionization cross-section when the ionizing electron approaches perpendicularly, $\sigma_{\perp}(E)$, is considered to be the sum of the cross-section of all "exposed" sub-units, i.e. two CH_3 and n CH_2. It then follows that the ionization cross-section, $\sigma(E)$, is taken to be the average over all possible orientation:

$$\sigma(E) = \frac{1}{3}\sigma_{||}(E) + \frac{2}{3}\sigma_{\perp}(E) \tag{3.49}$$

Kistemaker's modified additivity rule provides an easy and straightforward method for reproducing ionization cross-sections. It achieves around 20% accuracy compared to experimental results for incident energies above 50 eV, and also shows reasonable agreement with cross-sections calculated by using DM method [12] and Jain-Khare

method [24]. The only limitations of the method claimed by authors are the larger discrepancies between the results of the model and experimental measurements in the threshold area below 30 eV.

3.3.5 The polarizability model

The existence of a linear relationship between the polarizability of target atoms or molecules and their ionization cross-sections was first discovered unexpectedly by Lampe, Franklin, and Field [30] when plotting one quantity against the other. The theoretical basis was the proportionality between the matrix elements contained within the ionization cross-section and within the dipole moment matrix element. This linear relationship was utilised by Bartmess and Georgiadis [31] to predict the chemical sensitivity of an ionization gauge for a series of molecular species, and was later verified by Nishimura and Tawara [32] for some simple hydrocarbon molecules. The observation suggests that the incident electron "recognises" not only all electrons in the target molecule, but also the structure of the electron cloud, i.e. polarizability. A few years later, Vallance and Harland [33] further demonstrated the strong linear correlation between the maximum electron ionization cross-section $\sigma_{\max}$, and the polarizability α, by examining a large collection of atoms and molecules. The proportionality constant, in the case of atoms, appears to be dependent on the group to which the atom belongs in the periodic table. They also found that a better correlation is present between the maximum electron ionization cross-section and the quantity $(\alpha/E_0)^{1/2}$, where E_0 is the ionization potential of the atom or molecule. This dependence on $(\alpha/E_0)^{1/2}$ has been successfully reasoned from electrostatic principles by considering the interaction between the approaching electron de Broglie wave and the target molecule. In the context of describing the response of an atom or molecule to an external electric field, average polarizability, rather than the full polarizability in second rank tensor form, is often used. The average polarizability may be visualised in terms of a sphere of charge that can be distorted by approach of

the incident electron. It follows that the polarizability volume manifests itself as the "effective size" of a target molecule as "seen" by the bombarding incident electron. The radius of this polarizability sphere of charge is:

$$r = \left(\frac{3\alpha}{4\pi}\right)^{\frac{1}{3}} \tag{3.50}$$

The root-mean-square radius for the electron distribution is $\sqrt{\frac{3}{5}}r$, assuming the existence of an equally distributed molecular electronic charge, which leads to the effective diameter for the molecule:

$$d_{\text{rms}} = 2\sqrt{\frac{3}{5}}\left(\frac{3\alpha}{4\pi}\right)^{\frac{1}{3}} \tag{3.51}$$

From the theoretical postulate mentioned in first paragraph of section 3.3.5, the electron energy at which the ionization cross-section reaches its maximum occurs when the de Broglie wavelength of the incident electron λ and the molecular diameter d_{rms} are quantitatively comparable. The de Broglie wavelength of the electron, λ, is given by:

$$\lambda = \frac{h}{p} = \left(\frac{h^2}{2mqE}\right)^{\frac{1}{2}} \tag{3.52}$$

where h is Planck's constant, and p, m, and E are the momentum, mass, and kinetic energy of the electron, respectively. Equating Equations (3.51) and (3.52) and rearranging yields the electron energy where the ionization cross-section is maximum:

$$E_{\text{max}} = \frac{5h^2}{24mq}\left(\frac{4\pi}{3}\right)^{\frac{2}{3}}\alpha^{-\frac{2}{3}} \tag{3.53}$$

As the electron wavelength becomes longer or shorter than the molecular diameter when its energy departs from the E_{max}, the interaction with the molecular electrons weakens, and the ionization cross-section accordingly decreases to a certain extent. The expression for the ionization cross-section as a function of electron energy is then given by:

$$\sigma \propto 1 - \frac{|\lambda - \lambda_{\text{max}}|}{\lambda_{\text{max}}} \quad \text{or} \quad \sigma = \sigma_{\text{max}}\left[1 - \frac{|\lambda - \lambda_{\text{max}}|}{\lambda_{\text{max}}}\right] \tag{3.54}$$

where $\lambda_{\max}$ is given by Equation (3.52) when $E = E_{\max}$.

This formula can describe ionization cross-section curves of methyl halides [34] moderately well, but for small molecules, it generally leads to a rapidly decreasing tail after the peak, as compared with experimental data reported by Rapp and Englander-Golden [35] and by Djurić *et al.* [36]. Its performance within threshold region is not fully satisfactory either, as overestimation is not trivial for small molecules. Improvements were made by incorporating the function $(E - E_0)/E$ from the classical binary encounter treatment of electron ionization [37]. This function was normalized to unity peak value by multiplying by $E_{\max}/(E_{\max} - E_0)$ before adding to Equation (3.54) and normalizing again to the maximum cross-section, leading to the expression:

$$\sigma = \frac{\sigma_{\max}}{2}\left[\left(\frac{E_{\max}}{E_{\max} - E_0}\right)\left(\frac{E - E_0}{E}\right) + 1 - \frac{|\lambda - \lambda_{\max}|}{\lambda_{\max}}\right] \tag{3.55}$$

The improved function is capable of predicting the threshold to within 1 or 2 eV for most molecules.

The most notable advantage of this function is its fairly good reproducibility of the ionization cross-section while retaining a relatively simple form only requiring three parameters, i.e. molecular polarizability volume, ionization potential, and maximum ionization cross-section. Even though there is a discontinuity point at the maximum of the cross-section curve, it only affects a limited region and still renders satisfactory cross-section values around it. The simplicity and applicability of this function makes it a favourable choice for calculating total ionization cross-sections.

3.4 Discussion

Both semi-classical and semi-empirical models generally produce counting total cross-sections $\sum_i \sigma_i$, which is the unweighted sum of partial cross-sections (i.e. the cross-section for forming a particular type of ion) for all ions formed. This is different from the gross

total ionization cross-section $\sum_i z_i \sigma_i$, which is the charge-weighted sum of partial cross-sections for all ions, and the quantity most often measured experimentally. This is the case because most experimental approaches involve measurement of total ion current rather than individual ionization events. Formation of a doubly charged ion then generates twice the current of a singly charged ion. Since gross cross-sections will generally be greater than counting cross-sections, particularly at higher energies when multiple ionization becomes energetically possible, it is expected that theoretically determined cross-section will usually be smaller than that of the experimental measurements, especially in the high incident energy region.

Apart from providing simple and reasonable estimates of cross-sections for molecules where disagreement and uncertainty are found in experimental data, semi-classical and semi-empirical method also offer a basis for evaluating cross-sections for targets that are not well known terrestrially and extremely unstable under normal conditions, such as many molecules detected in the interstellar medium, many of which are beyond current experimental competence.

As part of current work, one popular semi-classical method, the BEB model, and one novel semi-empirical formula, the polarizability model, will be used for calculating total ionization cross-sections for the molecules in question, i.e. molecules relevant to astrochemistry and fusion edge plasmas. Results from these calculations will be presented in Chapter 5, along with data from experimental total ionization cross-section measurements.

3.5 Current work

3.5.1 Total ionization cross-section calculation of molecules relevant to astrochemistry by using BEB model

The molecular orbital parameters required for performing BEB calculations, as discussed in section 3.2.2, were obtained using the Gaussian 09 electronic structure package [38],

and used as input for a customised Fortran 95 programme developed by Vallance and edited by Bull to carry the BEB calculation. The resultant output is in the form of the BEB cross-section as a function of incident electron energy.

The optimal computational methodology was determined previously [39] through a comprehensive benchmarking study where accurate orbital kinetic energies and binding energies were determined accordingly. For each molecule, a geometry optimisation was performed at Hartree-Fock (HF) method [40] with aug-cc-pVTZ basis set [41–43]. For closed-shell and open shell molecules, restricted and unrestricted HF methods were used, respectively [44–46]. Energy calculation was then carried out on the optimised geometry of the molecule, and orbital binding energies were calculated through the use of partial third-order (P3) electron propagator theory [47] which introduced an electron correlation correction where accurate ionization potentials and binding energies are attainable [48, 49]. P3 binding energies show a linear dependence with the HF energies, and the electron correlation effect on the binding energies is attributed to the linear scaling factor, which is then used to scale the orbital kinetic energies.

3.5.2 Total ionization cross-section calculation of molecules relevant to astrochemistry by using polarizability model

To implement total ionization cross-section calculation using polarizability model, the only quantities needed are the polarizability volume and ionization potential. Calculations of polarizability volume were again performed within the Gaussian 09 software package. For geometry optimisation, the Sadlej triple-ζ quality basis set [50], which was developed for the purpose of calculating polarizability, was chosen, based on systematic work by Sekino and Bartlett [51]. A slight modification was introduced to augment one set of additional uncontracted *d* functions with orbital exponent $\zeta = 0.1$ [39]. Polarizability and frequency calculations were performed using the same basis set. The PBE0 hybrid density functional theory (DFT) functional [52, 53], which uses 25%

exact exchange and 75% DFT exchange, was used based on its suitability in other polarizability calculations [54, 55].

Since almost all target molecules in the current work can be classified as many-atom organic or halocarbon species, the same as those included in Bull and co-workers' recent benchmarking work [39], the proportionality constant between maximum cross-section and polarizability volume is taken from the fitted result therein. Maximum cross-section is therefore calculated by using the following equation:

$$\sigma = 1.478\alpha \tag{3.56}$$

It is then straightforward to use Equation (3.53) to obtain $E_{\max}$, the energy at which maximum cross-section occurs, which is used for calculating $\lambda_{\max}$ by Equation (3.52). Provided the ionization potential is known, the cross-section function is then easily attainable from Equation (3.55). For the current work, molecular ionization potentials were taken from NIST recommended data [56]. They may, however, also be obtained from electronic structure calculations.

References

[1] T. D. Märk and G. H. Dunn. *Electron Impact Ionization*. Vienna: Springer, 1985.

[2] M. R. H. Rudge. "Theory of the Ionization of Atoms by Electron Impact". In: *Reviews of Modern Physics* 40.3 (1968), pp. 564–590.

[3] J. J. Thomson. "XLII. Ionization by moving electrified particles". In: *The London, Edinburgh, and Dublin Philosophical Magazine and Journal of Science* 23.136 (1912), pp. 449–457.

[4] H. Bethe. "Zur Theorie des Durchgangs schneller Korpuskularstrahlen durch Materie". In: *Annalen der Physik* 397.3 (1930), pp. 325–400.

[5] H. Bethe. "Bremsformel für Elektronen relativistischer Geschwindigkeit". In: *Zeitschrift für Physik* 76.5 (1932), pp. 293–299.

[6] M. Gryziński. "Two-Particle Collisions. I. General Relations for Collisions in the Laboratory System". In: *Physical Review* 138.2A (1965), A305–A321.

[7] A. Burgess. "The semi-classical treatment of the excitation and ionization of atoms and positive ions by electron impact". In: *Atomic collision processes: the proceedings of the Third International Conference on the Physics of Electronic and Atomic Collisions*. Ed. by M. R. C. McDowell. Amsterdam: North-Holland, 1963, p. 237.

[8] L. Vriens. "Binary-Encounter Electron-Atom Collision Theory". In: *Physical Review* 141.1 (1966), pp. 88–92.

[9] H. Deutsch and T. D. Märk. "Calculation of absolute electron impact ionization cross-section functions for single ionization of He, Ne, Ar, Kr, Xe, N and F". In: *International Journal of Mass Spectrometry and Ion Processes* 79.3 (1987), R1–R8.

[10] D. Margreiter, H. Deutsch, and T. D. Märk. "A semiclassical approach to the calculation of electron impact ionization cross-sections of atoms: from hydrogen to uranium". In: *International Journal of Mass Spectrometry and Ion Processes* 139 (1994), pp. 127–139.

[11] J. W. Otvos and D. P. Stevenson. "Cross-sections of Molecules for Ionization by Electrons". In: *Journal of the American Chemical Society* 78.3 (1956), pp. 546–551.

[12] D. Margreiter, H. Deutsch, M. Schmidt, and T. D. Märk. "Electron impact ionization cross sections of molecules: Part II. Theoretical determination of total (counting) ionization cross sections of molecules: a new approach". In: *International Journal of Mass Spectrometry and Ion Processes* 100 (1990), pp. 157–176.

[13] W. Hwang, Y.-K. Kim, and M. E. Rudd. "New model for electron-impact ionization cross sections of molecules". In: *Journal of Chemical Physics* 104.8 (1996), pp. 2956–2966.

[14] Y.-K. Kim and M. E. Rudd. "Binary-encounter-dipole model for electron-impact ionization". In: *Physical Review A* 50.5 (1994), pp. 3954–3967.

[15] N. F. Mott. "The collision between two electrons". In: *Proceedings of the Royal Society of London. Series A. Containing Papers of a Mathematical and Physical Character* 126.801 (1930), p. 259.

[16] L. Vriens. In: *Case Studies in Atomic Collision Physics*. Ed. by E. W. McDaniel and M. R. C. McDowell. Vol. 1. Amsterdam: North-Holland, 1969, p. 335.

[17] W. Lotz. "An empirical formula for the electron-impact ionization cross-section". In: *Zeitschrift für Physik* 206.2 (1967), pp. 205–211.

[18] W. Lotz. "Electron-impact ionization cross-sections and ionization rate coefficients for atoms and ions from hydrogen to calcium". In: *Zeitschrift für Physik* 216.3 (1968), pp. 241–247.

[19] W. Lotz. "Electron-impact ionization cross-sections for atoms up to Z=108". In: *Zeitschrift für Physik A Hadrons and nuclei* 232.2 (1970), pp. 101–107.

[20] M. R. H. Rudge and S. B. Schwartz. "The ionization of hydrogen and of hydrogenic positive ions by electron impact". In: *Proceedings of the Physical Society* 88.3 (1966), p. 563.

[21] A. Burgess, H. P. Summers, D. M. Cochrane, and R. W. P. McWhirter. "Cross-sections for ionization of positive ions by electron impact". In: *Monthly Notices of the Royal Astronomical Society* 179 (1977), pp. 275–292.

[22] A. Burgess and M. C. Chidichimo. "Electron impact ionization of complex ions". In: *Monthly Notices of the Royal Astronomical Society* 203.4 (1983), pp. 1269–1280.

[23] D. K. Jain and S. P. Khare. "Electron impact ionization of molecular gases". In: *the IXth International Conference on the Physics of Electronic and Atomic Collisions*. Ed. by J. S. Risley and R. Geballe. Seattle: University of Washington Press, 1975, p. 484.

[24] D. K. Jain and S. P. Khare. "Ionizing collisions of electrons with CO_2, CO, H_2O, CH_4 and NH_3". In: *Journal of Physics B: Atomic, and Molecular Physics* 9.8 (1976), p. 1429.

[25] S. P. Khare. "Energy spectrum of the secondary electrons and the fluorescent efficiency of electrons in the 3914-Å band". In: *Planetary and Space Science* 17.6 (1969), pp. 1257–1268.

[26] W. F. Miller and R. L. Platzman. "On the Theory of the Inelastic Scattering of Electrons by Helium Atoms". In: *Proceedings of the Physical Society. Section A* 70.4 (1957), p. 299.

[27] C. B. Opal, E. C. Beaty, and W. K. Peterson. "Tables of secondary-electron-production cross sections". In: *Atomic Data and Nuclear Data Tables* 4 (1972), pp. 209–253.

[28] K. L. Bell, H. B. Gilbody, J. G. Hughes, A. E. Kingston, and F. J. Smith. "Recommended Data on the Electron Impact Ionization of Light Atoms and Ions". In: *Journal of Physical and Chemical Reference Data* 12.4 (1983), pp. 891–916.

[29] M. Bobeldijk, W. J. van der Zande, and P. G. Kistemaker. "Simple models for the calculation of photoionization and electron impact ionization cross sections of polyatomic molecules". In: *Chemical Physics* 179.2 (1994), pp. 125–130.

[30] F. W. Lampe, J. L. Franklin, and F. H. Field. "Cross sections for ionization by electrons". In: *Journal of the American Chemical Society* 79.23 (1957), pp. 6129–6132.

[31] J. E. Bartmess and R. M. Georgiadis. "Empirical methods for determination of ionization gauge relative sensitivities for different gases". In: *Vacuum* 33.3 (1983), pp. 149–153.

[32] H. Nishimura and H. Tawara. "Total electron impact ionization cross sections for simple hydrocarbon molecules". In: *Journal of Physics B: Atomic, Molecular and Optical Physics* 27.10 (1994), pp. 2063–2074.

[33] P. W. Harland and C. Vallance. "Ionization cross-sections and ionization efficiency curves from polarizability volumes and ionization potentials". In: *International Journal of Mass Spectrometry* 171.1-3 (1997), pp. 173–181.

[34] C. Vallance, S. A. Harris, J. E. Hudson, and P. W. Harland. "Absolute electron impact ionization cross sections for CH_3X, where X=H, F, Cl, Br, and I". In: *Journal of Physics B: Atomic, Molecular and Optical Physics* 30.10 (1997), pp. 2465–2475.

[35] D. Rapp and P. Englander-Golden. "Total Cross Sections for Ionization and Attachment in Gases by Electron Impact. I. Positive Ionization". In: *The Journal of Chemical Physics* 43.5 (1965), pp. 1464–1479.

[36] N. L. Djurić, I. M. Čadež, and M. V. Kurepa. "H_2O and D_2O total ionization cross-sections by electron impact". In: *International Journal of Mass Spectrometry and Ion Processes* 83.3 (1988), R7–R10.

[37] H. S. W. Massey and E. H. S. Burhop. In: *Electronic and Ionic Impact Phenomena*. 2nd. Oxford: Clarendn Press, 1969, p. 187.

[38] M. J. Frisch, G. W. Trucks, H. B. Schlegel, G. E. Scuseria, M. A. Robb, J. R. Cheeseman, G. Scalmani, V. Barone, G. A. Petersson, H. Nakatsuji, X. Li, M. Caricato, A. V. Marenich, J. Bloino, B. G. Janesko, R. Gomperts, B. Mennucci, H. P. Hratchian, J. V. Ortiz, A. F. Izmaylov, J. L. Sonnenberg, Williams, F. Ding, F. Lipparini, F. Egidi, J. Goings, B. Peng, A. Petrone, T. Henderson, D. Ranasinghe, V. G. Zakrzewski, J. Gao, N. Rega, G. Zheng, W. Liang, M. Hada, M. Ehara, K. Toyota, R. Fukuda, J. Hasegawa, M. Ishida, T. Nakajima, Y. Honda, O. Kitao, H. Nakai, T. Vreven, K. Throssell, J. A. Montgomery Jr., J. E. Peralta, F. Ogliaro, M. J. Bearpark, J. J. Heyd, E. N. Brothers, K. N. Kudin, V. N. Staroverov, T. A. Keith, R. Kobayashi, J. Normand, K. Raghavachari, A. P. Rendell, J. C. Burant, S. S. Iyengar, J. Tomasi, M. Cossi, J. M. Millam, M. Klene, C. Adamo, R. Cammi, J. W. Ochterski, R. L. Martin, K. Morokuma, O. Farkas, J. B. Foresman, and D. J. Fox. *Gaussian 09 Revision D.01*. Gaussian Inc. Wallingford, CT. 2016.

[39] J. N. Bull, P. W. Harland, and C. Vallance. "Absolute Total Electron Impact Ionization Cross-Sections for Many-Atom Organic and Halocarbon Species". In: *Journal of Physical Chemistry A* 116.1 (2012), pp. 767–777.

[40] C. C. J. Roothaan. "New Developments in Molecular Orbital Theory". In: *Reviews of Modern Physics* 23.2 (1951), pp. 69–89.

[41] T. H. Dunning Jr. "Gaussian basis sets for use in correlated molecular calculations. I. The atoms boron through neon and hydrogen". In: *The Journal of Chemical Physics* 90.2 (1989), pp. 1007–1023.

[42] R. A. Kendall, T. H. Dunning Jr., and R. J. Harrison. "Electron affinities of the first-row atoms revisited. Systematic basis sets and wave functions". In: *The Journal of Chemical Physics* 96.9 (1992), pp. 6796–6806.

[43] D. E. Woon and T. H. Dunning Jr. "Gaussian basis sets for use in correlated molecular calculations. III. The atoms aluminum through argon". In: *The Journal of Chemical Physics* 98.2 (1993), pp. 1358–1371.

[44] C. C. J. Roothaan. "New Developments in Molecular Orbital Theory". In: *Reviews of Modern Physics* 23.2 (1951), pp. 69–89.

[45] J. A. Pople and R. K. Nesbet. "Self-Consistent Orbitals for Radicals". In: *The Journal of Chemical Physics* 22.3 (1954), pp. 571–572.

[46] R. McWeeny and G. Diercksen. "Self-Consistent Perturbation Theory. II. Extension to Open Shells". In: *The Journal of Chemical Physics* 49.11 (1968), pp. 4852–4856.

[47] J. V. Ortiz. “Partial third-order quasiparticle theory: Comparisons for closed-shell ionization energies and an application to the Borazine photoelectron spectrum”. In: *The Journal of Chemical Physics* 104.19 (1996), pp. 7599–7605.

[48] J. Linderberg and Y. Öhrn. *Propagators in Quantum Chemistry*. Hoboken, NJ: Wiley, 2004.

[49] J. V. Ortiz. “Electron propagator theory: an approach to prediction and interpretation in quantum chemistry”. In: *Wiley Interdisciplinary Reviews: Computational Molecular Science* 3.2 (2012), pp. 123–142.

[50] A. J. Sadlej. “Medium-size polarized basis sets for high-level correlated calculations of molecular electric properties”. In: *Collection of Czechoslovak Chemical Communications* 53.9 (1988), pp. 1995–2016.

[51] H. Sekino and R. J. Bartlett. “Molecular hyperpolarizabilities”. In: *The Journal of Chemical Physics* 98.4 (1993), pp. 3022–3037.

[52] C. Adamo and V. Barone. “Toward reliable density functional methods without adjustable parameters: The PBE0 model”. In: *The Journal of Chemical Physics* 110.13 (1999), pp. 6158–6170.

[53] M. Ernzerhof and G. E. Scuseria. “Assessment of the Perdew–Burke–Ernzerhof exchange-correlation functional”. In: *The Journal of Chemical Physics* 110.11 (1999), pp. 5029–5036.

[54] C. Adamo, M. Cossi, G. Scalmani, and V. Barone. “Accurate static polarizabilities by density functional theory: assessment of the PBE0 model”. In: *Chemical Physics Letters* 307.3 (1999), pp. 265–271.

[55] C. Van Caillie and R. D. Amos. “Static and dynamic polarisabilities, Cauchy coefficients and their anisotropies: an evaluation of DFT functionals”. In: *Chemical Physics Letters* 328.4 (2000), pp. 446–452.

[56] S. G. Lias. *Ionization Energy Evaluation. In: Linstrom, P. J. and Mallard, W. G. (eds.) NIST Chemistry WebBook, NIST Standard Reference Database Number 69*. Gaithersburg, MD, 20899: National Institute of Standards and Technology.

4

Experimental design

Contents

4.1 Overall set-up **72**
4.2 Optimisation of cell design **74**
4.2.1 Optimisation of electron beam emitter 76
4.2.2 Optimisation of ion optics 78
4.2.3 Experimental optimisation of static potentials 81
4.2.4 Optimisation of sample pressure 85
4.2.5 Optimisation of gas tubing and feedthroughs 87
4.3 Summary of optimised cell design **88**
4.3.1 Electron source 88
4.3.2 First Einzel lens 88
4.3.3 Collision cell 89
4.3.4 Lens elements L4 and L5, and Faraday cup 90
4.4 Electronics **91**
4.4.1 Filament power supply 91
4.4.2 Electrostatic Lens Power supply 91
4.4.3 Electron and ion detection 91
4.4.4 Capacitance manometer and absolute pressure measurement . . 93
4.4.5 Thermocouple 95
4.4.6 Instrument control and data acquisition 95
4.5 Vacuum system **95**
4.6 Sample preparation and sample line set-up **96**
4.7 Calibration of the new cell design **98**
4.7.1 Calibration factors to be considered 98
4.7.2 Testing and optimisation with N_2 100
4.7.3 Comparison with other common permanent gas molecules . . . 101
4.8 Common issues **103**

4.8.1 Cell and ion optics contamination 103
4.8.2 Stability and hysteresis of gas pressure reading 107
4.9 Standard operating procedures 108
References 109

4.1 Overall set-up

The instrument used to perform the absolute total ionization cross-section measurements described in this thesis is based on an original design by Professor Peter Harland at the University of Canterbury, New Zealand [1–7]. As part of the present work, a number of modifications and improvements have been made to the earlier design. The basic elements of the instrument are illustrated schematically in Figure 4.1.

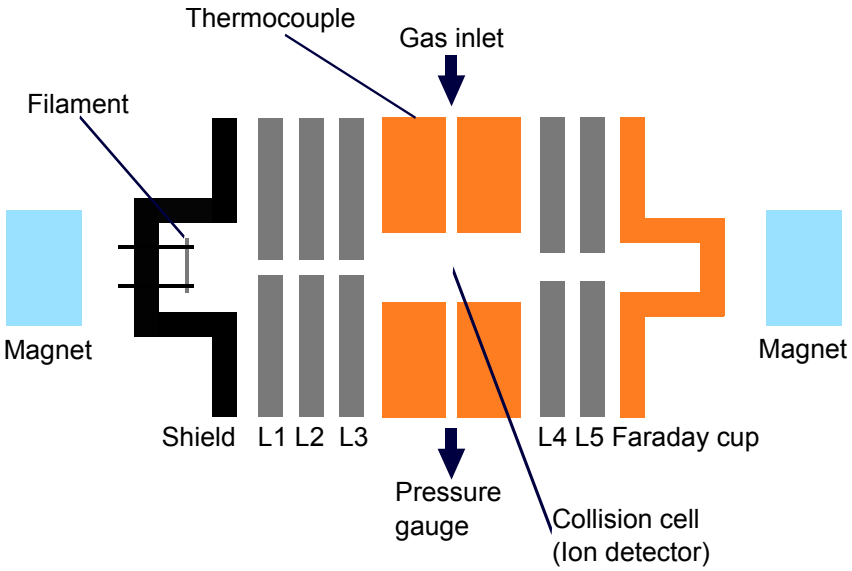


Figure 4.1: Schematic diagram of current instrument used to measure absolute total electron ionization cross-sections.

Electrons are generated by thermionic emission at a resistively heated tungsten-rhenium filament. They are focused and collimated into a beam by the combined electric field from a "top-hat" shaped shield located behind the filament and an Einzel lens (formed from lens elements L1, L2, and L3), before passing through the collision cell, where

they collide with and ionize the target gas molecules. The resulting positive ions are collected at the negatively biased walls of the collision cell as an ion current I^+, while the electrons transmitted through the cell are re-collimated by a second Einzel lens (formed from lens elements L4 and L5 in Figure 4.1) and detected as an electron current, I^-, at the positively-biased Faraday cup.

A homogeneous axial magnetic field is formed by positioning two grade N42 Neodymium-Iron-Boron circular disc magnets on each end of the apparatus. The magnets are connected together by a U-shaped iron yoke in order to increase the magnetic field strength along the axial direction. The field strength at the centre of the collision cell was measured to be 200 G.

The temperature, T, is recorded by a chromel-alumel thermocouple embedded in the wall of the collision cell, with the assumption that the sample gas reaches thermal equilibrium with the walls of the cell. The sample gas is fed in from one side of the cell, and a capacitance manometer is connected to the opposite side of the cell to measure the gas pressure p. The number density n of the sample gas can then be determined from the measured pressure and temperature using Equation (2.27). If all ions formed inside the cell can be detected, then the effective pathlength over which electron ionization occurs is simply the width of the cell. However, calibration is needed to account for (i) the fact that ions formed outside the cell might be detected, and/or ions formed at the edges of the cell might not be detected, and (ii) the magnetic field adds a helical component to the electron beam trajectory. In practice the latter of these is generally insignificant. Therefore, all quantities required for determining the total ionization cross-section can be measured directly.

The "top-hat" shield and all lens elements (L1, L2, L3, L4 and L5) are made of Type 316L stainless steel. The collision cell and Faraday cup, which act as the detectors for the ion and electron currents, respectively, are made of low-resistance copper. All metal parts (i.e.

shield, lens elements, cell, and Faraday cup) are heated to 300 °C for 20 minutes before applying colloidal graphite to reduce scattering of electrons and ions from their surfaces.

Polyether ether ketone (PEEK) is used to make the insulating spacers that electrically isolate each lens element, the collision cell, and the Faraday cup. The main advantage of PEEK as opposed to the widely-used alternative polytetrafluoroethylene (PTFE) is its better machinability. A set of insulating spacers made from machinable glass ceramic are used between the shield and lens element L1, since the local temperature is likely to approach the melting point of PEEK when the filament is on.

4.2 Optimisation of cell design

The original Canterbury cell was used for many years to perform total ionization cross-section measurements on a variety of molecules. However, it was discovered during test measurements in late 2013 that the advanced age of the apparatus was causing numerous problems with the integrity of vacuum feedthroughs, insulators, and other components, and it was decided that manufacture of a new cell was the best solution. This also provided an opportunity to optimise the cell design further via a series of field and particle trajectory simulations performed using the SIMION® [8–10] ion trajectory simulation package. SIMION allows a user to build a virtual model of their experiment, defining electrode positions and potentials, and to model the electric fields and resulting charged particle trajectories for user-defined initial particle positions and velocities. SIMION trajectory simulations using the original design of the Canterbury cell showed that the potential along the axis of the collision cell was not uniform, which introduced a considerable uncertainty between 17.120 eV and 10.604 eV into the electron energy (Figure 4.2). The simulation also indicated that the electron beam collimation and the ion collection efficiencies could potentially be improved (Figure 4.3). In the following, we explain the various steps involved in optimising the design via a combination of simulation and experiment.

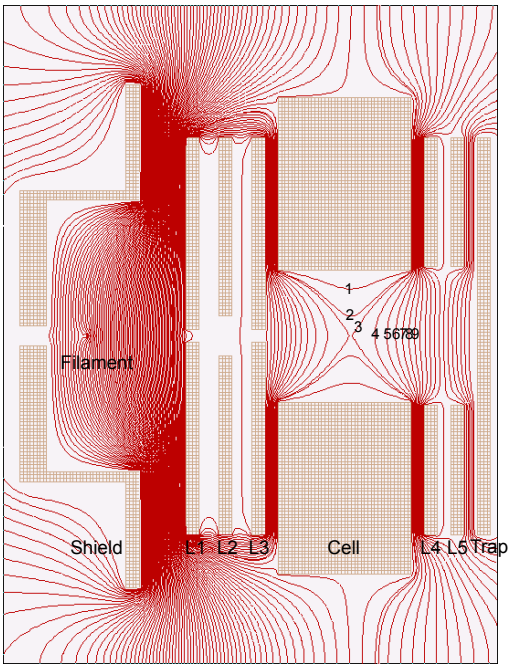
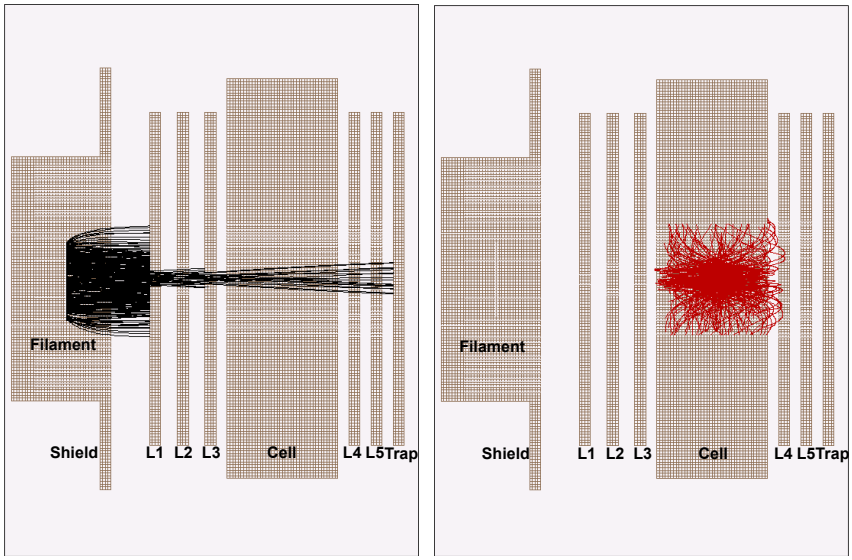


Figure 4.2: Schematic cross-sectional view of original Canterbury cell and SIMION simulated equipotential lines. Values of equipotential lines: 1 = −18.846 V, 2 = −17.473 V, 3 = −17.120 V, 4 = −16.099 V, 5 = −14.725 V, 6 = −13.352 V, 7 = −11.978 V, 8 = −10.604 V, 9 = −9.231 V. Simulation conditions: filament = −100 V, shield = −115 V, L1 = L2 = L5 = −2 V, L3 = L4 = 0 V, Cell = −20 V, Trap = 10 V.



(a) **(b)**

Figure 4.3: Schematic cross-sectional view of original Canterbury cell and SIMION simulated (a) primary electron beam trajectories and (b) molecular nitrogen ion trajectories. It can be seen that the primary electron beam has noticeable divergence especially near the trap. Simulation conditions: filament = −100 V, shield = −115 V, L1 = L2 = L5 = −2 V, L3 = L4 = 0 V, Cell = −20 V, Trap = 10 V. Number of particles: 500.

4.2.1 Optimisation of electron beam emitter

The original electron beam emitter design is comprised of a "top-hat" shaped shield, a ceramic filament base, and a pair of filament posts across which the tungsten-rhenium filament is attached. This design has been proved to provide a compact and robust electron beam source, which yields a reliable and uniform electron beam. Modifications within the present work have been focused on improving ease of use by using a commercially available pre-mounted filament, which is more straightforward to install and uninstall than the in-house designed version. The filament has a finite lifetime, and care must be taken when operating it (see Appendix B).

Thermionic emission is the phenomenon that hot bodies emit charged particles, particularly electrons, as a result of thermal excitation of mobile electrons contained within the body to sufficiently high energies to overcome the image-charge force and escape out of the hot bodies. This is called electron evaporation, or more formally, thermionic emission. The phenomenon was studied by Owen Richardson in the early 20$^{\text{th}}$ century, earning him the award of the 1929 Nobel Prize in Physics [11].

The liberated electrons can be drawn from the hot bodies (i.e. cathode) to an anode if an external electric field is applied between them. Richardson's work on thermionic emission resulted in a mathematical description of the current density J:

$$J = AT^2 \exp\left(-\frac{W}{k_{\text{B}}T}\right) \tag{4.1}$$

Where A is Richardson's constant ($A = 1.2 \times 10^6$ A m^{-2} K^{-2}), T is the temperature in K; W is the work function of the cathode material, and k_{B} is the Boltzmann constant. Since W is a material specific constant and A and k_{B} are universal constants, the current density J only depends on the temperature of the hot body. For a filament, this is directly related to the heating current. Therefore, the electron gun current is controlled by varying the filament power supply.



Figure 4.4: Schematic diagram (left) and picture (right) of Agar Scientific AGA054 tungsten-rhenium filament.

4.2.1.1 Filament shape and material

Different shapes of filaments were investigated in order to achieve the highest quality electron beam emission. Initially, the hairpin-shaped Agar Scientific AGA054 tungsten-rhenium filament was tested (Figure 4.4). While this filament in principle generates a high quality beam, achieving optimum axial collimation was very challenging since the emission is effectively from a point source and the apertures of lens element L1, L2 and L3 have to be in perfect alignment with respect to the filament tip. This made the performance of the filament highly sensitive to installing and dismounting procedures. Presumably for related reasons, the point filament source also failed to provide a consistent and uniform current density.

Use of a straight filament overcomes the alignment issue. A straight tungsten-rhenium filament was spot welded between the two filament posts on the Agar Scientific AGA054 filament base after removing the original hairpin filament. The filament now only needs to be aligned in one direction, and achieving optimum alignment of the filament with respect to the various lens element apertures becomes easily achievable. This filament assembly was chosen as the electron emitter for the final instrument design.

Tungsten-rhenium alloys have improved strength and ductility of tungsten within the temperature range from 20-3000 °C, which is ideal when both smallest diameter and

highest strength are both required. Compared to tungsten, the resistivity of tungsten-rhenium alloys increases with rhenium content. Therefore, a thicker filament wire may be used with the same heating current, which increases the reliability, robustness, and durability of the filament [12].

4.2.1.2 Filament saturation and operating current

When operating a thermionic emission electron source, the flux of electrons emitted from the filament increases in proportion to the current through the filament increases. However, the emission saturates at a certain filament current, and further increasing the filament current does not increase electron emission. It does, however, shorten the lifetime of the filament, and can result in sudden breakage. The emitted current should therefore always be kept below the saturation current, in order to optimise both the electron emission and filament lifetime. In practice, the electron emission current is set to the minimum value at which reasonable signal-to-noise is achieved in the experiment. This is particularly important when employing relatively high sample pressures, since the rate of filament deterioration increases with ambient pressure. For most measurements conducted in the current project, the filament current is kept below 2.5 A, which produces an electron emission current below 50 nA, with corresponding ion currents up to 2 nA.

4.2.2 Optimisation of ion optics

The experimental conditions employed in the SIMION simulation were:

1) Electron energy (filament potential): 0 to 300 eV.
2) Static potentials on "top-hat" shield: 0 to 20 volts more negative than electron energy.
3) Static potentials on lens elements L1, L2, L5: negative potential between −1V and −10V.

4) Static potentials on collision cell: negative potential and as small as possible, while still ensuring that all ions formed along the axis of the collision cell are collected on the cell walls.
5) Static potentials on Faraday cup: positive potential and as small as possible, provided that no transmitted electron and secondary electrons can escape the Faraday cup, and no other particles formed outside Faraday cup can enter and be collected by the Faraday cup.

These conditions, together with the dimensions and locations of the ion optics, were varied in a systematic way to improve the performance of the design, with the goal of satisfying the following optimisation criteria:

1) To produce a well collimated, near-linear, and intense electron beam which is transmitted to the Faraday cup without scattering from any of the lens elements L1 to L5.
2) All ions formed within the collision cell should be collected by the ion detector (i.e. inner wall of the collision cell).
3) All electrons transmitted through the collision cell should be collected by the Faraday cup; High energy electrons that are back-scattered when hitting Faraday cup should not escape and should eventually be collected; Secondary electrons formed from the surface of Faraday cup should not escape and will be collected by the Faraday cup.
4) The electric field along the axis of the collision cell should be as uniform as possible. Grounded lens element L3 and L4 should have apertures as small as possible in order to avoid field penetration from lens elements further downstream in either direction.

The optimised design is shown in cross-sectional view in Figure 4.5. The potential along the axis of the cell is now reduced to between −7.870 V and −2.674 V. This range of

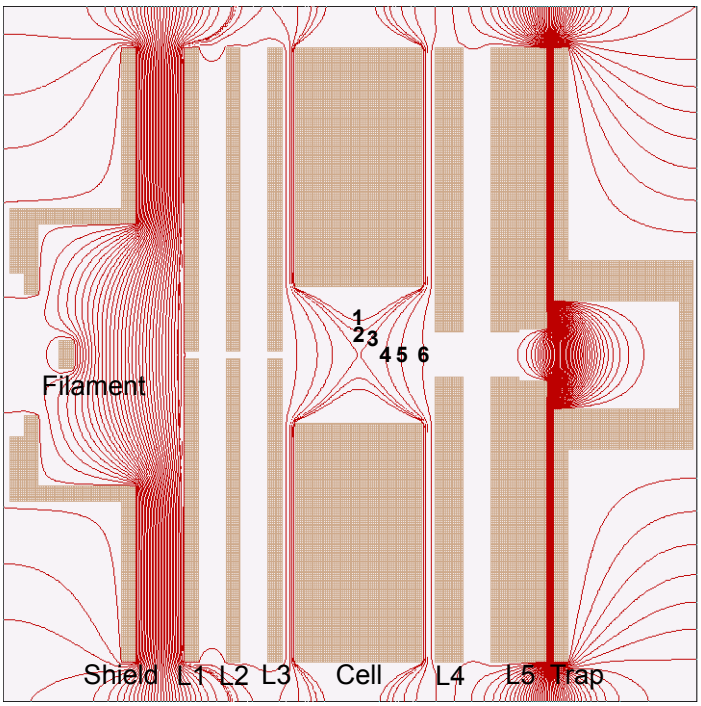
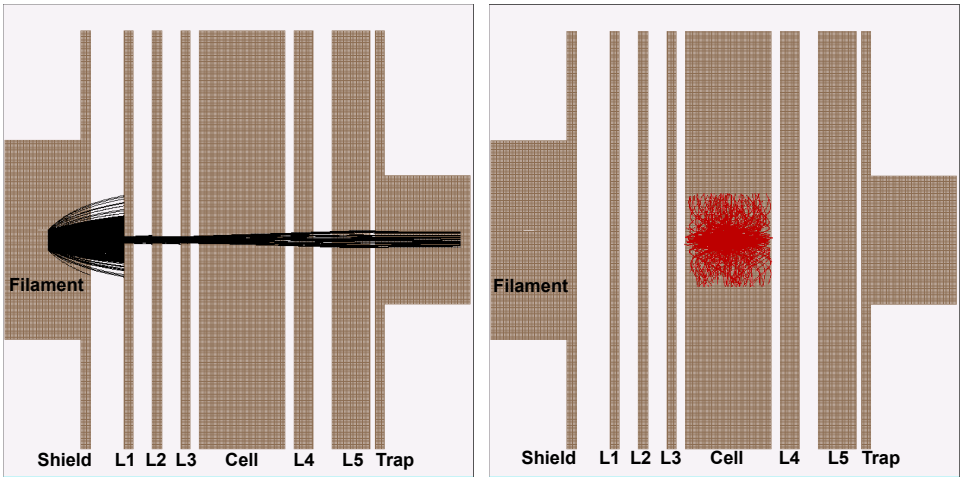


Figure 4.5: Schematic cross-sectional view of new cell and SIMION simulated equipotential lines. Values of equipotential lines: 1 = −8.547 V, 2 = −8.200 V, 3 = −7.870 V, 4 = −7.000 V, 5 = −5.610 V, 6 = −2.674 V. Simulation conditions: filament = −100 V, shield = −102.5 V, L1 = L2 = L5 = −2 V, L3 = L4 = 0 V, Cell = −10 V, Trap = 150 V.



(a) **(b)**

Figure 4.6: Schematic cross-sectional view of new cell and SIMION simulated (a) primary electron beam trajectories and (b) molecular nitrogen ions trajectories. Simulation conditions: filament = −100 V, shield = −102.5 V, L1 = L2 = L5 = −2 V, L3 = L4 = 0 V, Cell = −10 V, Trap = 150 V. Number of particles: 1000.

uncertainty can be further reduced by deconvoluting the measured cross-section data from the instrument function describing the potential distribution along the axis of the cell. Detailed procedures can be found in Appendix C. Figure 4.6 shows simulated trajectories for the primary electron beam and molecular nitrogen ions formed inside the collision cell. Compared to the trajectories shown in Figure 4.3 for the original Canterbury design, the primary electron beam is now much better collimated, and the ion collection efficiency is improved.

The new cell assembly was fabricated by the Physical and Theoretical Chemistry (PTCL) mechanical workshops within the Department of Chemistry, University of Oxford, and was installed in the existing high vacuum system.

4.2.3 Experimental optimisation of static potentials

The SIMION optimised cell design, once manufactured and installed, needs to be verified experimentally by testing combinations of various static potentials and electron energies, to ensure that: a) the optimisation goals listed above are indeed achieved; b) optimal static potentials are determined; and c) the optimised potentials are able to satisfy all criteria listed in Section 4.2.2 irrespective of the incident electron energy. The experimental tests were performed for four representative nominal incident electron energies spanning the range from 50 eV to 290 eV. In most cases, filament potentials of −50 V, −100 V, −150 V, and −290 V were employed.

The first of the optimisation criteria, that the electron beam is transmitted to the Faraday cup without scattering from L4 and L5, can be tested by measuring the current from L4 and L5 to determine whether any electrons reach these lens elements. A better approach in practice is to assess the electron current recorded from L4 and L5 as a fraction of the total electron current recorded from L4, L5, and the electron detector (Faraday cup). This is shown in Figure 4.7 as a function of the potential applied to the Faraday cup. Both the

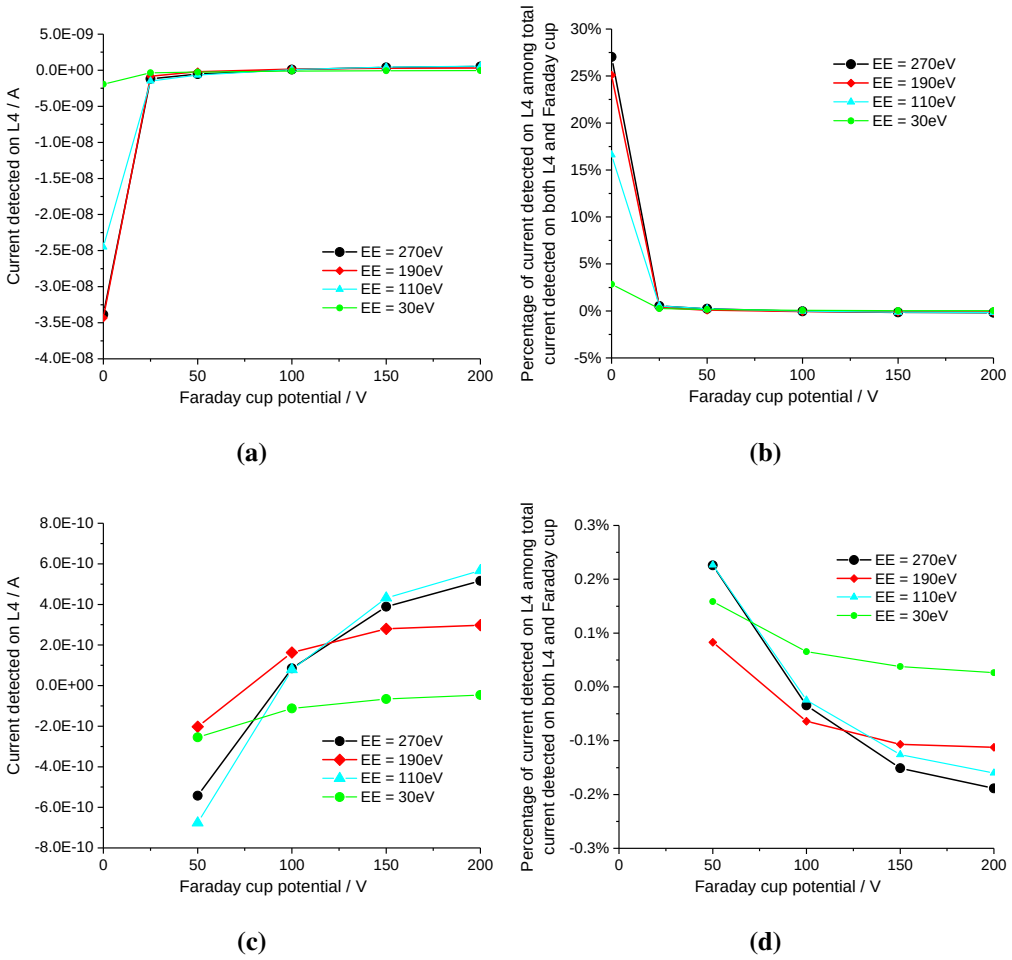
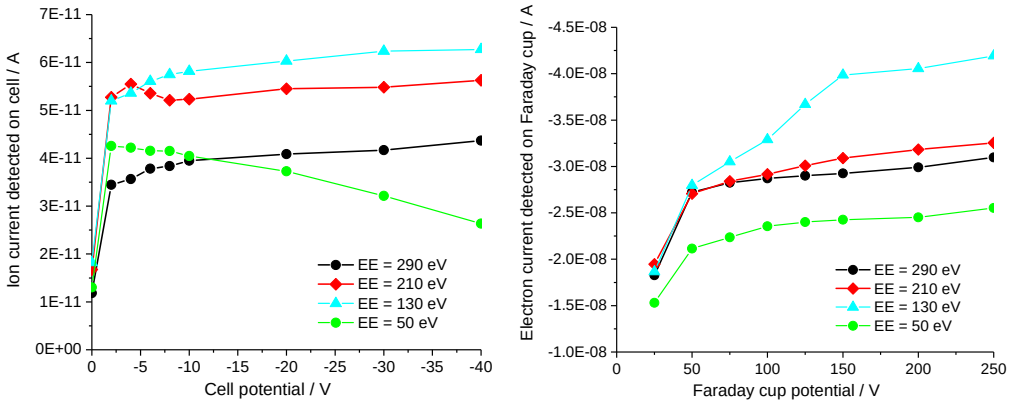


Figure 4.7: (a) Currents on L4 by varying incident electron energies from 0 to 200 eV; (b) Percentage of currents on L4 among total currents on both L4 and Trap; (c) Same as top-left figure but only shows close-up area when trap potential $\geq$ 50 V; (d) Same as Top-right figure but only shows close-up area when trap potential $\geq$ 50 V (to test goal 1 in Section 4.2.2).

absolute value of the electron current recorded from L4 and the percentage of the total electron signal recorded on L4 rapidly tend towards zero when the Faraday cup potential is increased above 50 V. Under these conditions, the electron current from L4 is less than ±0.2% of the total current recorded from both L4 and the Faraday cup, demonstrating that the first optimisation criterion is satisfied to a high degree.

The second and third optimisation criteria, that all ions generated within the collision cell are detected at the cell walls, and that all transmitted electrons are detected at the Faraday cup, can be tested by recording the current from each detector as the detector



(a) **(b)**

Figure 4.8: Collection efficiency of (a) ion and (b) electron detectors (to test optimisation criteria 2 and 3 in Section 4.2.2).

potential is increased gradually. The results are shown in Figure 4.8. The detected current increases as the applied static potential increases, until all the relevant particles are being detected, at which point further increasing the potential will not lead to an significant increase in the detected current. As shown in Figure 4.8, this condition is satisfied for the ion detector and electron detector at applied potentials of −10 V and +150 V, respectively. These potentials were subsequently used in the experiment. The unusual behaviour of ion current as a function of cell potential when electron energy is at 50 eV is probably due to the fact that when cell potential increases towards −40 V, the majority of the electron beam with energy of 50 eV cannot pass through the cell easily.

The final design criterion, achieving a constant and near-zero potential along the axis of the collision cell in order to ensure that the electron energy is well defined, was simulated in SIMION, as described in Section 4.2.2. However, the extent to which a high Faraday cup potential affects the electric field inside the cell can be verified experimentally by varying the Faraday cup potential while applying a constant potential to the cell. It is expected that if Faraday cup potential can distort the electric field distribution inside the cell, the proportion of ions that can reach the cell will also be affected and thus full collection efficiency will unlikely be possible. As can be seen from Figure 4.9, the ion

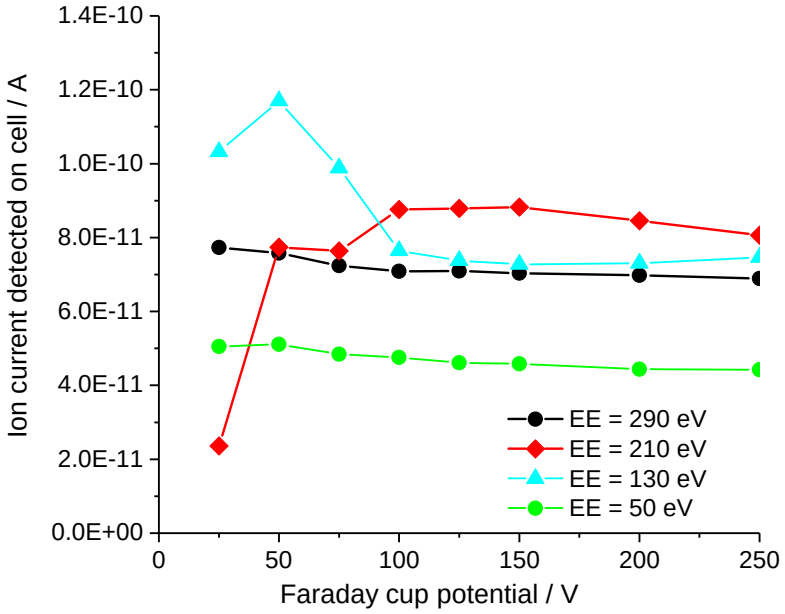


Figure 4.9: Effects of varying Faraday cup potential on ion detector collection efficiency (To test goal 4 in Section 4.2.2).

collection efficiency is independent of Faraday cup potential in the range of +150 V to +200 V, which suggested that +150 V is a reasonable choice. Goal 2 and goal 4 can only be tested when sample gas is admitted into the cell, while goal 1 and 3 may be run at vacuum.

Goal 4 was achieved by incorporating very small apertures into lens elements L4 and L5. This minimises field penetration into the collision cell from other electrostatic lens elements, while allowing the electron beam to pass through undisturbed. Characterisation was performed in SIMION to sample the distribution of electron beam spot on the bottom of the Faraday cup for 7 representative electron energies from 10 eV to 290 eV (Figure 4.10). It can be seen that at most electron energies, the electron beam profile lies within a circle of diameter of 2 mm. This is understandable given the fact that lens element L1, L2, and L3 all have defining apertures of 1 mm diameter and the distance between L3 and Faraday cup is unlikely to lead to significant divergence. It was proposed to drill a 4 mm diameter aperture on both L4 on L5. The cross-sectional electron beam profile was sampled at position when electrons just pass L4 and L5 (Figure

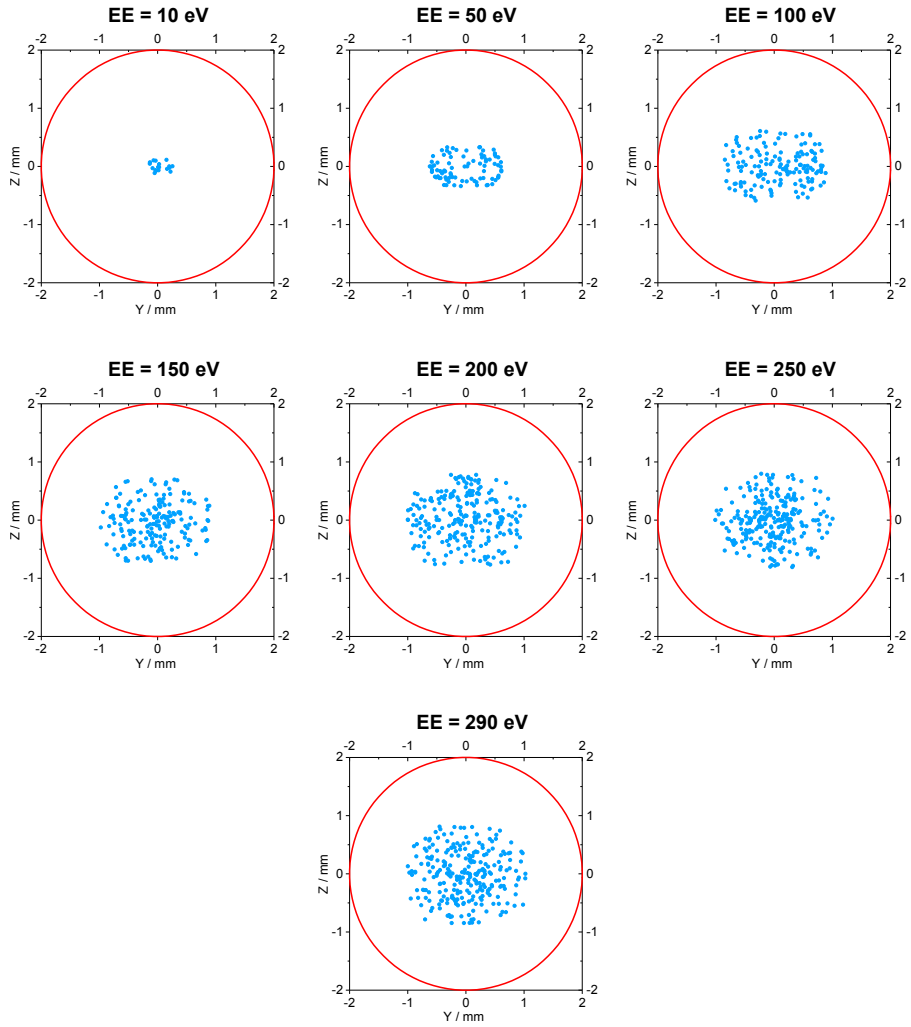


Figure 4.10: SIMION simulated electron beam spot distribution on the bottom of Faraday cup at 7 representative electron energies. Red circles have diameters of 4 mm. Total number of trajectories for each simulation: 5000. Number of trajectories reaching the bottom of the Faraday cup are 18, 87, 154, 189, 232, 251, and 256 at EE = 10 eV, 50 eV, 100 eV, 150 eV, 200 eV, 250 eV, and 290 eV, respectively.

4.11) which shows that no electron hits the aperture. It was then decided to adopt the proposed aperture size on L4 and L5.

The optimal static potentials used for current project are summarised in Table 4.1.

4.2.4 Optimisation of sample pressure

According to Equation (2.27) in Chapter 2, if the sample pressure p increases or decreases, the number density n changes accordingly. Since the total ionization cross-section is an

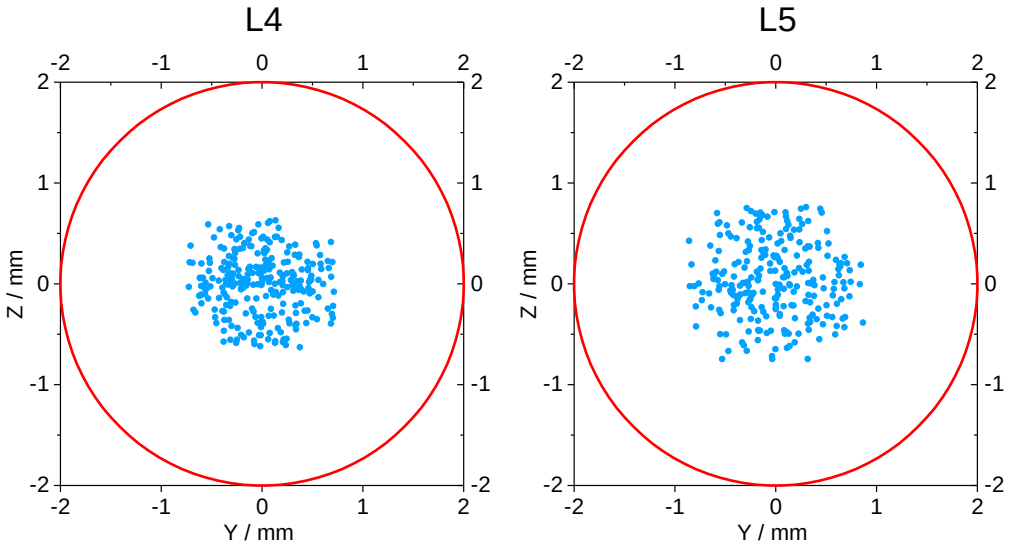


Figure 4.11: SIMION simulated cross-sectional electron beam distribution when passing through lens elements (a) L4 and (b) L5 at EE = 290 eV. Red circles have diameters of 4 mm.

Table 4.1: Static potentials on various elements in the electron ionization cross-section instrument after experimental optimisation.

Ion optics	**Potential**
Filament	0 to −290 V
Shield	−2.5 V relative to filament potential
L1	−2 V
L2	−2 V
L3	0 V
Cell	−10 V
L4	0 V
L5	−2 V
Faraday cup	+150 V

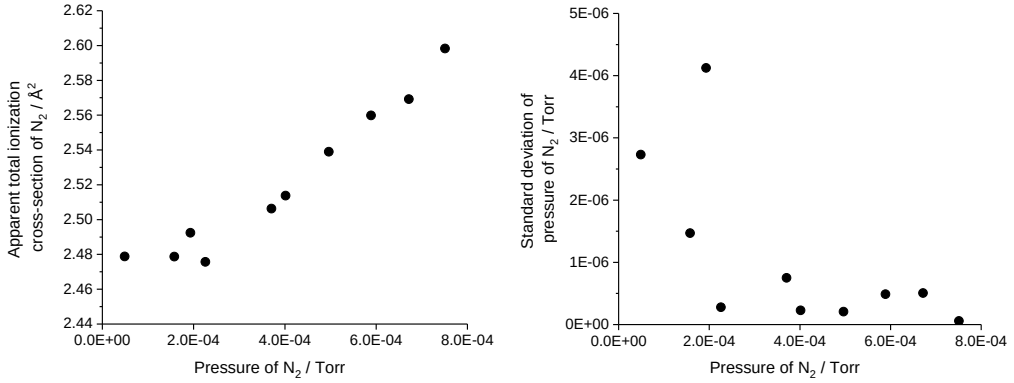


Figure 4.12: (a) Effects of gas pressure on apparent ionization cross-section and (b) standard deviation of each pressure measurement vs apparent pressure values.

intrinsic property of a molecule, the cross-section σ determined from a measurement should remain constant if the pressure is changed. To verify this, total cross-sections of molecular nitrogen gas molecules were measured at a range of pressures from 4.91×10^{-5} Torr to 8.18×10^{-4} Torr. Figure 4.12 shows that the apparent cross-section value increases with gas pressure when the pressure is above 2.26×10^{-4} Torr, but remains relatively constant at pressures below this value. At high pressures, the approximation made in deriving Equation (2.26), that the transmitted and incident electron currents are approximately equal, breaks down. However, it is difficult to achieve a stable gas pressure within the cell at pressures below 2.00×10^{-4} Torr, which increases the uncertainly of the measurements. The ideal range of operating gas pressures is therefore between 2.00×10^{-4} Torr and 3.00×10^{-4} Torr. These pressures are also compatible with a reasonable filament lifetime (see Section 4.2.1.2) and a relatively low degree of cell contamination (see Section 4.8.1).

4.2.5 Optimisation of gas tubing and feedthroughs

The sample gas is admitted to the collision cell via a Series 203 Granville-Phillips® variable leak valve. The valve is connected to the collision cell inside the vacuum chamber by Type 316L stainless steel 1/4 inch tubing and fittings. The stainless steel

tubing that connects the collision cell to the Baratron capacitance manometer is kept as short as possible in order to reduce any time delay between a change in pressure within the cell and the corresponding change in pressure reading. The same applies to the tubing connecting the variable leak valve to the cell, to reduce the delay between manual adjustment of variable leak valve and a change in pressure reading.

Copper or copper alloys should be avoided before the variable leak valve to the sample line as some sample molecules, such as acrylonitrile, are incompatible with copper and copper alloys, but may be used after the variable leak valve to the high vacuum side since the pressure (hence number density) of sample molecule is much lower, ranging from 10^{-7} Torr to 10^{-4} Torr.

4.3 Summary of optimised cell design

4.3.1 Electron source

The electron source, shown in Figure 4.13, consists of a "top-hat" shield, within which the filament is mounted. The filament assembly consists of a ceramic mounting block, into which the two molybdenum filament posts are mounted. The tungsten-rhenium filament is soldered between the rods. Under normal experimental conditions, a current of 2.5 A is passed through the filament, which is negatively biased at between 0 and −290 V. The "top-hat" shield is set to a potential of −2.5 V with respect to the filament potential, deflecting the emitted electrons towards lens element L1.

4.3.2 First Einzel lens

The first Einzel lens consists of three circular electrostatic lens elements: L1, L2, and L3 (Figure 4.1). All lens elements are fabricated from 1 mm thick stainless steel, have 1 mm apertures, and are spaced 1.5 mm apart by PEEK washers. Due to its proximity to the electron source, lens element L1 defines the diameter of the electron beam. Lens

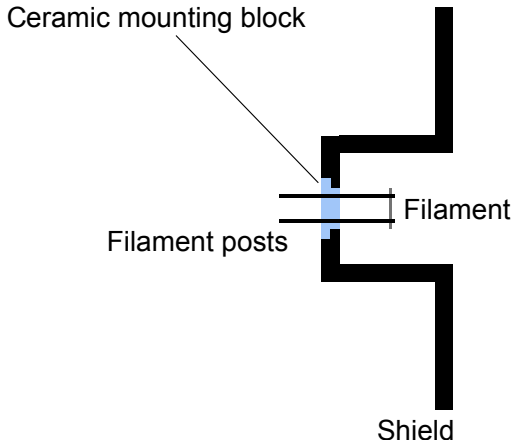


Figure 4.13: Cross-sectional view of electron source.

element L3 is grounded, and the potential applied to lens element L2 may be tuned to optimise the collimation of the electron beam.

4.3.3 Collision cell

The unique innovation introduced by Harland and co-workers was to design the collision cell with a cylindrical geometry, rather than employing the two parallel plates used in many pre-1970s experiments [13–19]. With a cylindrical design, the electric field within the collision region is directed radially towards the inner walls of the cell. Ions formed along the central axis are therefore attracted to and collected by the ion detector in all radial direction, reducing any possible loss of ions. The grounded lens elements L3 and L4 act as guard plates to improve the level of uniformity of the electric field in the axial direction. As can be seen from the SIMION simulations presented in Figure 4.5, the actual potential along the axis of the cell is not perfectly zero. The minimum potential is found in the centre of the cell, which, under normal experimental conditions, is approximately –7.870 V. On both ends of the cell, the potentials are slightly less negative, approximately –2.674 V. The difference between the potential applied to the filament and the potential inside the cell defines the collision energy of the electron-molecule collision. The method used to determine the collision energy accurately will be discussed in Chapter 5.

As illustrated in Figure 4.1, the collision cell measures 10 mm in length, with inner and outer diameters of 10 mm and 20 mm, respectively. The cell is sealed at both ends by two 1 mm thick PEEK insulating rings and two grounded lens elements L3 and L4, which have apertures of 1 mm and 4 mm diameter, respectively. Two diametrically opposed holes of 5 mm inner diameter were drilled through the cell wall to act as the gas sample inlet port, controlled by a Series 203 Granville-Phillips® variable leak valve, and to connect to a MKS Type 690A Series Absolute Baratron® pressure transducer. A screw terminal on the outer surface of the collision cell was served to connect a chromel-alumel thermocouple wire to measure the cell temperature. The sample gas is assumed to reach thermal equilibrium with the cell walls, such that the cell temperature is the same as the sample gas temperature.

4.3.4 Lens elements L4 and L5, and Faraday cup

L4 and L5 act to re-collimate the electron beam and to suppress any backscattered and secondary electron from escaping the Faraday cup. The apertures of L4 and L5 are both 4 mm in diameter, as detailed in Section 4.2.3.

A significant improvement relative to the original Canterbury cell is to use a deep electron trap (Faraday cup) rather than a flat plate. This helps to improve the collection efficiency. Virtually no electron can fly out of the Faraday cup if a potential of +150 V is set. The inner surface of the Faraday cup is coated with a layer of colloidal graphite (“Aquadag”) which further reduces the scattering of bombarding electrons. The collection efficiency was measured at multiple representative incident electron energies, and revealed that “saturation status” is achieved when electron detector potential is at +150 V (Figure 4.8(b)). Since this is independent of incident electron energy, a constant potential of +150 V was set on the Faraday cup for all total ionization cross-section experiment.

4.4 Electronics

4.4.1 Filament power supply

The filament is resistively heated by passing DC current supplied by an Aim-TTi (Thurlby Thandar instruments) Model PL 155-Power supply. The filament power supply is always gradually turned on before admitting sample gas into the cell to protect the filament from poisoning. The filament is given 30 minutes warm-up time to achieve a stable emitting current before introducing sample gas.

4.4.2 Electrostatic Lens Power supply

The static potentials on the ion optics are supplied by a multiple channel power supply unit manufactured by the PTCL electronics workshops in the Department of Chemistry, University of Oxford. The power supply unit consists of eight positive and eight negative channels with output ranges and connections as shown in Table 4.2.

The power supply unit is controlled by a LabVIEW instrument control and data acquisition program via a U3-HV LabJack measurement and automation device.

4.4.3 Electron and ion detection

The electron current and ion current are measured by Keithley model 486 and Model 6487 picoammeters, respectively. As mentioned in Section 4.2.1.2, under typical experimental conditions, the electron current is around 50 nA, whereas the corresponding ion current is just under 2 nA. Therefore, the range for the 486 and 6487 picoammeter are set to and fixed at 2 nA and 200 nA, respectively.

In order to measure such small currents accurately, care had been taken to minimize sources of measurement error. One common unwanted source of current is due to the triboelectric effect, which occurs when the outer shield of the coaxial cable rubs against

Table 4.2: Details of multichannel power supply.

Channel	Range of output potentials (V)	Electrostatic element
+1	+10	-
+2	+10	-
+3	+10	-
+4	+10	-
+5	+500	-
+6	+500	Faraday cup
+7	+500	-
+8	+1000	-
−1	−10	L1 and L2
−2	−10	-
−3	−10	L3 and L4
−4	−10	L5
−5	−500	Shield
−6	−500	Filament
−7	−500	Cell
−8	−1000	-

its insulation if the cable is flexed. This causes electrons to be stripped from the insulation, falsely increasing the measured current by as much as tens of nanoamps. Low-noise triaxial cable with length as short as possible was employed in order to minimise such effects [20]. The cable setup is isolated from possible sources of vibration, such as rotary pumps, and is taped to a stable bench.

The piezoelectric effect, which generates current by mechanical stress on susceptible materials, should also be minimized by introducing the least possible mechanical stress on the cable insulator and using insulating materials with minimal piezoelectric properties.

Another common source of degraded low-current measurement accuracy is contamination on the surface of the exposed insulation layer in triaxial cables, such as moisture, oil, fingerprints, and dirt, which act to form a low-current battery at a sensitive current node within the insulator, and the noise current can be as much as a few nanoamps. It is therefore

crucial to wear gloves when handling the cables, and make sure to polish the feedthrough connector pins by sand paper and clean them by appropriate solvents such as ethanol.

Both picoammeters are fixed to the stable bench away from any known magnetic fields. If they are not to be used for a long time, they should be turned off to elongate the lifetime and protect from possible power surge. In order to achieve stable current measurements, a four-hour warm-up time is needed for both picoammeters after being turned on, followed by zero correction, before running any experiments.

4.4.4 Capacitance manometer and absolute pressure measurement

As noted previously, the pressure within the collision cell is measured by an MKS Type 690A.1 high accuracy Baratron capacitance manometer (Figure 4.14). The sensor capsule of the capacitance manometer contains a diaphragm and a fixed metal-on-ceramic electrode structure. On the back side of the diaphragm is a built-in "zero" pressure reference cavity. When connected to sample gas at pressure above the reference "zero" pressure, the diaphragm deflects, and the pressure difference is determined by measuring the change in capacitance between the deflected metal diaphragm and the fixed electrode. This provides a reliable absolute pressure measurement, which is independent of the gas species. The Baratron sensor is maintained at an internal temperature of 45 °C, i.e. above ambient temperature, in order to reduce any temperature fluctuations that could affect the measurement.

The Baratron transducer must be mounted horizontally upon its vibration isolation base. An isolation valve should be connected to the sensor between the inlet port and the vacuum chamber, or the whole vacuum chamber should always be kept under vacuum, to protect the sensor from overpressure in excess of its specification. After turning the sensor on, a minimum of four hours is required in order for the sensor within the transducer to become thermally stabilized at its control temperature. After such warm-up time, and

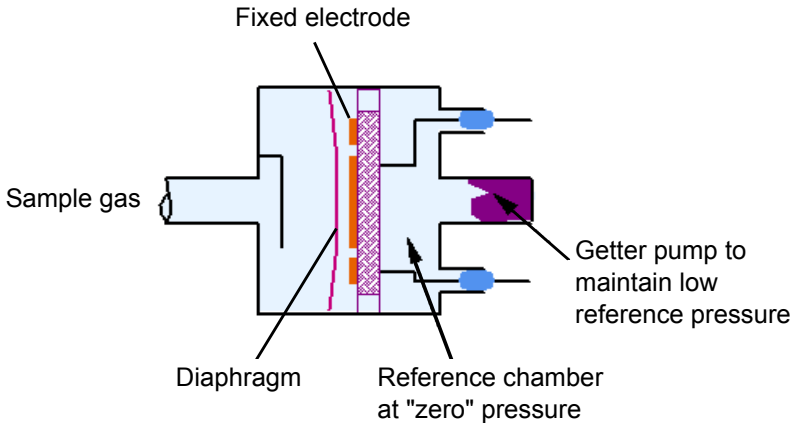


Figure 4.14: Cross-sectional view of internal structure of MKS Baratron® Capacitance Manometer.

when the background vacuum chamber pressure is below 1×10^{-7} Torr, a zero adjustment can be performed. This should be repeated frequently when making measurements.

Under typical experimental conditions, there exists a temperature gradient between the heated sensor, regulated at $T_s = 318.15$ K, and the relatively cooler collision cell, which reaches a temperature just above room temperature, around $T_c = 300$ K. This creates a small but significant pressure difference between the gas near at the sensor (P_s) and the gas inside the cell (P_c). When the mean free path of gas molecule is much greater than the diameter of the tubing connecting the cell and the sensor, the molecular flow condition is satisfied, and thermal transpiration introduces the following pressure ratio:

$$\frac{p_s}{p_c} = \sqrt{\frac{T_s}{T_c}} \tag{4.2}$$

The pressure reading from the Baratron capacitance manometer is therefore always expected to be higher than the actual pressure inside the collision cell (normally 2 to 5% depending on the values of the two temperatures), and thus needs to be corrected using Equation (4.2) [21].

4.4.5 Thermocouple

A thermocouple is made from two different metal wires fused together at a junction. A junction potential is generated at the point where the wires join, which is temperature dependent. The junction potential has been characterised in detail for a number of different wire pairs, allowing thermocouples to be used to make reliable and accurate temperature measurements over a wide temperature range. The junction potential is small, and requires amplification to allow precise temperature determination. In the present experiment, a LabJack LJTick-InAmp (LJTIA) signal-conditioning module is used to amplify the voltage from the thermocouple and convert it to temperature.

4.4.6 Instrument control and data acquisition

The multichannel power supply and data acquisition are automated via a LabVIEW interface and a LabJack U3-HV Series multifunction DAQ device. During a typical experiment, the incident electron energy is scanned from 290 eV to 10 eV with a 5 eV step size. Instead of using the nominal potential applied to the filament to determine the electron energy, the LabVIEW program reads back the actual filament potential and uses this to calculate the electron energy. At each electron energy, data acquisition is paused for 5 seconds to allow the system to equilibrate, before 35 readings of the electron current, ion current, temperature, and pressure are recorded at 1 Hz frequency. In addition, a 60 second waiting time is provided between each full scan. All readings, especially pressure, are displayed in real-time for monitoring purposes during the experiment. Data is saved in the form of a plain text, tab-separated values file for each run, and can be easily processed and analysed within numerical computing packages such as MATLAB [22].

4.5 Vacuum system

The schematic layout of the vacuum system, together with the collision cell assembly and control electronics, is shown in Figure 4.15. The high vacuum chamber measures

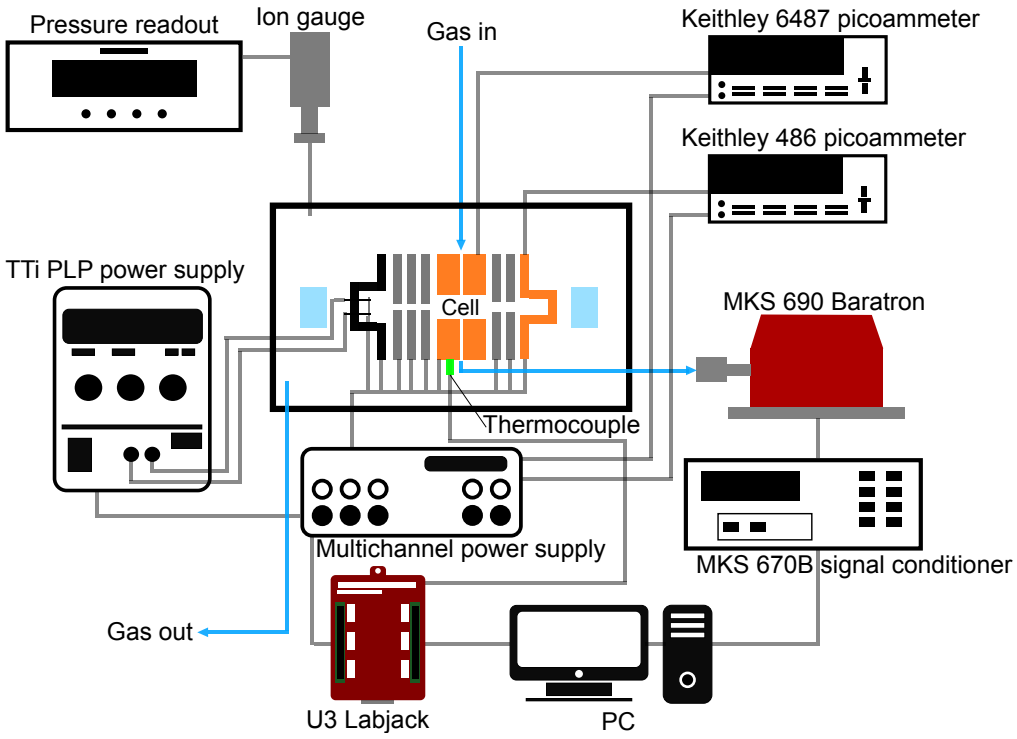


Figure 4.15: A schematic diagram of vacuum system with collision cell assembly and external electronics.

400 × 300 × 300 mm, and is maintained at a background pressure of 1×10^{-7} Torr by a Pfeiffer HiPace 700 turbomolecular pump backed by an Edwards RV5 rotary vane pump. This rises to 5×10^{-6} Torr when sample gas is admitted to the collision cell. The collision cell assembly is mounted to the inner side of the top flange of the chamber, and all of the required electrical and gas feedthroughs are integrated into this flange. The collision cell is not completely gas-tight, and is pumped out by the turbo pump when the sample gas supply is shut off.

4.6 Sample preparation and sample line set-up

All samples used for testing and calibration of the instrument are gases at room temperature. The relevant gas cylinder can easily be attached to the variable leak valve used to admit sample gas to the collision cell, enabling fine control over the gas flow into the cell. A RS Pro 9684692 analogue Bourdon tube positive pressure gauge is installed between

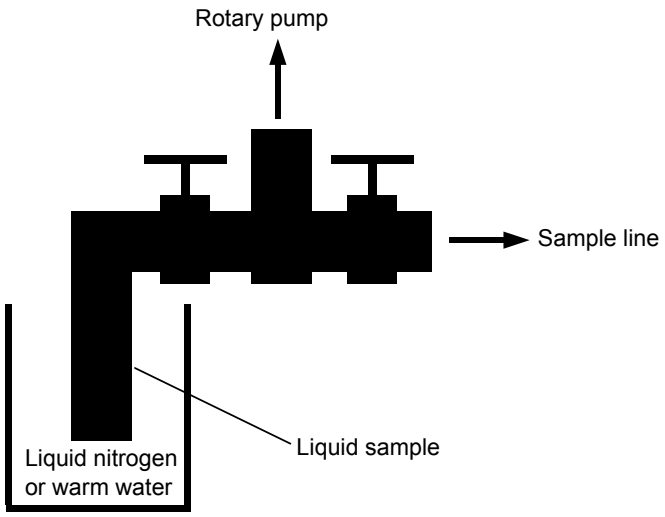


Figure 4.16: Schematic diagram of cold finger trap utilising freeze-pump-thaw cycle technique.

the cylinder and the leak valve to measure the pressure within the sample delivery line, which is usually maintained below 2 bar. A Pfeiffer DUO 2.5 rotary vane pump is used for evacuating the sample line in between each sample.

Many of the samples investigated in this work are liquids at room temperature. A freeze-pump-thaw cycle technique is used to prepare the sample in the vapour phase for measurement. The sample is introduced into an L-shaped cold finger, shown in Figure 4.16. The cold finger is immersed into liquid nitrogen for 10 minutes. It is then pumped for 1 minute to remove any unwanted gas, mostly air. The cold finger is then immersed in lukewarm water in order to thaw the frozen liquid. This process is repeated twice more, after which the purity of the sample can be considered sufficient for total cross-section measurement. The sample can then be connected to the variable leak valve and operated in the same manner as described above for samples contained within gas cylinders.

Early measurements suggested that the variable leak valve is unable to achieve fine flow control for sample line pressures below 50 mbar. This was problematic for three of the molecules studied, ethyl cyanide, propyl cyanide, and isopropyl cyanide, which have vapour pressures below this value. The problem was overcome by diluting the samples

at a known partial pressure in an inert buffer gas such as N_2, for which the ionization cross-section has already been well characterised. The overall measured total ionization cross-section is a weighted average of the cross-sections for the two molecules

$$\sigma = c_1\sigma_1 + c_2\sigma_2 \tag{4.3}$$

where c_1 and c_2 are the mole fractions of the sample and buffer gas, respectively, and σ_1 and σ_2 are their total ionization cross-sections.

4.7 Calibration of the new cell design

4.7.1 Calibration factors to be considered

Total ionization cross-sections for the inert gases and common diatomic molecules have been widely reported, and generally show good agreement. De Heer and Inokuti compared published papers from Joint Institute for Laboratory Astrophysics (JILA) tabulations, and concluded that the total cross-sections of N_2, O_2, CO and NO by Rapp and Englander-Golden [19] are likely to be the most reliable within the reported error limit (7%). Other authors have also recommended the data of Rapp and Golden for these molecules [23–26]

As mentioned in Chapter 2, the only quantity in Equation (2.26) that cannot be measured directly is the pathlength l over which ions are formed. There are two different approaches to determining the pathlength, one based on an experimental calibration, and one based on computer simulation. In the first, the ionization cross-section for N_2 is measured, and the known value of the cross-section from Rapp and Englander-Golden's N_2 data is used together with Equation (2.26) to determine the pathlength. This yielded a pathlength of 13.53 mm.

In the second approach, SIMION trajectory simulations are employed to simulate the trajectories of ions formed at different points along the electron beam axis. If all ions that originate from a specific segment along the electron beam path eventually reach

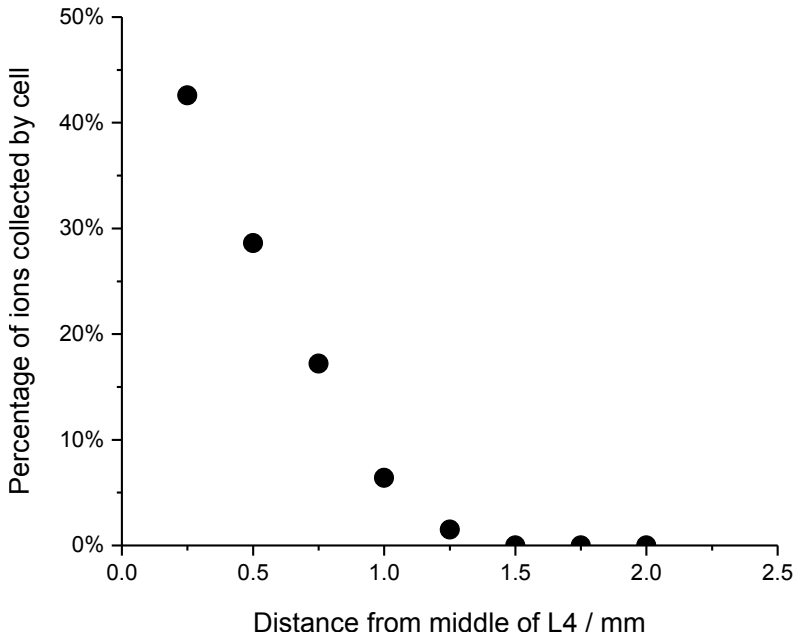


Figure 4.17: SIMION simulated percentage of ions collected by the cell as a function of distance from the middle of L4 towards L5.

the ion detector, this segment is considered to form part of the total pathlength. If only a fraction of the ions formed within a segment reach the ion detector, then the same fraction of the length of the segment is considered to contribute to the total pathlength. The simulations consider ion trajectories originating from the region between L3 and L5. Ions that are formed between L3 and L4 are fully collected by the cell (Figure 4.6). Ions that are formed from the middle of L4 to the middle of L5 are partially collected by the cell. The percentage of ions detected are shown in Figure 4.17 as a function of the distance from L4. The region between L4 and L5 contributes 0.24 mm to the effective pathlength, which when added to the distance of 13.5 mm between L3 and L4 yields a total effective pathlength of 13.74 mm.

The calibrated pathlength of 13.52 mm and the simulated pathlength of 13.74 only differ by 1.6%. For all molecules, measurements were repeated between 5 to 10 times, and the standard deviations of these measurements were found to be well below 5% of the mean values. Since the uncertainty of Rapp and Englander-Golden's data is stated to be 7%, it was decided to use the SIMION simulated pathlength in the calculation of

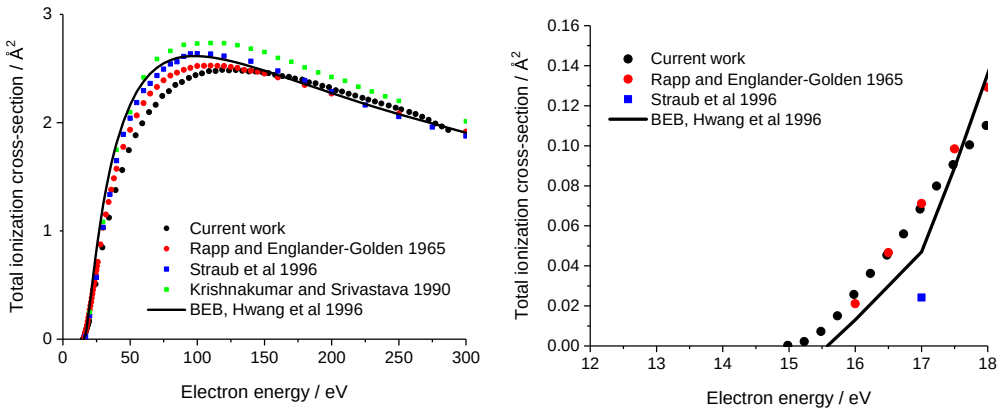


Figure 4.18: (a) Absolute total ionization cross-section of N_2 recorded in the current work, Rapp and Englander-Golden's experiment, BEB calculation, and other literature values [19, 27–29]; (b) Data from current work, Rapp and Englander-Golden's, and Straub *et al.*'s near threshold region.

the cross-sections from the experimental measurements in this thesis in order to achieve a lower overall uncertainty in the measurement.

4.7.2 Testing and optimisation with N_2

Due to the established reliability of the recommended N_2 total cross-section data, the N_2 molecule was used for any optimisation and calibration procedures and to check periodically that the instrument was performing optimally. Figure 4.18 presents the total ionization cross-section for N_2 recorded with the present instrument (estimated error: $\leq$ ±5%, data are also tabulated in Appendix D.2.1), compared with Rapp and Englander-Golden's data (estimated error: ±7%), BEB calculation data, and measurements from a number of other authors [19, 27–29]. It can be seen that the cross-section measured in the current work lies within the limits of error of Rapp and Englander-Golden. The threshold behaviour also shows very good agreement with that of Rapp and Englander-Golden, with an estimated ionization potential, 15.31 eV, compared to 16 eV in Rapp and Englander-Golden's measurement, and a NIST recommended value [30] of 15.581 eV.

In addition to being used in the initial testing of the apparatus, the cross-section for N_2

was measured in between different samples in order to verify that the signal had returned to baseline and that there were no residual traces of the previous sample molecule. If the measured N_2 cross-section data differed significantly from that shown in Figure 4.18, the cause was investigated and resolved. Often this required dismounting and cleaning of the collision cell.

As noted previously, the N_2 cross-section is needed when using N_2 as a buffer gas in measurements of the cross-section of organic cyanide molecules.

4.7.3 Comparison with other common permanent gas molecules

Once the reliability of the measured N_2 cross-section had been established, the instrument was used to measure ionization cross-sections for a series of small molecules in order to compare with existing literature values. These included CO_2, C_2H_4, C_3H_6, N_2O, CF_4, SF_6. The measured cross-sections are shown in Figure 4.19 (a)-(f) (data are also tabulated in Appendix D.2.2 to D.2.7), together with literature values and BEB calculated results. In general, the cross-section recorded in the current work show good agreement with literature values, but tend to fall off more slowly at high electron energies. This might be due to the fact that considerable effort has been directed towards ensuring collection of all ions formed during ionization, whereas in earlier designs faster ions were not always detected with the same efficiency as slower ions.

The optimised experimental parameters used in these measurements (e.g. potentials of ion optics, filament current, electron current, gas pressure etc.) were then used for subsequent experiments on all molecules. These parameters are summarised in Table 4.3.

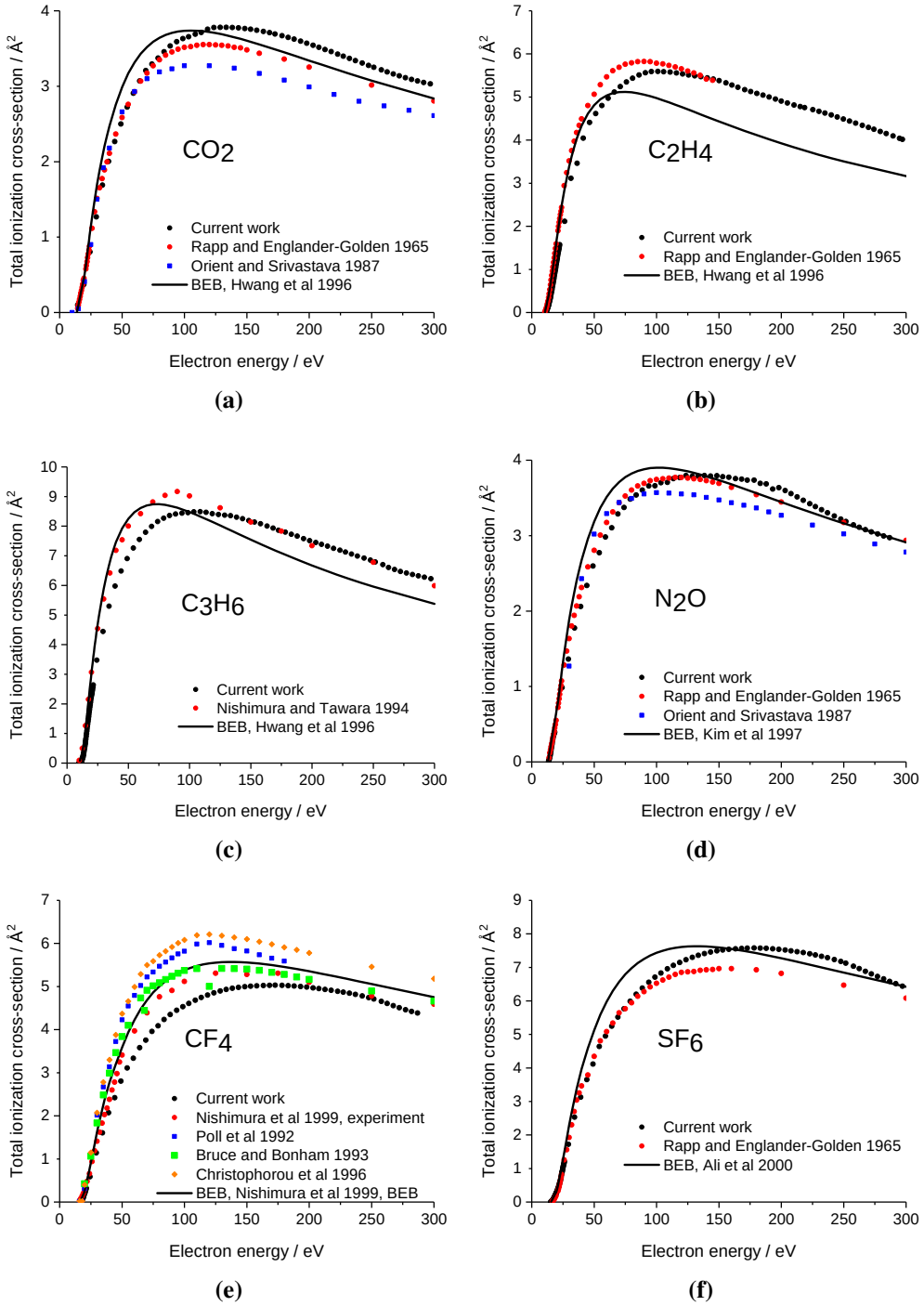


Figure 4.19: Absolute total ionization cross-section of common permanent gas molecules of current work, BEB calculation, and other literature values. (a) Carbon dioxide [19, 28, 31]; (b) Ethylene [19, 28]; (c) Propene [32, 33]; (d) Nitrous oxide [19, 34, 35]; (e) Tetrafluoromethane [36–39]; (f) Sulfur hexafluoride [19, 40].

Table 4.3: Experimental parameters of current work.

Parameter	Values
Filament potential	0 to −300 V
Shield potential	−2.5 V w.r.t. filament potential
L1 potential	−2 V
L2 potential	−2 V
L3 potential	Grounded
Cell potential	−10 V
L4 potential	Grounded
L5 potential	−2 V
Faraday cup potential	+150 V
Filament power supply current	$\leq$ 2.5 A
Cell pressure	$\sim 2 \times 10^{-4}$ Torr
Electron beam current	$\leq$ 50 nA
Ion current	$\leq$ 2 nA
Background chamber pressure	$< 1 \times 10^{-7}$ Torr
Minimum warm-up time:	
Filament	30 mins
Collision cell	30 mins
Picoammeters	4 hours
MKS Baratron transducer	4 hours

4.8 Common issues

4.8.1 Cell and ion optics contamination

While care was taken to maintain the best experimental conditions, it was noticed that the measured total ionization cross-sections were highly reproducible for a certain period of time, before artefacts began to appear, most notably a pronounced peak near 70 eV (Figure 4.20). The peak could not be eliminated through adjustment of the lens potentials, and on dismounting the cell assembly, an extensive and thick layer of contamination was visible on surfaces that were directly in contact with the electron beam, such as the inner side of the shield, the front side of lens element L1, the aperture on lens elements L1, L2, and L3,

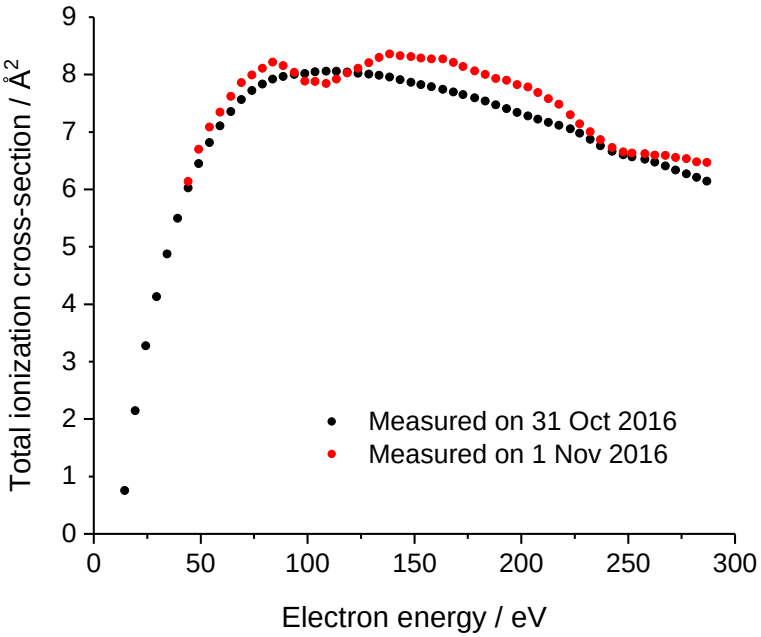


Figure 4.20: Comparison of total ionization cross-section data of acrolein, measured on 31 Oct 2016 (normal) and 1 Nov 2016 (uneven "spikes" at several electron energies).

and the bottom of Faraday cup. This oxide contamination layer leads to charge build-up and modification of the electric fields within the instrument. The rate of build-up was found to be positively associated with the pressure of the sample gas and the intensity of the electron beam. Several literature sources mentioned the encounter of same or similar phenomena and proposed cleaning of the surfaces to be an effective solution [41, 42].

Nelson found out that, in his work, there were build-up of contamination layers on electrodes and conducting surfaces within the electron gun assembly. These non-conducting contamination layers effectively act as insulators and thus responsible for the accumulation of charged particles, which then altered and distorted the desired electric field produced by electrodes, and eventually changed the fate of electron trajectories and caused "spikes" features on the total ionization cross-section curve (Figure 4.21) [41]. Bart also reported similar issues at a slightly different electron energy range (Figure 4.22) [42]. According to Bart, chlorocarbon molecules appear to be particularly problematic in causing deterioration of the instrument's performance. However, in the current work, no specific molecules appeared to be more problematic than others.

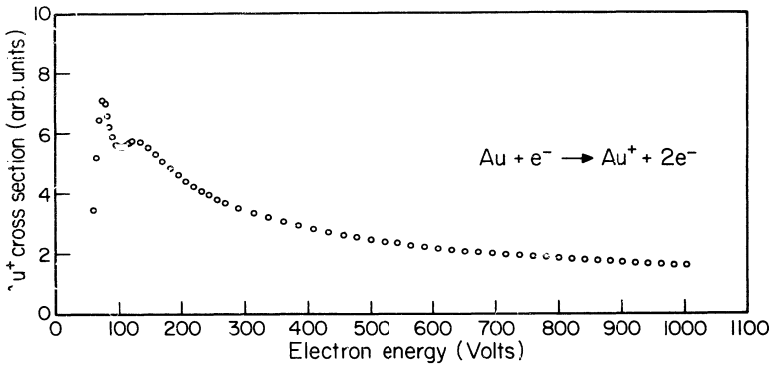


Figure 4.21: Uneven "spikes" feature developed on the total ionization cross-section curve from Nelson's work, at around 70 eV [41].

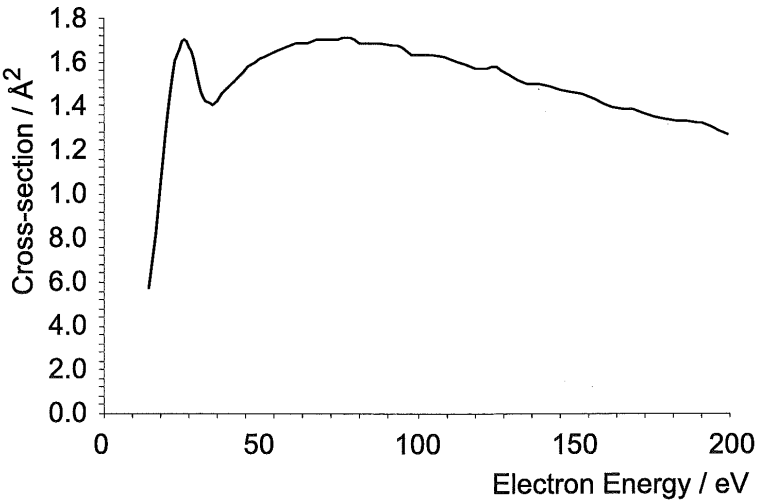
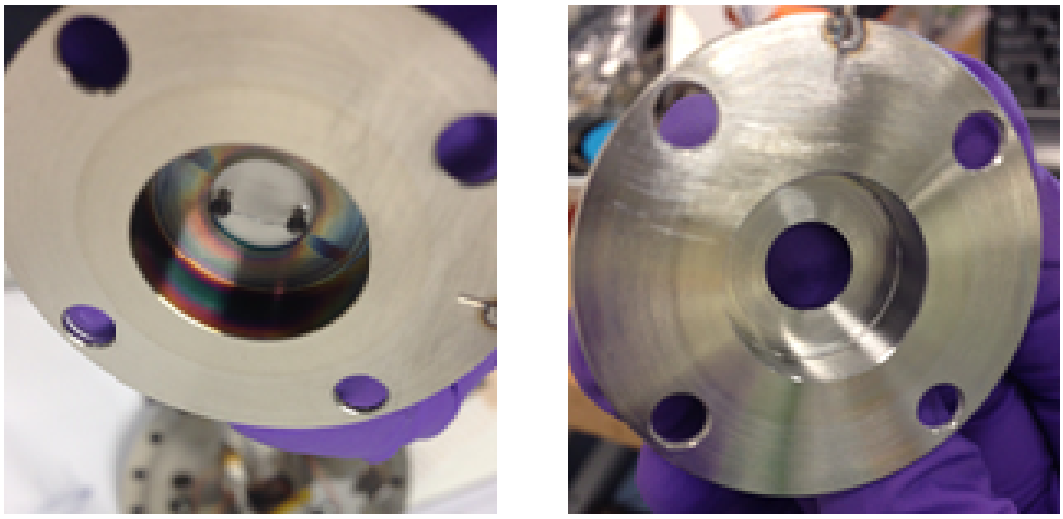


Figure 4.22: Uneven "spikes" feature developed on total ionization cross-section curve from Bart's work, at around 30 eV [42].

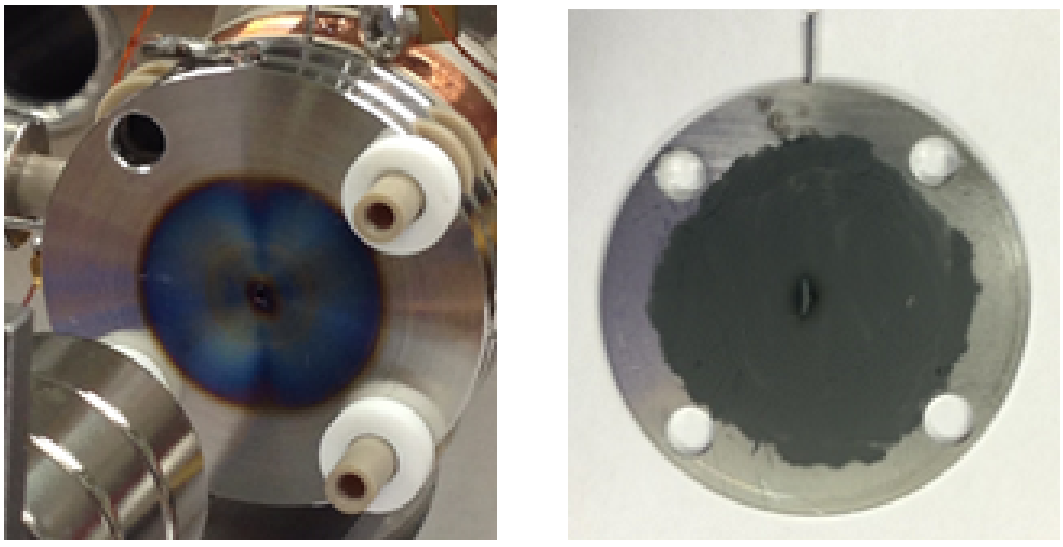
The contamination layer can easily be removed using an abrasive. Emery paper can be used on larger areas. However, areas such as the inside of the shield, and other small apertures, are difficult to access. These areas were cleaned using an electric toothbrush with Inoxi Clean chalk powder (Figure 4.23 and Figure 4.24). Following cleaning, all ion optics are re-coated with a layer of water soluble Aquadag colloidal graphite. As well as preventing scattering of charged particles from surfaces, the Aquadag layer also facilitates the removal of contamination layers.

In order to extend the interval between cleaning of the source, the electron current and sample gas pressure were maintained towards the low end of the values that yielded



(a) **(b)**

Figure 4.23: Before (a) and after (b) cleaning the inside of the shield, when Aquadag was not coated beforehand.



(a) **(b)**

Figure 4.24: (a) An extreme example of contamination layer on lens element L1 after long running hours, note the filament being used was a hairpin shape, i.e. point source. (b) The same lens element L1 (coated with Aquadag) after long running hours when using a line filament.

acceptable signal to noise ratio.

4.8.2 Stability and hysteresis of gas pressure reading

The stability of gas pressure is manageable when it is at 2×10^{-4} Torr and above. While it is not an issue to achieve this pressure for gas phase molecule, saturated vapour from liquid sample often present a significant challenge when being controlled via a variable leak valve. Sample vapour above 50 Torr can practically be controlled at 2×10^{-4} Torr inside the collision cell. High vapour pressure such as those formed from liquid ethanethiols are no different from gas molecules. However, due to possible condensation of vapour on cold parts along the sample line and the valve, a complete blockage or a surge of gas is not uncommon. Surge of gas flow is harmful in a way that gas pressure as high as 5×10^{-3} Torr may be introduced into the collision cell within seconds, causing sudden and massive build-up of contaminations over ion optics and severely damage the functionality of the rig. It is therefore imperative to shut down the electron gun as soon as a gas surge is observed when working on low vapour pressure gas samples.

Since gas flows through the cell and maintains a dynamical equilibrium pressure, any changes of ion current and electron current are the result of the change of gas pressure, and all the changes should be observed as having simultaneously happened. However, due to the inevitably long tubing that connects the cell and the MKS Baratron transducer, there exists a delay between change in currents and change in pressure reading, normally between 3 to 5 seconds. This delay introduces virtually no risk when gas pressure is stable to some extent, which can be easily dealt with by averaging certain number of readings (e.g. 40), but it does require explicit solutions when there is significant pressure rise or drop, let alone gas blockage and surge. A straightforward approach is to keep only those readings whose standard deviations are below a pre-set value, e.g. 1×10^{-6} Torr.

4.9 Standard operating procedures

Detailed standard operating procedures can be found in Appendix B, as a reference for future work on this apparatus.

References

[1] C. Vallance, S. A. Harris, J. E. Hudson, and P. W. Harland. "Absolute electron impact ionization cross sections for CH_3X, where X=H, F, Cl, Br, and I". In: *Journal of Physics B: Atomic, Molecular and Optical Physics* 30.10 (1997), pp. 2465–2475.

[2] M. Bart, P. W. Harland, J. E. Hudson, and C. Vallance. "Absolute total electron impact ionization cross-sections for perfluorinated hydrocarbons and small halocarbons". In: *Physical Chemistry Chemical Physics* 3.5 (2001), pp. 800–806.

[3] J. E. Hudson, C. Vallance, M. Bart, and P. W. Harland. "Absolute electron-impact ionization cross sections for a range of C1 to C5 chlorocarbons". In: *Journal of Physics B: Atomic, Molecular and Optical Physics* 34.15 (2001), pp. 3025–3039.

[4] J. E. Hudson, M. L. Hamilton, C. Vallance, and P. W. Harland. "Absolute electron impact ionization cross-sections for the C1 to C4 alcohols". In: *Physical Chemistry Chemical Physics* 5.15 (2003), pp. 3162–3168.

[5] J. E. Hudson, C. Vallance, and P. W. Harland. "Absolute electron impact ionization cross-sections for CO, CO_2, OCS and CS_2". In: *Journal of Physics B: Atomic, Molecular and Optical Physics* 37.2 (2004), pp. 445–455.

[6] J. E. Hudson, Z. F. Weng, C. Vallance, and P. W. Harland. "Absolute electron impact ionization cross-sections and polarizability volumes for the C2 to C6 methanoates and C3 to C7 ethanoates". In: *International Journal of Mass Spectrometry* 248.1-2 (2006), pp. 42–46.

[7] J. N. Bull and P. W. Harland. "Absolute electron impact ionization cross-sections and polarisability volumes for C2 to C4 aldehydes, C4 and C6 symmetric ethers and C3 to C6 ketones". In: *International Journal of Mass Spectrometry* 273.1-2 (2008), pp. 53–57.

[8] D. A. Dahl, J. E. Delmore, and A. D. Appelhans. "SIMION PC/PS2 electrostatic lens design program". In: *Review of Scientific Instruments* 61.1 (1990), pp. 607–609.

[9] D. A. Dahl. "SIMION for the personal computer in reflection". In: *International Journal of Mass Spectrometry* 200.1–3 (2000), pp. 3–25.

[10] D. Manura and D. A. Dahl. *SIMION (R) 8.0 User Manual*. Report. Scientific Instrument Services, Inc. Ringoes, NJ 08551, 2008.

[11] O. W. Richardson. "On the Negative Radiation from Hot Platinum". In: *Proceedings of the Cambridge Philosophical Society* 11 (1901), pp. 286–295.

[12] E. M. Savitskii, M. A. Tylkina, S. I. Ipatova, and E. I. Pavlova. "Properties of tungsten-rhenium alloys". In: *Metal Science and Heat Treatment of Metals* 2.9 (1960), pp. 483–486.

[13] K. T. Compton and C. C. Van Voorhis. "Probability of Ionization of Gas Molecules by Electron Impacts". In: *Physical Review* 26.4 (1925), pp. 436–453.

[14] W. W. Lozier. "A study of the velocities of H^+ ions formed in hydrogen by dissociation following electron impact". In: *Physical Review* 36.8 (1930), pp. 1285–1292.

[15] P. T. Smith. "The Ionization of Helium, Neon, and Argon by Electron Impact". In: *Physical Review* 36.8 (1930), pp. 1293–1302.

[16] J. T. Tate and W. W. Lozier. "The Dissociation of Nitrogen and Carbon Monoxide by Electron Impact". In: *Physical Review* 39.2 (1932), pp. 254–269.

[17] J. T. Tate and P. T. Smith. “The Efficiencies of Ionization and Ionization Potentials of Various Gases Under Electron Impact”. In: *Physical Review* 39.2 (1932), pp. 270–277.

[18] D. D. Briglia and D. Rapp. “Ionization of H_2 by Electron Impact Near Threshold”. In: *Journal of Chemical Physics* 42.9 (1965), pp. 3201–3213.

[19] D. Rapp and P. Englander-Golden. “Total Cross Sections for Ionization and Attachment in Gases by Electron Impact. I. Positive Ionization”. In: *The Journal of Chemical Physics* 43.5 (1965), pp. 1464–1479.

[20] J. L. Tucker. *Optimizing Low-Current Measurements and Instruments*. Keithley white paper. Cleveland, OH, 2013, pp. 1–8.

[21] K. F. Poulter, M. J. Rodgers, P. J. Nash, T. J. Thompson, and M. P. Perkin. “Thermal transpiration correction in capacitance manometers”. In: *Vacuum* 33.6 (1983), pp. 311–316.

[22] MATLAB. *version 9.3.0.713579 (R2017b)*. Natick, MA: The MathWorks Inc., 2017.

[23] F. J. de Heer and M. Inokuti. “Total Ionization Cross Sections”. In: *Electron Impact Ionization*. Ed. by T. D. Märk and G. H. Dunn. Vienna: Springer, 1985. Chap. 7, p. 235.

[24] Y. Itikawa. “Cross Sections for Electron Collisions with Nitrogen Molecules”. In: *Journal of Physical and Chemical Reference Data* 35.1 (2006), pp. 31–53.

[25] Y. Itikawa, M. Hayashi, A. Ichimura, K. Onda, K. Sakimoto, K. Takayanagi, M. Nakamura, H. Nishimura, and T. Takayanagi. “Cross Sections for Collisions of Electrons and Photons with Nitrogen Molecules”. In: *Journal of Physical and Chemical Reference Data* 15.3 (1986), pp. 985–1010.

[26] W. M. Huo and Y.-K. Kim. “Electron collision cross-section data for plasma modeling”. In: *IEEE Transactions on Plasma Science* 27.5 (1999), pp. 1225–1240.

[27] E. Krishnakumar and S. K. Srivastava. “Cross sections for the production of N_2^+ , N^+ + N_2^{2+} and N^{2+} by electron impact on N_2”. In: *Journal of Physics B: Atomic, Molecular and Optical Physics* 23.11 (1990), p. 1893.

[28] W. Hwang, Y.-K. Kim, and M. E. Rudd. “New model for electron-impact ionization cross sections of molecules”. In: *The Journal of Chemical Physics* 104.8 (1996), pp. 2956–2966.

[29] H. C. Straub, P. Renault, B. G. Lindsay, K. A. Smith, and R. F. Stebbings. “Absolute partial cross sections for electron-impact ionization of H_2, N_2, and O_2 from threshold to 1000 eV”. In: *Physical Review A* 54.3 (1996), pp. 2146–2153.

[30] S. G. Lias. *Ionization Energy Evaluation. In: Linstrom, P. J. and Mallard, W. G. (eds.) NIST Chemistry WebBook, NIST Standard Reference Database Number 69*. Gaithersburg, MD, 20899: National Institute of Standards and Technology.

[31] O. J. Orient and S. K. Strivastava. “Electron impact ionisation of H_2O, CO, CO_2 and CH_4”. In: *Journal of Physics B: Atomic and Molecular Physics* 20.15 (1987), p. 3923.

[32] H. Nishimura and H. Tawara. “Total electron impact ionization cross sections for simple hydrocarbon molecules”. In: *Journal of Physics B: Atomic, Molecular and Optical Physics* 27.10 (1994), pp. 2063–2074.

[33] Y.-K. Kim and K. K. Irikura. “Electron-impact ionization cross sections for polyatomic molecules, radicals, and ions”. In: *AIP Conference Proceedings* 543.1 (2000), pp. 220–241.

[34] I. Iga, M. V. V. S. Rao, and S. K. Srivastava. “Absolute electron impact ionization cross sections for N_2O and NO from threshold up to 1000 eV”. In: *Journal of Geophysical Research: Planets* 101.E4 (1996), pp. 9261–9266.

[35] Y.-K. Kim, W. Hwang, N. M. Weinberger, M. A. Ali, and M. E. Rudd. "Electron-impact ionization cross sections of atmospheric molecules". In: *The Journal of Chemical Physics* 106.3 (1997), pp. 1026–1033.

[36] H. U. Poll, C. Winkler, D. Margreiter, V. Grill, and T. D. Märk. "Discrimination effects for ions with high initial kinetic energy in a Nier-type ion source and partial and total electron ionization cross-sections of CF_4". In: *International Journal of Mass Spectrometry and Ion Processes* 112.1 (1992), pp. 1–17.

[37] M. R. Bruce and R. A. Bonham. "On the partial ionization cross-sections for CF_4 by use of the pulsed-electron-beam time-of-flight method". In: *International Journal of Mass Spectrometry and Ion Processes* 123.2 (1993), pp. 97–100.

[38] L. G. Christophorou, J. K. Olthoff, and M. V. V. S. Rao. "Electron Interactions with CF_4". In: *Journal of Physical and Chemical Reference Data* 25.5 (1996), pp. 1341–1388.

[39] H. Nishimura, W. M. Huo, M. A. Ali, and Y.-K. Kim. "Electron-impact total ionization cross sections of CF_4, C_2F_6, and C_3F_8". In: *The Journal of Chemical Physics* 110.8 (1999), pp. 3811–3822.

[40] M. A. Ali, K. K. Irikura, and Y.-K. Kim. "Electron-impact total ionization cross sections of SF_x(x = 1–5)". In: *International Journal of Mass Spectrometry* 201.1 (2000), pp. 187–195.

[41] A. N. Nelson. *Electron impact ionization cross sections of gold, chromium and iron*. Technical Report. Massachusetts Institute of Technology, 1976.

[42] M. Bart. "Electron Impact Ionization: Measurements of Absolute Cross-Sections and Cross-Beam Studies". Ph.D. thesis, University of Canterbury. 2003.

5

Absolute total ionization cross-section of interstellar molecules

Contents

5.1 Molecules discovered in the interstellar medium 114
5.1.1 The interstellar medium 114
5.1.2 Molecules in the ISM 114
5.1.3 Ionization processes in the ISM 114
5.2 Results 117
5.2.1 Acrolein 119
5.2.2 Acrylonitrile 120
5.2.3 Methyl cyanide 120
5.2.4 Ethyl cyanide 121
5.2.5 Propyl cyanide 122
5.2.6 Isopropyl cyanide 122
5.2.7 Ethanethiol 124
5.2.8 Methyl oxirane 124
5.2.9 Benzene 126
5.3 Discussion 126
5.3.1 General features 126
5.3.2 Comparison of experimental maximum cross-section and maximum cross-section calculated using the polarizability volume method 127
5.4 New database of partial and total ionization cross-section of ISM molecules 131
References 133

5.1 Molecules discovered in the interstellar medium

5.1.1 The interstellar medium

The interstellar medium (ISM) refers to the material that exists between stars within a galaxy, which mainly consists of gas (99%) and dust. By terrestrial standards, the pressure or number density is extremely low, close to the best level of vacuum artificially achievable on Earth. However, with a density of 1 to 10^6 particles cm^{-3}, the ISM plays a key role in the formation of stars and planets due to a wealth of chemistry that can occur [1]. The ISM is composed of approximately 70% hydrogen, 28% helium, and 2% of other heavy elements, which in total accounts for about 5% of the total galactic mass [2].

5.1.2 Molecules in the ISM

Molecules in the ISM can be studied by analysing molecular spectra observed through telescopes, and by investigating the chemical chains of reactions which lead to the diverse range of observed molecular species. An ever-increasing collection of molecules have been detected in the ISM or circumstellar shells. A list of molecules whose presence has been confirmed in the ISM is documented and updated by the University of Cologne, and comprises the Cologne Database for Molecular Spectroscopy (CDMS). To date, around 200 molecules have been detected in the interstellar medium or circumstellar shells [3, 4], and many more are known to be present, with many unassigned lines in observed spectra. Table 5.1 shows the confirmed molecules ordered by the number of atoms that compose them, as of September 2018.

5.1.3 Ionization processes in the ISM

The very low temperatures and densities in the ISM mean that only barrierless reactions occur at non-negligible rates in gas phase. Important processes include ion-molecule

Table 5.1: List of detected ISM molecules, ordered by number of constitute atoms.

2 atoms	3 atoms	4 atoms	5 atoms	6 atoms	7 atoms	8 atoms	9 atoms	10 atoms	11 atoms	12 atoms	>12 atoms
H_2	C_3	*c*-C_3H	C_5	C_5H	C_6H	CH_3C_3N	CH_3C_4H	CH_3C_5N	HC_9N	*c*-C_6H_6	$HC_{11}N$
AlF	C_2H	*l*-C_3H	C_4H	*l*-H_2C_4	CH_2CHCN	$HC(O)OCH_3$	CH_3CH_2CN	$(CH_3)_2CO$	CH_3C_6H	*n*-C_3H_7CN	C_{60}
AlCl	C_2O	C_3N	C_4Si	C_2H_4	CH_3C_2H	CH_3COOH	$(CH_3)_2O$	$(CH_2OH)_2$	C_2H_5OCHO	*i*-C_3H_7CN	C_{70}
C_2	C_2S	C_3O	*l*-C_3H_2	CH_3CN	HC_5N	C_7H	CH_3CH_2OH	CH_3CH_2CHO	$CH_3OC(O)CH_3$	$C_2H_5OCH_3$	C_{60}^+
CH	CH_2	C_3S	*c*-C_3H_2	CH_3NC	CH_3CHO	C_6H_2	HC_7N	CH_3CHCH_2O			
CH^+	HCN	C_2H_2	H_2CCN	CH_3OH	CH_3NH_2	CH_2OHCHO	C_8H				
CN	HCO	NH_3	CH_4	CH_3SH	*c*-C_2H_4O	*l*-HC_6H	$CH_3C(O)NH_2$				
CO	HCO^+	HCCN	HC_3N	HC_3NH^+	H_2CCHOH	CH_2CHCHO	C_8H^-				
CO^+	HCS^+	$HCNH^+$	HC_2NC	HC_2CHO	C_6H^-	CH_2CCHCN	C_3H_6				
CP	HOC^+	HNCO	HCOOH	NH_2CHO	CH_3NCO	H_2NCH_2CN	CH_3CH_2SH				
SiC	H_2O	HNCS	H_2CNH	C_5N		CH_3CHNH					
HCl	H_2S	$HOCO^+$	H_2C_2O	*l*-HC_4H							
KCl	HNC	H_2CO	H_2NCN	*l*-HC_4N							
NH	HNO	H_2CN	HNC_3	*c*-H_2C_3O							
NO	MgCN	H_2CS	SiH_4	H_2CCNH							
NS	MgNC	H_3O^+	H_2COH^+	C_5N^-							
NaCl	N_2H^+	*c*-SiC_3	C_4H^-	HNCHCN							
OH	N_2O	CH_3	HC(O)CN								
PN	NaCN	C_3N^-C3N–	HNCNH								
SO	OCS	PH_3	CH_3O								
SO^+	SO_2	HCNO	NH_4^+								
SiN	*c*-SiC_2	HOCN	H_2NCO^+								
SiO	CO_2	HSCN	$NCCNH^+$								
SiS	NH_2	H_2O_2									
CS	H_3^+	C_3H^+									
HF	SiCN	HMgNC									
HD	AlNC	HCCO									
FeO	SiNC										
O_2	HCP										
CF^+	CCP										
SiH	AlOH										
PO	H_2O_+										
AlO	H_2Cl_+										
OH^+	KCN										
CN^-	FeCN										
SH^+	HO_2										
SH	TiO_2										
HCl^+	C_2N										
TiO	Si_2C										
ArH^+											
NO^+											

reactions, radiative association, dissociative recombination, photodissociation, and photoionization. Photoionization is not generally an important initiation process for ion-molecule chemistry in dense clouds. Visible and UV light with sufficient energy to ionize atoms and molecules only penetrates into the outer regions of interstellar gas clouds, with optical absorption and scattering preventing penetration of such light into the core. Infrared light may penetrate molecular clouds, but infrared photons do not have sufficiently high energy to ionize neutral molecules.

In dense clouds, the most important ionization mechanism is collision with cosmic rays, which are extremely high-energy particles emitted from stars. Protons are the major constituent particles of cosmic rays (approximately 84%); the rest are alpha particles (14%), and electrons, heavier nuclei, and other exotic particles (2%) [1]. Although comprising a relatively small fraction of the cosmic rays, electrons have been demonstrated to lead to a rich molecular synthesis by electron-induced chemistry [5–7]. Electrons may drive processes on the surface of ices and/or dust grains which dominate molecular formation and reactions. Electron spectroscopy also plays an important role in interpreting the spectroscopy and dissociation pathways of molecules in the interstellar region [8]. As noted earlier in Section 2.3.1, electron ionization is classified as a "hard" ionization technique, which produce a wide range of fragment ions with significant kinetic energy release [9, 10]. Electron ionization cross-sections are one of the key parameters that needed for modelling radiation chemistry in interstellar region [11].

In this chapter, electron ionization cross-sections of nine molecules whose presence has been confirmed in the interstellar medium have been measured over the energy range from 0 to 300 eV using the instrument described in Chapter 4. The measured cross-section data will be shown, together with the cross-sections predicted by the BEB model (see Section 3.5.1).

5.2 Results

A key goal of the current project is to build up a database that contains absolute total and partial ionization cross-sections from both experimental and theoretical work for all the molecules listed in Table 5.1. Absolute total ionization cross-sections of a significant number of molecules have been measured by Harland and co-workers and are regarded as the most recent and reliable source of data [12–23], covering almost all of the smaller molecules listed in Table 5.1. In the present work, while we have repeated measurements for some molecules that have been studied previously, most of the effort has been devoted to studying molecules that have not been studied to date. Other selection criteria include: 1) molecules to be studied need to be stable under normal experimental conditions, which excludes radicals and molecules that are readily oligomerize, such as thioformaldehyde (H_2CS); 2) molecules need to be available, which exclude those that are not well known terrestrially such as ethanimine; 3) the choice of molecules must also fulfil safety considerations, so flammable and harmful candidates are reviewed carefully.

By considering the criteria mentioned above, a total of nine molecules known in the ISM were selected for experimental measurement [24]. They are acrolein, acrylonitrile, methyl cyanide, ethyl cyanide, propyl cyanide, isopropyl cyanide, ethanethiol, methyl oxirane, and benzene. Almost all of these molecules are flammable, toxic, and volatile, and must be handled in a chemical fume hood with care when preparing the samples for measurement. All molecules have melting points higher than the boiling point of molecular nitrogen, so the freeze-pump-thaw cycle technique is feasible using liquid nitrogen as the coolant. Nearly all of the molecules present a potential explosion hazard, so heating of the sample line above ambient temperature was avoided.

The physical and chemical properties of each molecule are summarised below, along with the measured absolute total cross-section data (data are also tabulated in Appendix D.1), calculated data using BEB model, and calculated data using polarizability volume

Table 5.2: Basic physical properties of molecules measured in current project.

Molecule	Formula	First detected	Appearance	Odor	Flammable	Toxic	Chemical compatibility
Acrolein	CH_2CHCHO	2004 [25]	colourless liquid	disagreeable and piercing smell	yes	yes	
Acrylonitrile	CH_2CHCN	1975 [26]	colourless liquid	unpleasant and onion-like odor	yes	yes	attacks copper and copper alloys
Methyl Cyanide	CH_3CN	1971 [27]	colorless limpid liquid	aromatic odor	yes	yes	
Ethyl Cyanide	CH_3CH_2CN	1977 [28]	colorless liquid	sweetish and ether-like odor	yes	yes	
propyl cyanide	n-C_3H_7CN	2009 [29]	clear colorless liquid	sharp and suffocating odor	yes	yes	
isopropyl cyanide	i-C_3H_7CN	2014 [30]	clear colorless liquid	almond-like odor	yes	yes	
Ethanethiol	CH_3CH_2SH	2014 [31]	clear colorless and very volatile liquid	strong and skunk-like odor	yes	yes	
Methyl Oxirane	CH_3CHCH_2O CH3CHCH2O	2016 [32]	colorless volatile liquid	benzene-like odor	yes	yes	
Benzene	c-C_6H_6 c-C6H6	2001 [33]	clear and colorless liquid	gasoline-like odor	yes	yes	

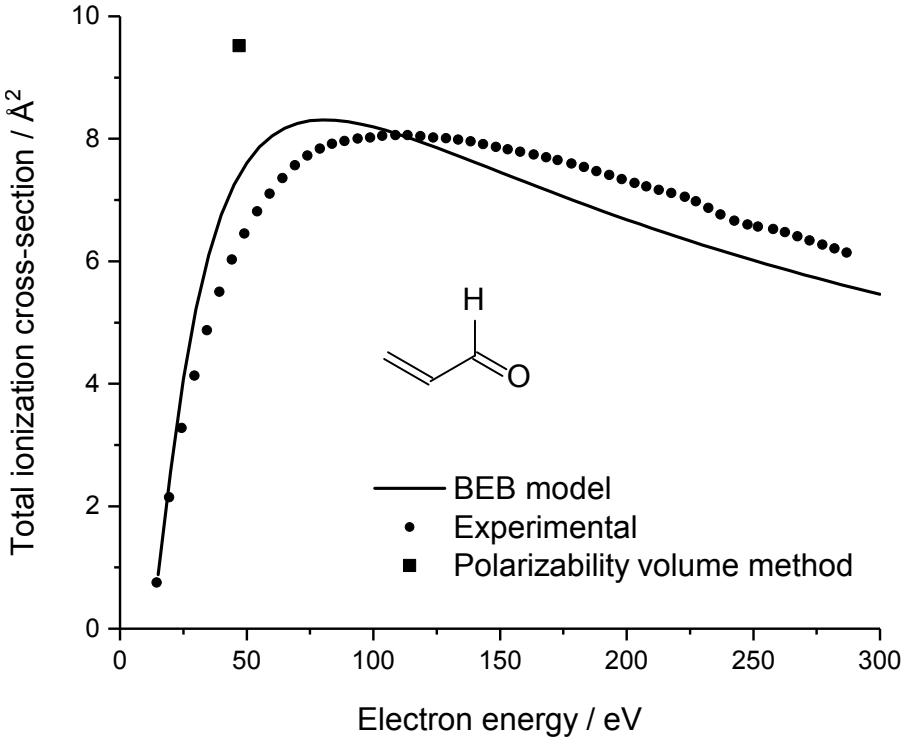


Figure 5.1: Total ionization cross-section of acrolein from current experimental measurement, BEB calculation, and calculation using the polarizability volume method described in Chapter 3.

method described in Chapter 3. A summary of physical properties for all molecules studied is presented in Table 5.2.

5.2.1 Acrolein

Acrolein is the simplest unsaturated aldehyde. It was detected in 2004 toward the star-forming region Sagittarius B2(N), which helped to build the hypothesis that hydrogen addition on interstellar grains is a key step in successively forming larger molecular species, in this case transforming from propynal to propenal and from propenal to propanal [25]. Acrolein has also been detected recently in three Galactic centre molecular clouds [34]. It is a colourless liquid with a disagreeable and piercing odour. Acrolein is highly flammable, toxic and fatal if swallowed, and hazardous to the aquatic environment.

The total ionization cross-section of acrolein is shown in Figure 5.1.

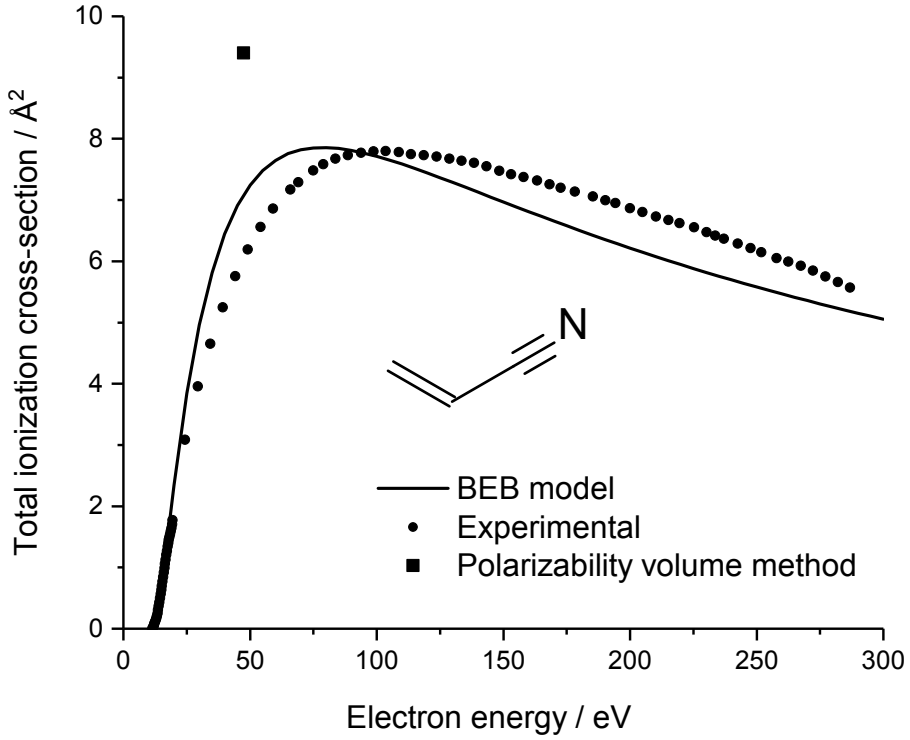


Figure 5.2: Total ionization cross-section of acrylonitrile from current experimental measurement, BEB calculation, and calculation using the polarizability volume method described in Chapter 3.

5.2.2 Acrylonitrile

Acrylonitrile, or vinyl cyanide, was first detected towards Sagittarius B2 [26], and then in a dark cloud [35], in one translucent cloud [36], and in a circumstellar envelope [37]. It is a colourless, volatile, and highly toxic liquid with an unpleasant and onion-like odour. Acrylonitrile attacks copper and copper alloys, which should be avoided when making tubing and choosing fittings.

The total ionization cross-section of acrylonitrile is shown in Figure 5.2.

5.2.3 Methyl cyanide

Methyl cyanide is the simplest organic nitrile. It was detected first in the Sagittarius B and Sagittarius A molecular clouds [27], toward dark clouds [38] and a low mass proto-star [39], and more recently in diffuse clouds [40]. It is a colourless limpid liquid

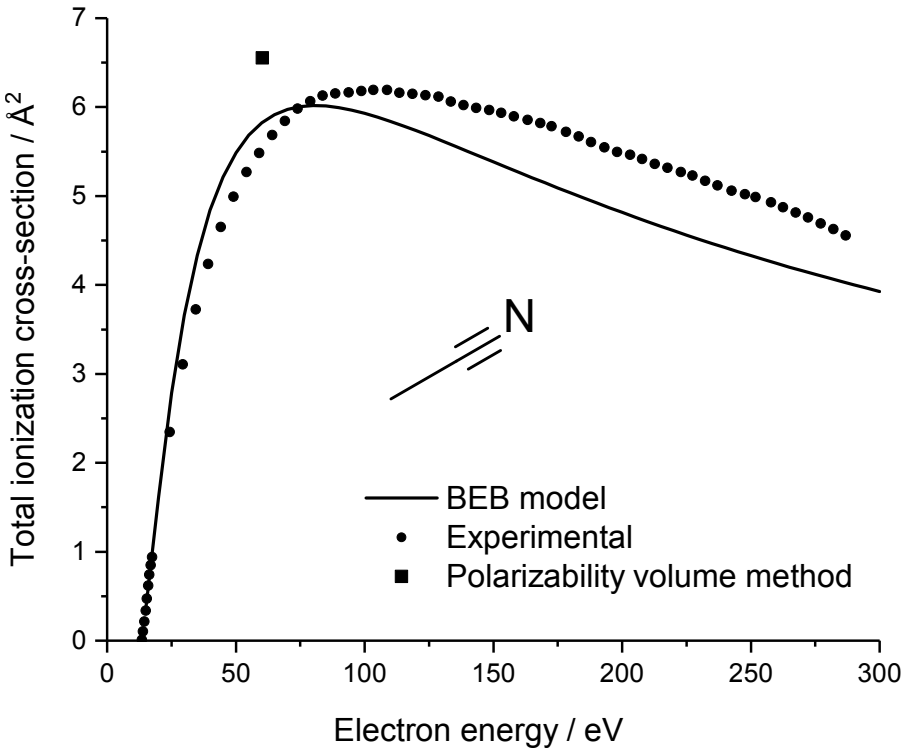


Figure 5.3: Total ionization cross-section of methyl cyanide from current experimental measurement, BEB calculation, and calculation using the polarizability volume method described in Chapter 3.

with an aromatic odour, and its vapor density is higher than air. It is highly flammable in both liquid and vapour form, and harmful if inhaled.

The total ionization cross-section of methyl cyanide is shown in Figure 5.3.

5.2.4 Ethyl cyanide

Ethyl cyanide was first detected within the Orion Molecular Cloud 1 and Sagittarius B2 [28], and within a low-mass star-forming region [39]. It is a colourless liquid with a sweetish and ether-like odour, and is both highly flammable and toxic.

The total ionization cross-section of ethyl cyanide is shown in Figure 5.4.

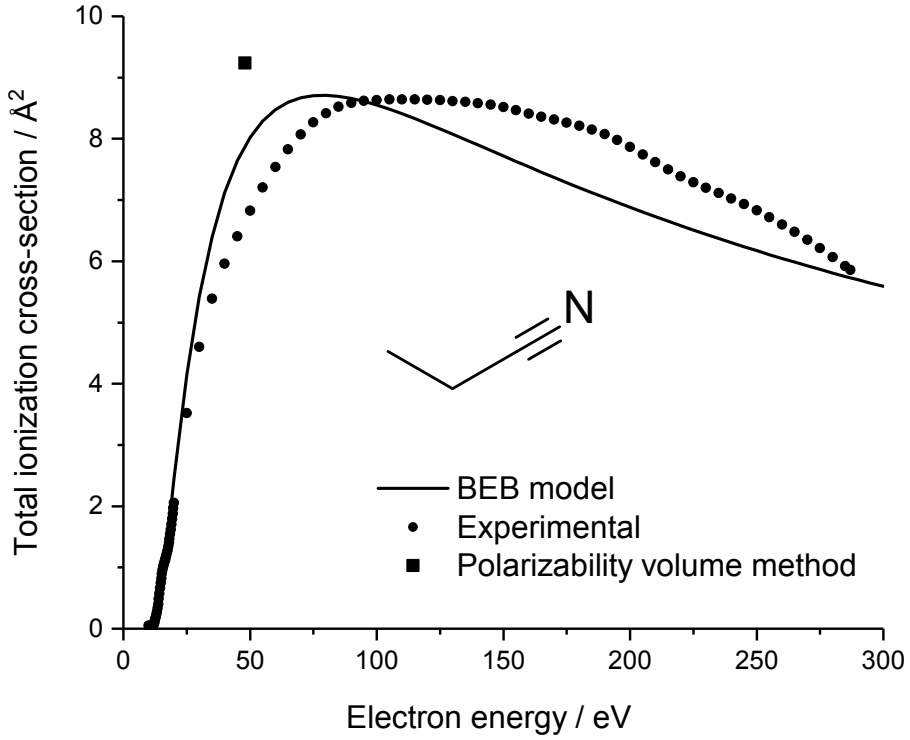


Figure 5.4: Total ionization cross-section of ethyl cyanide from current experimental measurement, BEB calculation, and calculation using the polarizability volume method described in Chapter 3.

5.2.5 Propyl cyanide

The third alkyl cyanide to be detected, after methyl cyanide and ethyl cyanide, is propyl cyanide [29]. It is a clear colorless liquid with a sharp and suffocating odour, and is both highly flammable and toxic.

The total ionization cross-section of propyl cyanide is shown in Figure 5.5.

5.2.6 Isopropyl cyanide

The recent detection of isopropyl cyanide, the fourth alkyl cyanide and the first molecule found in the ISM with a branched carbon backbone, confirms the existence and abundance of branched molecules in space [30]. Confirmation of the presence of such molecules provides considerable encouragement in the ongoing search for amino acids and biogenic molecules in space.

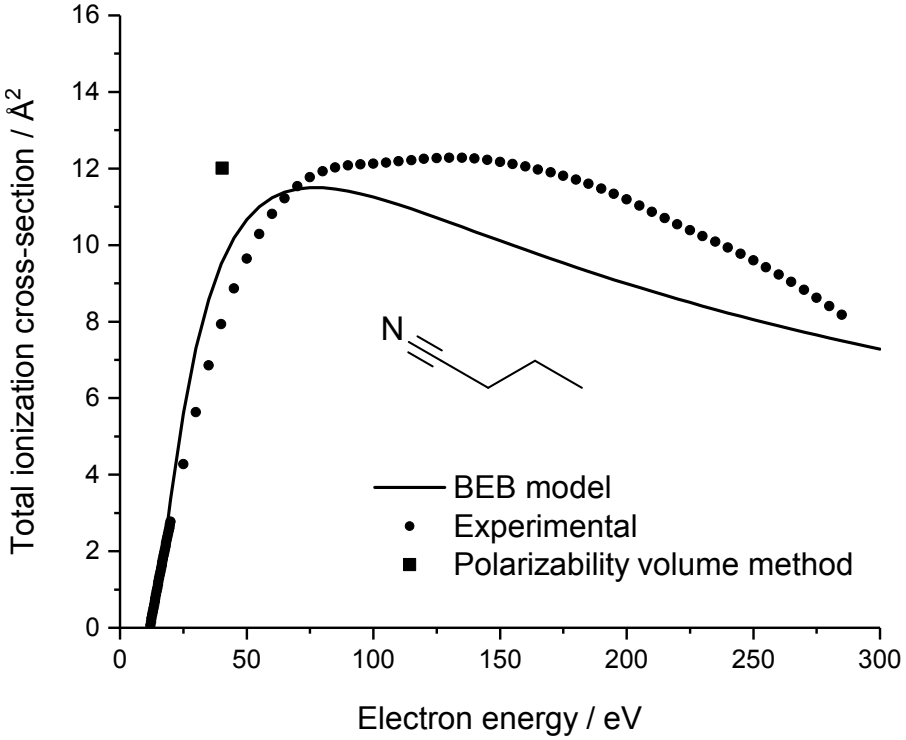


Figure 5.5: Total ionization cross-section of propyl cyanide from current experimental measurement, BEB calculation, and calculation using the polarizability volume method described in Chapter 3.

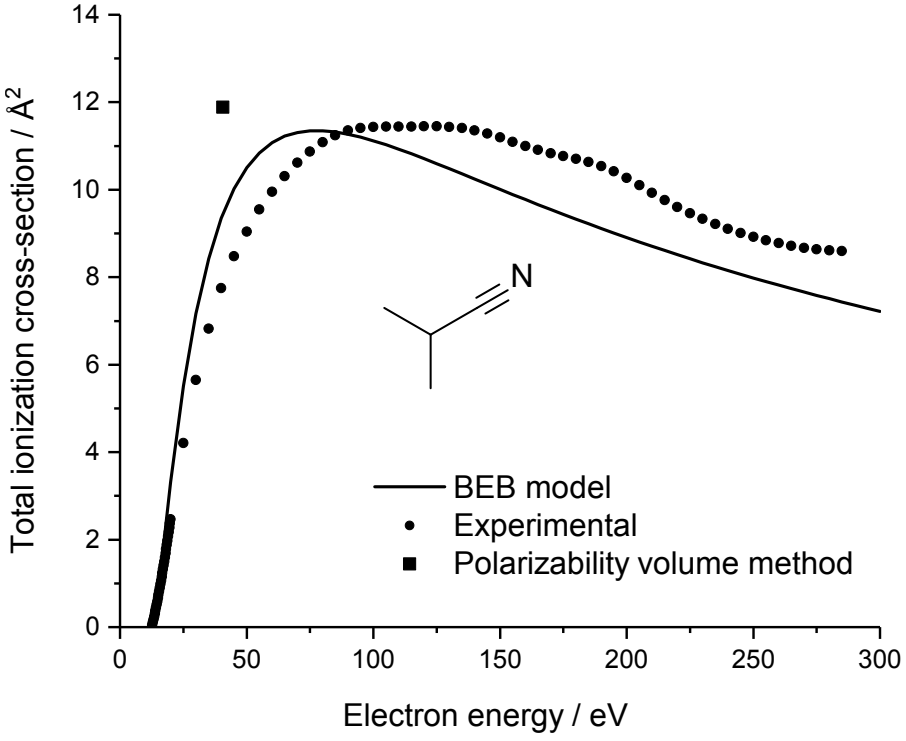


Figure 5.6: Total ionization cross-section of isopropyl cyanide from current experimental measurement, BEB calculation, and calculation using the polarizability volume method described in Chapter 3.

Isopropyl cyanide is a clear colorless liquid with an almond-like odour. It has similar hazardous properties to the other alkyl cyanides, such as high flammability and toxicity.

The total ionization cross-section of isopropyl cyanide is shown in Figure 5.6.

5.2.7 Ethanethiol

Detection of ethanethiol has been reported very recently [31]. Ethanethiol is a clear, colourless and very volatile liquid with a strong and skunk-like odour. When running the experiment for a batch of different molecules, it is advisable to schedule ethanethiol as the last task before cleaning the instrument as the odor might not be easily removed, both within the instrument and in the lab. This is believed to be the very small amount of residual ethanethiol left within the exhaust line of the pump as ethanethiol has odor detection threshold as low as 0.2 ppb [41]. Ethanethiol is very toxic to aquatic life and causes various health hazard such as muscular weakness, convulsions, respiratory paralysis, and pulmonary irritation. It is also extremely flammable and should be handled with care.

The total ionization cross-section of ethanethiol is shown in Figure 5.7.

5.2.8 Methyl oxirane

Methyl oxirane, or propylene oxide, has recently been detected in the envelope of the Sagittarius B2 star-forming region [32]. It is the first chiral molecule detected without ambiguity. Methyl oxirane is a colourless volatile liquid with a benzene-like odour. It is extremely flammable and toxic if inhaled or comes into contact with skin.

The total ionization cross-section of methyl oxirane is shown in Figure 5.8.

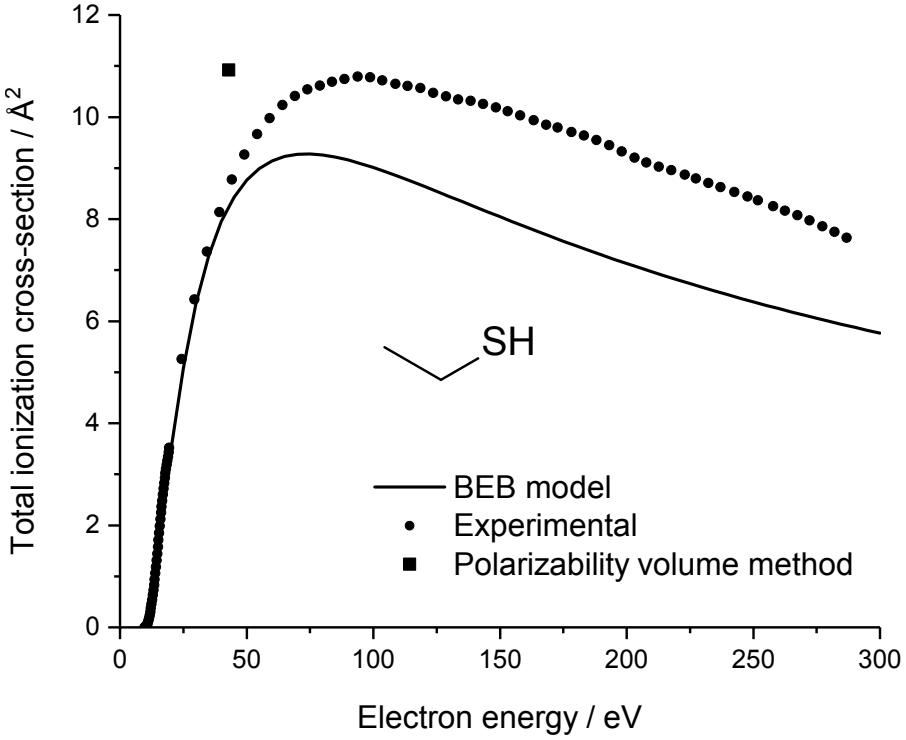


Figure 5.7: Total ionization cross-section of ethanethiol from current experimental measurement, BEB calculation, and calculation using the polarizability volume method described in Chapter 3.

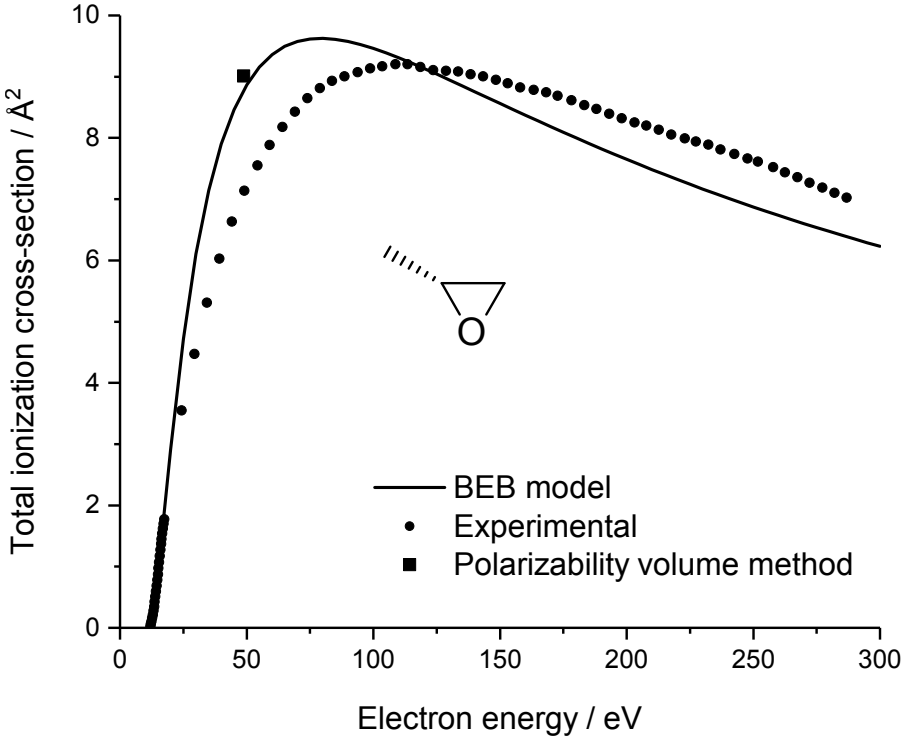


Figure 5.8: Total ionization cross-section of methyl oxirane from current experimental measurement, BEB calculation, and calculation using the polarizability volume method described in Chapter 3.

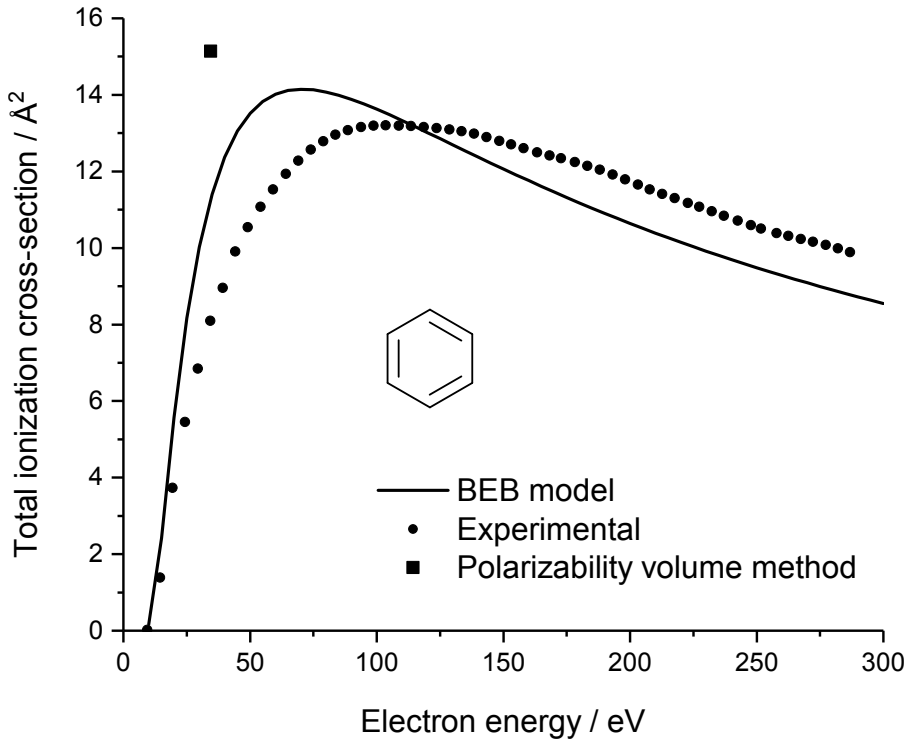


Figure 5.9: Total ionization cross-section of Benzene from current experimental measurement, BEB calculation, and calculation using the polarizability volume method described in Chapter 3.

5.2.9 Benzene

Detection of benzene was reported in the circumstellar medium in 2001 [33]. Benzene is a clear, colourless, flammable and toxic liquid which is widely used as an industrial solvent and has a gasoline-like odour.

The total ionization cross-section of benzene is shown in Figure 5.9.

5.3 Discussion

5.3.1 General features

The measured absolute total ionization cross-section curves for all nine molecules, shown in Figures 5.1 to 5.9, share the common features of rising abruptly above their respective ionization potential, reaching a maximum at an electron energy of around 100 to 130 eV, and then tapering off at higher electron energies. Comparing the experimental

results with the predictions of the BEB model, we find that there is good agreement at low energies, particularly near the threshold region. However, the agreement is less good at higher electron energies. In general, the experimentally measured curves taper off more gradually than the BEB curves, and the electron energy at which the cross-section reaches a maximum is always lower for the BEB cross-sections than for the experimentally measured cross-sections. There is no definite pattern in the mismatch between the experimental and BEB curves, but for all organic cyanides and ethanethiol, the experimentally-determined cross-section in the higher electron energy region above 150 eV tends to be much higher than the BEB cross-section (i.e. up to 15% for methyl cyanide, 15% for ethyl cyanide, 25% for propyl cyanide, 15% for isopropyl cyanide, 30% for ethanethiol). This is possibly due to multiple ionization at higher electron energies. Formation of doubly or triply charged ions at higher energies would increase the measured ion current, and therefore the measured cross-section. However, the BEB model does not account for this possibility. This underestimation of the ionization cross-section at high energies has been observed previously in other systems [17].

For the 4 organic cyanides, the cross-section is observed to increase as the number of carbon atoms increases. The branched isopropyl cyanide has slightly lower cross-section values than the linear propyl cyanide, presumably reflecting the somewhat more compact molecular structure (Figure 5.10).

5.3.2 Comparison of experimental maximum cross-section and maximum cross-section calculated using the polarizability volume method

The empirical correlation between the maximum in the electron ionization cross-section and the molecular polarizability has been studied previously by Bull *et al.* [21] for some 63 polyatomic organic and halocarbon species. As part of this earlier work, an empirical expression was proposed to provide an approximation of the maximum

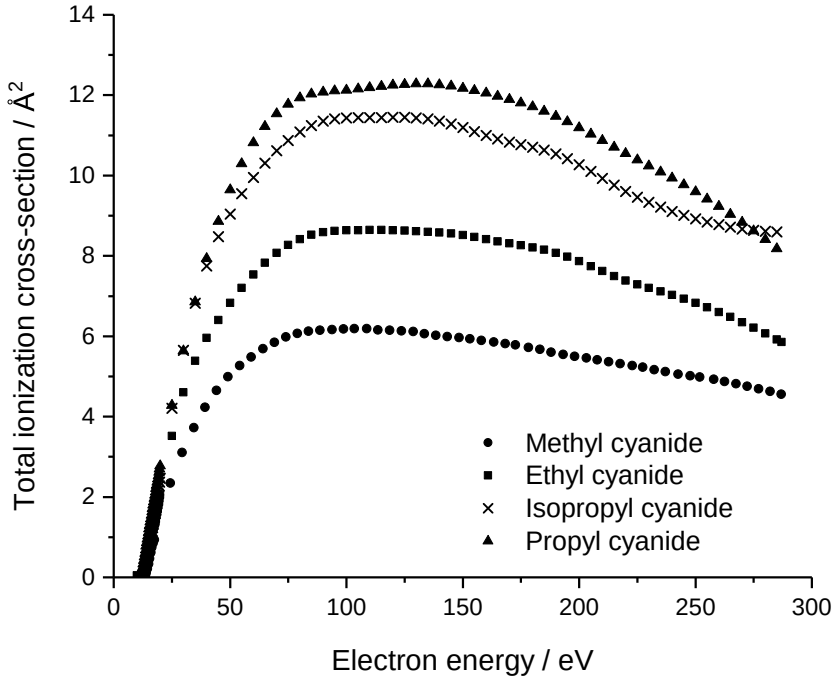


Figure 5.10: Total ionization cross-section of the 4 organic cyanides.

ionization cross-section, σ_{max}, based simply on the molecule's polarizability volume α (Equation (5.1) and Figure 5.11).

$$\sigma_{max} = (1.478)\,\alpha \tag{5.1}$$

Figure 5.12 shows a plot of the experimentally measured maximum ionization cross-section against the polarizability volume (as calculated from the electronic structure calculations described in Section 3.5.2) for the nine molecules studied in the current work. The data can be fitted to a straight line with slope = 1.380 and R^2 = 0.9947. A straight line with a slope of 1.478, as found for the much larger data set used by Bull *et al.* [21], is also shown.

If the data for just the five organic nitrile molecules, acrylonitrile, methyl cyanide, ethyl cyanide, propyl cyanide, and isopropyl cyanide, are plotted (Figure 5.13), the coefficient of determination R^2 is increased to 0.9954, and the proportionality coefficient becomes 1.405.

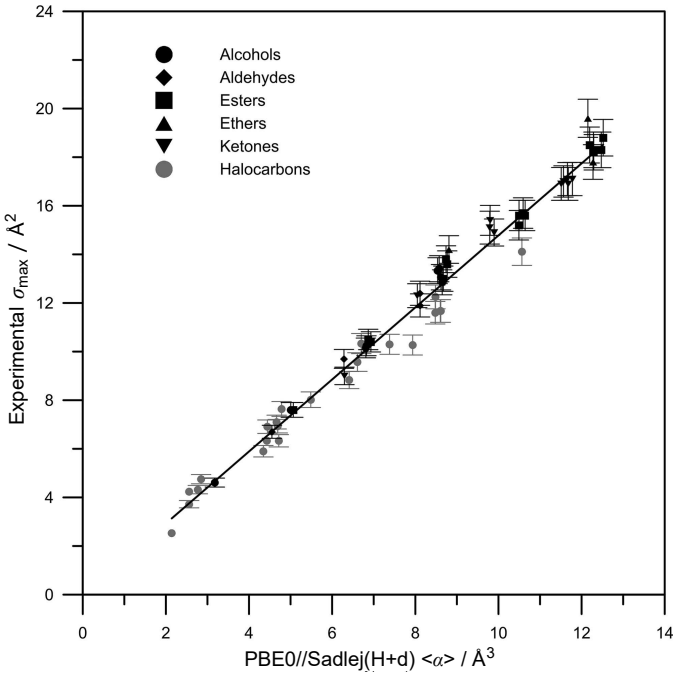


Figure 5.11: Empirical correlation between experimental σ_{max} and calculated polarizability volume for 63 medium size organic and halocarbon species studied Bull *et al.* [21]. $R^2 = 0.979$ and slope = 1.478. PBE0//Sadlej(H+d) denotes that the polarizability volume was calculated by using PBE0 hybrid DFT [42, 43] with Sadlej triple-ζ quality basis set [44].

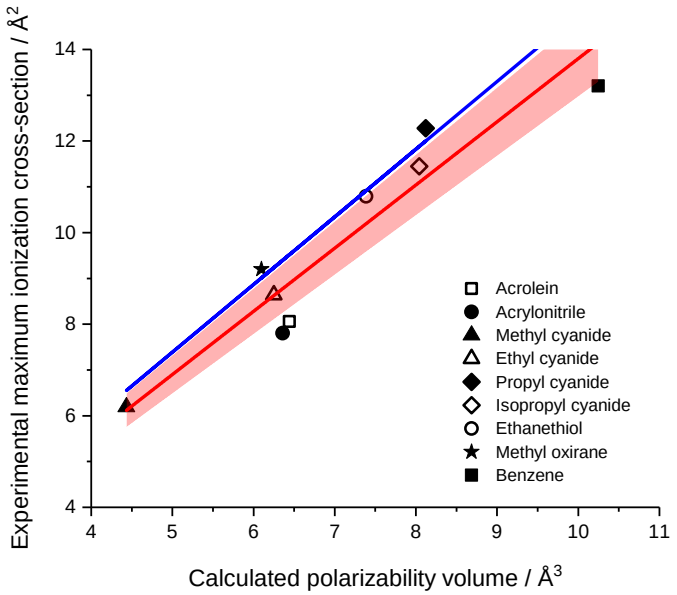


Figure 5.12: Empirical correlation between experimental σ_{max} and calculated polarizability volume for 9 astrochemistry molecules in current work. Red line and pink area: linear fit of 9 astrochemistry molecules in current work (slope = 1.380, $R^2 = 0.9947$) and its 95% confidence band, respectively; Blue line: linear fit of 63 medium size organic and halocarbon species studied Bull *et al.* [21] (slope = 1.478, $R^2 = 0.9790$).

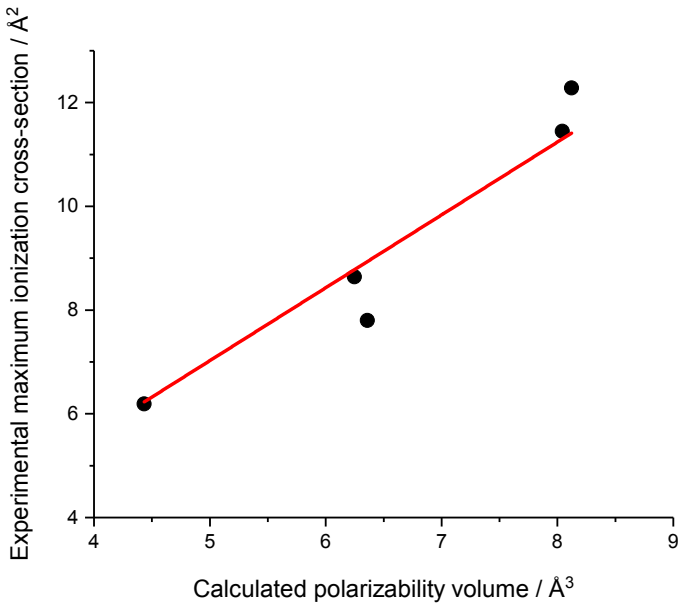


Figure 5.13: Empirical correlation between experimental σ_{max} and calculated polarizability volume for 5 organic nitrile molecules in the current work; R^2 = 0.9954 and slope = 1.405.

However, if the data points of all current 9 molecules are to be included into the original plot of the 63 molecules, the updated proportionality coefficient will be 1.479, only 0.07% increase from 1.478 (Figure 5.14).

When plotting data for 63 medium size molecules in Bull *et al.* 2012's work (Figure 5.11), species such as alcohols, aldehydes, ethers, esters, ketones, halocarbons, and amides were all included. Organic nitriles (apart from methyl cyanide) were a key missing class of molecules. Therefore, current data on organic nitriles, as well as other species such as thiol (ethanethiol) and epoxide (propylene oxide) can be regarded as a significant contribution to the data set.

Using this empirical polarizability correlation model, maximum cross-sections may be determined with the need to perform only relatively simple electronic structure calculations. A larger number of data points are needed in order to gain a better understanding of this linear relationship, and especially to gain insight into the possible different coefficients for different species.

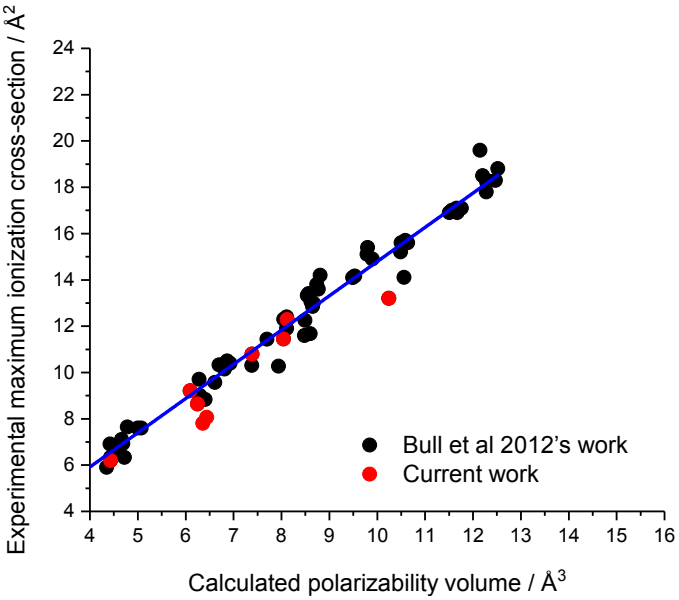


Figure 5.14: Empirical correlation between experimental σ_{max} and calculated polarizability volume for 9 astrochemistry molecules in the current work with 63 medium size organic and halocarbon species in Bull *et al.* 2012's work [21]; R^2 = 0.9978 and slope = 1.479.

5.4 New database of partial and total ionization cross-section of ISM molecules

In addition to being valuable data in their own right, the measured absolute total ionization cross-sections can also be used to normalize the relative partial ionization cross-sections that can be measured using an electron-molecule crossed-beam velocity-map imaging apparatus within our laboratory [45]. This will allow absolute total and partial ionization cross-sections to be measured for formation of all observed fragment ions for a wide variety of molecules of interest in astrochemistry and other fields of science. The cross-section data will form part of a more comprehensive database that also contains kinetic energy release distribution information for all observed ionic fragments for each molecule.

It has been demonstrated that the apparatus developed in this work is capable of measuring absolute electron ionization cross-sections as a function of electron energy for any gas phase molecules and for liquid phase molecules with sufficiently high vapor pressure. The database will provide valuable data for use in modelling of chemical systems of

relevance to astrochemistry and plasma science more generally. As a result of the detailed simulations and calibration that has been carried out, we believe the uncertainty in our measurements to be better than 5%. A detailed standard operating procedure, which should always be followed when running experiment and dismounting any parts of the instrument, can be found in Appendix B.

References

[1] C. Vallance. *Astrochemistry*. Essential Textbooks in Chemistry. London: World Scientific, 2015, p. 228.

[2] J. Lequeux, E. Falgarone, and C. Ryter. *The Interstellar Medium*. Springer Berlin Heidelberg, 2006.

[3] H. S. P. Müller, S. Thorwirth, D. A. Roth, and G. Winnewisser. "The Cologne Database for Molecular Spectroscopy, CDMS". In: *Astronomy & Astrophysics* 370.3 (2001), pp. L49–L52.

[4] H. S. P. Müller, F. Schlöder, J. Stutzki, and G. Winnewisser. "The Cologne Database for Molecular Spectroscopy, CDMS: a useful tool for astronomers and spectroscopists". In: *Journal of Molecular Structure* 742.1 (2005), pp. 215–227.

[5] V. I. Shematovich. "Formation of complex chemical species in astrochemistry (a review)". In: *Solar System Research* 46.6 (2012), pp. 391–407.

[6] N. J. Mason, B. Nair, S. Jheeta, and E. Szymańska. "Electron induced chemistry: a new frontier in astrochemistry". In: *Faraday Discussions* 168.0 (2014), pp. 235–247.

[7] C. Arumainayagam and J. Cambell. "The Role of Low-Energy Electrons in Astrochemistry: A Tale of Two Molecules". In: *The 228th American Astronomical Society Meeting*. San Diego, CA, 2016.

[8] K. H. Becker, C. W. McCurdy, T. M. Orlando, and T. N. Rescigno. *Current status and future perspectives of electron interactions with molecules, clusters, surfaces, and interfaces [Workshop on Fundamental challenges in electron-driven chemistry; Workshop on Electron-driven processes: Scientific challenges and technological opportunities]*. Report. Stevens Institute of Technology, Hoboken, NJ, 2000.

[9] J. N. Bull, J. W. L. Lee, and C. Vallance. "Quantification of ions with identical mass-to-charge (m/z) ratios by velocity-map imaging mass spectrometry". In: *Physical Chemistry Chemical Physics* 15.33 (2013), pp. 13796–13800.

[10] J. N. Bull, J. W. L. Lee, and C. Vallance. "Electron ionization dynamics of N_2 and O_2 molecules: Velocity-map imaging". In: *Physical Review A* 91.2 (2015), p. 022704.

[11] C. N. Shingledecker. "On cosmic rays in astrochemical models". Ph.D. thesis, University of Virginia. 2018.

[12] C. Vallance, P. W. Harland, and R. Maclagan. "Quantum mechanical calculation of maximum electron impact single ionization cross sections for the inert gases and small molecules". In: *Journal of Physical Chemistry* 100.37 (1996), pp. 15021–15026.

[13] P. W. Harland and C. Vallance. "Ionization cross-sections and ionization efficiency curves from polarizability volumes and ionization potentials". In: *International Journal of Mass Spectrometry* 171.1-3 (1997), pp. 173–181.

[14] C. Vallance, S. A. Harris, J. E. Hudson, and P. W. Harland. "Absolute electron impact ionization cross sections for CH_3X, where X=H, F, Cl, Br, and I". In: *Journal of Physics B: Atomic, Molecular and Optical Physics* 30.10 (1997), pp. 2465–2475.

[15] M. Bart, P. W. Harland, J. E. Hudson, and C. Vallance. "Absolute total electron impact ionization cross-sections for perfluorinated hydrocarbons and small halocarbons". In: *Physical Chemistry Chemical Physics* 3.5 (2001), pp. 800–806.

[16] J. E. Hudson, C. Vallance, M. Bart, and P. W. Harland. “Absolute electron-impact ionization cross sections for a range of C1 to C5 chlorocarbons”. In: *Journal of Physics B: Atomic, Molecular and Optical Physics* 34.15 (2001), pp. 3025–3039.

[17] J. E. Hudson, M. L. Hamilton, C. Vallance, and P. W. Harland. “Absolute electron impact ionization cross-sections for the C1 to C4 alcohols”. In: *Physical Chemistry Chemical Physics* 5.15 (2003), pp. 3162–3168.

[18] J. E. Hudson, C. Vallance, and P. W. Harland. “Absolute electron impact ionization cross-sections for CO, CO_2, OCS and CS_2”. In: *Journal of Physics B: Atomic, Molecular and Optical Physics* 37.2 (2004), pp. 445–455.

[19] J. E. Hudson, Z. F. Weng, C. Vallance, and P. W. Harland. “Absolute electron impact ionization cross-sections and polarizability volumes for the C2 to C6 methanoates and C3 to C7 ethanoates”. In: *International Journal of Mass Spectrometry* 248.1-2 (2006), pp. 42–46.

[20] J. N. Bull and P. W. Harland. “Absolute electron impact ionization cross-sections and polarisability volumes for C2 to C4 aldehydes, C4 and C6 symmetric ethers and C3 to C6 ketones”. In: *International Journal of Mass Spectrometry* 273.1-2 (2008), pp. 53–57.

[21] J. N. Bull, P. W. Harland, and C. Vallance. “Absolute Total Electron Impact Ionization Cross-Sections for Many-Atom Organic and Halocarbon Species”. In: *Journal of Physical Chemistry A* 116.1 (2012), pp. 767–777.

[22] J. N. Bull, M. Bart, C. Vallance, and P. W. Harland. “Electron-impact-ionization dynamics of five C2 to C4 perfluorocarbons”. In: *Physical Review A* 88.6 (2013), p. 10.

[23] J. N. Bull, J. W. L. Lee, and C. Vallance. “Absolute electron total ionization cross-sections: molecular analogues of DNA and RNA nucleobase and sugar constituents”. In: *Physical Chemistry Chemical Physics* 16.22 (2014), pp. 10743–10752.

[24] W. Zhou, L. Wilkinson, J. W. L. Lee, D. Heathcote, and C. Vallance. “Total electron ionization cross-sections for molecules of astrochemical interest”. In: *Molecular Physics* (2019), DOI: 10.1080/00268976.2019.1583389.

[25] J. M. Hollis, P. R. Jewell, F. J. Lovas, A. Remijan, and H. Møllendal. “Green Bank Telescope Detection of New Interstellar Aldehydes: Propenal and Propanal”. In: *The Astrophysical Journal Letters* 610.1 (2004), p. L21.

[26] F. F. Gardner and G. Winnewisser. “The detection of interstellar vinyl cyanide (acrylonitrile)”. In: *The Astrophysical Journal Letters* 195 (1975), pp. L127–L130.

[27] P. M. Solomon, K. B. Jefferts, A. A. Penzias, and R. W. Wilson. “Detection of Millimeter Emission Lines from Interstellar Methyl Cyanide”. In: *The Astrophysical Journal Letters* 168 (1971), p. L107.

[28] D. R. Johnson, F. J. Lovas, C. A. Gottlieb, E. W. Gottlieb, M. M. Litvak, M. Guelin, and P. Thaddeus. “Detection of interstellar ethyl cyanide”. In: *The Astrophysical Journal* 218 (1977), pp. 370–376.

[29] A. Belloche, R. T. Garrod, H. S. P. Müller, K. M. Menten, C. Comito, and P. Schilke. “Increased complexity in interstellar chemistry: detection and chemical modeling of ethyl formate and n-propyl cyanide in Sagittarius B2(N)”. In: *Astronomy & Astrophysics* 499.1 (2009), pp. 215–232.

[30] A. Belloche, R. T. Garrod, H. S. P. Müller, and K. M. Menten. "Detection of a branched alkyl molecule in the interstellar medium: iso-propyl cyanide". In: *Science* 345.6204 (2014), p. 1584.

[31] L. Kolesniková, B. Tercero, J. Cernicharo, J. L. Alonso, A. M. Daly, B. P. Gordon, and S. T. Shipman. "Spectroscopic Characterization and Detection of Ethyl Mercaptan in Orion". In: *The Astrophysical Journal Letters* 784.1 (2014), p. L7.

[32] B. A. McGuire, P. B. Carroll, R. A. Loomis, I. A. Finneran, P. R. Jewell, A. J. Remijan, and G. A. Blake. "Discovery of the interstellar chiral molecule propylene oxide (CH_3CHCH_3O)". In: *Science* 352.6292 (2016), p. 1449.

[33] J. Cernicharo, A. M. Heras, A. G. G. M. Tielens, J. R. Pardo, F. Herpin, M. Guélin, and L. B. F. M. Waters. "Infrared Space Observatory's Discovery of C_4H_2, C_6H_2, and Benzene in CRL 618". In: *The Astrophysical Journal Letters* 546.2 (2001), p. L123.

[34] M. A. Requena-Torres, J. Martín-Pintado, S. Martín, and M. R. Morris. "The Galactic Center: The Largest Oxygen-bearing Organic Molecule Repository". In: *The Astrophysical Journal* 672.1 (2008), p. 352.

[35] H. E. Matthews and T. J. Sears. "The detection of vinyl cyanide in TMC-1". In: *The Astrophysical Journal* 272 (1983), pp. 149–153.

[36] B. E. Turner, R. Terzieva, and H. Eric. "The Physics and Chemistry of Small Translucent Molecular Clouds. XII. More Complex Species Explainable by Gas-Phase Processes". In: *The Astrophysical Journal* 518.2 (1999), p. 699.

[37] M. Agúndez, J. P. Fonfría, J. Cernicharo, J. R. Pardo, and M. Guélin. "Detection of circumstellar CH_2CHCN, CH_2CN, CH_3CCH, and H_2CS". In: *Astronomy & Astrophysics* 479.2 (2008), pp. 493–501.

[38] H. E. Matthews and T. J. Sears. "Detection of the $J = 1 \rightarrow 0$ transition of CH_3CN". In: *The Astrophysical Journal* 267 (1983), pp. L53–L57.

[39] S. Cazaux, A. G. G. M. Tielens, C. Ceccarelli, A. Castets, V. Wakelam, E. Caux, B. Parise, and D. Teyssier. "The Hot Core around the Low-Mass Protostar IRAS 16293–2422: Scoundrels Rule!" In: *The Astrophysical Journal Letters* 593.1 (2003), p. L51.

[40] V. Thiel, A. Belloche, K. M. Menten, R. T. Garrod, and H. S. P. Müller. "Complex organic molecules in diffuse clouds along the line of sight to Sagittarius B2". In: *Astronomy & Astrophysics* 605 (2017), p. L6.

[41] M. J. O'Neil. *The Merck Index: An Encyclopedia of Chemicals, Drugs, and Biologicals*. Cambridge: Royal Society of Chemistry, 2013.

[42] C. Adamo and V. Barone. "Toward reliable density functional methods without adjustable parameters: The PBE0 model". In: *The Journal of Chemical Physics* 110.13 (1999), pp. 6158–6170.

[43] M. Ernzerhof and G. E. Scuseria. "Assessment of the Perdew–Burke–Ernzerhof exchange-correlation functional". In: *The Journal of Chemical Physics* 110.11 (1999), pp. 5029–5036.

[44] A. J. Sadlej. "Medium-size polarized basis sets for high-level correlated calculations of molecular electric properties". In: *Collection of Czechoslovak Chemical Communications* 53.9 (1988), pp. 1995–2016.

[45] H. Köckert, D. Heathcote, J. W. L. Lee, W. Zhou, V. Richardson, and C. Vallance. “C–I and C–F bond-breaking dynamics in the dissociative electron ionization of CF_3I”. In: *Physical Chemistry Chemical Physics* (2019), DOI: 10.1039/c8cp06682e.

6

Simulating Coulomb explosion imaging from first principles

Contents

6.1 Introduction **137**
6.2 Coulomb explosion imaging experiments **138**
6.3 Review of simulating Coulomb explosion imaging **140**
6.3.1 Classical molecular dynamics simulation 142
6.3.2 *Ab initio* molecular dynamics simulation 143
6.3.3 *Ab initio* classical trajectory calculation 144
6.3.4 Simulating velocity-map images for Coulomb explosion products 145
6.4 Novel approach of simulating Coulomb explosion from first principles **147**
6.4.1 Aims and algorithm 147
6.4.2 Adjustment, benchmarking and testing 153
6.4.3 Limitation and technique issues 173
6.5 Summary **174**
References **175**

6.1 Introduction

In the work presented so far in this thesis, we have been concerned primarily with singly charged ions, formed in our case in collisions of molecules with low-energy electrons. In contrast, many other ionization processes, such as electrospray ionization or photoionization with an intense laser pulse, yield multiply charged ions [1]. Interest in the physics and chemistry of multiply charged ions originated in the field of mass spectrometry, but has expanded to much wider scientific communities over the past 40 years [2, 3]. For example, fundamental studies on small, multiply charged ions led to improved understanding of chemical bonding in the presence of multiple charges [4]. It is also known that small multiply charged ions tend to be very reactive due to their high charge density [5]. Recent progress on understanding the role of multiply charged ions in extreme environments such as planetary ionospheres and the interstellar medium also confirms the significance of this broad and lively research field [6, 7].

Improved access to high power femtosecond laser systems has provided a new route to the facile production of multiply charged ions on a rapid timescale. The presence of multiple charges within a single molecule opens up a dissociation mechanism not seen in low charged species, that of Coulomb explosion. The extreme repulsion between multiple charges located in a small region of space leads to rapid dissociation on a timescale of tens to hundreds of femtoseconds. This mechanism was first identified by Carlson and White in the 1960s [8], and has been the subject of numerous investigations spanning gas-phase molecules, cluster, solids, and various targets in liquids [9]. In this and the following chapter, we describe the development of a new software package to simulate the dynamics of Coulomb explosions, and to generate velocity-map images and covariance images (both of which will be described in details in Section 7.3) for comparison with data from recent experiments.

6.2 Coulomb explosion imaging experiments

The first Coulomb explosion experiments were not performed with high power lasers. Instead, a beam of singly charged $CH_4{}^+$ cations was accelerated to approximately 2% of the speed of light before passing through a metal "stripping film" of around 30 Å thickness (Figure 6.1) [10]. As the ions pass through the film, all of the electrons except for the tightly bound carbon K-Shell electrons are stripped off within a time scale of about 10^{-16} s. Since this is much faster than the timescale for nuclear motion, the original geometry of the singly charged cation is retained in the newly formed multiply charged ions. However, the multiple charges lead to rapid Coulomb explosion into smaller, mostly atomic fragments, with the initial positions of the atoms within the molecule mapping onto the final velocities of the resulting atomic ions. The ions are incident on a position-sensitive detector, with the resulting images enabling reconstruction of the original molecular cation structure. The versatility of this technique was demonstrated on determining absolute configurations of chiral molecules by foil-induced Coulomb explosion imaging technique [11]. More recently, the foil stripping method has largely been replaced by laser photoionization using intense femtosecond laser fields. In addition to simplifying the experimental arrangement, the measurements are no longer limited to cations, allowing structural information to be obtained on neutral molecules. A large number of studies of this type have been carried out to investigate Coulomb explosion dynamics in diatomic, triatomic, and small polyatomic molecules [12–18].

Over the past few years, Coulomb-explosion imaging has been applied to determining elements of molecular structure in much larger polyatomic species such as a substituted biphenyl molecule (Figure 6.2) [19, 20]. This was achieved by measuring the momenta of all Coulomb-explosion fragment ions using the pixel-imaging mass-spectrometry (PImMS) multimass imaging camera [21, 22] in tandem with a velocity-map [23] ion-imaging (VMI) [24] spectrometer. The data obtained from these experiments provide

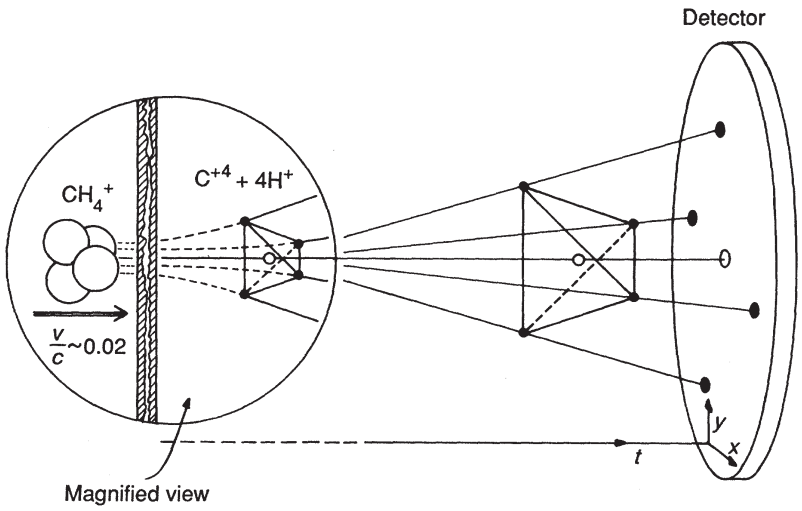


Figure 6.1: A schematic representation of the original Coulomb explosion experiment carried out by Vager and co-workers [10].

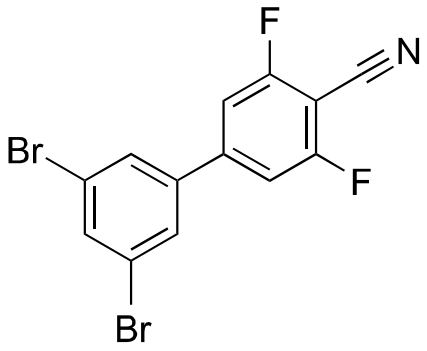


Figure 6.2: The 3,5-dibromo-3',5'-difluoro-4'-cyanobiphenyl (DBrDFCNBph) molecule in skeletal formula, as used in Slater *et al.*'s work [20].

detailed information on the correlated velocity distributions of all fragment ions. A statistical covariance analysis of the data allowed "covariance" images to be generated (see Figure 6.3 for steps of generating recoil frame covariance image), which reveal the correlated velocity distributions of two fragments, and make it possible to infer information on the parent molecular structure. Figure 6.4(a) shows laboratory frame images as recorded in the experiments for H^+ fragment ion when the molecule is in a parallel alignment. Figure 6.4(b) shows the corresponding covariance-map image of H^+ with respect to N^+ in the same orientation.

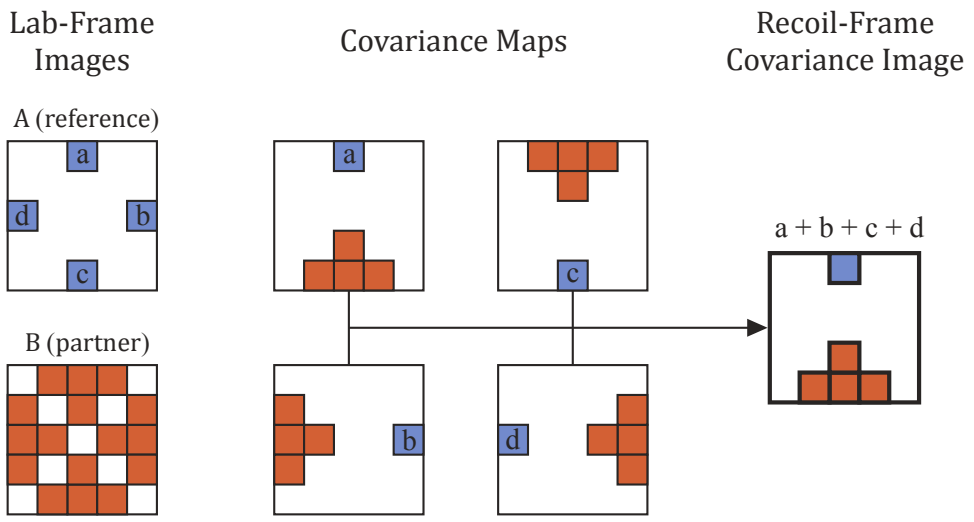


Figure 6.3: Steps of generating recoil frame covariance image as described in Slater *et al.*'s work [20]. Two lab-frame images of ion A and B are designated as "reference" ion and "partner" (or "plotted") ion, respectively. Covariance maps essentially plot the correlation of each pixel from reference frame to each pixel from partner frame. By rotating each of the covariance maps, the velocity of the reference ion is positioned vertically upwards, and a recoil-frame covariance image is generated by summing over all such images.

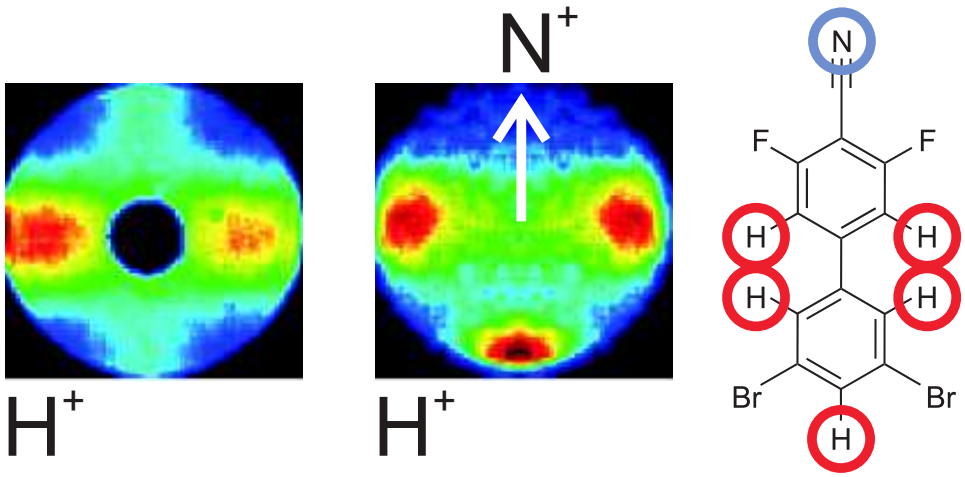


Figure 6.4: Laboratory-frame image of H^+ (left) and covariance image of H^+ with respect to N^+ of DBrDFCNBph in parallel alignment (middle) as shown in the skeleton representation (right) [20].

6.3 Review of simulating Coulomb explosion imaging

Simulation of Coulomb explosion processes and comparison of the simulation results with experimental data plays an important role in understanding the complex series of ionization, charge redistribution, and bond cleavage processes that occur in a typical Coulomb-explosion imaging experiment. In recent years, the types of simulations that can be attempted have been broadened dramatically thanks both to the ever-increasing supercomputer resources available and to advances in computation methods spanning both classical molecular dynamics and *ab initio* molecular dynamics.

6.3.1 Classical molecular dynamics simulation

Classical molecular dynamics aims to determine the dynamic evolution such as trajectories (i.e. $r_i(t)$ for all atoms i at time t) and velocities (i.e. $\frac{\mathrm{d}r_i(t)}{\mathrm{d}t}$ for all atoms i at time t) of a molecular system by solving Newton's equation of motion:

$$F_i = m_i \sum_j a_{ij} = m_i \sum_j \frac{\mathrm{d}^2 r_{ij}}{\mathrm{d}t^2} \tag{6.1}$$

where F_i, m_i, a_{ij}, r_{ij} are the forces acting on atom i, the mass of atom i, the acceleration of atom i due to the presence of atom j, and the distance between atom i and j respectively.

From the classical molecular dynamics perspective, the interatomic forces are calculated from the predefined potential U of the system (Equation (6.2)), which is approximated by considering two-body and many-body contributions. Equation (6.3) gives an example potential including only two-body Coulomb interactions:

$$F_i = -\sum_j \frac{\partial U}{\partial r_{ij}} \tag{6.2}$$

$$U = \frac{1}{4\pi\varepsilon_0} \sum_j \frac{q_i q_j}{r_{ij}} \tag{6.3}$$

where q_i and q_j are the charges of fragment ion i and j, respectively [25].

Classical molecular dynamics have been used to simulate Coulomb explosion processes in clusters and larger systems by Last *et al.* [26]. Common outputs to be calculated include the time dependence of the kinetic and potential energies of the fragment ions and the interatomic distances. A number of assumptions are often made when using this approach: (1) vertical ionization is assumed, with the resulting ions in their ground electronic states; (2) the total charge of the ionized cluster is distributed amongst all cluster atoms in such a way as to minimise the cluster energy; (3) the atoms possess constant charge throughout the Coulomb explosion; (4) direct Coulomb interactions between charged ions dominate the Coulomb explosion process. With these assumption, the simplified model is sufficient to explain kinetic energies found in experiments [25–27].

It is noteworthy that simulations based only on a repulsive Coulomb potential do not always predict the right outcomes. For example, when molecule is at low charge state such as CH_3I^{2+}, repulsive Coulomb potential approach will certainly predict a complete Coulomb explosion with all bonds broken, but experiments observed formation of fragment ion such as $CH_3{}^+$ [28, 29]. It is therefore important to include other intermolecular forces.

6.3.2 *Ab initio* molecular dynamics simulation

Ab initio literally means "from first principles" in Latin. In the context of quantum chemistry, it means to perform computations by only knowing the number of each type of nucleus and the total number of electrons of the system, as well as physical constants such as speed of light, Planck constant etc. With these inputs, the electronic Schrödinger equation is solved to determine electronic energies, electron densities, and other properties, and is only limited by the pre-specified model chemistries. *Ab initio* quantum chemistry, or electronic structure methods, redefined the field of theoretical chemistry, and pioneering researchers John Pople and Walter Kohn were awarded the Nobel Prize in Chemistry in 1998 to recognise their contributions [30].

A number of methods have been developed which combine molecular dynamics simulations with *ab initio* calculation of the potential energy surface. This family of techniques, known as "*ab initio* molecular dynamics" (AIMD) methods [31], are sometimes also referred to as "first principles", "on-the-fly", or "direct" dynamics approaches [32]. In all of these methods, *ab initio* electronic structure calculations are performed in order to compute the interatomic forces on all nuclei, after which the molecular dynamics trajectory is determined from the classical equations of motion. A key underlying assumption is the Born-Oppenheimer approximation, which separates the electronic motion and nuclear motion in molecules. With this approach, even for systems where the electronic structure changes considerably on the molecular dynamics time scale (femtosecond), potentials can still be calculated directly at each point of the trajectories. Of course, the level of accuracy of the results will be subject to the model chemistries chosen.

6.3.3 *Ab initio* classical trajectory calculation

When the target species are gas-phase molecules, the term "*ab initio* molecular dynamics" is usually replaced by "*ab initio* classical trajectories". *Ab initio* classical trajectory calculations were first carried out by Leforestier in the 1970s on the gas-phase nucleophilic substitution reaction $H^- + CH_4$ [33]. The method grew in popularity through the 1990s [34] and has become a mainstream technique in chemical physics. It was included the Physics and Astronomy Classification Scheme (PACS) with a special classification number in 1996 [35]

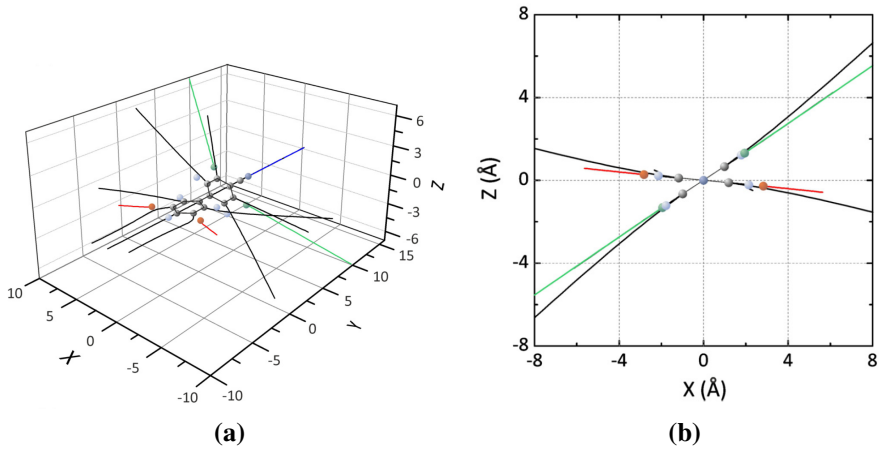
Possibly the most evident drawback of *ab initio* classical trajectories is that when multiple trajectories with different initial conditions must be run in order to obtain an averaged result, each trajectory, and the associated points on the potential energy surface, has to be repeated individually.

Early applications of *ab initio* classical trajectory calculations to the study of Coulomb explosions were usually limited to unimolecular dissociation of diatomic and triatomic

molecules [36, 37]. In the early 90s, Chang and co-workers performed an *ab initio* classical trajectory calculation to simulate the unimolecular dissociation of formaldehyde, H_2CO, in its ground electronic state [38]. In their work, experimental conditions were mimicked by assigning vibrational excitation energy into normal modes of the molecule based on normal mode analysis. Each of the five bound normal mode was assigned its respective zero-point vibrational energy, and remaining energy is given to the normal mode with imaginary frequency, i.e., along reaction coordinate. Similar simulation work were later performed on H_2CO [39], HXCO (X = F, Cl) [40], C_2H_5F [41], HCNH [42], CH_2NH [43], and other small molecules. To implement *ab initio* classical trajectory calculations, both the electronic structure calculations and the classical trajectory calculations were carried out using the BOMD keyword (i.e. Born-Oppenheimer Molecular Dynamics) within Gaussian [44] or similar packages such as MOLPRO [45]. Other free computer codes such as CPMD [46], CP2K [47], NWChem [48] are also available.

6.3.4 Simulating velocity-map images for Coulomb explosion products

Our understanding of recent experimental data from Coulomb explosion imaging experiments may be improved by comparison with data from classical trajectory calculations. In addition to the femtosecond laser-induced Coulomb explosion imaging experiment of DBrDFCNBph mentioned in Section 6.2, Slater and co-workers presented data from a classical trajectory simulation [20]. The simulations employed a simple model in which each atom in the molecule carries a single charge and charge redistribution is not possible. The potential used in the simulations included only Coulomb repulsions between the charged atoms. No other interaction terms were included. The simulated atomic ion trajectories following Coulomb explosion of the DBrDFCNBph parent molecule are shown in Figure 6.5(a). With a total charge of +23 and a purely repulsive potential, it is not surprising that the atomic ions rapidly fly away from each other. However, there are some subtleties to the trajectories which yield insight into the dynamics of the Coulomb



(a) **(b)**

Figure 6.5: Plots of simulated ion trajectories following Coulomb explosion of DBrDFCNBph with a single positive charge on each atom, (a) in three dimensions and (b) plotted onto *xz*-plane, as described in Slater *et al.*'s work. Trajectories time = 70 fs after onset of simulation [20].

explosion process. For example, the constituent carbon atoms of both phenyl rings have trajectories that depart substantially from axial recoil, as opposed to trajectories of the peripheral substituents N, F, and Br. The most extreme examples are the two carbon atoms that were initially bonded to the two Br atoms. The lighter carbon atoms struggle to follow axial recoil due to the presence of the much heavier and slower moving Br atoms. Instead, they recoil almost parallel to the principal axis of the molecule (i.e. *y*-axis, which is also coincident with axis that lies along the C-C bond between the two phenyl rings). Furthermore, If the ion trajectories are plotted onto the *xz*-plane (Figure 6.5(b)), it becomes clear that both Br^+ and F^+ atomic ions follow almost perfect trajectories that are confined to the planes of their respective phenyl rings. This observation confirms earlier findings that the relative recoil of Br^+ and F^+ ions may be used to infer the dihedral angle between the two rings [19, 49].

The final velocities of the atomic ions after the Coulomb explosion are used to generate the simulated velocity-map images. Each trajectory describes the Coulomb explosion of a single parent molecule. In order to make meaningful comparisons with measured velocity-map images which are a summation of the final velocities of many thousands of such

events, a large number of trajectories ($\sim$ 30000 in Slater *et al.*'s work) should be simulated, with the initial conditions sampled from a predefined distribution. The two main initial conditions are: (1) the angle of rotation about the principal axis of the molecule (the molecules are laser aligned relative to a laboratory axis, but undergo free rotation about this axis); (2) the total charge on the parent ion was sampled from a Poisson distribution with a mean value of 15 charges per molecule, as estimated from the experimental data. With appropriate averaging over these distributions, the simulated velocity-map images can be compared directly with the experimental data. Figure 6.6 shows the simulated and experimental VMI images in (a) perpendicular and (b) parallel alignments. The agreement between simulated and experimental data in parallel alignment is very good, with most features detected in the experiments also found in the simulated counterpart. The broad nature of the features in the experimental images appear to be due primarily to the variable initial charge states of the molecular ions. However, the simulations perform less satisfactorily for the perpendicular alignment, except for the F^+ and Br^+ fragments. Specifically, while the radial features are similar in the experimental and simulated covariance images, the simulations generally show much sharper and more well-resolved angular distributions than the experimental data. It has been suggested [20] that there might be a deformation of the parent molecule out of the planes defined by the phenyl rings at the early stages of Coulomb explosion in experiment, which leads to a lower degree of angular correlation between many of the fragment ions than might be expected.

6.4 Novel approach of simulating Coulomb explosion from first principles

6.4.1 Aims and algorithm

As summarized in the preceding section, so far simulations of Coulomb explosion processes have either exclusively relied on Gaussian functionality (BOMD keyword) for both electronic structure and classical trajectories calculation, or merely adopted simple

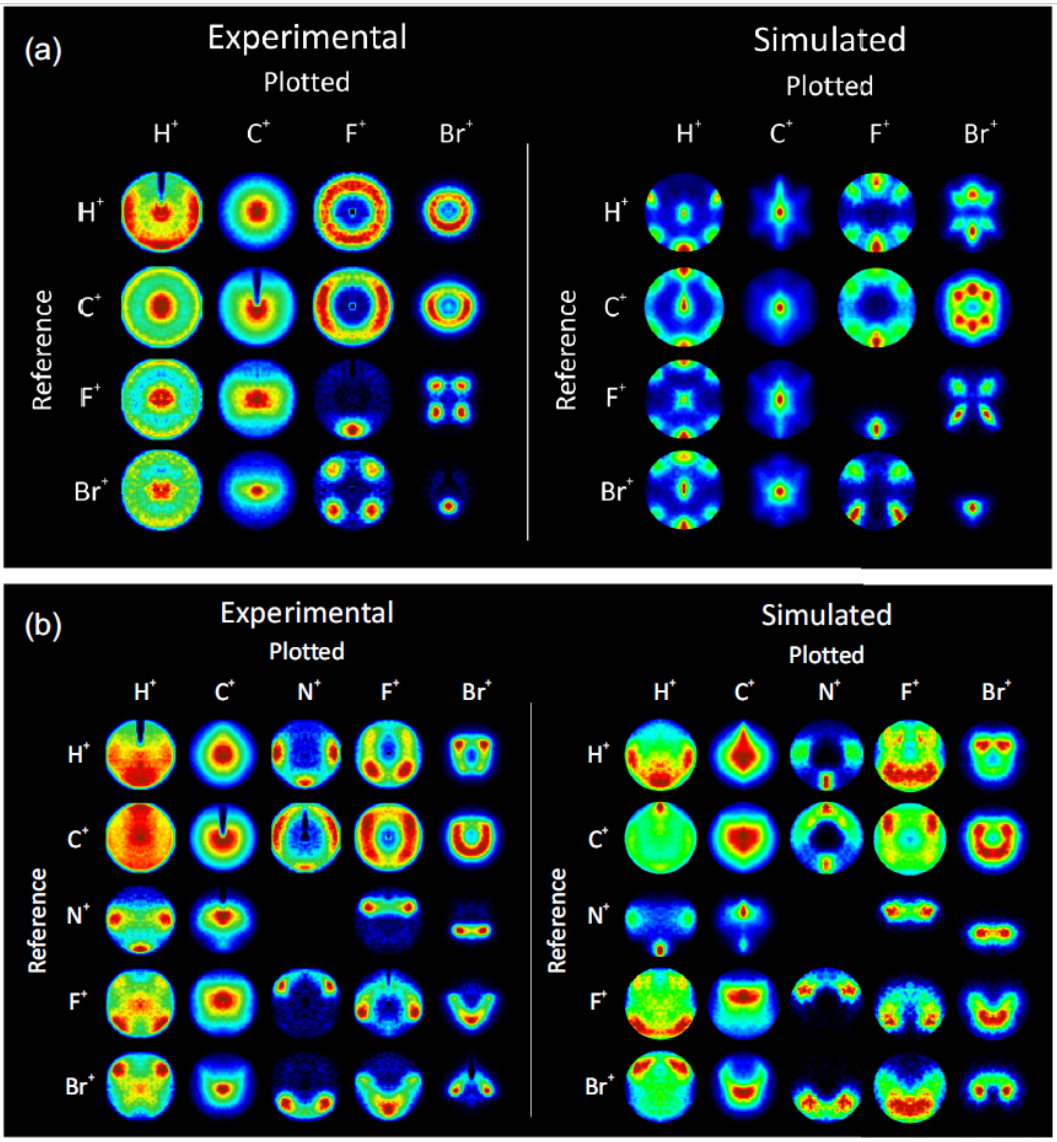


Figure 6.6: Covariance images of DBrDFCNBph recorded in (left column) experiment and (right column) simulation in (top row) perpendicular and (bottom row) parallel alignment, as described in Slater *et al.*'s work [20].

laws of classical motion in order to achieve computational tractability at the expense of imposing assumptions and approximations without *ab initio* input. When it comes to determination of the most appropriate model chemistries to use for *ab initio* classical trajectory simulations, most studies have only reported limited benchmarking, rather than testing different levels of theory and basis sets across a wide range of molecular systems. The Gaussian keyword BOMD offers many optional inputs, but the time step can only be specified as a fixed value, which largely determines the total trajectory time.

Most of the free software packages mentioned in Section 6.3.3 are rather complex to use, and often impose a long learning curve before a user can perform even a relatively simple task. In the context of the current project, in which we wish to simulate covariance velocity-map images of Coulomb explosion products for comparison with experimental data, there are a number of improvements that can be made on previously used methods in order to provide a better physical description of the process and hopefully to improve agreement with experiment. Implementing these improvements forms the core of the work described in this and the following chapter.

The software developed to address the issues outlined above separates the functionality of electronic structure and classical trajectory calculations into Gaussian and Matlab packages, respectively, and was coded as a single executable Matlab program. A flow chart of the program algorithm is provided in Figure 6.7. Classical trajectories are propagated by using the ordinary differential equation (ODE) solver that forms part of the Matlab package to solve Newton's equations (Equation (6.1)). At each time step, the potential energy and interatomic forces are calculated through a call to the Gaussian software package. The simulation may be terminated either by setting a total trajectory time, setting a threshold on the interatomic forces (i.e. stopping when the forces are reduced to approximately zero), or setting a threshold on the change in atomic velocities at each timestep (i.e. stopping when the atoms or molecular fragments have reached their terminal velocities). Dynamical and chemical information such as coordinates, velocities, forces, energies, atomic partial charges, bond orders etc. are written to external file at each time step to enable detailed interrogation of the trajectories at the end of the calculation.

Bond orders are obtained by calculating the Wiberg bond index [50] between atom A and B which is defined by Equation (6.4), and is calculated from a natural bond orbital (NBO) analysis [51] in Gaussian:

$$W_{AB} = \sum_{i \in A} \sum_{j \in B} P_{ij}^2 \tag{6.4}$$

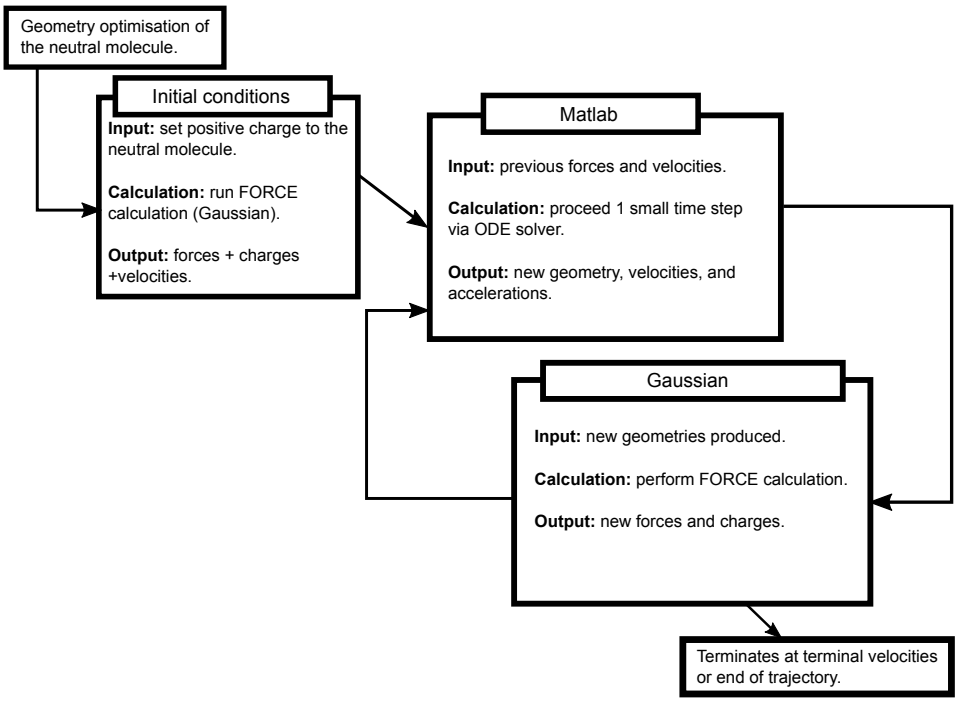


Figure 6.7: Flow chart of the algorithm of the current *ab initio* classical trajectories simulation program.

where P is density matrix. Wiberg bond indices are numerically close to bond order derived from valence bond theory. In general, a smaller Wiberg bond index suggests a weaker bond.

For Coulomb explosions yielding molecular fragments, the charge of the fragment is the sum of the charges on all constituent atoms, and the velocity is taken to be the velocity of the centre of mass of the fragment, as calculated from Equation (6.5):

$$v_{\mathrm{cm}} = \frac{1}{M}\sum_{i=1}^{N} m_i v_i \tag{6.5}$$

where the sum is over the N constituent atoms within the fragment, m_i and v_i are the mass and velocity of ith atom, and $M = m_1 + m_2 + \cdots + m_N$.

Gaussian checkpoint files containing the molecular wavefunction are also written at each timestep, and are used as the initial guess for the electronic structure calculation in the next timestep. This reduces the computational time, and also prevents unphysical jumps

between different electronic potential energy surfaces as the trajectory proceeds.

The detailed steps followed in a given trajectory calculation are:

(1) Perform a geometry optimization on the neutral parent molecule at Hartree-Fock (HF) self-consistent field method [52], Møller-Plesset perturbation theory method (MP2, MP3, MP4, etc.) [53], and Coupled Cluster (CC) method [54] to determine the molecule's initial geometry. It is assumed that the geometry does not change during the ionization step, so that this is also the initial geometry of the multiply charged ion that undergoes Coulomb explosion.

(2) For the optimized molecular geometry obtained in step (1), perform a single point calculation for a chosen total charge state z, using the keywords "stable=opt, Guess=(mix,read)" to test the stability of the wavefunction and to reoptimize it if an instability is found [55, 56]. Save the resulting wavefunction to a checkpoint file.

(3) Using the wavefunction from step (2), loaded from the checkpoint file, perform a single point calculation at the same total charge state z, with keywords "pop=(MK, NBORead, Hirshfeld), IOp(6/76=8) Force, Guess=read" to calculate the interatomic forces on each atom as well as atomic partial charges determined according to the Merz-Singh-Kollman [57, 58] scheme, Natural Bond Oder (NBO) analysis [51], and Hirshfeld population analyses [59]. The IOp keyword, iop(6/76=8), acts to tighten the criteria for determining basis set linear dependence in the NBO analysis from the default value of 10^{-6} to 10^{-8} in order to help obtain a correct total charge state [60].

(4) Using the starting geometry obtained in step (1) and the forces obtained in step (3), and assuming that all atoms are at rest at $t = 0$ fs, i.e. all atomic velocities are zero, use the Matlab ODE solver to integrate Equation (6.1). The size of the integration time step is determined automatically by the ODE solver, and varies at different points in the trajectory according to the potential gradient. At each time step, the

forces are calculated by performing a "stability test" and a "force" single-point calculation in Gaussian, with the same keywords as detailed in step (2) and (3), respectively. When each time step is complete, the trajectory time point, partial charges, velocities, coordinates, forces, and energies of the molecular system are all written to an ASCII file for later analysis.

Once the defined termination criterion, based on trajectory duration, atomic forces, or atomic velocities, has been met, the simulation is terminated.

A separate Matlab program has been written in order to analyse and plot outcomes such as the trajectories. In addition, if assuming V is the extraction voltage, d is length of flight tube, m and q are the mass and charge of ions, respectively, the time of flight of the ions, t, is

$$t = d\sqrt{\frac{m}{2qV}} \tag{6.6}$$

Terminal velocities are then multiplied with time of flight of the ions, t, to produce the velocity-map images in xy, xz, and yz-plane. A more detailed description of the file system and a standard operating procedure for the software can be found in Appendix E.

The program is written in Matlab which calls at the classical trajectories part and also coordinates the communication between Gaussian and Matlab. Both Gaussian and the main Matlab program are run at advanced computing resources at Department of Chemistry, University of Oxford.

While similar to some of the common *ab initio* classical trajectory methods introduced in Section 6.3.3, in particular the BOMD approach, the current implementation has a number of advantages:

(1) It exerts minimum constraints on the system to be simulated. The only pre-determined conditions are: a) the total charge of the system remains constant

throughout the time of a trajectory, b) the initial velocities are zero, and c) the Born–Oppenheimer approximation applies so that motions of electrons and nuclei may be calculated separately.

(2) It does not require any knowledge of the optimum size of time step, as this is entirely controlled by Matlab's ODE solver in order to meet the integration tolerances. The time step is not fixed, but variable depending on the difference between the estimated error and the specified error tolerance at each time step. The estimated error is usually dependent on the gradient of the force field. The benefit is twofold: the required time steps are generally very small during the early stages of a Coulomb explosion in order to describe fine details of the dynamics in a region where the potential is changing rapidly. However, the required time step becomes increasingly larger at later stages of the process, when the potential landscape is changing much more slowly, and the atomic velocities are close to their terminal values. Varying the timestep in accordance with these criteria provides a significant reduction in the overall trajectory time relative to implementing a fixed time step, as well as providing an optimised time step at each point in the simulation.

(3) As the software comprises Matlab code that invokes the Gaussian software package, the functionalities of both Gaussian and Matlab are available. The code exploits functionality such as testing wavefunction stability, continuously recording data, and adjusting classical trajectory parameters.

6.4.2 Adjustment, benchmarking and testing

6.4.2.1 General considerations

While developing and testing the program, a number of problems and challenges were encountered and needed to be overcome, and a number of parameters needed to be optimised. Some of these are summarised below.

(1) An option is needed to allow users to choose between better accuracy of results and a shorter total running time.

(2) Apart from calibrating against experimental data, which may not always be a straightforward task, the program outputs need to be monitored to ensure that they are physically realistic. For example, the atomic charges must reach integer values at some point when the Coulomb explosion is considered to be complete.

(3) Any limitations associated with using Gaussian to perform electronic structure calculations on highly charged ions need to be fully understood.

(4) Intermediate data and checkpoint files need to be stored periodically to allow the calculation to be resumed (rather than restarted from the beginning) in the event of an unexpected termination of a running program. This is a common issue when studying a new molecular system.

(5) Log and error messages need to be documented in detail to allow straightforward debugging of the software.

(6) From the user's perspective, the program ideally needs to be highly automated and to require a minimum amount of input/change when being used to study a new molecule. General programming good practice, such as code that is robust, compact, and easy to read, maintain, and modify, is important.

To meet these objective, extensive adjustments, benchmarking, and testing were performed on a number of test systems before moving on to study molecules of specific interest. The variables that were considered and optimised during this phase are listed in Table 6.1. These are investigated one by one in the following.

6.4.2.2 Effect of level of theories

The level of theory, or model chemistry, is the combination of method and basis set specified in Gaussian when performing the electronic structure calculation at each time step to determine the atomic forces [61]. The method encapsulates the theoretical

Table 6.1: Initial parameters of simulation before characterization.

Factor	Value
Theoretical method	MP2 or B3LYP
Basis set	6-311G(d,p)
SCF convergence criterion	10^{-6}
ODE solver - Relative error tolerance	10^{-3}
ODE solver - Absolute error tolerance (geometry)	10^{-6}
ODE solver - Absolute error tolerance (velocity)	10^{-4}

procedure and set of approximation used when solving the Schrödinger equation to determine the molecular wavefunction, and the basis set is the set of mathematical functions in which the wavefunction is expanded. The basis set employed in a given calculation essentially determines the region of space to which the electrons are confined. A sub-optimal choice of the method or choice of an insufficiently flexible basis set can have a highly detrimental effect on the accuracy of the electronic structure calculations.

The commonly used methods in Gaussian are the HF, MP2, the Coupled Cluster (CC) method, Quadratic Configuration Interaction (QCI) [62], and various flavours of density functional theory. The HF method treats each electron's motion in terms of a one-electron wavefunction which is not dependent on the instantaneous position of any other electrons. The method is a useful starting point for initial calculations on many systems, but it does not tend to predict accurate energies due to its neglect of electron correlation. To treat electron correlation, one can employ Møller-Plesset perturbation theory to determine the appropriate second-order (MP2), third-order (MP3), or fourth order (MP4) corrections to the wavefunction and energy [63]. The MP2 method is the least computationally expensive of these methods. The CC and QCI methods are alternative methods which include electron correlation by allowing mixing of electronically excited states into the ground-state wavefunction. They iteratively include the effects of single and double substitutions to add higher order terms to both the wavefunctions and energies.

Another distinctively different and popular family of methods called Density Functional Theory (DFT) [64] was developed to account for electron correlation via functionals of electron density based on the Hohenburg-Kohn theorem which stated that the electron density determines the total energy of the system, rather than describing the system in terms of a wavefunction. DFT methods greatly reduce the computational cost compared with other post-HF methods while achieve significantly higher accuracy than HF method [65].

As for the choice of basis sets, larger basis sets impose fewer constraints on the molecular electrons, and hence are capable of representing molecular orbitals more accurately but at an unfavourable cost of CPU time. However, sufficiently accurate determination of particular molecular properties can sometimes require the use of different basis sets [66]. Careful characterisation of the performance of a model with different basis sets is often needed in order to identify the optimum basis set for a given calculation. A wealth of basis sets have been developed over the years, including the most common and popular Pople-style basis sets, Ahlrichs Def2 type basis sets [67, 68], and cc-pVXZ type basis sets [69–71] etc. Gaussian has a large number of built-in basis sets, and non-standard basis sets may also be specified within the input file. Most basis sets in current use are catalogued in the Basis Set Exchange (BSE) database (https://bse.pnl.gov/bse/portal) [72, 73].

When employing adequate methods and basis sets, Gaussian is undoubtedly a powerful tool for calculating many properties of molecular systems. For our goal of performing *ab initio* classical trajectory calculations on Coulomb explosions, the only information needed for propagating the trajectory (and hence for considering the choice of level of theories) is the interatomic forces, calculated from the gradient of the energy. Although atomic partial charges are calculated and written out at each time step, they are not used to propagate the trajectory.

In the next three sections, trans-2,3-dideuterooxirane and chloroiodomethane molecules will be used for testing the effects of methods (in Sections 6.4.2.2.1 and 6.4.2.2.2) and

basis sets (in Section 6.4.2.2.3).

6.4.2.2.1 Methods (trans-2,3-dideuterooxirane)

A comparison between the charge distribution on the molecular ion and the charges on the detected ionic fragments implies that Coulomb explosions involve a significant amount of charge transfer on very short timescales. Correct treatment of electron correlation is therefore likely to be important, with the consequence that the HF method is unlikely to provide a satisfactory treatment of the Coulomb explosion process. On the other hand, most trajectory calculations typically involve a few hundred time steps. Computational accuracy must therefore be weighed against computational cost. For example, CC and QCI methods are not feasible except for very small systems due to the rather long CPU times required. Accordingly, the decision is realistically between MP*n* and DFT methods. Tests [61] have shown that MP3 calculations barely improve over MP2 calculations, while imposing considerable additional computational cost, and MP4 calculations tend to be unacceptably expensive, though considerably more accurate. MP2 was therefore tested for use in the present application. With regard to DFT methods, the most widely used functional, B3LYP [74, 75], was chosen for initial testing. B3LYP is a hybrid functional that includes Hartree-Fock exact exchange, and generally performs well across a wide range of systems.

A gas-phase chiral molecule, trans-2,3-dideuterooxirane ($C_2OD_2H_2$) (Figure 6.8) was selected for testing the effect of *ab initio* theoretical methods. Trans-2,3-dideuterooxirane has been studied by Herwig and co-workers for absolute configuration assignment using foil-induced Coulomb explosion imaging [11, 76]. It is noteworthy that in order to compare with the experiments, the initial geometry of trans-2,3-dideuterooxirane needs to be optimized for the +1 charge state i.e. $C_2OD_2H_2{}^+$, as the molecule is present in a beam of singly charged ions before stripping of additional electrons by passage through the foil initiates the Coulomb explosion. Additionally, in the experiments, the C^{2+}, O^{2+},

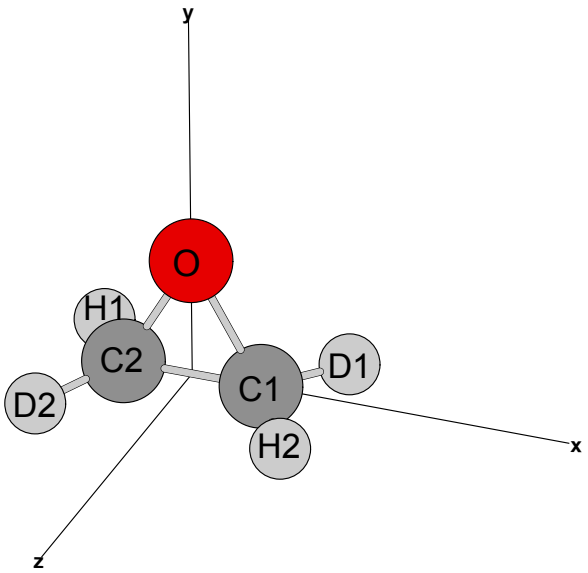


Figure 6.8: Ball and stick representation of the (*R*,*R*)-trans-2,3-dideuterooxirane molecule.

and D^+ ions were all detected, while H^+ ions were diverted outside of the detector region. This implies that a total charge of +10 on the molecular ion is possible. Since it is expected that the (*R*,*R*) and (*S*,*S*) configurations will yield symmetric results, only the (*R*,*R*) configuration is considered in the present work. The coordinate system of the molecule is chosen in accordance with Herwig and co-workers' paper (see Figure 6.8), so that direct comparisons are easily made.

Trans-2,3-dideuterooxirane was then simulated with a total charge state of +10 using both the MP2 and B3LYP methods, with all other parameters set to the values listed in Table 6.1. Figure 6.9 shows the evolution of the atomic charges obtained using the two methods. It is clear that although for some atoms the initial partial charge states might vary moderately, after 50 fs, the partial charges are almost identical for all atoms by using both methods, and agree with the charges on the ions detected in the experiments, i.e. C^{2+}, O^{2+}, D^+ and H^+.

Similarly, the evolution of the atomic velocities and the interatomic forces are compared in Figure 6.10 and Figure 6.11, respectively. Both Figures can be used to derive the duration of the Coulomb explosion. The explosion is complete when the velocities reach

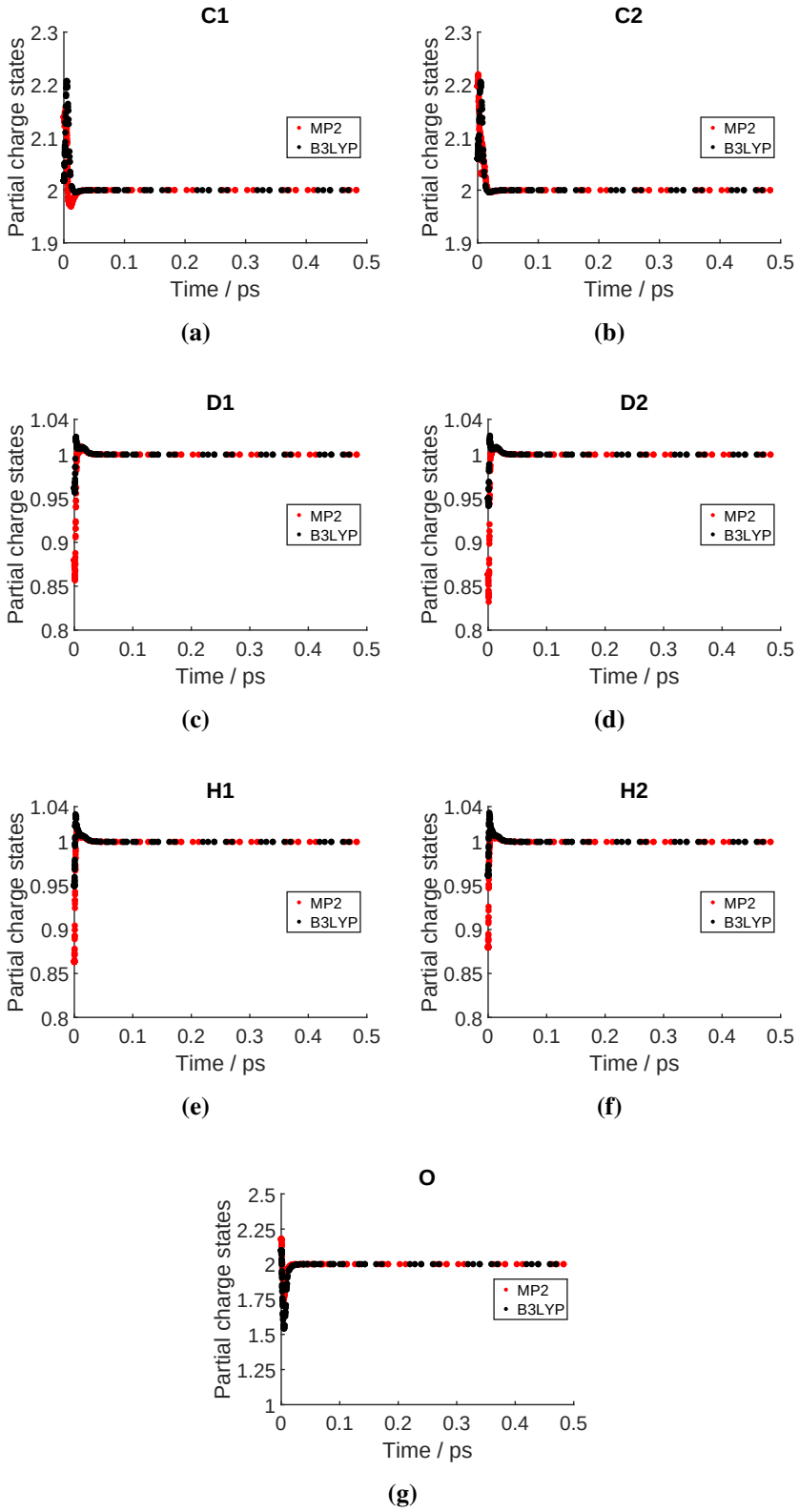


Figure 6.9: Evolution of the atomic charge states during Coulomb explosion of trans-2,3-dideuterooxirane (*R*,*R*) at $z = +10$ using the MP2 and B3LYP method, with 6-311G(d,p) basis set. Note that atoms are numbered in the same way as in the picture of the molecule in Figure 6.8.

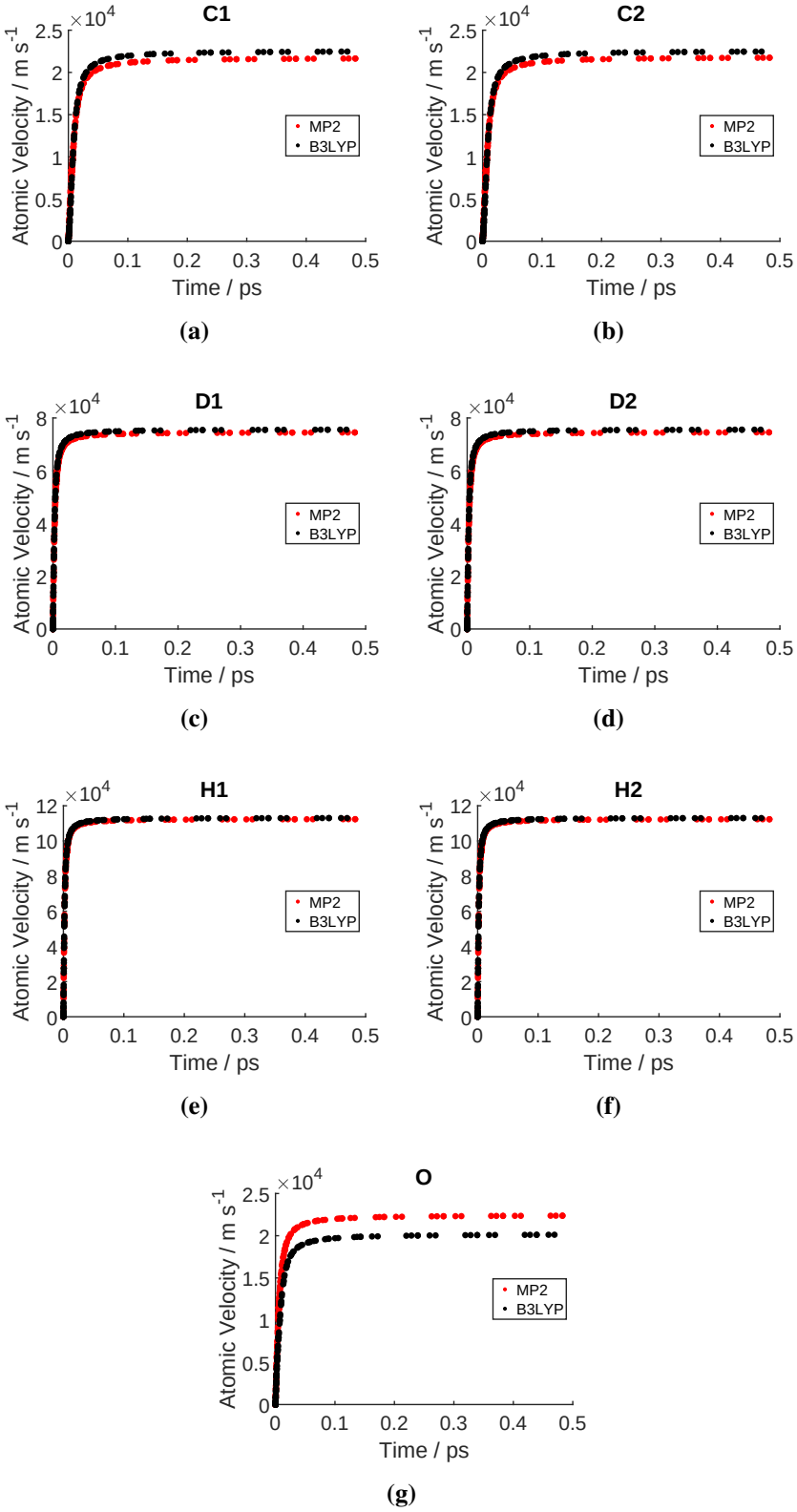


Figure 6.10: Evolution of atomic velocities during Coulomb explosion of trans-2,3-dideuterooxirane (*R*,*R*) at $z = +10$ using the MP2 and B3LYP method, with 6-311G(d,p) basis set. Note that atoms are numbered in the same way as in the picture of the molecule in Figure 6.8.

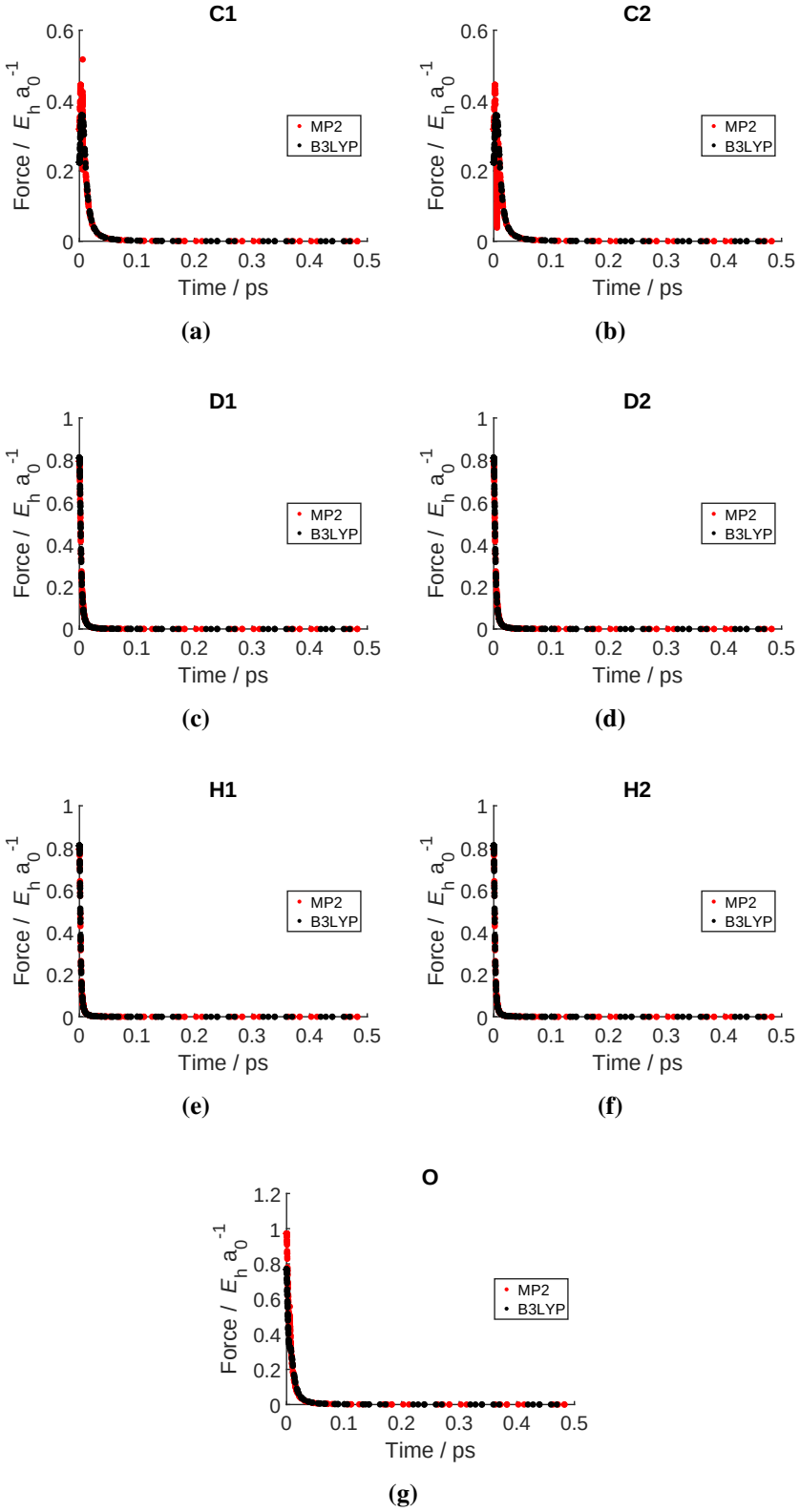


Figure 6.11: Evolution of Interatomic forces during Coulomb explosion of trans-2,3-dideuterooxirane (*R*,*R*) at z = +10 using the MP2 and B3LYP method, with 6-311G(d,p) basis set. Note that atoms are numbered in the same way as in the picture of the molecule in Figure 6.8.

their asymptotic values or, equivalently, when the forces reach zero. Both the MP2 and B3LYP methods yielded almost identical force evolution curves. Discrepancies are seen in the velocity curves, which seems to be larger for heavier atoms. However, if the terminal velocities are used to construct velocity-map images assuming a typical 0.5 m flight tube and 10 kV extraction voltage, both methods yield very similar images (Figure 6.12) with the discrepancy on a millimetre scale, which, in the case of Herwig and co-workers' instrument where the diameter of the active area of the detector is 118 mm [77], can be considered insignificant.

The terminal velocities of D^+ obtained in the current simulation work may be compared with the asymptotic velocities of D^+ measured in Herwig and co-workers' experiment [11], as shown in Figure 6.13. The two sets of velocities are in qualitative, but not quantitative agreement, with the current simulations (using both MP2 and B3LYP methods) predicting somewhat higher final velocities than the Herwig and co-workers' experimental measurement.

The results so far for trans-2,3-dideuterooxirane do not provide strong evidence to favour one theoretical method out of MP2 and B3LYP over the other. However, different conclusion will be presented for other test molecules in the next section.

6.4.2.2.2 Methods (chloroiodomethane)

Aside from comparing with reliable experimental data, information obtained directly from the simulations may be utilised to check the validity of the theoretical methods being used. In the initial stages of the Coulomb explosion, the atoms within the ionized molecule may possess non-integer partial charges. As the atomic or molecular fragments fly apart from each other, each fragment must eventually end up with an integer charge when the fragments have reached sufficiently large separations. This behaviour must be reproduced in the simulations.

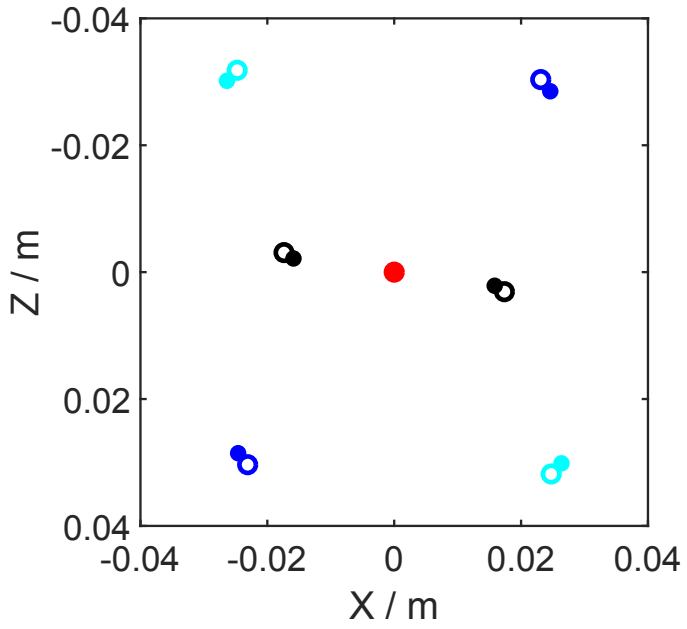


Figure 6.12: Velocitiy-map image of trans-2,3-dideuterooxirane (*R*,*R*) on *xz*-plane. O, C, D, and H are respectively colored red, black, blue, and cyan. Filled and open circles represent MP2 and B3LYP method, respectively.

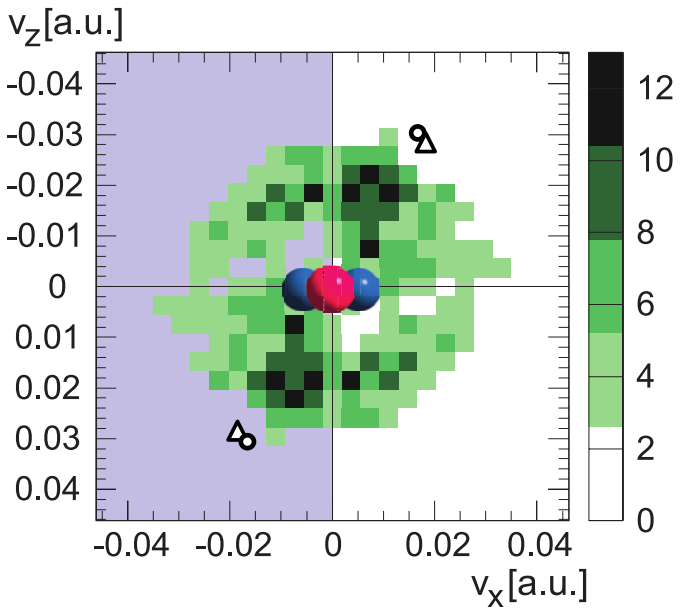


Figure 6.13: Comparison of velocities of D atom in trans-2,3-dideuterooxirane(*R*,*R*) in *xz*-plane between experimental measurement by Herwig *et al.* [76] and current simulation. Experimental events are colored as green, and the coordinate system is chosen such that the velocities of two C atoms lie on the v_x-axis, and the velocity of the C-O-C centre of mass lies on the positive v_y-axis. Simulated velocities by MP2 and B3LYP methods (with 6-311G(d,p) basis set) are labelled as triangle and circle, respectively.

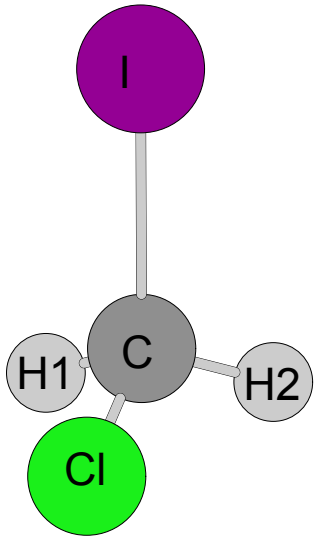


Figure 6.14: Ball and stick representation of the chloroiodomethane molecule.

Chloroiodomethane (CH_2ICl), a halomethane molecule with one chlorine atom and one iodine atom (Figure 6.14), is a popular target for studying ionization and dissociation processes in intense femtosecond laser fields [78, 79]. *Ab initio* Coulomb-explosion simulations were performed on chloroiodomethane with a total charge state of +4 using both the MP2 and B3LYP method, with trajectories simulated up to 324 fs. Due to the presence of a heavy iodine atom, an Effective Core Potential (ECP) basis set is needed to describe deep core electrons, and only the valence electrons are treated quantum mechanically. This significantly reduces the computational cost. Since the triple-ζ Pople basis set 6-311G(d,p) is chosen for non-heavy atoms, the equivalent triple-ζ Def2-TZVP basis set [67] is used for Chloroiodomethane.

The simulations (see Figure 6.15) predicted that the molecule fragments into an I atom, a CClH molecular fragment, and an H atom when the electronic structure calculations are performed using the MP2 method, but yields an I atom, an H_2 molecular fragment, and a CCl molecular fragment when the B3LYP method is employed.

The partial charge on each fragment is plotted as a function of time for the two simulations

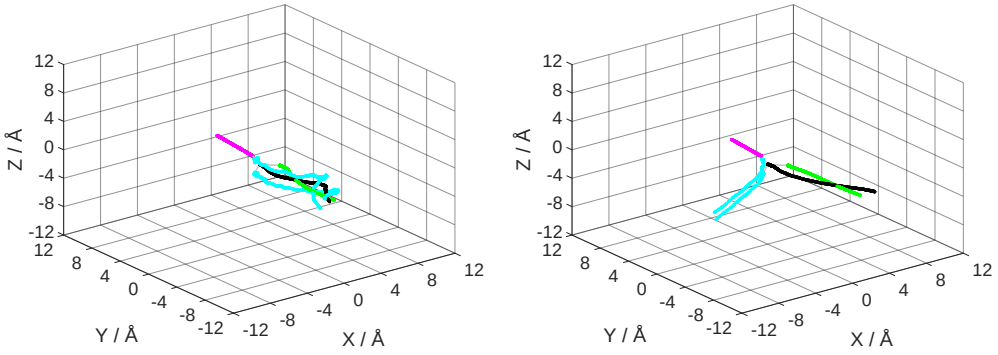


Figure 6.15: Trajectories of atoms of CH_2ICl during Coulomb explosion at z = +4 simulated using (a) MP2 and (b) B3LYP method, with Def2-TZVP basis set. I, Cl, C, and H are respectively colored magenta, green, black, and cyan.

in Figure 6.16, along with the relevant Wiberg bond index. When using MP2 electronic structure calculations the C-I bond and C-H1 bond break at around 100 fs and 30 fs, respectively. The I atom, H1 atom, and the C-Cl-H2 fragment reach stable integer charge states at +1, +1, and +2, respectively. When the electronic structure calculations employ the B3LYP density functional, neither the iodine nor the CCl fragment reach integer charge states, even though the fragments have separated to distances of 18 to 19 Å.

The time evolution of the charge distribution indicates that the MP2 method provides more physically reasonable results than B3LYP in the case of chloroiodomethane, while the two methods appeared to show equivalent performance in the case of trans-2,3-dideuterooxirane. The performance of density functionals is often quite specific to a particular type of chemical system, so it's not surprising that the generic B3LYP functional doesn't perform very well for the fairly exotic highly charged species we're dealing with here.

The only drawback of using the MP2 method for the simulations is its relative computational expense. When running on Intel® Xeon® dual 10-Core 2.60 GHz E5-2660 v3 CPU with 64 GB memory and using 16 cores of the CPU (for both the Gaussian calculation and overall Matlab program) with 8 GB memory (for Gaussian program only),

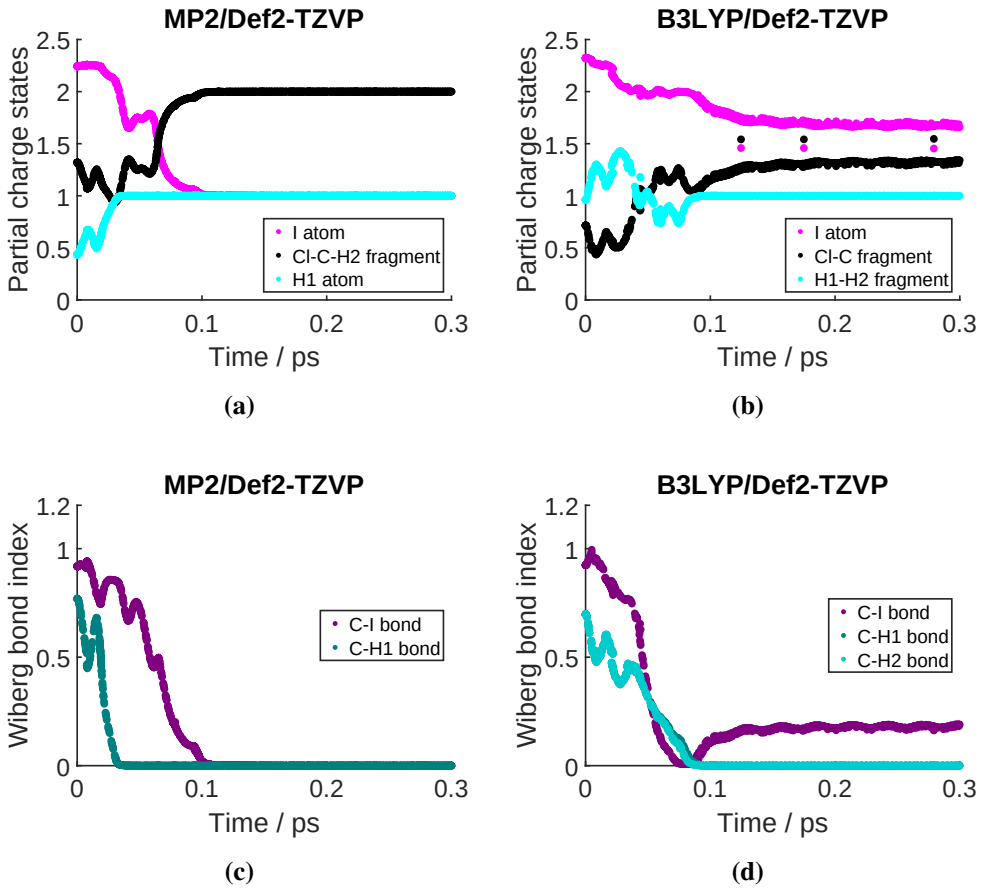


Figure 6.16: Evolution of (a,b) partial charge states and (c,d) Wiberg bond indices of atoms and molecular fragments during Coulomb explosion of CH_2ICl at z = +4 simulated using (a,c) MP2/Def2-TZVP and (b,d) B3LYP/Def2-TZVP.

simulations on the CH_2ICl^{4+} molecular system took 21 hours and 43 minutes using the B3LYP method, but took 6 days and 6 hours using the MP2 method. In the case of the trans-2,3-dideuterooxirane molecule in a charge state of +10, simulations employing the B3LYP method took 22 minutes and 12 seconds, while MP2 simulations required 45 minutes and 38 seconds. The total computational time is the sum of the run time for all the Matlab and Gaussian subroutines. This is affected by many parameters, including the specification of the molecular system, and is almost impossible to predict in advance. For molecules whose constituent atoms are from the top four rows of the periodic table and the charge state is high enough to provide a significant reduction in the number of electrons in the electronic structure calculations, the MP2 method outperforms B3LYP

Table 6.2: Terminal atomic partial charge states of trans-2,3-dideuterooxirane (z = +10) simulated using MP2 method with different basis sets.

	6-31G(d,p)	**6-311G(2d,p)**	**6-311+G(d,p)**	**cc-pVTZ**	**6-311G(d,p)**
O	2.000370	2.000326	2.000351	2.000336	2.000327
C1	1.999997	2.000161	2.000136	2.000119	2.000159
C2	1.999997	1.999984	1.999958	1.999958	1.999985
D1	0.999909	0.999882	0.999889	0.999897	0.999882
D2	0.999909	0.999882	0.999889	0.999897	0.999882
H1	0.999909	0.999882	0.999889	0.999897	0.999882
H2	0.999909	0.999882	0.999889	0.999897	0.999882

in almost all aspects. It was therefore decided to use MP2 as the theoretical method of choice for the remainder of the simulation work presented in this thesis.

6.4.2.2.3 Basis set effects

The effects of the choice of basis set on electronic structure calculations is a broad and complex topic, and largely depends on the properties to be calculated. Based on previous *ab initio* classical trajectory work, the 6-311G(d,p) basis was selected for initial test simulations. To systematically address the issue of the number of contracted Gaussians describing the valence orbitals, polarization functions, and diffuse functions, as well as effects of correlation-consistent basis sets, the 6-31G(d,p), 6-311G(2d,p), 6-311+G(d,p) and cc-pVTZ basis sets were used in simulations of the trans-2,3-dideuterooxirane molecule with a +10 charge state, as described in Section 6.4.2.2.1. Terminal fragment charge states, atomic velocities, interatomic forces, and SCF energies are tabulated in Tables 6.2 to 6.6. It is immediately clear that, across all properties, the 6-311G(d,p) basis yields almost identical results to the 6-311G(2d,p) and 6-311+G(d,p), i.e. an addition of one more *d* function on heavy[1] atoms and a diffuse function, respectively, has little effect on basis set performance. The 6-31G(d,p) basis set yielded the fastest run time, but gave results that differed significantly from all the other basis sets, demonstrating the necessity of including at least three contracted functions to describe the valence orbitals.

[1] In the context of adding polarization functions to Pople basis sets, heavy atoms mean any atoms apart from H. This is different from those atoms in 4th or lower rows when discussing ECP basis sets.

It was decided that the 6-311G(d,p) achieves a reasonable balance between accuracy and time, and will be used for simulation work presented in this thesis.

Table 6.3: Terminal atomic velocities (in m s^{-1}) of trans-2,3-dideuterooxirane (z = +10) simulated using MP2 method with different basis sets.

	6-31G(d,p)	**6-311G(2d,p)**	**6-311+G(d,p)**	**cc-pVTZ**	**6-311G(d,p)**
O	21005.06	22440.08	22426.46	22329.12	22422.71
C1	22838.13	21697.76	21709.58	21657.17	21708.18
C2	22985.87	21790.73	21800.70	21756.10	21802.96
D1	75062.78	74592.88	74606.42	74621.48	74591.24
D2	74968.34	74635.07	74651.36	74665.73	74636.56
H1	112601.85	112451.63	112458.44	112465.24	112450.55
H2	112660.34	112416.34	112420.84	112428.77	112413.01

Table 6.4: Terminal atomic forces (in Hartrees $Bohr^{-1}$) of trans-2,3-dideuterooxirane (z = +10) simulated using MP2 method with different basis sets.

	6-31G(d,p)	**6-311G(2d,p)**	**6-311+G(d,p)**	**cc-pVTZ**	**6-311G(d,p)**
O	1.455E-05	1.438E-05	1.438E-05	1.448E-05	1.439E-05
C1	1.331E-05	1.404E-05	1.403E-05	1.410E-05	1.403E-05
C2	1.326E-05	1.403E-05	1.402E-05	1.409E-05	1.402E-05
D1	3.122E-06	3.152E-06	3.152E-06	3.151E-06	3.153E-06
D2	3.130E-06	3.149E-06	3.148E-06	3.147E-06	3.149E-06
H1	1.658E-06	1.653E-06	1.653E-06	1.653E-06	1.653E-06
H2	1.655E-06	1.653E-06	1.654E-06	1.654E-06	1.654E-06

Table 6.5: Terminal SCF energies (in Hartrees) of trans-2,3-dideuterooxirane (z = +10) simulated using MP2 method with different basis sets.

	6-31G(d,p)	**6-311G(2d,p)**	**6-311+G(d,p)**	**cc-pVTZ**	**6-311G(d,p)**
SCF energies	-145.9155	-145.8100	-145.8082	-145.8309	-145.8038

Table 6.6: Total computational time (in hh:mm:ss) of simulating of trans-2,3-dideuterooxirane (z = +10) using MP2 method with different basis sets.

	6-31G(d,p)	**6-311G(2d,p)**	**6-311+G(d,p)**	**cc-pVTZ**	**6-311G(d,p)**
Computing time	00:29:03	01:22:23	00:54:12	01:35:36	00:45:38

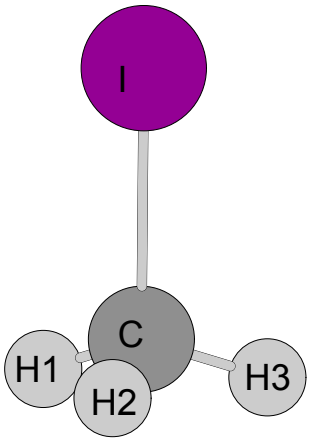


Figure 6.17: Ball and stick representation of the methyl iodide molecule.

6.4.2.3 Effect of initial vibrational excitation energy

Hitherto, the molecule has been assumed to be completely motionless at the very beginning of the trajectory. In reality, the ionization process is likely to form the ion in a variety of vibrational states, populated according to the Franck-Condon principle. Vibrational motion of the atoms *i* may lead to geometrical distortion in the early stages of the Coulomb explosion, potentially resulting in population of different fragmentation channels. Ideally, initial vibrational excitation should therefore be taken into account as part of the initial conditions for the simulation.

In Coulomb explosion experiments on methyl iodide (CH_3I) (Figure 6.17), a number of different Coulomb explosion channels were identified using VMI techniques. A typical channel is $CH_3I^{2+} \rightarrow CH_3{}^+ + I^+$, reported by Wang and co-workers [28] and Corrales and co-workers [29]. Following photoionization, the photon energy (given that number of photons involved is known) can be used to determine the highest accessible vibrational state of the ion, assuming the ion is formed in the electronic ground states. After a normal mode analysis on the +2 molecular ion at the ground state equilibrium geometry, all bound normal modes are given energies equal to the zero-point vibrational energy. The remaining energy is then assigned to the unbound mode coordinates, and initial

velocities for all coordinates are calculated for all atoms. These initial velocities can then be used as initial input data for the trajectory simulations. Interestingly, it is found that when vibrational excitation is not included in the simulation, the molecular ion does not dissociate. However, with vibrational excitation the molecular ion dissociates in the same way as observed experimentally. Figure 6.18 compares the trajectories obtained for Coulomb explosion of CH_3I^{2+} both with and without vibrational excitation.

The molecule vibrates until the C-I bond breaks at around 100 fs. The relatively long Coulomb explosion time appears to be due to the presence of the heavy iodine atom, which hinders the trajectory of the $CH_3{}^+$ fragment, and forces it to find an efficient way to escape the moving direction of iodine atom. The resulting ions are I^+ and $CH_3{}^+$, as observed experimentally by Wang *et al.* [28] and Corrales *et al.* [29].

6.4.2.4 Effect of classical trajectory parameters

The core Matlab function used to propagate the classical trajectories is the ODE solver. For certain ODE problems, a very large number of steps are required in order to describe the problem properly over the complete interval of integration. This can lead either to failure of the integration, or unreasonably long run times. Such problems are termed stiff. Non-stiff solvers, such as ode45, ode23, and ode113, are very slow when applying to a stiff problem. Stiff solvers, such as ode15s and ode23s, are capable of taking much larger steps with improved numerical stability. A summery of common ODE solvers can be found in Table 6.7. Ode45 is capable of handling most ODE problems, and should always be the first solver to start with. For most simulation jobs in the current project, stiffness is not an issue. Hence the ode45 solver is selected for all simulation tasks.

More importantly, the "odeset" command modifies the option structures for the ODE solvers. To control errors during the integration procedures, two odeset parameters need to be specified correctly, namely the relative error tolerance, RelTol, and the absolute error tolerance, AbsTol. RelTol is usually set at its default value of 10^{-3}, which yields

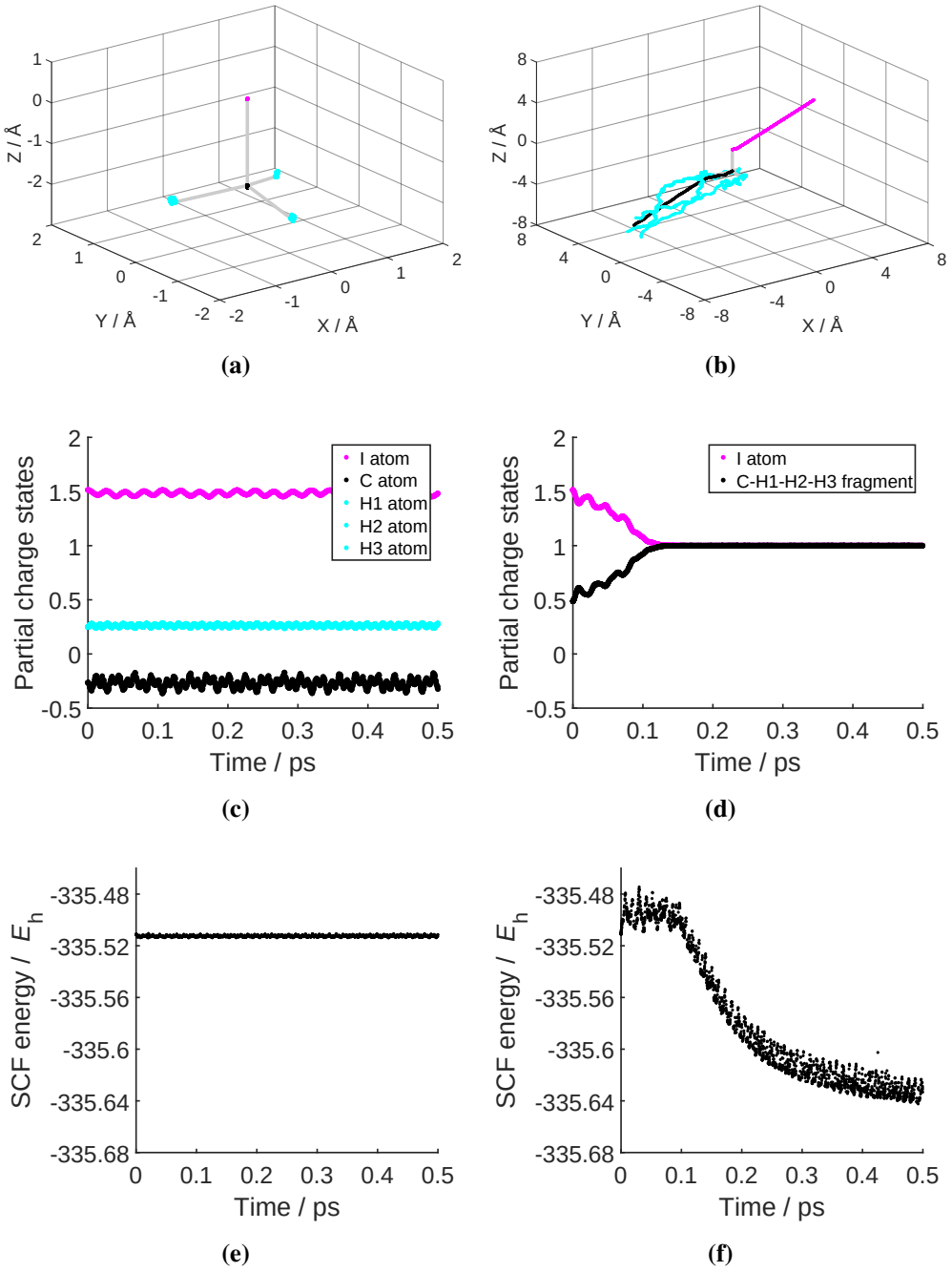


Figure 6.18: Trajectory plots, evolution of partial charge states, and evolution of SCF energy during Coulomb explosion of methyl iodide at z = +2 simulated (a,c,e) without initial vibrational excitation and (b,d,f) with initial vibrational excitation. I, C, and H are respectively colored magenta, black, and cyan in trajectory plots.

Table 6.7: Summary of ODE solvers in Matlab.

Solver	Algorithm	Stiff/non-stiff
ode45	Explicit Runge-Kutta (4,5) formula, the Dormand-Prince pair [80, 81].	Non-stiff
ode23	Explicit Runge-Kutta (2,3) pair of Bogacki and Shampine [81, 82].	Non-stiff
ode113	A variable-step, variable-order (VSVO) Adams-Bashforth-Moulton PECE solver of orders 1 to 13 [81, 83].	Non-stiff
ode15s	A variable-step, variable-order (VSVO) solver based on the numerical differentiation formulas (NDFs) of orders 1 to 5 [81, 84].	Stiff
ode23s	Based on a modified Rosenbrock formula of order 2. The 23 in the name indicates that two simultaneous single-step formulas, one of second order and one of third order, are involved [81].	Stiff

correct solutions up to a tolerance 10^{-3}, i.e. such solutions may have errors in the fourth decimal place. AbsTol controls the error when the solution has very small values. It needs to be specified for each parameter, i.e. for the three position and three velocity components of each atom in the simulation. By considering the very different orders of magnitude of the atomic positions (defined on the Ångström scale) and the atomic velocities (typically several thousand m s^{-1}), geometry components require AbsTol = 10^{-6}, and velocity components may be given AbsTol = 10^{-4}. Both RelTol and AbsTol values will have an effect on the total computational time.

6.4.2.5 Effect of system setup

Due to the nature of the current simulation program, both Matlab and Gaussian must be running in the same environment, ideally Linux, to minimise the time required for the frequent communication between the two packages. In each calculation step, results are saved as a checkpoint file which is then used as the starting point for a subsequent calculation to greatly shorten the total running time. Checkpoint files are used not only between each time step, but also between stability test and force calculation within each time step. Assuming that data communication is efficient and stable, the overwhelming

Table 6.8: Typical values of parameters for current simulation program.

Parameter	Value
Theoretical method	MP2
Basis set	6-311G(d,p) (non-heavy atom containing molecules)
	Def2-TZVP (heavy atom containing molecules)
SCF convergence criterion	10^{-6}
%NProcShared=N	16
%Mem=N	8
ODE solver	ode45
ODE solver option - RelTol	10^{-3}
ODE solver option - AbsTol (geometry)	10^{-6}
ODE solver option - AbsTol (velocity)	10^{-4}
Trajectory time	1 picosecond

majority of the run time corresponds to the Gaussian calculations. Thus, it is advisable to specify the number of processors/cores (%NProcShared=N) and amount of dynamic memory (%Mem=N) in a rational manner. For most jobs performed in the current work, %NProcShared=16 and %Mem=8gb was found to ensure the most efficient use of the system resources.

Gaussian 09 RevD.01 was used for electronic structure calculations. Matlab programs were written and ran on Matlab R2015b (8.6.0.267246). The operating system is Linux 3.10.0-693. Typical values for several key simulation parameters are summarised in Table 6.8.

6.4.3 Limitation and technique issues

The biggest assumption within the current simulation program is that the ion undergoes Coulomb explosion from its ground electronic state even though vibrational excitation may be accounted for, as described in Section 6.4.2.3; electronic excitation is beyond the scope of the current algorithm. Time-dependent density functional theory (TDDFT) could potentially be used to include excited electronic states of the ion in the simulations, and will be investigated in future work.

The total computational time increases with the number of electrons in the system and the level of the model chemistry to be used. Computational time is currently the biggest limitation on the types of system for which simulations can be performed.

In general, although the current chapter aims to identify the optimal setup for simulations on any system, careful investigation and benchmarking is always beneficial when studying a completely new system, particularly when it contains heavy atoms or in a relatively high charge state. Common issues when running Gaussian single point calculations, such as convergence errors, may usually be remedied by adjusting parameters within Gaussian, but the trajectory output parameters should always be checked to make sure they are physically reasonable.

6.5 Summary

A program has been developed to perform *ab initio* trajectory calculations for Coulomb explosions of charged molecules. In the present chapter, we have described testing and benchmarking of the approach for a range of molecular systems. The program incorporates the minimum necessary functionality and offers excellent adaptability and operability. In the following chapter, the program will be used to perform simulations on several different molecules of interest in order to gain insight in to their Coulomb-explosion dynamics.

References

[1] G. Siuzdak. “An Introduction to Mass Spectrometry Ionization: An Excerpt from The Expanding Role of Mass Spectrometry in Biotechnology, 2nd ed.; MCC Press: San Diego, 2005”. In: *Journal of the Association for Laboratory Automation* 9.2 (2004), pp. 50–63.

[2] M. Mann, C. K. Meng, and J. B. Fenn. “Interpreting mass spectra of multiply charged ions”. In: *Analytical Chemistry* 61.15 (1989), pp. 1702–1708.

[3] K. Vékey. “Multiply charged ions”. In: *Mass Spectrometry Reviews* 14.3 (1995), pp. 195–225.

[4] D. Schröder and H. Schwarz. “Generation, Stability, and Reactivity of Small, Multiply Charged Ions in the Gas Phase”. In: *The Journal of Physical Chemistry A* 103.37 (1999), pp. 7385–7394.

[5] S. D. Price and J. Roithová. “Multiply charged ions in the gas phase”. In: *Physical Chemistry Chemical Physics* 13.41 (2011), pp. 18251–18252.

[6] D. K. Böhme. “Multiply-charged ions and interstellar chemistry”. In: *Physical Chemistry Chemical Physics* 13.41 (2011), pp. 18253–18263.

[7] R. Thissen, O. Witasse, O. Dutuit, C. S. Wedlund, G. Gronoff, and J. Lilensten. “Doubly-charged ions in the planetary ionospheres: a review”. In: *Physical Chemistry Chemical Physics* 13.41 (2011), pp. 18264–18287.

[8] T. A. Carlson and R. M. White. “Measurement of the Relative Abundances and Recoil-Energy Spectra of Fragment Ions Produced as the Initial Consequences of X-Ray Interaction with CH_3I, HI, and DI”. In: *The Journal of Chemical Physics* 44.12 (1966), pp. 4510–4520.

[9] T. Yatsuhashi and N. Nakashima. “Multiple ionization and Coulomb explosion of molecules, molecular complexes, clusters and solid surfaces”. In: *Journal of Photochemistry and Photobiology C: Photochemistry Reviews* 34 (2018), pp. 52–84.

[10] Z. Vager, R. Naaman, and E. P. Kanter. “Coulomb Explosion Imaging of Small Molecules”. In: *Science* 244.4903 (1989), pp. 426–431.

[11] P. Herwig, K. Zawatzky, M. Grieser, O. Heber, B. Jordon-Thaden, C. Krantz, O. Novotný, R. Repnow, V. Schurig, D. Schwalm, Z. Vager, A. Wolf, O. Trapp, and H. Kreckel. “Imaging the Absolute Configuration of a Chiral Epoxide in the Gas Phase”. In: *Science* 342.6162 (2013), pp. 1084–1086.

[12] K. Codling and L. J. Frasinski. “Coulomb explosion of simple molecules in intense laser fields”. In: *Contemporary Physics* 35.7 (1994), p. 243.

[13] J. H. Posthumus. “The dynamics of small molecules in intense laser fields”. In: *Reports on Progress in Physics* 67.5 (2004), p. 623.

[14] C. Cornaggia. “Ultrafast Coulomb explosion imaging of molecules”. In: *Laser Physics* 19.8 (2009), pp. 1660–1670.

[15] S. L. Chin and H. Xu. “Tunnel ionization, population trapping, filamentation and applications”. In: *Journal of Physics B: Atomic, Molecular and Optical Physics* 49.22 (2016), p. 222003.

[16] H. Stapelfeldt, E. Constant, and P. B. Corkum. “Wave Packet Structure and Dynamics Measured by Coulomb Explosion”. In: *Physical Review Letters* 74.19 (1995), pp. 3780–3783.

[17] T. Ergler, A. Rudenko, B. Feuerstein, K. Zrost, C. D. Schröter, R. Moshammer, and J. Ullrich. "Spatiotemporal Imaging of Ultrafast Molecular Motion: Collapse and Revival of the D_2^+ Nuclear Wave Packet". In: *Physical Review Letters* 97.19 (2006), p. 193001.

[18] M. Pitzer, M. Kunitski, A. S. Johnson, T. Jahnke, H. Sann, F. Sturm, L. P. H. Schmidt, H. Schmidt-Böcking, R. Dörner, J. Stohner, J. Kiedrowski, M. Reggelin, S. Marquardt, A. Schießer, R. Berger, and M. S. Schöffler. "Direct Determination of Absolute Molecular Stereochemistry in Gas Phase by Coulomb Explosion Imaging". In: *Science* 341.6150 (2013), pp. 1096–1100.

[19] C. S. Slater, S. Blake, M. Brouard, A. Lauer, C. Vallance, J. J. John, R. Turchetta, A. Nomerotski, L. Christensen, J. H. Nielsen, M. P. Johansson, and H. Stapelfeldt. "Covariance imaging experiments using a pixel-imaging mass-spectrometry camera". In: *Physical Review A* 89.1 (2014), p. 011401.

[20] C. S. Slater, S. Blake, M. Brouard, A. Lauer, C. Vallance, C. S. Bohun, L. Christensen, J. H. Nielsen, M. P. Johansson, and H. Stapelfeldt. "Coulomb-explosion imaging using a pixel-imaging mass-spectrometry camera". In: *Physical Review A* 91.5 (2015), p. 053424.

[21] C. Vallance, M. Brouard, A. Lauer, C. S. Slater, E. Halford, B. Winter, S. J. King, J. W. L. Lee, D. E. Pooley, I. Sedgwick, R. Turchetta, A. Nomerotski, J. J. John, and L. Hill. "Fast sensors for time-of-flight imaging applications". In: *Physical Chemistry Chemical Physics* 16.2 (2014), pp. 383–395.

[22] *PImMS website*. http://pimms.chem.ox.ac.uk.

[23] A. T. J. B. Eppink and D. H. Parker. "Velocity map imaging of ions and electrons using electrostatic lenses: Application in photoelectron and photofragment ion imaging of molecular oxygen". In: *Review of Scientific Instruments* 68.9 (1997), pp. 3477–3484.

[24] D. W. Chandler and P. L. Houston. "Two-dimensional imaging of state-selected photodissociation products detected by multiphoton ionization". In: *The Journal of Chemical Physics* 87.2 (1987), pp. 1445–1447.

[25] L. Poth and A. W. Castleman. "Molecular dynamics simulation of Coulomb explosion processes". In: *Journal of Physical Chemistry A* 102.23 (1998), pp. 4075–4081.

[26] I. Last, I. Schek, and J. Jortner. "Energetics and dynamics of Coulomb explosion of highly charged clusters". In: *The Journal of Chemical Physics* 107.17 (1997), pp. 6685–6692.

[27] E. M. Bringa. "Molecular dynamics simulations of Coulomb explosion". In: *Nuclear Instruments and Methods in Physics Research Section B: Beam Interactions with Materials and Atoms* 209 (2003), pp. 1–8.

[28] Y. Wang, S. Zhang, Z. Wei, and B. Zhang. "Velocity Map Imaging of Dissociative Ionization and Coulomb Explosion of CH_3I Induced by a Femtosecond Laser". In: *The Journal of Physical Chemistry A* 112.17 (2008), pp. 3846–3851.

[29] M. E. Corrales, G. Gitzinger, J. González-Vázquez, V. Loriot, R. de Nalda, and L. Bañares. "Velocity Map Imaging and Theoretical Study of the Coulomb Explosion of CH_3I under Intense Femtosecond IR Pulses". In: *The Journal of Physical Chemistry A* 116.11 (2012), pp. 2669–2677.

[30] R. A. Friesner. "*Ab initio* quantum chemistry: Methodology and applications". In: *Proceedings of the National Academy of Sciences of the United States of America* 102.19 (2005), p. 6648.

[31] M. Ben-Nun and T. J. Martínez. "*Ab initio* Quantum Molecular Dynamics". In: *Advances in Chemical Physics* (2002).

[32] D. Marx and J. Hutter. "*Ab initio* Molecular Dynamics: Theory and Implementation". In: *Modern Methods and Algorithms of Quantum Chemistry*. Ed. by J. Grotendorst. Jülich, Germany: John von Neumann Institute for Computing, 2000, p. 329.

[33] C. Leforestier. "Classical trajectories using the full *ab initio* potential energy surface H^- + $CH_4 \rightarrow CH_4 + H^-$". In: *The Journal of Chemical Physics* 68.10 (1978), pp. 4406–4410.

[34] T. N. Truong. "A direct *ab initio* dynamics approach for calculating thermal rate constants using variational transition state theory and multidimensional semiclassical tunneling methods. An application to the $CH_4 + H \leftrightarrow CH_3 + H_2$ reaction". In: *The Journal of Chemical Physics* 100.11 (1994), pp. 8014–8025.

[35] *Physics and Astronomy Classification Scheme (PACS)*. http://publish.aps.org/PACS.

[36] H. Hartung, B. Fricke, T. Morović, W. D. Sepp, and A. Rosén. "An ab-initio calculation of the Coulomb explosion of N_2 after heavy-ion bombardment". In: *Physics Letters A* 69.2 (1978), pp. 87–89.

[37] R. Euler, B. Fricke, T. Morović, W. D. Sepp, and A. Rosén. "An attempt on the calculation of relativistic potential energy curves: Noble gas difluorides". In: *Zeitschrift für Physik A Atoms and Nuclei* 297.2 (1980), pp. 101–104.

[38] Y. Chang, C. Minichino, and W. H. Miller. "Classical trajectory studies of the molecular dissociation dynamics of formaldehyde: $H_2CO \rightarrow H_2 + CO$". In: *The Journal of Chemical Physics* 96.6 (1992), pp. 4341–4355.

[39] W. Chen, W. L. Hase, and H. B. Schlegel. "*Ab initio* classical trajectory study of $H_2CO \rightarrow H_2 + CO$ dissociation". In: *Chemical Physics Letters* 228.4 (1994), pp. 436–442.

[40] S. Anand and H. B. Schlegel. "Unimolecular dissociation of formyl halides $HXCO \rightarrow CO + HX$ (X = F, Cl): An *ab initio* direct classical trajectory study". In: *Journal of Physical Chemistry A* 106.47 (2002), pp. 11623–11629.

[41] L. P. Sun and W. L. Hase. "*Ab initio* direct dynamics trajectory simulation of $C_2H_5F \rightarrow C_2H_4 + HF$ product energy partitioning". In: *Journal of Chemical Physics* 121.18 (2004), pp. 8831–8845.

[42] T. Taketsugu, A. Tajima, K. Ishii, and T. Hirano. "*Ab initio* direct trajectory simulation with nonadiabatic transitions of the dissociative recombination reaction $HCNH + e^- \rightarrow$ HNC/HCN + H". In: *Astrophysical Journal* 608.1 (2004), pp. 323–329.

[43] J. Zhou and H. B. Schlegel. "*Ab initio* Classical Trajectory Study of the Dissociation of Neutral and Positively Charged Methanimine (CH_2NH^{n+} n = 0-2)". In: *The Journal of Physical Chemistry A* 113.37 (2009), pp. 9958–9964.

[44] M. J. Frisch, G. W. Trucks, H. B. Schlegel, G. E. Scuseria, M. A. Robb, J. R. Cheeseman, G. Scalmani, V. Barone, G. A. Petersson, H. Nakatsuji, X. Li, M. Caricato, A. V. Marenich, J. Bloino, B. G. Janesko, R. Gomperts, B. Mennucci, H. P. Hratchian, J. V. Ortiz, A. F. Izmaylov, J. L. Sonnenberg, Williams, F. Ding, F. Lipparini, F. Egidi, J. Goings, B. Peng, A. Petrone, T. Henderson, D. Ranasinghe, V. G. Zakrzewski, J. Gao, N. Rega, G. Zheng, W. Liang, M. Hada, M. Ehara, K. Toyota, R. Fukuda, J. Hasegawa, M. Ishida, T. Nakajima, Y. Honda, O. Kitao, H. Nakai, T. Vreven, K. Throssell, J. A. Montgomery Jr., J. E. Peralta, F. Ogliaro, M. J. Bearpark, J. J. Heyd, E. N. Brothers, K. N. Kudin, V. N. Staroverov, T. A. Keith, R. Kobayashi, J. Normand, K. Raghavachari, A. P. Rendell,

J. C. Burant, S. S. Iyengar, J. Tomasi, M. Cossi, J. M. Millam, M. Klene, C. Adamo, R. Cammi, J. W. Ochterski, R. L. Martin, K. Morokuma, O. Farkas, J. B. Foresman, and D. J. Fox. *Gaussian 09 Revision D.01*. Gaussian Inc. Wallingford, CT. 2016.

[45] H. J. Werner, P. J. Knowles, G. Knizia, F. R. Manby, and M. Schtz. "Molpro: a general-purpose quantum chemistry program package". In: *Wiley Interdisciplinary Reviews: Computational Molecular Science* 2 (2012), pp. 242–253.

[46] *CPMD*. http://cpmd.org.

[47] *CP2K*. https://www.cp2k.org.

[48] M. Valiev, E. J. Bylaska, N. Govind, K. Kowalski, T. P. Straatsma, H. J. J. Van Dam, D. Wang, J. Nieplocha, E. Apra, T. L. Windus, and W. A. de Jong. "NWChem: A comprehensive and scalable open-source solution for large scale molecular simulations". In: *Computer Physics Communications* 181.9 (2010), pp. 1477–1489.

[49] L. Christensen, J. H. Nielsen, C. B. Brandt, C. B. Madsen, L. B. Madsen, C. S. Slater, A. Lauer, M. Brouard, M. P. Johansson, B. Shepperson, and H. Stapelfeldt. "Dynamic Stark Control of Torsional Motion by a Pair of Laser Pulses". In: *Physical Review Letters* 113.7 (2014), p. 073005.

[50] K. B. Wiberg. "Application of the pople-santry-segal CNDO method to the cyclopropylcarbinyl and cyclobutyl cation and to bicyclobutane". In: *Tetrahedron* 24.3 (1968), pp. 1083–1096.

[51] J. P. Foster and F. Weinhold. "Natural hybrid orbitals". In: *Journal of the American Chemical Society* 102.24 (1980), pp. 7211–7218.

[52] C. C. J. Roothaan. "New Developments in Molecular Orbital Theory". In: *Reviews of Modern Physics* 23.2 (1951), pp. 69–89.

[53] C. Møller and M. S. Plesset. "Note on an Approximation Treatment for Many-Electron Systems". In: *Phys. Rev.* 46.7 (1934), pp. 618–622.

[54] R. J. Bartlett and G. D. Purvis. "Many-body perturbation theory, coupled-pair many-electron theory, and the importance of quadruple excitations for the correlation problem". In: *International Journal of Quantum Chemistry* 14.5 (1978), pp. 561–581.

[55] R. Seeger and J. A. Pople. "Self-consistent molecular orbital methods. XVIII. Constraints and stability in Hartree–Fock theory". In: *The Journal of Chemical Physics* 66.7 (1977), pp. 3045–3050.

[56] R. Bauernschmitt and R. Ahlrichs. "Stability analysis for solutions of the closed shell Kohn–Sham equation". In: *The Journal of Chemical Physics* 104.22 (1996), pp. 9047–9052.

[57] U. C. Singh and P. A. Kollman. "An approach to computing electrostatic charges for molecules". In: *Journal of Computational Chemistry* 5.2 (1984), pp. 129–145.

[58] B. H. Besler, K. M. Merz Jr., and P. A. Kollman. "Atomic charges derived from semiempirical methods". In: *Journal of Computational Chemistry* 11.4 (1990), pp. 431–439.

[59] F. L. Hirshfeld. "Bonded-atom fragments for describing molecular charge densities". In: *Theoretica Chimica Acta* 44.2 (1977), pp. 129–138.

[60] *Gaussian 16 IOps Reference*. http://gaussian.com/overlay6/#iop_(6/76).

[61] J. B. Foresman and Æ. Frisch. *Exploring Chemistry with Electronic Structure Methods*. Wallingford, CT: Gaussian, Inc., 2015.

[62] J. A. Pople, M. Head-Gordon, and K. Raghavachari. "Quadratic configuration interaction. A general technique for determining electron correlation energies". In: *The Journal of Chemical Physics* 87.10 (1987), pp. 5968–5975.

[63] D. Cremer. "Møller–Plesset perturbation theory: from small molecule methods to methods for thousands of atoms". In: *Wiley Interdisciplinary Reviews: Computational Molecular Science* 1.4 (2011), pp. 509–530.

[64] P. Hohenberg and W. Kohn. "Inhomogeneous Electron Gas". In: *Physical Review* 136.3B (1964), B864–B871.

[65] R. G. Parr and W. Yang. *Density-Functional Theory of Atoms and Molecules*. International Series of Monographs on Chemistry. Oxford: Oxford University Press, 1994.

[66] F. Jensen. "Atomic orbital basis sets". In: *Wiley Interdisciplinary Reviews: Computational Molecular Science* 3.3 (2012), pp. 273–295.

[67] F. Weigend and R. Ahlrichs. "Balanced basis sets of split valence, triple zeta valence and quadruple zeta valence quality for H to Rn: Design and assessment of accuracy". In: *Physical Chemistry Chemical Physics* 7.18 (2005), pp. 3297–3305.

[68] F. Weigend. "Accurate Coulomb-fitting basis sets for H to Rn". In: *Physical Chemistry Chemical Physics* 8.9 (2006), pp. 1057–1065.

[69] T. H. Dunning Jr. "Gaussian basis sets for use in correlated molecular calculations. I. The atoms boron through neon and hydrogen". In: *The Journal of Chemical Physics* 90.2 (1989), pp. 1007–1023.

[70] R. A. Kendall, T. H. Dunning Jr., and R. J. Harrison. "Electron affinities of the first-row atoms revisited. Systematic basis sets and wave functions". In: *The Journal of Chemical Physics* 96.9 (1992), pp. 6796–6806.

[71] D. E. Woon and T. H. Dunning Jr. "Gaussian basis sets for use in correlated molecular calculations. III. The atoms aluminum through argon". In: *The Journal of Chemical Physics* 98.2 (1993), pp. 1358–1371.

[72] D. Feller. "The role of databases in support of computational chemistry calculations". In: *Journal of Computational Chemistry* 17.13 (1996), pp. 1571–1586.

[73] K. L. Schuchardt, B. T. Didier, T. Elsethagen, L. Sun, V. Gurumoorthi, J. Chase, J. Li, and T. L. Windus. "Basis Set Exchange: A Community Database for Computational Sciences". In: *Journal of Chemical Information and Modeling* 47.3 (2007), pp. 1045–1052.

[74] C. Lee, W. Yang, and R. G. Parr. "Development of the Colle-Salvetti correlation-energy formula into a functional of the electron density". In: *Physical Review B* 37.2 (1988), pp. 785–789.

[75] A. D. Becke. "Density-functional thermochemistry. III. The role of exact exchange". In: *The Journal of Chemical Physics* 98.7 (1993), pp. 5648–5652.

[76] P. Herwig, K. Zawatzky, D. Schwalm, M. Grieser, O. Heber, B. Jordon-Thaden, C. Krantz, O. Novotný, R. Repnow, V. Schurig, Z. Vager, A. Wolf, O. Trapp, and H. Kreckel. "Absolute configuration assignment of a chiral molecule in the gas phase using foil-induced Coulomb explosion imaging". In: *Physical Review A* 90.5 (2014), p. 052503.

[77] R. Wester, F. Albrecht, M. Grieser, L. Knoll, R. Repnow, D. Schwalm, A. Wolf, A. Baer, J. Levin, Z. Vager, and D. Zajfman. “Coulomb explosion imaging at the heavy ion storage ring TSR”. In: *Nuclear Instruments and Methods in Physics Research Section A: Accelerators, Spectrometers, Detectors and Associated Equipment* 413.2 (1998), pp. 379–396.

[78] T. Zhang, C. Y. Ng, F. Qi, C. S. Lam, and W. K. Li. “A 193nm laser photofragmentation time-of-flight mass spectrometric study of chloroiodomethane”. In: *The Journal of Chemical Physics* 123.17 (2005), p. 174316.

[79] M. L. Murillo-Sánchez, S. Marggi Poullain, J. González-Vázquez, M. E. Corrales, G. Balerdi, and L. Bañares. “Femtosecond photodissociation dynamics of chloroiodomethane in the first absorption band”. In: *Chemical Physics Letters* 683 (2017), pp. 22–28.

[80] J. R. Dormand and P. J. Prince. “A family of embedded Runge-Kutta formulae”. In: *Journal of Computational and Applied Mathematics* 6.1 (1980), pp. 19–26.

[81] L. F. Shampine and M. W. Reichelt. “The MATLAB ODE Suite”. In: *SIAM Journal on Scientific Computing* 18.1 (1997), pp. 1–22.

[82] P. Bogacki and L. F. Shampine. “A 3(2) pair of Runge - Kutta formulas”. In: *Applied Mathematics Letters* 2.4 (1989), pp. 321–325.

[83] L. F. Shampine and M. K. Gordon. *Computer Solutions of Ordinary Differential Equations: The Initial Value Problem*. San Francisco, CA: W. H. Freeman, 1975.

[84] L. F. Shampine, M. W. Reichelt, and J. A. Kierzenka. “Solving Index-1 DAEs in MATLAB and Simulink”. In: *SIAM Review* 41 (1999), pp. 538–552.

7

Coulomb explosion simulation of small organic molecules

Contents

7.1 Introduction **181**
7.2 Simulated outcome as a function of initial parent ion charge states **182**
7.2.1 Formyl chloride (HClCO) 183
7.2.2 *cis*-1,2-dichloroethene ($C_2H_2Cl_2$) 188
7.2.3 Fluoromethane (CH_3F) 199
7.2.4 Chloroiodomethane (CH_2ICl) 207
7.3 Simulation of Velocity-Map Imaging experimental data **215**
7.3.1 3,5-dibromo-3',5'-difluoro-4'-cyanobiphenyl (DBrDFCNBph) . 215
7.4 Conclusion and future work **229**
References **236**

7.1 Introduction

Following the development, benchmarking, and optimisation of the Coulomb explosion simulation program as introduced in Chapter 6, simulations on a series of small organic molecules of interests to the reaction dynamics community will be presented in this chapter. Outcomes that are related to experimental measurements will be investigated, as

well as features that may not be directly observable through experiments.

The simulation program, in contrast to experiments, provides the ability to specify the charge state of the parent ions to be studied. This allows us to run simulations for a wide range of parent ion charge states in order to explore relationships between the initial charge state and the Coulomb explosion dynamics in a systematic way. Simulations on a number of halo-substituted formaldehyde, ethene, and methane analogues are simulated in order to address this question, and the results are presented in Section 7.2.

One of the original aims of developing the simulation program was to provide theoretical support for VMI experiments, and to compare the results with existing Coulomb explosion simulation approaches. In Section 7.3, we present simulations on the DBrDFCNBph molecule, first introduced in Chapter 6, to compare with experimental data and with the predictions of purely classical simulations.

For all simulation work presented in this chapter, the optimised parameters given in Table 6.8 are used. The trajectory time is set to 500 fs for all molecules except for DBrDFCNBph, where 2 ps was found to be a more appropriate choice. Program codes can be found in Appendix E.

7.2 Simulated outcome as a function of initial parent ion charge states

For the following small halo-substituted organic molecules, simulations were performed for selected initial charge states (z) from +2 to up to +30, with the range chosen depending on the number of electrons possessed by the neutral molecule. Simulated data recorded at each time step included trajectory time, atomic partial charges, interatomic forces in Cartesian coordinates, atomic positions in Cartesian coordinates, velocities in Cartesian coordinates, Wiberg bond indices between any two atoms, and the energy of the system. Magnitudes of forces and velocities are calculated.

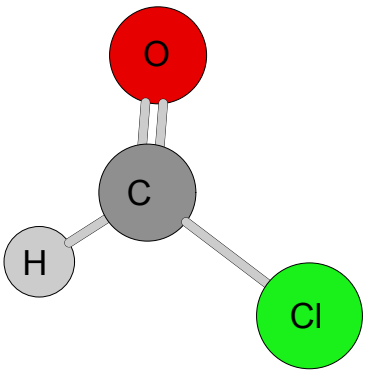


Figure 7.1: Ball and stick representation of the formyl chloride molecule.

7.2.1 Formyl chloride (HClCO)

Formyl chloride (HClCO) (Figure 7.1), a chlorine-substituted analogue of formaldehyde H_2CO, is a typical intermediate product in the degradation of atmospheric hydrochlorofluorocarbons (HCFCs). Due to their contribution to lower stratosphere ozone depletion, photodissociation processes of chlorinated molecules such as HClCO are of great interest [1, 2], and have been the subject of several *ab initio* studies [3–5].

The current *ab initio* classical trajectory simulations on HClCO aim to explore the factors that affect the terminal velocities and terminal atomic partial charges following a Coulomb explosion. The simulations were performed for charge states ranging from +2 to +22. The forces at each time step were calculated at the MP2/6-311G(d,p) [6, 7] level of theory, and the simulations were run for a total trajectory time of 500 ps.

7.2.1.1 Partial charge and Wiberg bond index evolution

Since the Cartesian coordinates of each atom are recorded throughout the trajectory, the fragmentation channels may be easily visualised. Examples for the two extreme charge states, +2 and +22, are shown in Figure 7.2. For the +2 charge state, the atoms vibrate around their equilibrium positions, but bond breaking does not occur as there is simply not enough energy available. In contrast, the +22 charge state undergoes rapid and complete Coulomb explosion into atomic fragments.

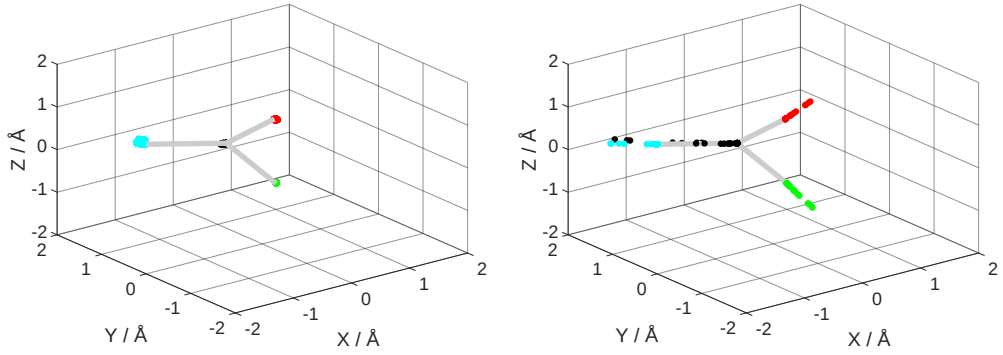


Figure 7.2: Trajectories of atoms of HClCO during Coulomb explosion at $z = +2$ and (b) $z = +22$. O, H, C, and Cl are respectively colored red, cyan, black, and green.

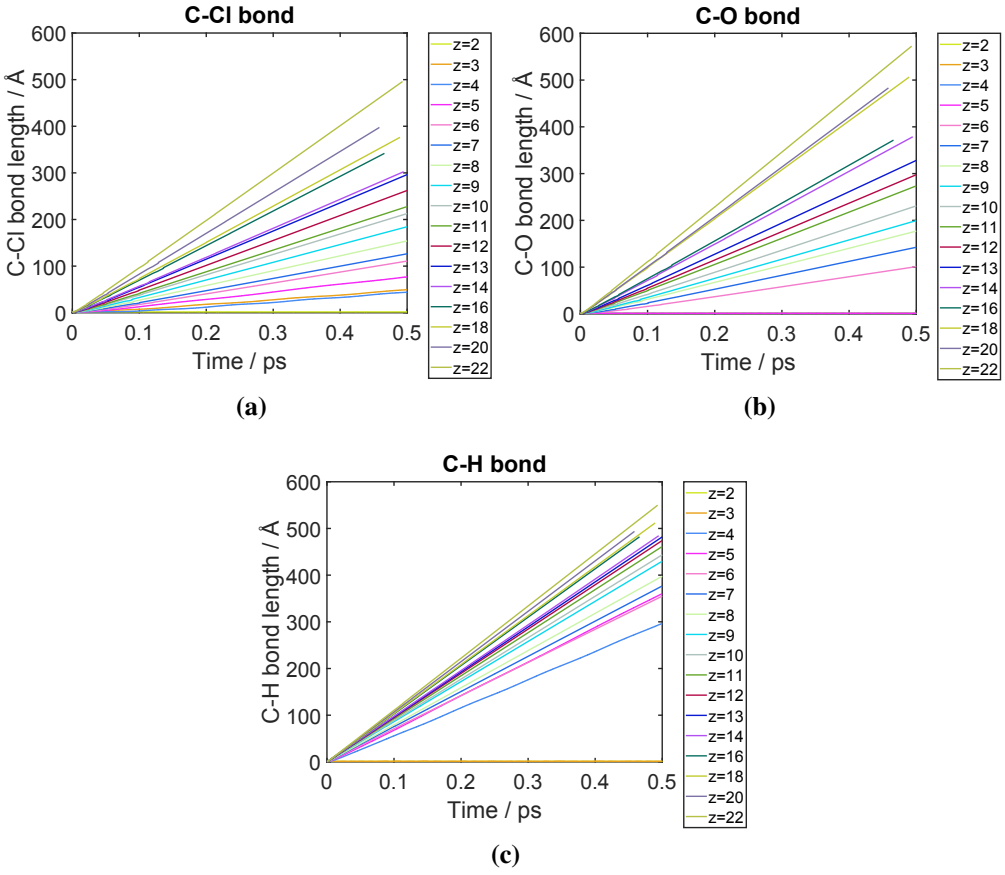


Figure 7.3: Evolution of bond lengths during Coulomb explosion of HClCO at $z = +2$ to $z = +22$ for (a) C-Cl bond, (b) C-O bond, and (c) C-H bond. Note that missing data are due to early termination of simulation at some charge states.

We can also investigate the evolution of chosen bond lengths as a function of initial charge state, as shown in Figure 7.3. When z = +2, all three bond lengths remain unchanged. For z = +3, the C-Cl bond increases from 1.77 Å at t = 0 fs to 49.44 Å at t = 500 fs, indicating C-Cl bond breakage, while the other two bonds, i.e. C-O and C-H, hardly change in length at all. Thus, there are two fragment ions, Cl^+ and HCO^{2+}. As the initial charge increases, so does the degree of fragmentation. For z = +4 and +5, it is evident that both the C-H and the C-Cl bonds break, resulting in three fragment ions, Cl^{2+}, H^+, and CO^+ when z = +4, and Cl^{2+}, H^+, and CO^{2+} when z = +5. For z $\geq$ +6, all three bond lengths increase with time, corresponding to complete Coulomb explosion into atomic ions.

Bond breakage can also be inferred by examining chemical information such as partial charge states and Wiberg bond index. Figure 7.4 plots the evolution of the atomic charges for all four atoms of HClCO. After Coulomb explosion, each atom or molecular fragment has an integer charge. In the case of a molecular fragment, though the total charge reaches a constant value, the time evolution of the charges on the constituent atoms can be quite complex. The overall charges on molecular fragments as a function of time, when z = +3, +4, and +5, are plotted in Figure 7.6. An even more obvious illustration is the Wiberg bond index evolution curve as shown in Figure 7.5 (and Figure 7.6 bottom row for molecular fragments), where a zero Wiberg bond index corresponds to bond breakage and a non-zero index implies an intact bond. For example, the C-H bond survives when z = +2 or +3, but not for higher charge states.

There is very good correspondence between the times at which the Wiberg bond index reaches zero and the fragment charges reach their final integer values. We note that the C-H bond breaks much faster than the C-Cl and C-O bonds, a consequence of the very light mass of H^+ leading to a very high velocity for the departing atom in the early stages of the Coulomb explosion.

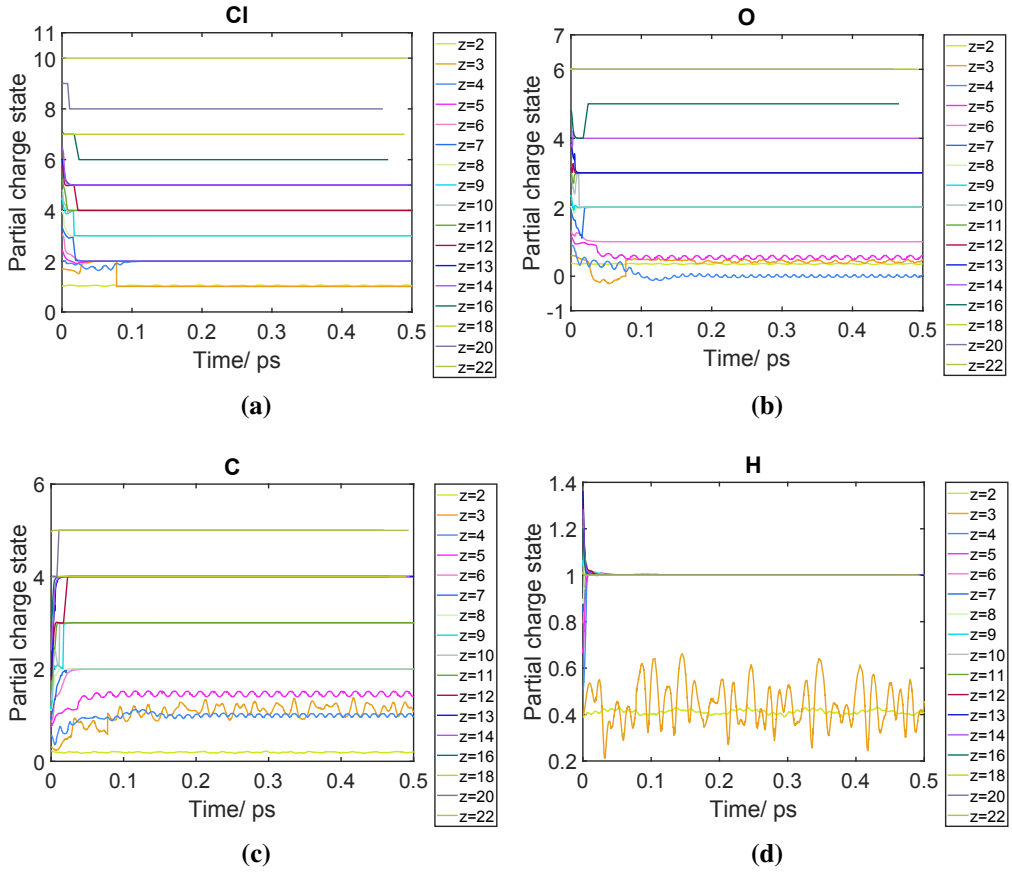


Figure 7.4: Evolution of atomic charges during Coulomb explosion of HClCO at z = +2 to z = +22 for (a) Cl, (b) O, (c) C, and (d) H. Note that missing data are due to early termination of simulation at some charge states.

7.2.1.2 Velocity evolution

Figure 7.7 shows the atomic velocities as a function of time for the four constituent atoms of HClCO in various initial charge states. In most cases, the velocities approach their asymptotic values well before 50 fs, in good agreement with the charge evolution (Figure 7.4) and Wiberg bond index evolution (Figure 7.5). The oscillating nature of the atomic velocities for low initial charge states reflects the formation of molecular fragments. As an illustrative example, Figure 7.8 compares the fragment velocity evolution of HClCO (z = +4) when considering all atoms individually and when treating CO^+ as a molecular fragment and plotting the velocity of its centre of mass. The higher velocity of CO^+ compared with the Cl^{2+} atomic ion reflects their small difference in mass

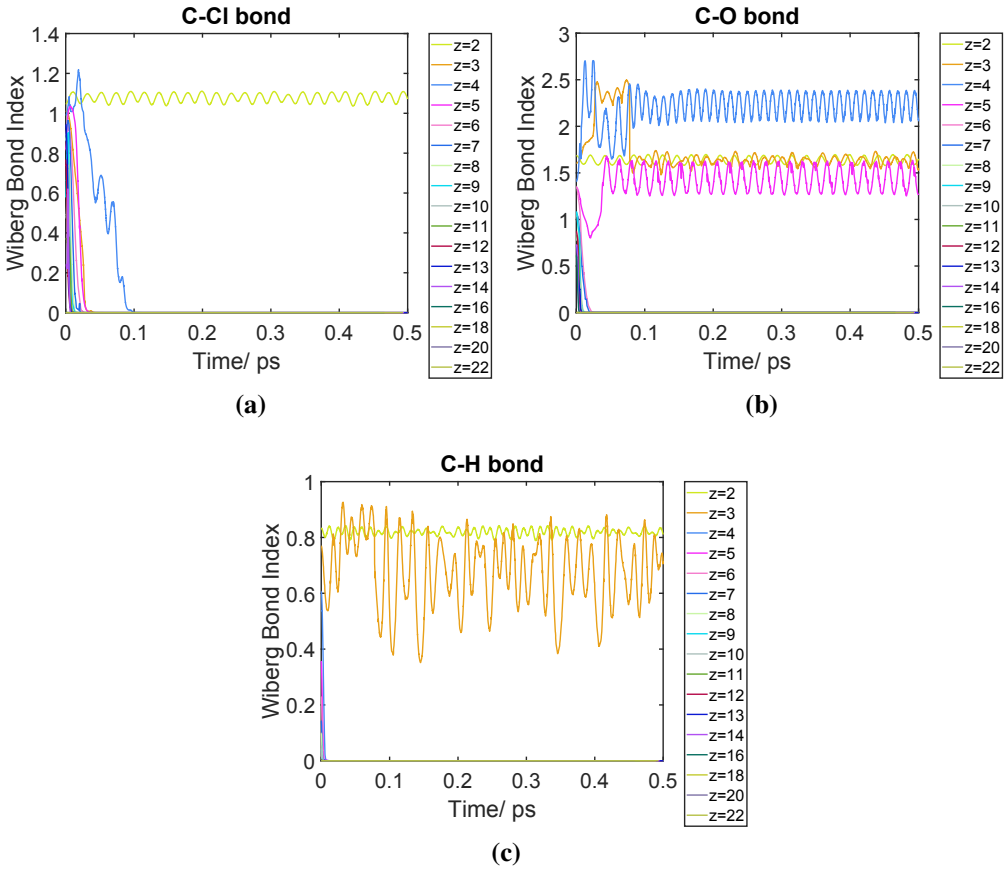


Figure 7.5: Evolution of Wiberg bond index during Coulomb explosion of HClCO at z = +2 to z = +22 for (a) C-Cl bond, (b) C-O bond, and (c) C-H bond. Note that missing data are due to early termination of simulation at some charge states.

(Cl: 35 u and C-O: 28 u).

7.2.1.3 Terminal velocity

The Coulomb explosion fragments reach their terminal velocities once their separations are large enough for the interatomic forces to have reduced essentially to zero. As expected, there is a strong correlation between the atomic terminal velocities and the initial charge on the parent ion. This correlation is shown in Figure 7.9. The detailed shapes of the curves depend on a variety of factors, including the fragment masses, the initial geometry of the molecule, and the evolution of the fragment charges during the dissociation. The time taken for each fragment to reach its respective terminal velocity (defined as the time at which the fragment is within 1% of its asymptotic velocity) is

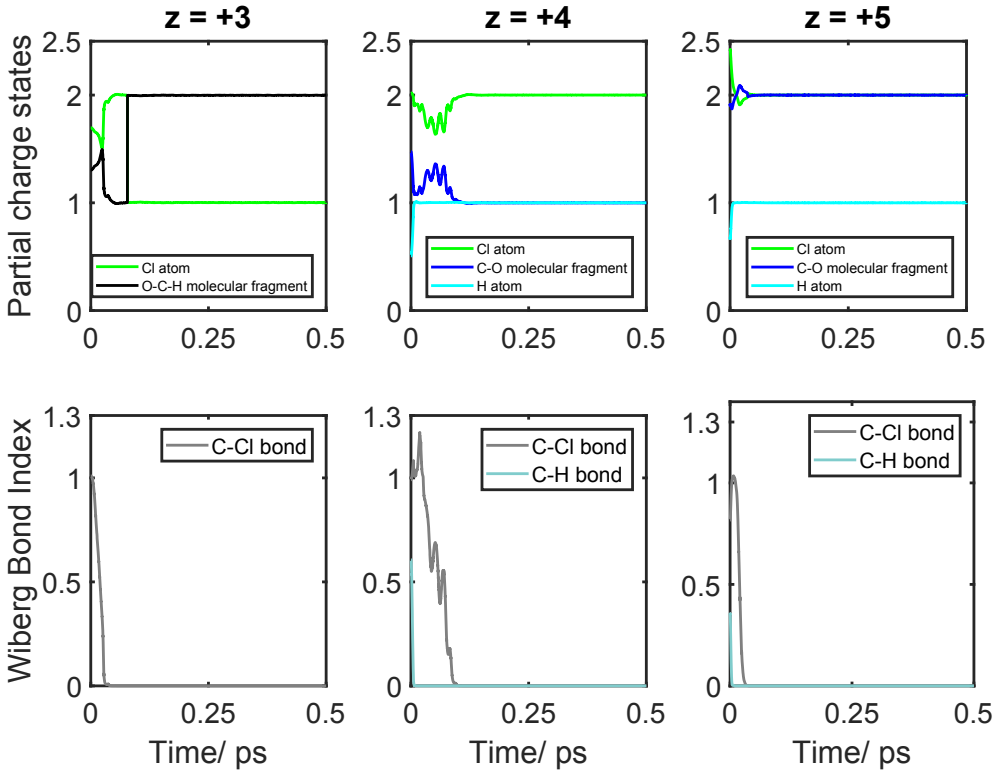


Figure 7.6: Evolution of partial charges (top) and Wiberg bond indices (bottom) of atoms and molecular fragments during Coulomb explosion of HClCO at (a) z = +3, (b) z = +4, and (c) z = +5.

shown as a function of initial charge state in Figure 7.10.

7.2.2 *cis*-1,2-dichloroethene ($C_2H_2Cl_2$)

cis-1,2-dichloroethene is one of three structural isomers of dichloroethene ($C_2H_2Cl_2$), the other two being 1,1-dichloroethene and *trans*-1,2-dichloroethene. Both *cis*-1,2-dichloroethene and *trans*-1,2-dichloroethene are ideal systems for investigating Coulomb explosion processes initiated by an intense laser field, and offer the opportunity to use the resulting fragment angular distributions to identify which structural isomer(s) is(are) present [8].

Ab initio classical trajectory simulations on *cis*-1,2-dichloroethene will provide data to compare with our results from simulations on HClCO, as well as for comparison

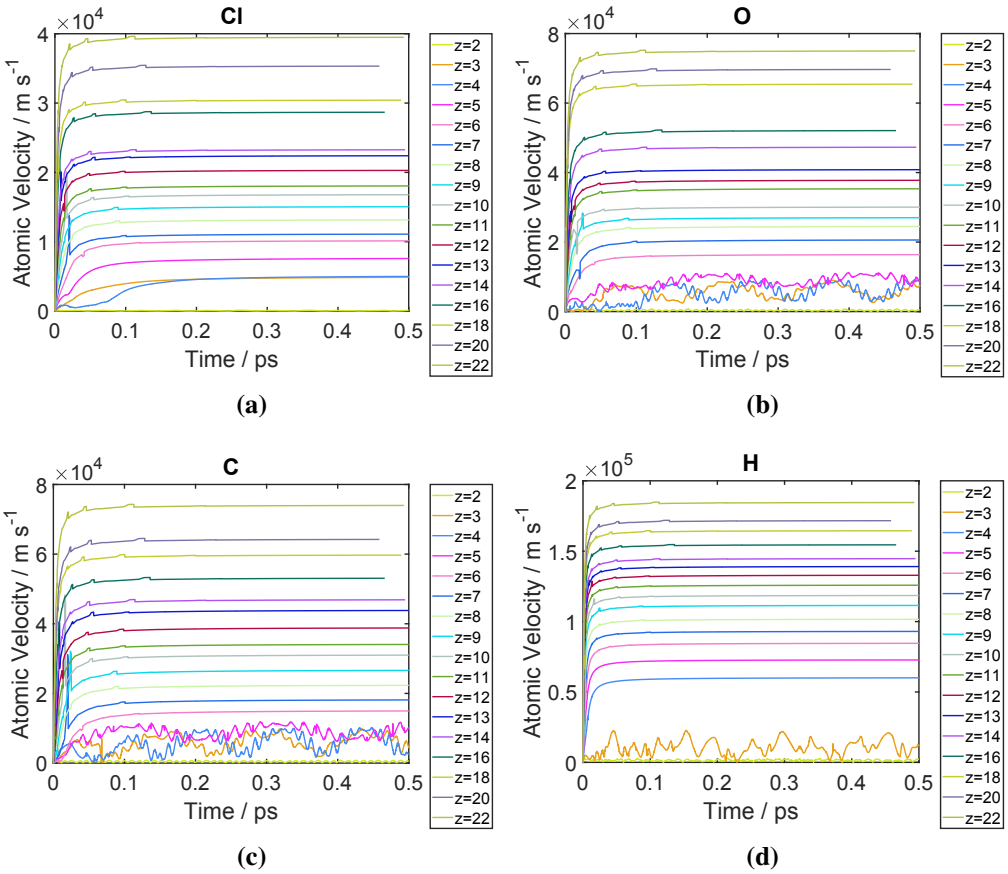


Figure 7.7: Evolution of atomic velocities during Coulomb explosion of HClCO at z = +2 to z = +22 for (a) Cl, (b) O, (c) C, and (d) H. Note that missing data are due to early termination of simulation at some charge states.

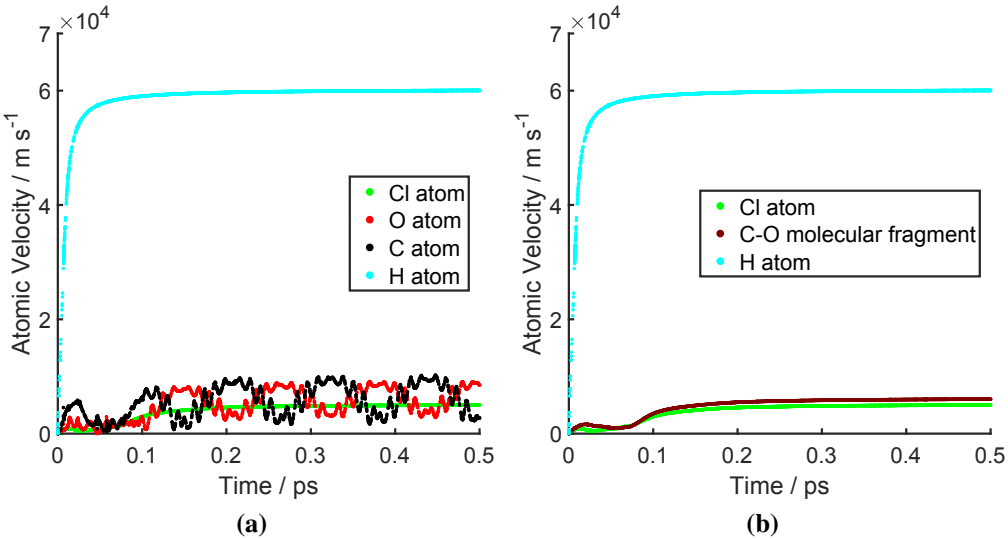


Figure 7.8: Evolution of velocities of atoms and molecular fragments during Coulomb explosion of HClCO at z = +4. (a) Individual atoms. (b) Cl and H atoms with CO^+ treated as a molecular fragment rather than individual atoms.

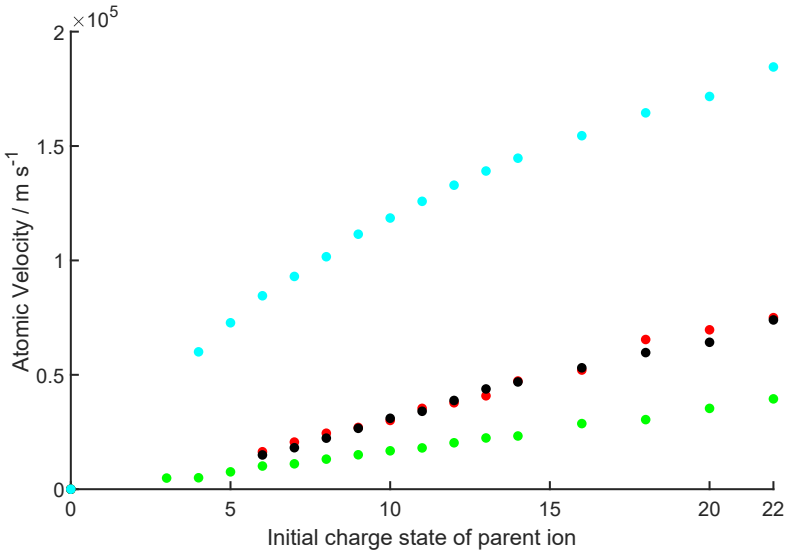


Figure 7.9: Atomic terminal velocity as a function of initial charge state of parent ion of HClCO. O, H, C, and Cl are respectively colored red, cyan, black, and green.

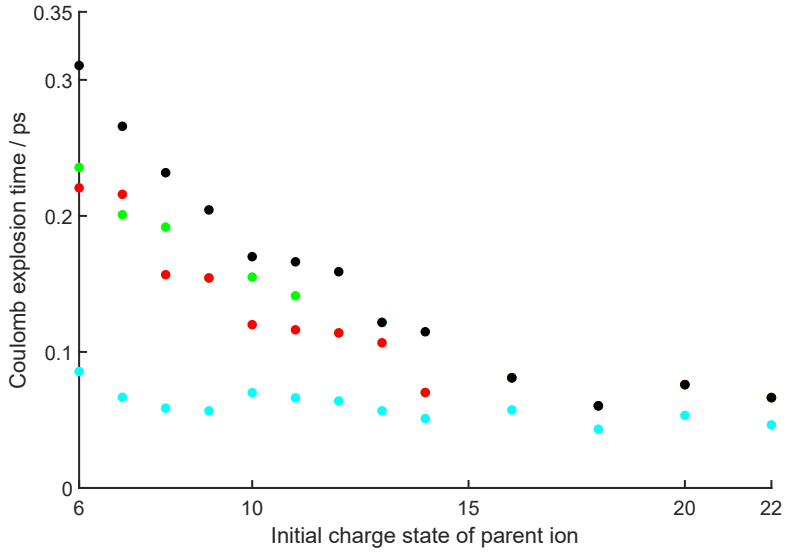


Figure 7.10: Relationship between Coulomb explosion time (defined as the time at which the fragment is within 1% of its asymptotic velocity) and initial charge state of parent ion of HClCO. O, H, C, and Cl are respectively colored red, cyan, black, and green. Note that chlorine and Oxygen at z $\geq$ +16 are overlapped with Carbon; Chlorine at z = +14 and +12 is overlapped with Oxygen; Chlorine at z = +13 is overlapped with Carbon.

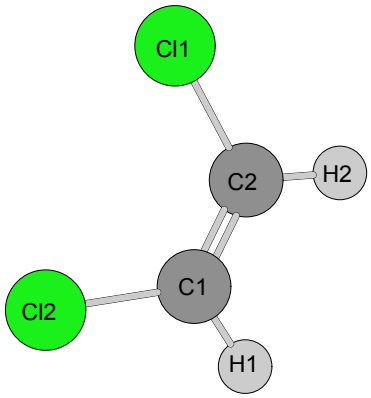


Figure 7.11: Ball and stick representation of the *cis*-1,2-dichloroethene molecule. Note the unconventional naming of the two chlorine atoms.

with experimental work [9] [1]. Simulations were performed for initial charge states from +2 to +22, with forces calculated at the MP2/6-311G(d,p) [6, 7] level of theory, and simulations running for 500 ps. The molecular configuration and numbering of atoms are depicted in Figure 7.11.

7.2.2.1 Fragment charge and Wiberg bond index evolution

As introduced in Section 7.2.1, observing the evolution of atomic distances is the first and most efficient way to work out the preferred fragmentation channels for each total charge state. It is usually sufficient simply to compare the initial (t = 0 fs) and final (t = 500 fs) atomic distances to determine whether or not a particular bond breaks during the Coulomb explosion. These are tabulated in Table 7.1. A bond is generally considered to be intact if the distance is less than 2 Å, with higher values indicating bond cleavage. This allows us to generate a schematic diagram of the fragmentation channels for each initial charge state, illustrated in Figure 7.12. The C=C double bond starts to break when the total charge state is as low as +3, while full Coulomb explosion is achieved at z = +8 or higher.

Similarly, instead of plotting partial charge evolution curves, the fragmentation channels

[1] Although this paper studied *cis*/*trans*-1,2-dibromoethene, qualitative comparison to *cis*-1,2-dichloroethene can still be made. The choice of *cis*-1,2-dichloroethene in current simulation is due to the smaller number of electrons that chlorine atom possesses compared to bromine, which significantly reduces computational time.

Table 7.1: Atomic separations in *cis*-1,2-dichloroethene at t = 0 fs and t = 500 fs during Coulomb explosion at z = +2 to z = +22. Unit: Å.

z	C2-Cl1		C1-Cl2		C1-C2		C1-H1		C2-H2	
	0 fs	**500 fs**	**0 fs**	**500 fs**	**0 fs**	**500 fs**	**0 fs**	**500 fs**	**0 fs**	**500 fs**
+2	1.72	1.64	1.72	1.59	1.33	1.79	1.08	1.15	1.08	1.18
+3	1.72	1.48	1.72	1.43	1.33	30.10	1.08	1.25	1.08	1.13
+4	1.72	1.61	1.72	1.55	1.33	54.27	1.08	2.38	1.08	1.18
+5	1.72	58.07	1.72	1.48	1.33	68.90	1.08	1.10	1.08	213.91
+6	1.72	1.44	1.72	1.40	1.33	53.90	1.08	311.29	1.08	311.29
+7	1.72	73.26	1.72	1.70	1.33	40.14	1.08	367.74	1.08	369.60
+8	1.72	81.10	1.72	81.10	1.33	68.76	1.08	358.12	1.08	358.12
+9	1.72	126.61	1.72	87.09	1.33	99.59	1.08	385.79	1.08	373.28
+10	1.72	126.26	1.72	126.38	1.33	149.10	1.08	388.01	1.08	388.06
+11	1.72	133.71	1.72	156.89	1.33	157.17	1.08	411.94	1.08	417.72
+12	1.72	164.66	1.72	164.66	1.33	167.25	1.08	426.68	1.08	426.68
+13	1.72	166.58	1.72	194.90	1.33	187.95	1.08	439.45	1.08	450.14
+14	1.72	198.35	1.72	198.34	1.33	211.64	1.08	462.67	1.08	462.67
+16	1.72	239.25	1.72	238.62	1.33	247.47	1.08	482.22	1.08	481.57
+18	1.72	279.41	1.72	279.41	1.33	272.31	1.08	500.28	1.08	500.29
+20	1.72	327.94	1.72	323.71	1.33	356.22	1.08	505.69	1.08	504.44
+22	1.72	362.93	1.72	362.93	1.33	382.29	1.08	520.17	1.08	520.17

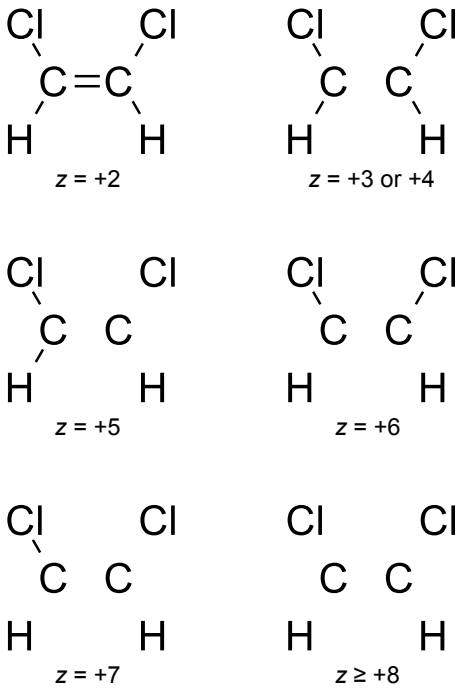


Figure 7.12: Schematic diagram of fragmentation channels of *cis*-1,2-dichloroethene during Coulomb explosion at z = +2 to z = +22.

may be verified by comparing initial and final atomic partial charges, as tabulated in Table 7.2. The charges of the H1-C1-Cl2^{2+} and H2-C2-Cl1^{+} molecular fragments that form in the case z = +3 and the charges of the H1-C1-Cl2^{2+} and H2-C2-Cl1^{2+} molecular fragments that form in the case z = +4 may not be obvious from the individual atomic charges, but the sum of the charges of each constituent atoms of the molecular fragments does indeed reach integer value at t = 500 fs. In addition, Table 7.3 compares the initial and final Wiberg bond index, which reinforces the findings from Table 7.1.

Figure 7.13 shows the classical trajectories for the fragments formed from *cis*-1,2-dichloroethene with initial charge states of z = +4, +5, +6, +7, +8, and +9. These charge states span the 6 representative fragmentation channels as shown in Figure 7.12.

We can conclude from the above that once the total charge of the *cis*-dichloroethene parent ion is +8 or higher, full Coulomb explosion into atomic ions is achieved, resulting in trajectories similar to those shown in Figure 7.13 (e) and (f). If the trajectories are mapped into the *yz*-plane, as shown in Figure 7.14 for initial charge states from z = +8 to +13, it is noticeable that atoms on the two HCCl^{n+} ($4 \leq n \leq 7$) molecular fragments show symmetric trajectories (relative to the z-axis) when the initial charge state is an even number, and nonsymmetric trajectories when the initial charge state is an odd number. This reflects the different charges on the two Cl atoms when the initial charge state is odd.

7.2.2.2 Velocity evolution

The velocity evolution for the various Coulomb explosion fragments are shown in Figure 7.15. As expected, all but bonded atoms show characteristic asymptotic curves.

7.2.2.3 Terminal velocity

The correlation between atomic velocities and the initial charge of parent ion, and Coulomb explosion time and initial charge of parent ion are shown in Figures 7.16 and

Table 7.2: Atomic partial charges of *cis*-1,2-dichloroethene at t = 0 fs and t = 500 fs during Coulomb explosion at z = +2 to z = +22. Charges differ from nearest integer value under 0.001 are displayed as integer number with no decimal places.

z	Cl1		Cl2		C1		C2		H1		H2	
	0 fs	500 fs	0 fs	500 fs	0 fs	500 fs	0 fs	500 fs	0 fs	500 fs	0 fs	500 fs
+2	0.677	0.476	0.677	0.532	0.069	0.181	0.069	0.219	0.254	0.296	0.254	0.297
+3	1.043	0.503	0.935	1.052	0.227	0.512	0.110	0.227	0.275	0.434	0.411	0.272
+4	1.549	0.994	1.268	0.855	0.137	0.272	0.149	0.465	0.475	0.872	0.422	0.542
+5	1.790	1.001	1.787	1.057	0.227	0.500	0.287	1.001	0.462	0.441	0.448	1
+6	1.989	1.096	1.989	1.112	0.519	0.887	0.519	0.902	0.492	1.001	0.492	1.001
+7	2.297	2.001	2.231	1.058	0.471	0.939	0.688	1.002	0.609	1.001	0.704	1.001
+8	2.597	2	2.597	2	0.652	1	0.652	1	0.751	1	0.751	1
+9	3.037	2	3.017	2	0.659	1.001	0.656	2	0.810	1	0.821	1
+10	3.187	2	3.187	2	0.978	2	0.978	2	0.834	1	0.834	1
+11	3.812	2	3.357	3	0.882	2	1.167	2	0.890	1	0.892	1
+12	3.972	3	3.972	3	1.072	2	1.072	2	0.955	1	0.955	1
+13	4.298	3	4.298	3	1.133	3	1.133	2	1.070	1	1.070	1
+14	4.689	3	4.689	3	1.231	3	1.231	3	1.080	1	1.080	1
+16	5.190	4	5.190	4	1.508	3	1.508	3	1.302	1	1.302	1
+18	5.857	4	5.857	4	1.784	4	1.784	4	1.359	1	1.359	1
+20	6.395	5	6.395	5	2.305	4	2.305	4	1.300	1	1.300	1
+22	6.824	6	6.824	6	2.977	4	2.977	4	1.200	1	1.200	1

Table 7.3: Wiberg bond index of *cis*-1,2-dichloroethene at t = 0 fs and t = 500 fs during Coulomb explosion at z = +2 to z = +22.

z	C2-Cl1		C1-Cl2		C1-C2		C1-H1		C2-H2	
	0 fs	500 fs	0 fs	500 fs	0 fs	500 fs	0 fs	500 fs	0 fs	500 fs
+2	0.84	1.07	0.84	1.13	1.19	0.68	0.79	0.77	0.79	0.76
+3	0.81	1.21	0.78	1.49	1.13	0	0.77	0.65	0.77	0.78
+4	0.80	1.21	0.84	1.26	1.06	0	0.74	0.12	0.73	0.70
+5	0.72	0	0.74	1.41	1.11	0	0.71	0.75	0.71	0
+6	0.70	1.43	0.70	1.50	0.92	0	0.67	0	0.67	0
+7	0.68	0	0.69	0.90	0.98	0	0.59	0	0.47	0
+8	0.70	0	0.70	0	0.92	0	0.46	0	0.46	0
+9	0.67	0	0.68	0	0.98	0	0.42	0	0.42	0
+10	0.61	0	0.61	0	0.89	0	0.29	0	0.29	0
+11	0.59	0	0.62	0	0.86	0	0.27	0	0.25	0
+12	0.59	0	0.59	0	0.88	0	0.21	0	0.21	0
+13	0.53	0	0.53	0	0.95	0	0.13	0	0.13	0
+14	0.51	0	0.51	0	0.86	0	0.13	0	0.13	0
+16	0.48	0	0.48	0	0.84	0	0.01	0	0.01	0
+18	0.60	0	0.60	0	0.86	0	0.00	0	0.00	0
+20	0.36	0	0.36	0	0.77	0	0.00	0	0.00	0
+22	0.19	0	0.19	0	0.56	0	0.01	0	0.01	0

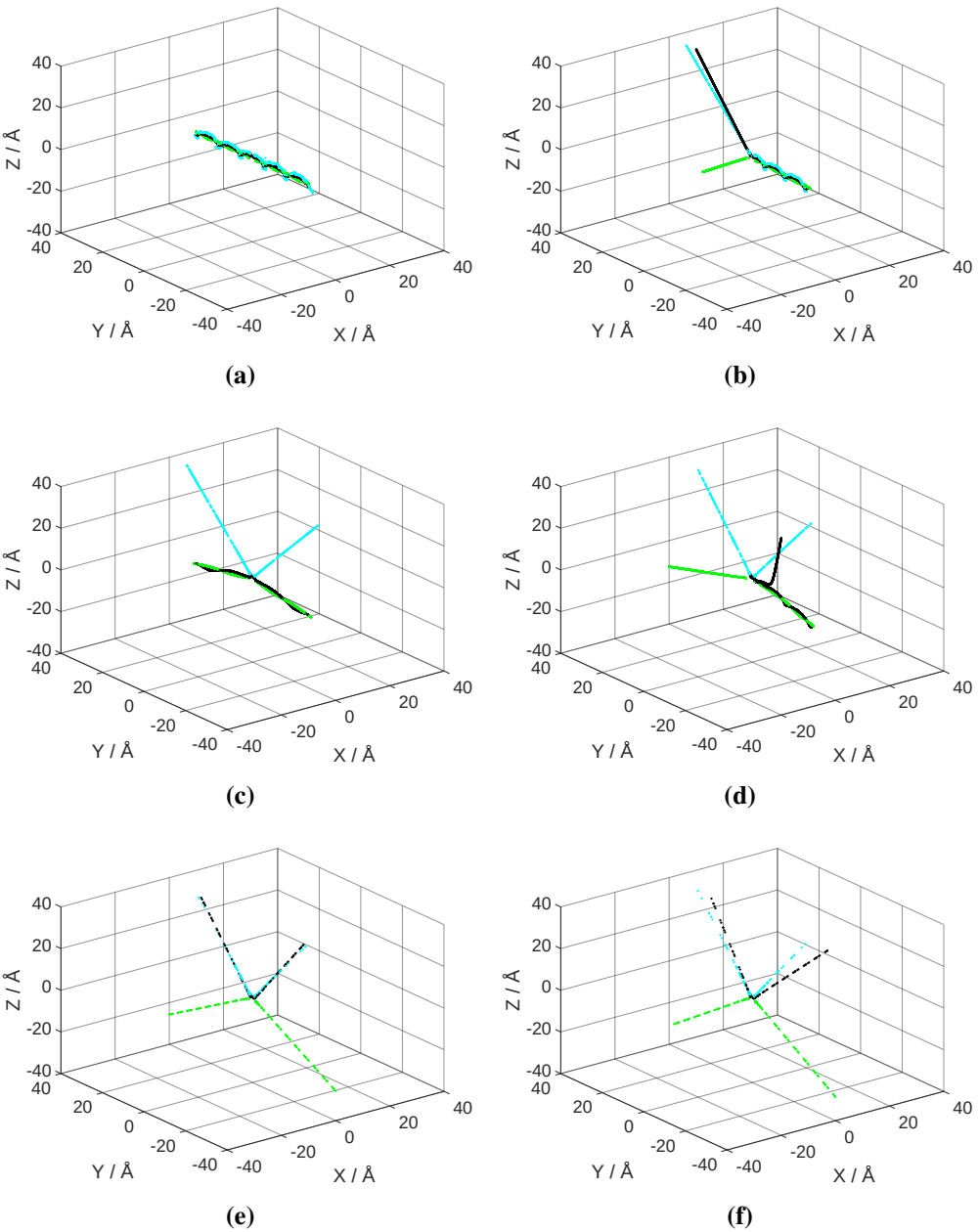


Figure 7.13: Trajectory of atoms of *cis*-1,2-dichloroethene during Coulomb explosion at (a) $z = +4$, (b) $z = +5$, (c) $z = +6$, (d) $z = +7$, (e) $z = +8$, and (f) $z = +9$. Cl, C, and H are respectively colored green, black, and cyan.

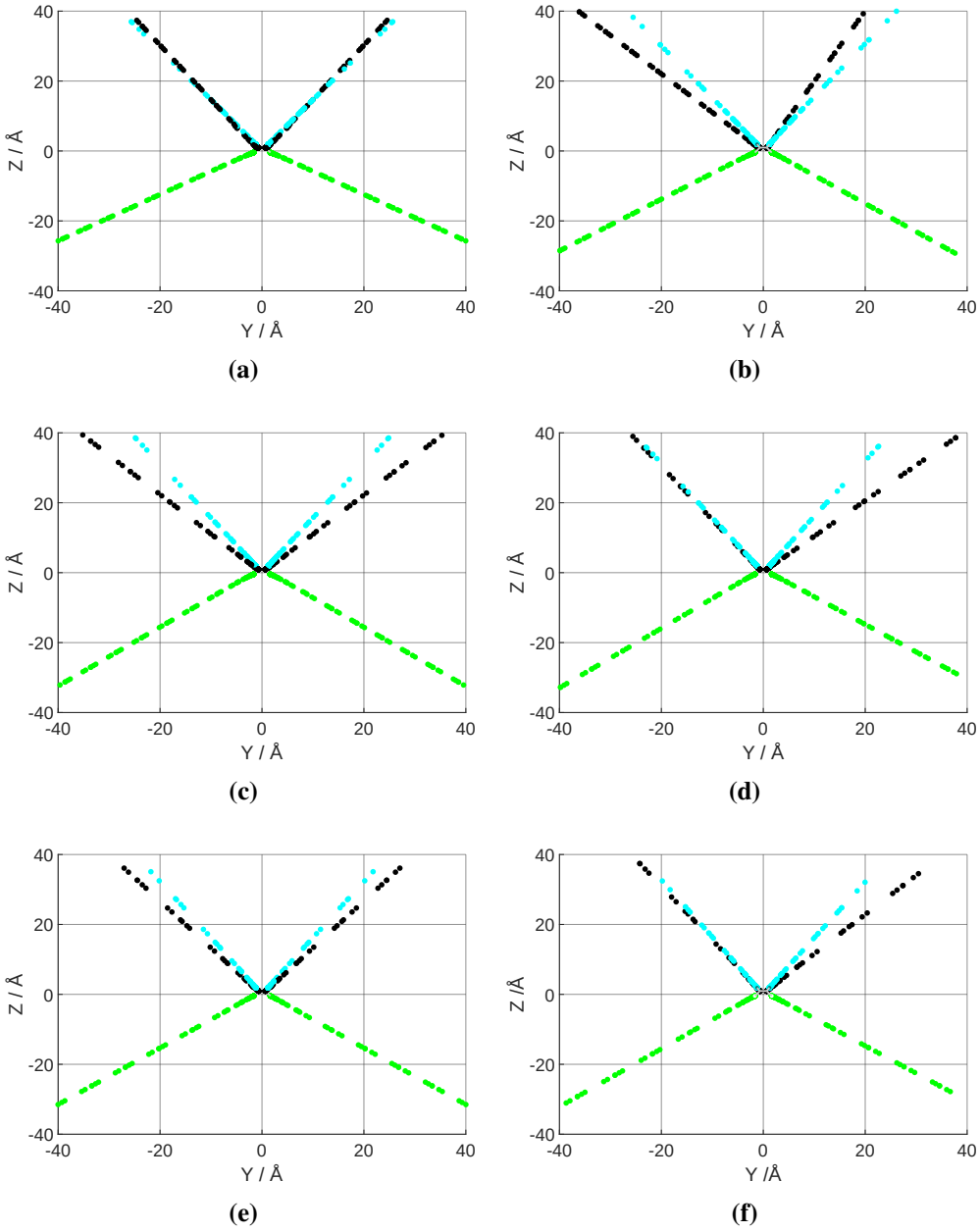


Figure 7.14: Trajectory of atoms of *cis*-1,2-dichloroethene on *yz*-plane during Coulomb explosion at (a) $z = +8$, (b) $z = +9$, (c) $z = +10$, (d) $z = +11$, (e) $z = +12$, and (f) $z = +13$. Cl, C, and H are respectively colored green, black, and cyan.

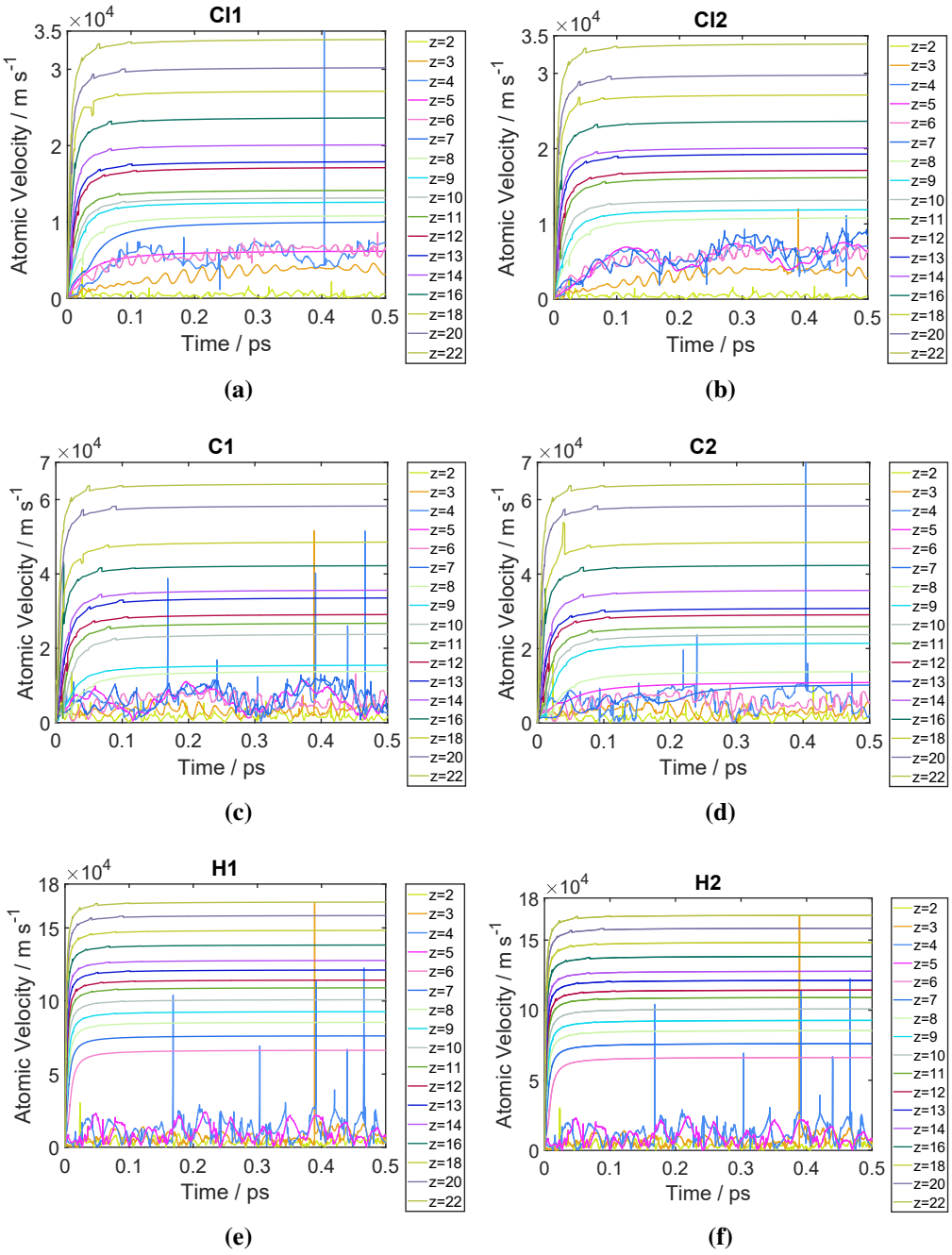


Figure 7.15: Evolution of atomic velocities during Coulomb explosion of *cis*-1,2-dichloroethene at $z = +2$ to $z = +22$ for (a) Cl1, (b) Cl2, (c) C1, (d) C2, (e) H1, and (f) H2. Note that occasional spikes are due to errors in solving the ODE function and are not real velocity values.

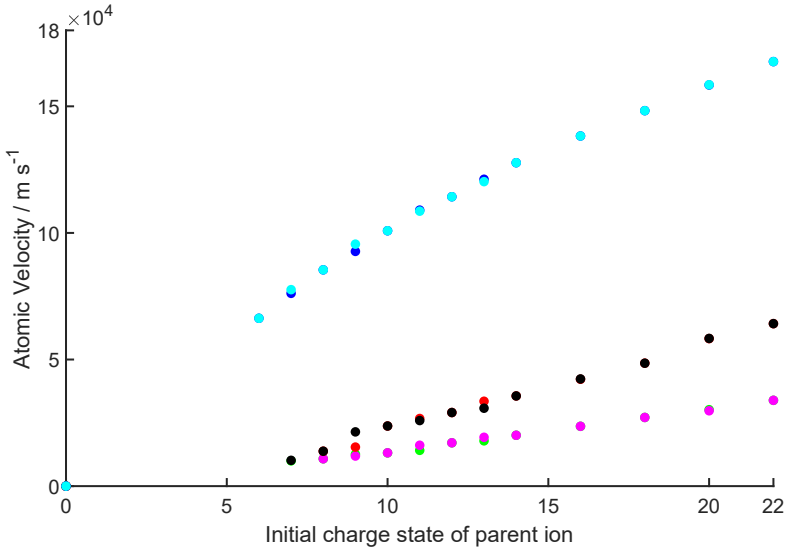


Figure 7.16: Atomic terminal velocity as a function of initial charge state of parent ion of *cis*-1,2-dichloroethene. Cl1, Cl2, C1, C2, H1, and H2 are respectively colored green, magenta, red, black, blue, and cyan.

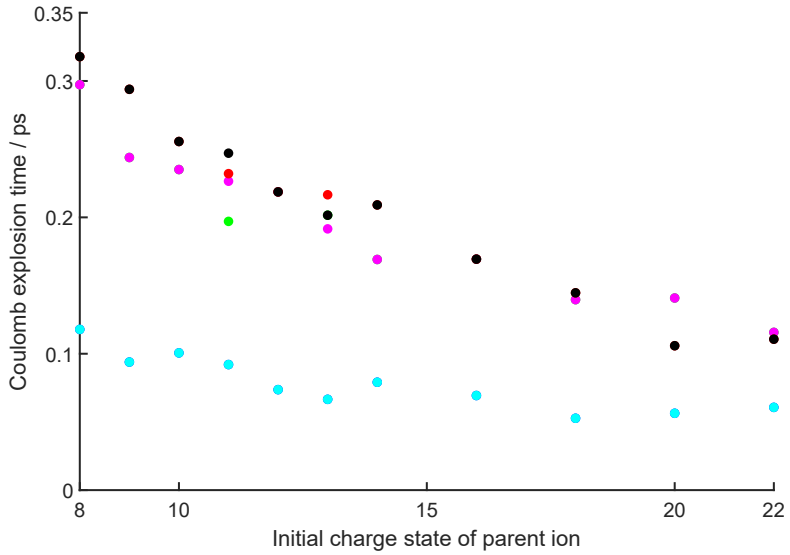


Figure 7.17: Relationship between Coulomb explosion time (defined as the time at which the fragment is within 1% of its asymptotic velocity) and initial charge state of parent ion of *cis*-1,2-dichloroethene. Cl1, Cl2, C1, C2, H1, and H2 are respectively colored green, magenta, red, black, blue, and cyan. Note that H1 and H2 are overlapped.

7.17, respectively. The shape of both curves demonstrate similar trends as observed in Figure 7.9 and 7.10 for HClCO.

Simulation results of *cis*-1,2-dichloroethene and the inferred conclusions demonstrated again the strong and versatile abilities of current program. Compared with HClCO, the

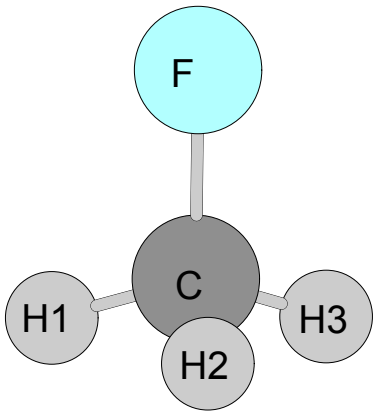


Figure 7.18: Ball and stick representation of the fluoromethane molecule.

asymmetrical nature of *cis*-1,2-dichloroethene with odd number of charges are reflected through trajectories and partial charge states.

7.2.3 Fluoromethane (CH_3F)

Simulations on fluoromethane were performed for charge states from charge +2 to +14, with forces calculated at the MP2/6-311G(d,p) [6, 7] level of theory, and simulations run for 500 fs. The molecular configuration and numbering of atoms are depicted in Figure 7.18.

7.2.3.1 Partial charge and Wiberg bond index evolution

According to the analysis plan introduced in section 7.2.2.1, initial and final bond lengths are tabulated in Table 7.4 for all constituent atoms. The C-H1 bond is clearly broken for all initial charge states, while the C-H2 and C-H3 bonds start to break for +3 and higher charge states. The strong C-F bond remains intact until z = +7. The possible fragmentation channels are shown in Figure 7.19.

In addition, the atomic charges and the Wiberg bond index are listed in Table 7.5 and 7.6, respectively. As for the other molecules presented so far, atoms that are not bonded in the products reach integer charge states at the final time step and are well separated from all

Table 7.4: Bond lengths of fluoromethane at t = 0 fs and t = 500 fs during Coulomb explosion at z = +2 to z = +14. Unit: Å.

z	C-F		C-H1		C-H2		C-H3	
	0 fs	**500 fs**	**0 fs**	**500 fs**	**0 fs**	**500 fs**	**0 fs**	**500 fs**
+2	1.38	1.18	1.09	178.41	1.09	1.02	1.09	0.97
+3	1.38	1.42	1.09	226.04	1.09	204.42	1.09	71.56
+4	1.38	1.20	1.09	278.17	1.09	276.41	1.09	286.95
+5	1.38	1.13	1.09	361.86	1.09	368.89	1.09	359.71
+6	1.38	1.36	1.09	433.38	1.09	433.50	1.09	434.35
+7	1.38	141.65	1.09	462.03	1.09	462.03	1.09	462.03
+8	1.38	181.70	1.09	509.77	1.09	510.27	1.09	510.00
+9	1.38	220.46	1.09	550.50	1.09	550.47	1.09	550.65
+10	1.38	269.15	1.09	578.04	1.09	578.00	1.09	578.11
+11	1.38	317.43	1.09	595.45	1.09	595.45	1.09	595.44
+12	1.38	360.52	1.09	609.51	1.09	609.51	1.09	609.50
+13	1.38	398.96	1.09	622.01	1.09	622.01	1.09	622.01
+14	1.38	436.74	1.09	633.88	1.09	633.87	1.09	633.87

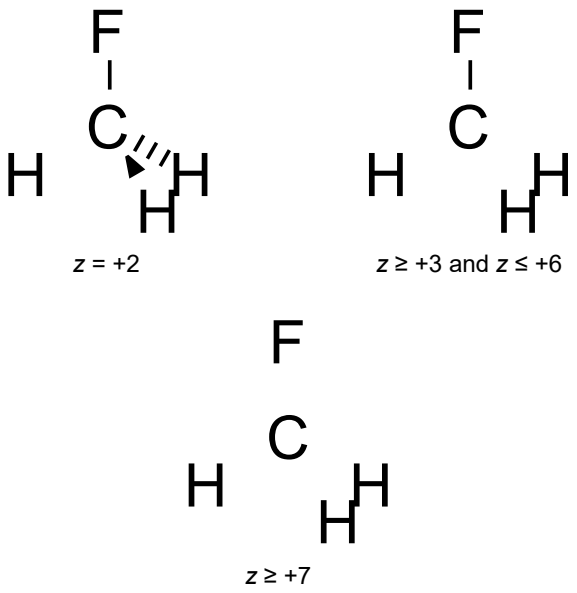


Figure 7.19: Schematic diagram of fragmentation channels of fluoromethane during Coulomb explosion at z = +2 to z = +14. Hydrogen atoms are named as H1, H2, and H3 from left to right according to Figure 7.18.

Table 7.5: Atomic partial charges of fluoromethane at t = 0 fs and t = 500 fs during Coulomb explosion at z = +2 to z = +14. Charges differ from nearest integer value under 0.001 are displayed as integer number with no decimal places.

z	F		C		H1		H2		H3	
	0 fs	**500 fs**	**0 fs**	**500 fs**	**0 fs**	**500 fs**	**0 fs**	**500 fs**	**0 fs**	**500 fs**
+2	0.593	-0.001	0.026	0.758	0.553	1	0.412	0.115	0.416	0.129
+3	0.794	0.093	0.294	0.909	0.666	0.998	0.597	0.998	0.648	0.001
+4	1.370	0.284	0.487	0.718	0.756	1	0.705	1	0.680	1
+5	1.572	0.341	1.022	1.658	0.809	1	0.787	1	0.810	1
+6	1.784	0.893	1.547	2.106	0.883	1	0.902	1	0.885	1
+7	2.251	2	1.685	2	1.021	1	1.022	1	1.021	1
+8	2.662	2	2.200	3	1.022	1	1.073	1	1.044	1
+9	3.183	3	2.514	3	1.103	1	1.104	1	1.097	1
+10	3.476	3	3.207	4	1.107	1	1.108	1	1.102	1
+11	4.325	4	3.404	4	1.091	1	1.091	1	1.088	1
+12	5.380	5	3.136	4	1.163	1	1.163	1	1.158	1
+13	6.232	6	3.467	4	1.101	1	1.102	1	1.099	1
+14	6.999	7	3.996	4	1.002	1	1.002	1	1.001	1

Table 7.6: Wiberg bond index of fluoromethane at t = 0 fs and t = 500 fs during Coulomb explosion at z = +2 to z = +14.

z	C-F		C-H1		C-H2		C-H3	
	0 fs	**500 fs**	**0 fs**	**500 fs**	**0 fs**	**500 fs**	**0 fs**	**500 fs**
+2	0.81	1.25	0.38	0	0.77	0.96	0.77	0.96
+3	0.92	1.05	0.32	0	0.45	0	0.37	0
+4	0.87	1.24	0.25	0	0.31	0	0.35	0
+5	0.76	1.55	0.18	0	0.17	0	0.18	0
+6	0.78	0.86	0.10	0	0.08	0	0.10	0
+7	0.53	0	0.05	0	0.05	0	0.05	0
+8	0.52	0	0.02	0	0.01	0	0.01	0
+9	0.42	0	0.01	0	0.01	0	0.01	0
+10	0.38	0	0	0	0	0	0	0
+11	0.15	0	0	0	0	0	0	0
+12	0.06	0	0	0	0	0	0	0
+13	0.01	0	0	0	0	0	0	0
+14	0.00	0	0	0	0	0	0	0

other atoms. One very interesting finding is that for charge state z = +3, the charge on atom H3 is nearly zero. This implies formation of a neutral H atom, which is not possible to simulate by more simplistic methods in which only the Coulomb potential is considered.

Trajectories for the lowest 6 charge states are plotted in Figure 7.20. For charge state z = +2, the two repelling fragment ions, $CFH_2{}^+$ and H^+, fly in opposite directions. For z = +3, the trajectories for the two H^+ ions and one H atom are slightly different from those formed from the z = +4 or higher charge states, due to the formation of the H3 atom as a neutral. As before, increasing the initial charge state correlates with increased fragment terminal velocities and a reduction in the time before these terminal velocities are reached.

As shown in Figure 7.21, if the C-F bond length is plotted as a function of time for charge states z = +2 to z = +6 as considered in Figure 7.20(a)-(e), clear oscillatory behaviour is seen (note that for z = +2, C is also bonded with two H atoms). The oscillation (except for z = +2) corresponds to a stretching vibration in the CF^{n+} ($1 \leq n \leq 3$) product, and may be used to determine the vibrational frequency of the C-F bond, which are found to be 1666.1 cm^{-1}, 1619.2 cm^{-1}, 2048.8 cm^{-1}, and 1357.8 cm^{-1} from Figure 7.21 for z = +3, +4, +5, and +6, respectively.

7.2.3.2 Velocity evolution

The atomic velocity evolution curves for the Coulomb explosion products of fluoromethane are plotted in Figure 7.22 as a function of initial charge state. The time that is required to asymptotically approach terminal velocity is noticeably shorter for all hydrogen atoms than for carbon and fluorine atoms due to the differences in mass.

7.2.3.3 Terminal velocity

The correlation between atomic terminal velocity and initial charge state of parent ion of fluoromethane, and between Coulomb explosion time and initial charge state of parent ion of fluoromethane are plotted in Figures 7.23 and 7.24, respectively.

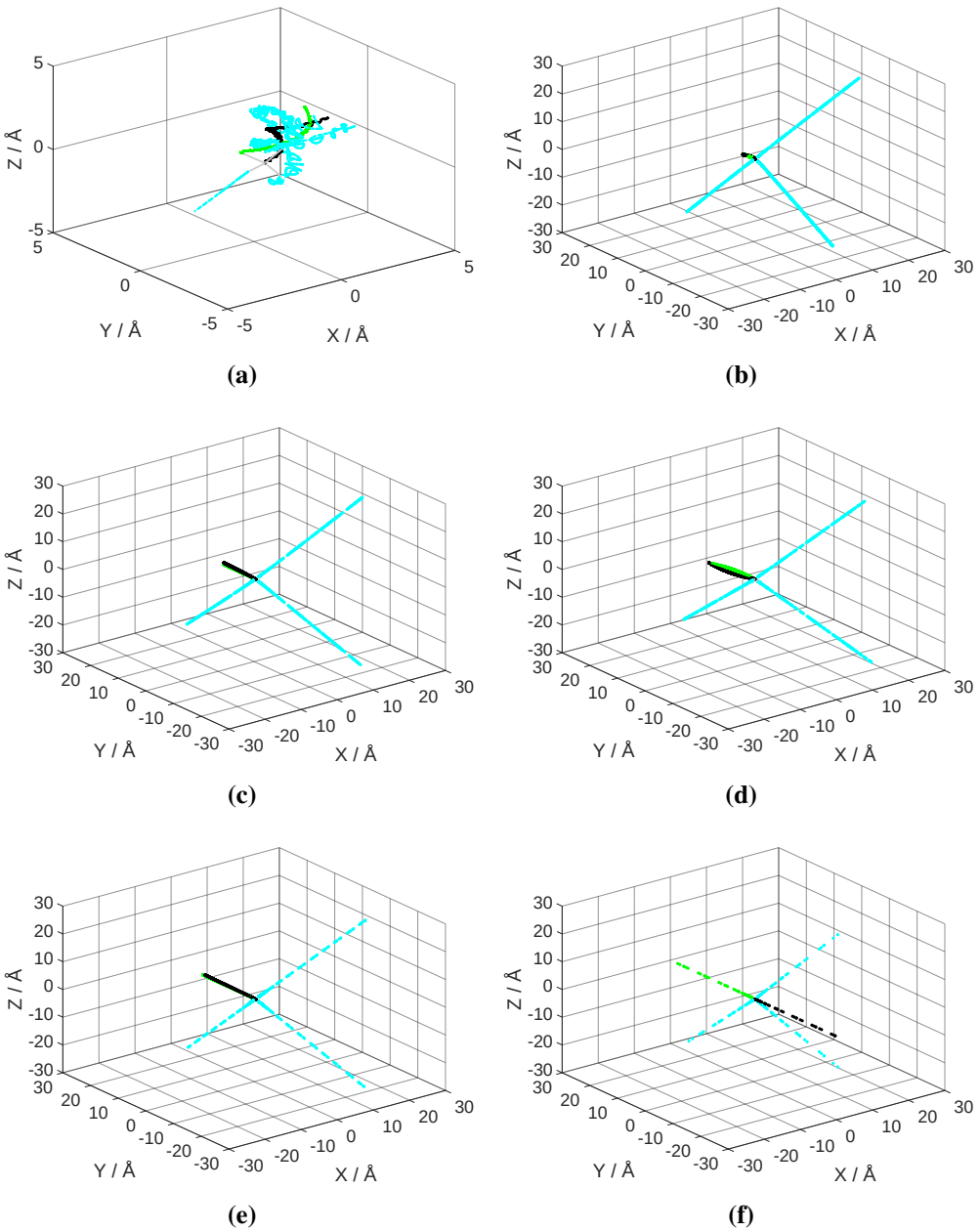


Figure 7.20: Trajectory of atoms of fluoromethane during Coulomb explosion at (a) $z = +2$, (b) $z = +3$, (c) $z = +4$, (d) $z = +5$, (e) $z = +6$, and (f) $z = +7$. F, C, and H are respectively colored green, black, and cyan.

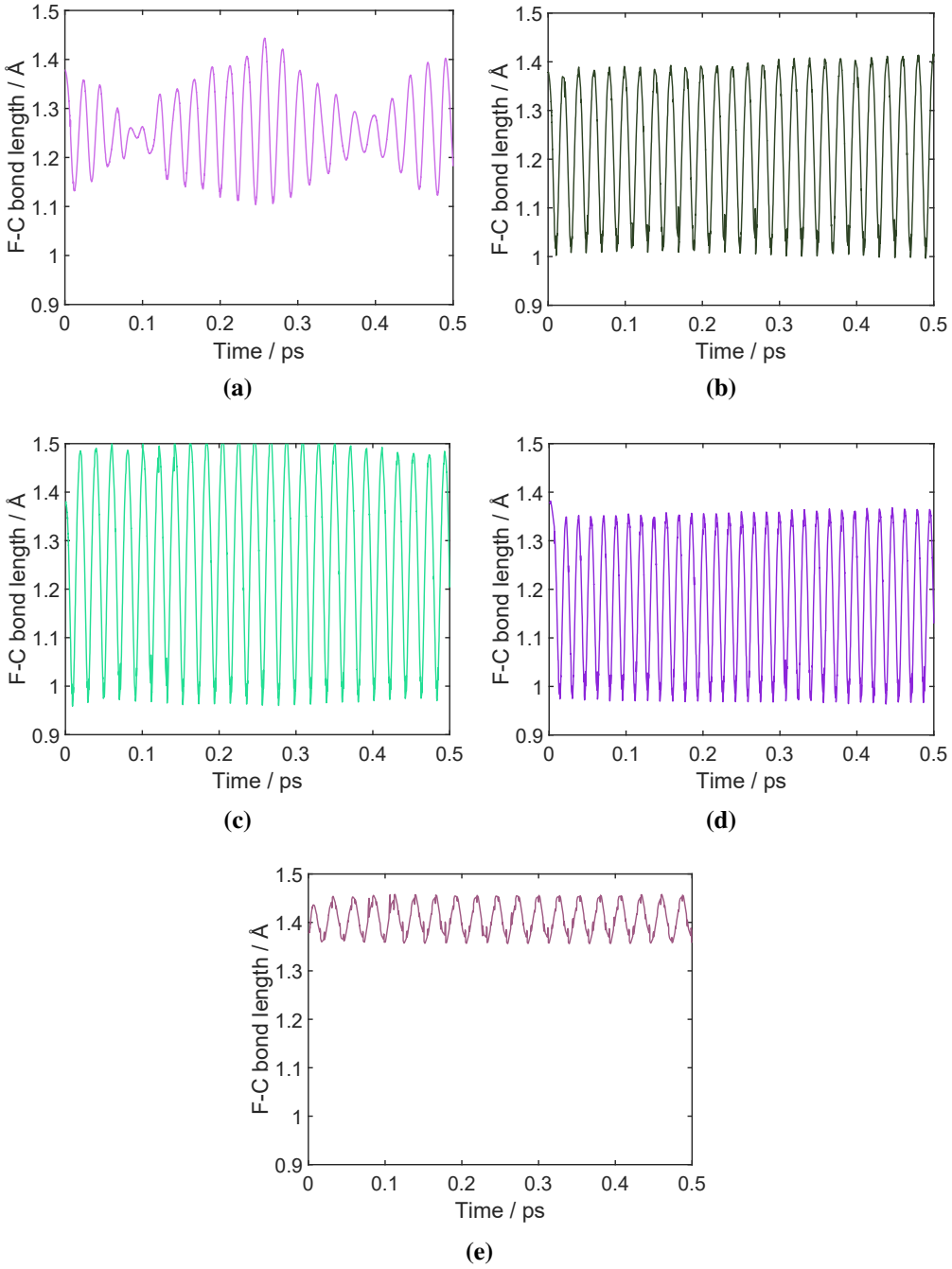


Figure 7.21: Evolution of C-F bond length of fragments (a) $CFH2H3^{+}$, (b) CF^{+}, (c) CF^{+}, (d) CF^{2+}, and (e) CF^{3+} formed during Coulomb explosion of fluoromethane at (a) z = +2, (b) z = +3, (c) z = +4, (d) z = +5, and (e) z = +6, respectively.

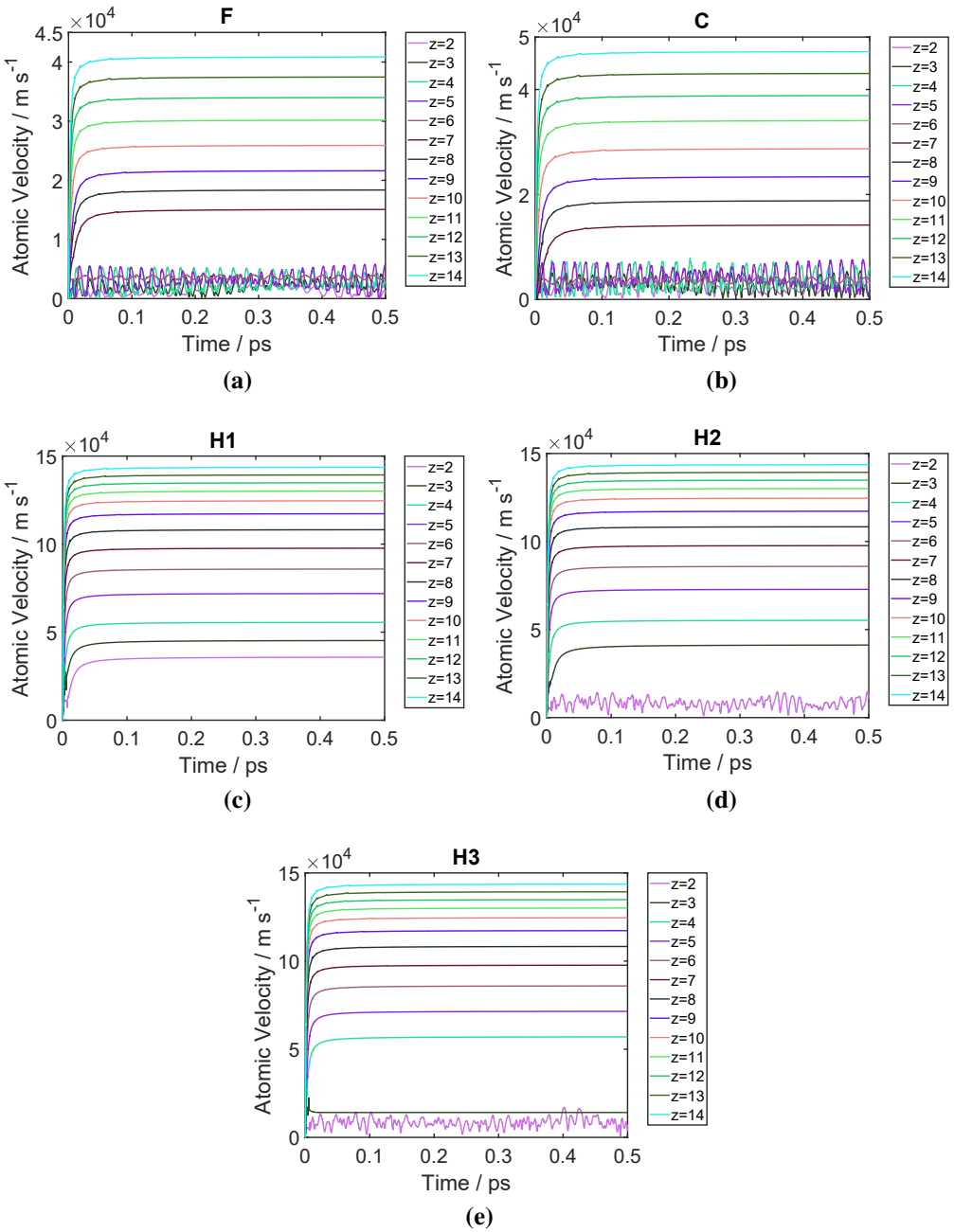


Figure 7.22: Evolution of atomic velocities of fluoromethane during Coulomb explosion at $z = +2$ to $z = +14$ for (a) F, (b) C, (c) H1, (d) H2, and (e) H3.

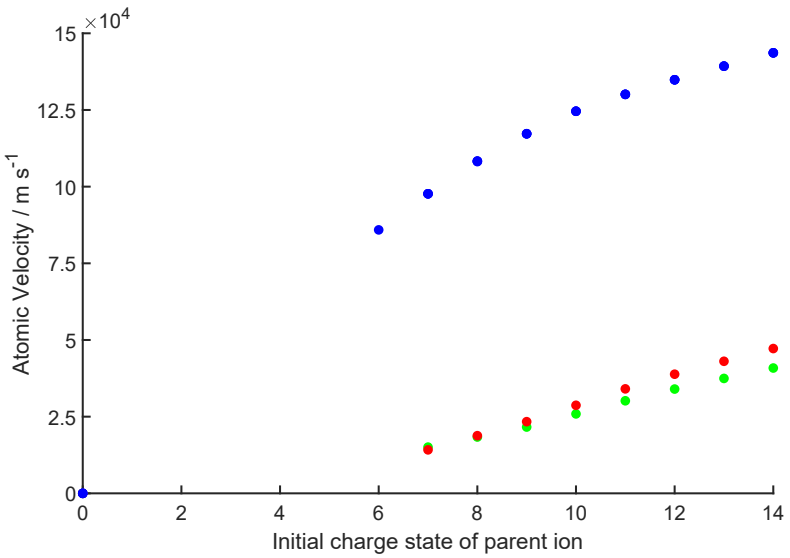


Figure 7.23: Atomic terminal velocity as a function of initial charge state of parent ion of fluoromethane. F, C, and H are respectively colored green, red, and blue. Note that H1, H2, and H3 are overlapped.

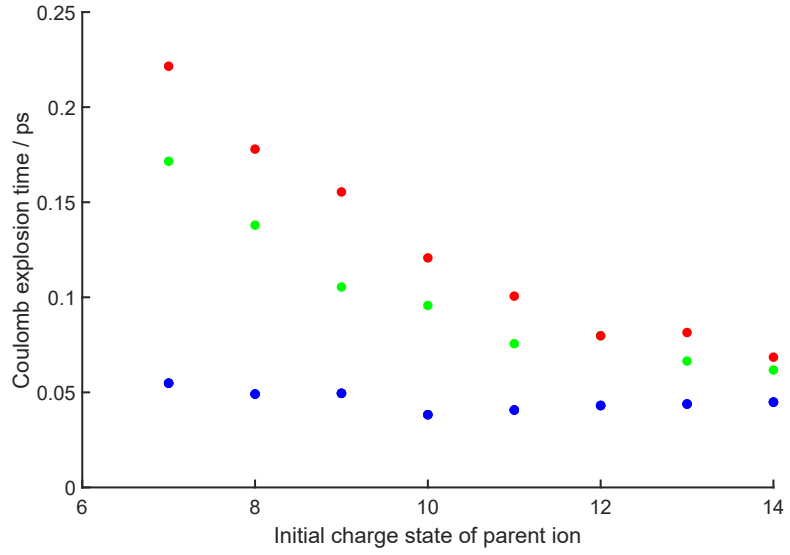


Figure 7.24: Relationship between Coulomb explosion time (defined as the time at which the fragment is within 1% of its asymptotic velocity) and initial charge state of parent ion of fluoromethane. F, C, and H are respectively colored green, red, and blue. Note that H1, H2, and H3 are overlapped.

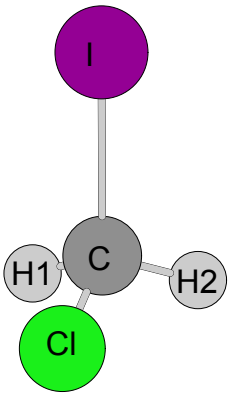


Figure 7.25: Ball and stick representation of the chloroiodomethane molecule.

Fluoromethane exhibits many interesting behaviours as simulated by the current program, especially the formation and dynamics of the CF molecular fragment at lower total charge states.

7.2.4 Chloroiodomethane (CH_2ICl)

Chloroiodomethane is another halogen-substituted methane with two hydrogen atoms replaced by a chlorine atom and an iodine atom. As described in Section 6.4.2.2.2, effective core potential basis set Def2-TZVP [10] is used. Simulations on chloroiodomethane were performed for charge states from +2 to +30, with a simulation time of 500 fs. The molecular configuration and numbering of atoms are depicted in Figure 7.25.

7.2.4.1 Partial charge and Wiberg bond index evolution

To gain a full picture of the bond breaking processes during the Coulomb explosion of chloroiodomethane, the initial and final values of the interatomic distances, atomic partial charges, and Wiberg bond index are tabulated in Tables 7.7, 7.8, and 7.9, respectively. From the data shown in the tables, it is clear that only the z = +2 charge state is stable. In higher charge states, the C-I bond breaks when z = +3, followed by the additional cleavage of the C-H1 bond at z = +4, C-H2 bond at +5, and C-Cl bond at z = +6,

Table 7.7: Bond lengths of chloroiodomethane at t = 0 fs and t = 500 fs during Coulomb explosion at z = +2 to z = +30. Unit: Å.

z	C-I		C-Cl		C-H1		C-H2	
	0 fs	500 fs	0 fs	500 fs	0 fs	500 fs	0 fs	500 fs
+2	2.13	2.11	1.77	1.74	1.08	1.10	1.08	1.10
+3	2.13	21.13	1.77	1.62	1.08	1.09	1.08	1.10
+4	2.13	24.72	1.77	1.40	1.08	231.46	1.08	1.18
+5	2.13	23.84	1.77	1.56	1.08	267.53	1.08	268.70
+6	2.13	65.21	1.77	41.63	1.08	321.55	1.08	313.99
+7	2.13	72.15	1.77	65.60	1.08	342.41	1.08	337.63
+8	2.13	72.17	1.77	81.06	1.08	378.59	1.08	380.32
+9	2.13	115.28	1.77	125.74	1.08	410.00	1.08	387.99
+10	2.13	141.17	1.77	137.70	1.08	438.93	1.08	429.88
+11	2.13	155.35	1.77	176.32	1.08	457.93	1.08	459.25
+12	2.13	185.28	1.77	202.09	1.08	477.27	1.08	477.27
+14	2.13	226.41	1.77	265.18	1.08	522.99	1.08	522.98
+16	2.13	267.54	1.77	329.26	1.08	562.53	1.08	562.53
+18	2.13	328.88	1.77	365.68	1.08	605.72	1.08	605.72
+20	2.13	350.76	1.77	449.88	1.08	635.87	1.08	635.87
+22	2.13	383.76	1.77	460.64	1.08	652.11	1.08	652.11
+24	2.13	415.31	1.77	469.96	1.08	667.72	1.08	667.71
+26	2.13	445.53	1.77	478.41	1.08	682.42	1.08	682.41
+28	2.13	474.39	1.77	486.23	1.08	696.27	1.08	696.27
+30	2.13	496.08	1.77	510.74	1.08	708.53	1.08	708.53

as illustrated in Figure 7.26.

When the total charge state of the parent ion is +20 and higher, so many electrons have been removed that the initial Wiberg bond indices are almost zero for the C-I bond and C-Cl bond, and completely zero for the two C-H bonds. This is also manifested in the near-integer values of the initial atomic charges for these very high charge states.

Trajectories of the chloroiodomethane Coulomb explosion products for initial charge states of z = +2 to +6, +10, +20, and +30 are plotted in Figure 7.27. These clearly agree with the conclusions drawn above. It is noted that the CCl^+ molecular ion is only formed from the initial charge state z = +5. As observed previously for the CF^+ fragments of

Table 7.8: Atomic partial charges of chloroiodomethane at t = 0 fs and t = 500 fs during Coulomb explosion at z = +2 to z = +30. Charges differ from nearest integer value under 0.001 are displayed as integer number with no decimal places.

z	I		Cl		C		H1		H2	
	0 fs	**500 fs**	**0 fs**	**500 fs**	**0 fs**	**500 fs**	**0 fs**	**500 fs**	**0 fs**	**500 fs**
+2	1.146	1.171	0.875	0.886	-0.669	-0.732	0.324	0.338	0.324	0.338
+3	1.963	1	1.004	1.129	-0.703	0.168	0.368	0.350	0.368	0.352
+4	2.243	1	1.721	1.028	-0.842	0.491	0.437	1	0.441	0.481
+5	3.008	2	1.877	0.363	-0.875	0.637	0.498	1	0.492	1
+6	3.612	2	2.056	1	-0.833	1	0.543	1	0.622	1
+7	4.090	2	2.264	2	-0.774	1	0.672	1	0.749	1
+8	4.539	2	2.844	2	-0.823	2	0.665	1	0.775	1
+9	4.805	3	3.084	2	-0.503	2	0.838	1	0.775	1
+10	5.079	3	3.324	3	-0.115	2	0.864	1	0.848	1
+11	5.219	4	3.913	3	0.105	2	0.881	1	0.881	1
+12	5.546	4	4.267	3	0.340	3	0.924	1	0.924	1
+14	6.314	5	4.889	4	0.840	3	0.978	1	0.978	1
+16	6.946	5	5.344	5	1.746	4	0.982	1	0.982	1
+18	6.998	7	6.128	5	2.877	4	0.999	1	0.999	1
+20	7.007	7	7.000	7	3.995	4	0.999	1	0.999	1
+22	9.002	9	7.000	7	3.998	4	1.000	1	1.000	1
+24	11.001	11	7.000	7	3.999	4	1.000	1	1.000	1
+26	13.001	13	7.000	7	3.999	4	1.000	1	1.000	1
+28	15.001	15	7.000	7	3.999	4	1.000	1	1.000	1
+30	17.001	16	7.000	8	3.999	4	1.000	1	1.000	1

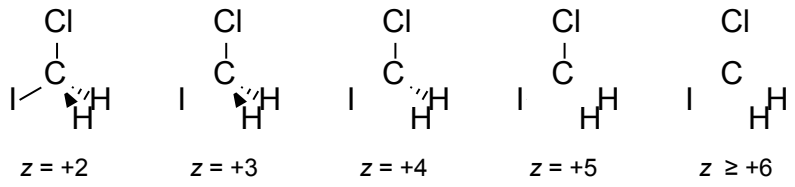


Figure 7.26: Schematic diagram of fragmentation channels of chloroiodomethane during Coulomb explosion at z = +2 to z = +30.

Table 7.9: Wiberg bond index of chloroiodomethane at t = 0 fs and t = 500 fs during Coulomb explosion at z = +2 to z = +30.

z	C-I		C-Cl		C-H1		C-H2	
	0 fs	500 fs	0 fs	500 fs	0 fs	500 fs	0 fs	500 fs
+2	0.999	0.995	1.019	1.036	0.864	0.851	0.864	0.850
+3	0.976	0	1.067	1.456	0.833	0.851	0.833	0.849
+4	0.920	0	1.078	2.560	0.769	0	0.765	0.760
+5	0.992	0	1.063	1.951	0.710	0	0.719	0
+6	0.830	0	1.094	0	0.668	0	0.531	0
+7	0.903	0	1.145	0	0.467	0	0.321	0
+8	0.548	0	1.222	0	0.516	0	0.298	0
+9	0.328	0	1.067	0	0.188	0	0.311	0
+10	0.279	0	0.928	0	0.166	0	0.194	0
+11	0.354	0	0.794	0	0.153	0	0.153	0
+12	0.750	0	0.755	0	0.092	0	0.092	0
+14	0.745	0	0.501	0	0.034	0	0.034	0
+16	0.095	0	0.603	0	0.033	0	0.033	0
+18	0.019	0	0.975	0	0.001	0	0.001	0
+20	0.011	0	0.0002	0	0	0	0	0
+22	0.004	0	0.0002	0	0	0	0	0
+24	0.003	0	0.0002	0	0	0	0	0
+26	0.001	0	0.0002	0	0	0	0	0
+28	0.002	0	0.0002	0	0	0	0	0
+30	0.001	0	0.0002	0	0	0	0	0

CH_3F, the CF^+ fragment is formed with significant vibrational excitation. The bond length is plotted as a function of time in Figure 7.28, and corresponds to a vibrational frequency of 1106.4 cm^{-1}, compared with experimental data of 1175.0 cm^{-1} [11].

7.2.4.2 Velocity evolution

The atomic velocities are shown as a function of time in Figure 7.29. Since the differences in mass of the H, C, Cl, and I atoms are large, the time that it takes to reach asymptotic terminal velocity varies considerably across the atoms. The oscillation in the C and Cl velocities for the z = +5 charge state corresponds to the stretching vibration of the C-Cl bond, as discussed above.

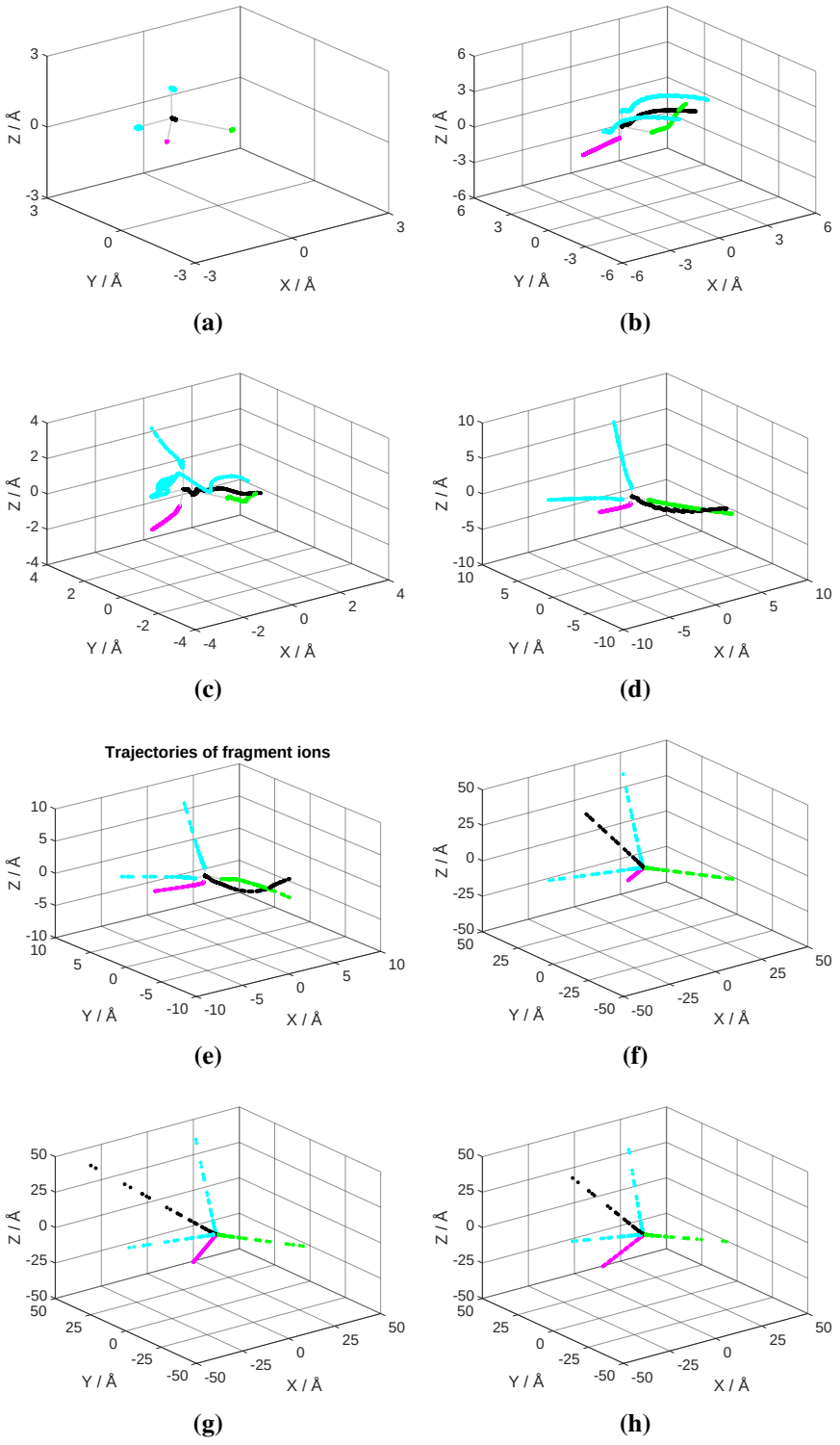
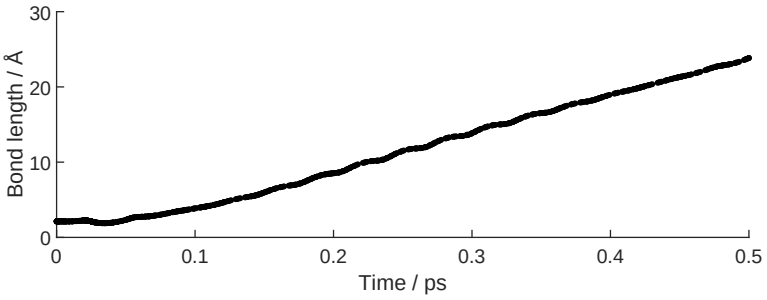
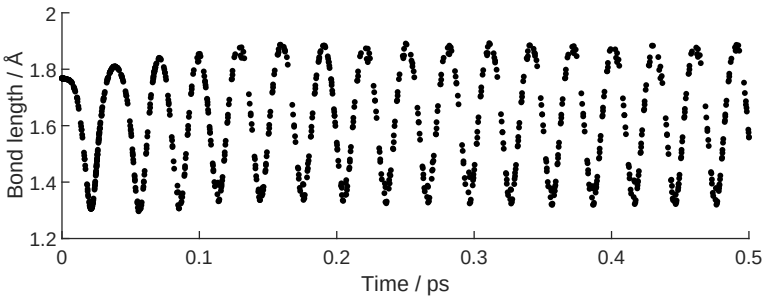


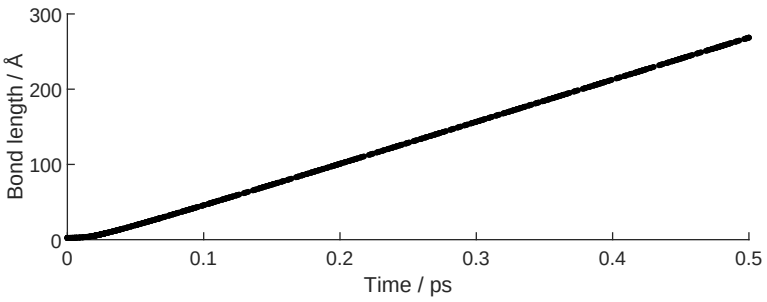
Figure 7.27: Trajectory of atoms of chloroiodomethane during Coulomb explosion at (a) $z = +2$, (b) $z = +3$, (c) $z = +4$, (d) $z = +5$, (e) $z = +6$, (f) $z = +10$, (g) $z = +20$, (h) $z = +30$. I, Cl, C, and H are respectively colored purple, green, black, and cyan.



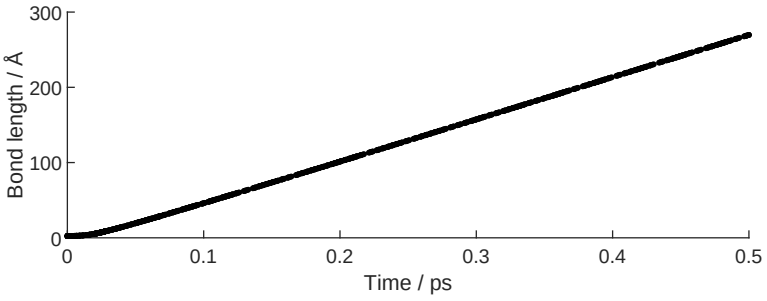
(a)



(b)



(c)



(d)

Figure 7.28: Evolution of bond lengths of chloroiodomethane during Coulomb explosion at z = +5 for (a) C-I bond, (b) C-Cl bond, (c) C-H1 bond, and (d) C-H2 bond.

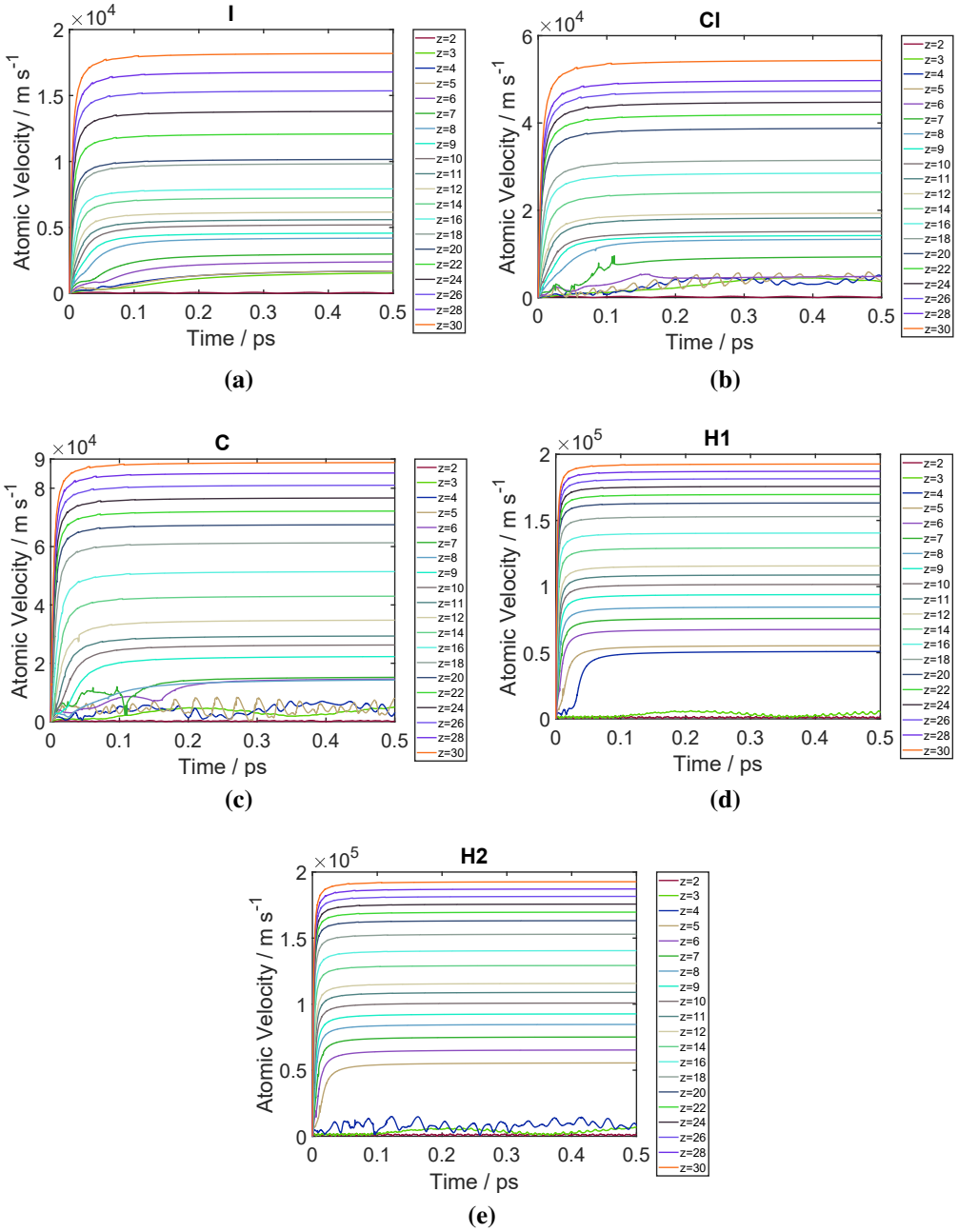


Figure 7.29: Evolution of atomic velocities of chloroiodomethane during Coulomb explosion at z = +2 to z = +30 for (a) I, (b) Cl, (c) C, (d) H1, and (e) H2.

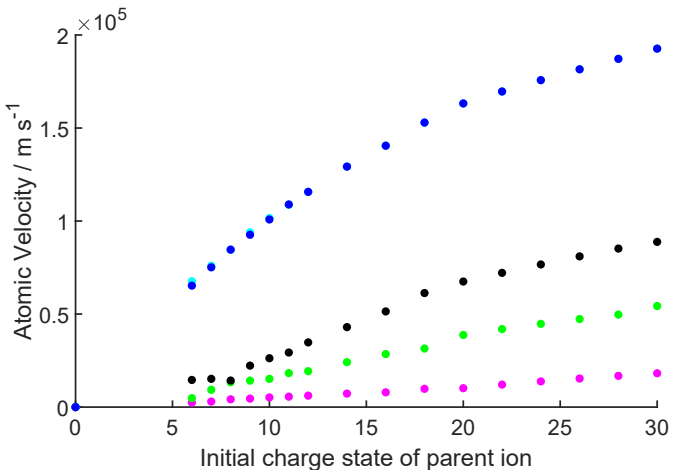


Figure 7.30: Atomic terminal velocity as a function of initial charge state of parent ion of chloroiodomethane. I, Cl, C, H1, and H2 are respectively colored magenta, green, black, cyan, and blue.

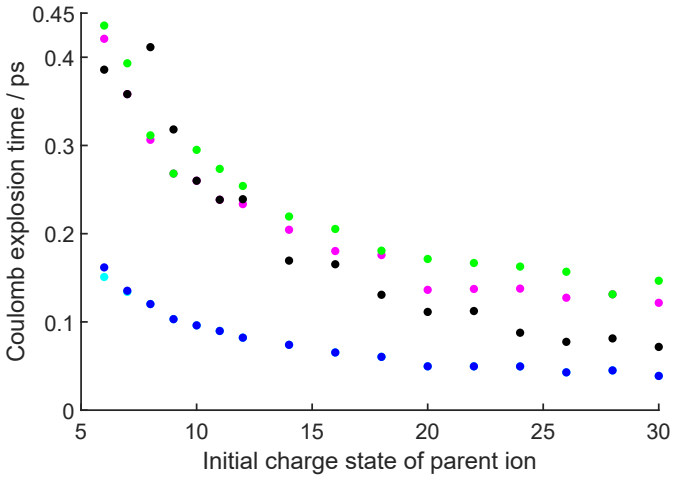


Figure 7.31: Relationship between Coulomb explosion time (defined as the time at which the fragment is within 1% of its asymptotic velocity) and initial charge state of parent ion of chloroiodomethane. I, Cl, C, H1, and H2 are respectively colored magenta, green, black, cyan, and blue.

7.2.4.3 Terminal velocity

The correlation between terminal velocity and initial charge state of parent ion of chloroiodomethane, and between Coulomb explosion time and initial charge state of parent ion of chloroiodomethane are shown in Figures 7.30 and 7.31, respectively.

7.3 Simulation of Velocity-Map Imaging experimental data

The terminal velocities obtained in the simulations may be converted into single-trajectory velocity-map images for comparison with experimental data from Coulomb-explosion imaging measurements. Images recorded in the experiments can be transformed into covariance-map images, which show the velocity of a chosen fragment relative to another, reference, fragment [12]. These can be compared directly with the direction of the relevant trajectories from the trajectory simulations. In the experiments on the DBrDFCNBph molecule [12, 13], the molecule was aligned in the laboratory frame, which further simplifies the comparison between experimental data and the current simulations.

7.3.1 3,5-dibromo-3',5'-difluoro-4'-cyanobiphenyl (DBrDFCNBph)

Femtosecond-laser induced Coulomb explosion of DBrDFCNBph was studied by Slater and co-workers in order to investigate the relationship between the initial molecular structure and the final fragment velocities [12, 13]. DBrDFCNBph was synthesized specifically for such experiments, with the nitrogen and halogen substitutes acting as useful mass and structural markers for the velocity-map imaging measurements (Figure 7.32).

In the experiments, the molecule was pre-aligned in the lab frame using a polarised laser pulse from a nanosecond Nd:YAG laser. This aligns the principal axis of the molecules along the laser polarisation vector prior to Coulomb explosion by a femtosecond laser pulse. As noted earlier in Section 6.3.4, some trajectory simulations of the Coulomb explosion of this molecule have been carried out previously [12], which assumed that the only force acting during the process is Coulomb repulsions between the charged fragments. In the present work, we aim to compare simulations including a full quantum-mechanical simulation of the molecular forces acting during the dissociation with the simplified model used previously.

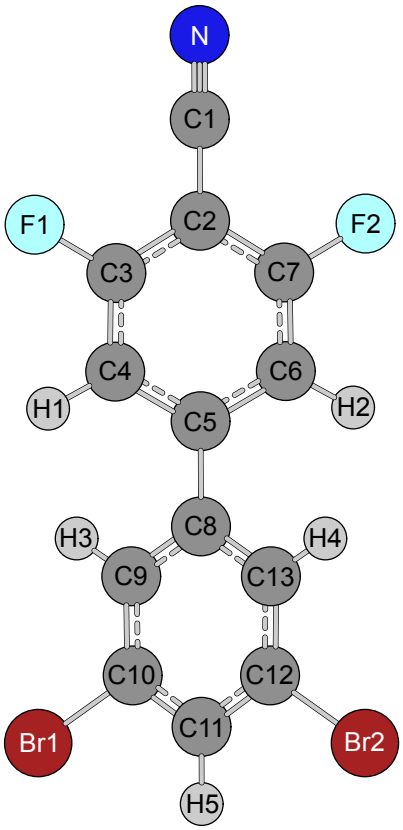


Figure 7.32: Ball and stick representation of the 3,5-dibromo-3,5-difluoro-4-cyanobiphenyl (DBrDFCNBph) molecule. Carbon atoms are labelled from C1 to C13. Hydrogen atoms are labelled as H1, H2, H3, H4, and H5. Halogen atoms are labelled as F1, F2, Br1, and Br2.

For comparison with the original simulations, the new trajectory simulations were performed for a total initial charge on the parent molecule of +23. As for the simulations described previously in this chapter, the forces were calculated at the MP2/6-311G(d,p) level of theory [6, 7]. The size and complexity of the molecule results in a slower Coulomb explosion, and a longer simulation time (relative to the simulations described earlier in the chapter) of 2 ps was used.

7.3.1.1 Trajectory and fate of each atom

From the trajectory plot of the Coulomb explosion of $DBrDFCNBph^{23+}$ shown in Figure 7.33(a), we see that peripheral atomic ions such as N^+, and Br^{2+} fly away in reasonably

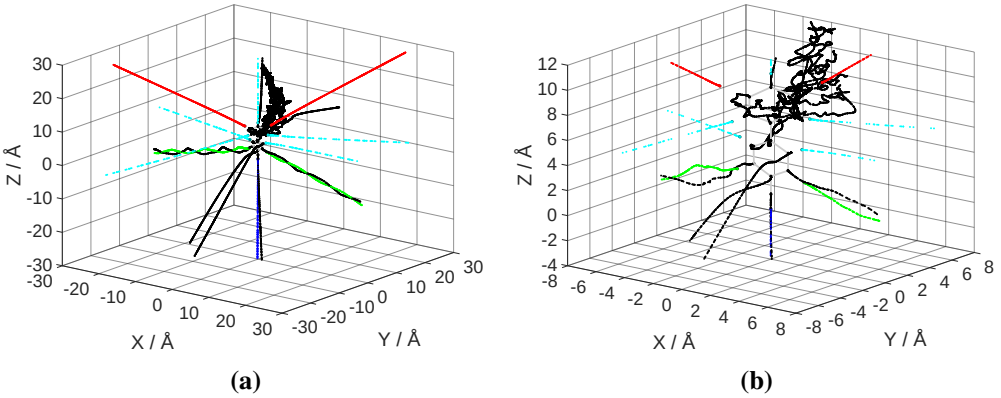


Figure 7.33: Trajectories of atoms of DBrDFCNBph during Coulomb explosion at z = +23. (a) Seen within a cubic space of 60 Å side. (b) Seen within a cubic space of 16 Å side. Br, F, N, C, and H are respectively colored red, green, blue, black, and cyan.

straight-line trajectories from the centre of the molecule. Two CF^+ ($F1C3^+$ and $F2C7^+$) are formed as molecular products. By zooming in the plot (Figure 7.33(b)), it is seen that most carbon atoms on the F-substituted ring are released and fly outwards, while many carbons on the Br-substituted ring seem to tangle together as a molecular fragment.

It is then helpful to explore the initial and final Wiberg bond index to confirm the breakage of bonds. As listed in Table 7.10, apart from the two C-F bonds that are seen to remain intact in the trajectories above, the bonds linking atoms C5, C6, C8, C9, C10, and C13 are also not broken during the dissociation, yielding a carbon molecular fragment. Interestingly, within this molecular fragment there is evidence for new bonds forming, specifically between C9 and C13, and C10 and C13. To assist in visualising the resulting structure, the final positions of carbon atoms C5, C6, C8, C9, C10, and C13 are plotted on three coordinate planes in Figure 7.34. The molecular fragment appears to have a chain-like structure, with all neighbouring atoms spaced by 1 to 2 Å.

Examination of the trajectories suggests that formation of the six-carbon molecular fragment on the Br-substituted ring is a result of the presence of the two heavy and slow Br atoms, which hinder the movement of most of the carbon atoms on the ring during the early stages of the Coulomb explosion. By the time that the carbon atoms

Table 7.10: Wiberg bond index of DBrDFCNBph during Coulomb explosion at z = +23 for original bonds and possible bonds on the Br-substituted ring at t = 0 ps and t = 2 ps.

Original bonds	Wiberg bond index 0 ps	2 ps	Bonds on the Br-substituted ring	Wiberg bond index 0	2 ps
Br1-C10	0.819	0	C8-C10	0.042	0.011
Br2-C12	0.880	0	C8-C12	0.035	0
F1-C3	0.911	1.306	C9-C11	0.018	0
F2-C7	0.927	1.212	C9-C12	0.018	0
N-C1	1.261	0	C9-C13	0.032	1.263
H1-C4	0.682	0	C10-C12	0.050	0
H2-C6	0.676	0	C10-C13	0.020	1.382
H3-C7	0.730	0	C11-C13	0.030	0
H4-C13	0.731	0	C6-C8	0.012	0.121
H5-C11	0.630	0	C5-C9	0.024	0.015
C1-C2	1.098	0			
C2-C3	1.105	0			
C2-C7	1.057	0			
C3-C4	1.063	0			
C6-C7	1.072	0			
C4-C5	0.990	0			
C5-C6	0.992	1.250			
C5-C8	1.038	2.396			
C8-C9	1.098	0.861			
C8-C13	1.047	0.031			
C9-C10	1.016	0.811			
C12-C13	1.081	0			
C10-C11	1.015	0			
C11-C12	1.095	0			

have sufficient space to “explode”, the total charge shared by the molecular fragment is +3, which is not high enough to yield a secondary Coulomb explosion of the newly formed C_6^{3+} fragment (Table 7.11). In terms of the objectives of the original experiment, the dynamics of the departing N^+, F^+, and Br^{2+} atomic ions are of greater interest. These will be discussed in the next section.

7.3.1.2 Ion images

The ion images predicted by the earlier Coulomb explosion simulations on DBrDFCNBph, in which only Coulomb forces were considered, as described in Chapter 6, are compared

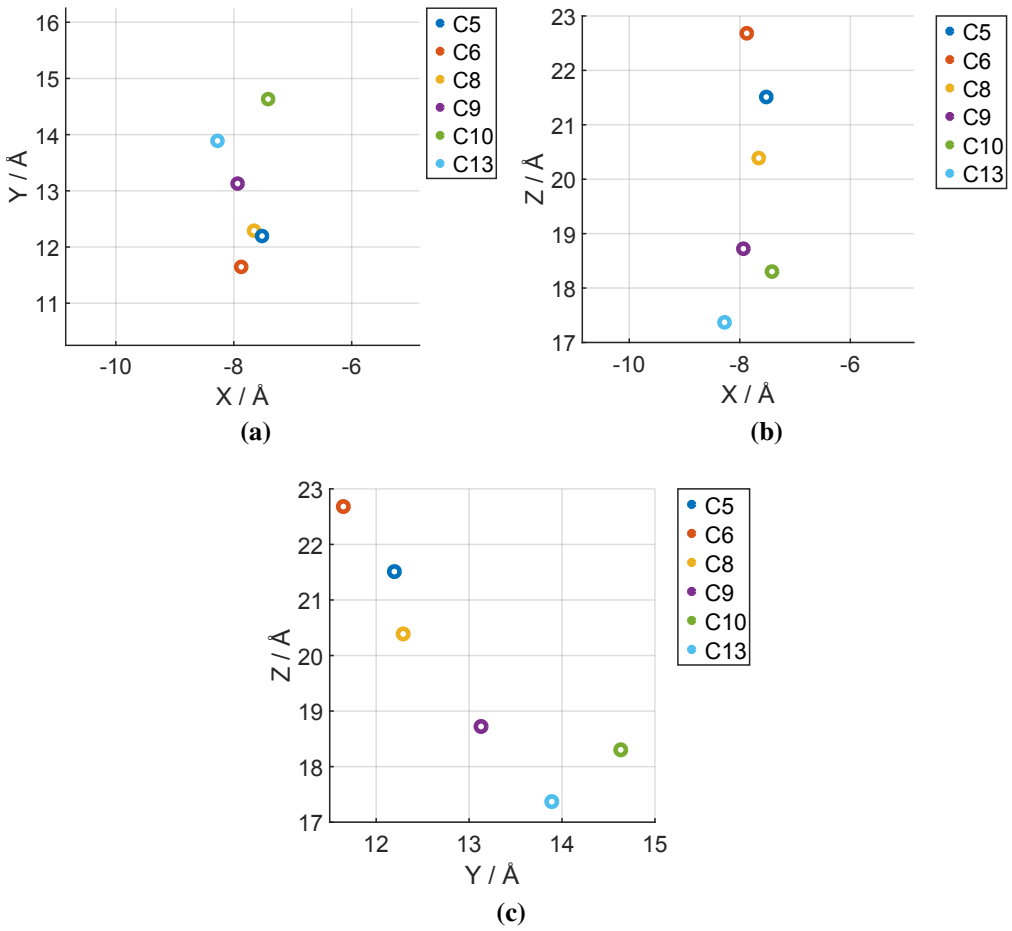


Figure 7.34: Location of C5, C6, C8, C9, C10, and C13 of DBrDFCNBph at t = 2 ps during Coulomb explosion at z = +23 on (a) xy-plane, (b) xz-plane, and (c) yz-plane.

with the results of the present simulations in Figure 7.35 (where identical fragment ions are generated from the same atoms between the two methods) and Figure 7.36 (where different fragment ions are generated from the same atoms between the two methods). When comparing the two sets of fragment ions, it is not too difficult to observe the following features:

1) For the H^+ ions (Figure 7.35 (c)), the Coulomb-only simulations (cyan empty circles) predicts higher velocities than the present method (cyan solid circles).
2) For Br^+ (or Br^{2+}) (Figure 7.36 (a,b)) and N^+ ions (Figure 7.35 (a)), the situation is reversed, with the new simulations predicting higher final velocities than the earlier simulations.

Table 7.11: Initial and final atomic partial charges of DBrDFCNBph during Coulomb explosion at z = +23 calculated at three different level of theories. Non-integer final partial charges of carbon ions, except for those formed CF molecular fragments, are coloured in red.

Atom	MP2/6-31G(d,p)		MP2/6-311G(d,p)		MP2/cc-pVTZ	
	0 ps	2 ps	0 ps	2 ps	0 ps	2 ps
Br1	4.066	2	4.068	2	4.078	2
Br2	3.994	2	3.998	2	4.005	2
F1	1.521	0.330	1.511	0.344	1.507	0.236
F2	1.507	1	1.499	0.257	1.508	0.362
N	2.198	1	2.182	1	2.237	1
C1	0.902	1	0.938	2	1.005	2
C2	0.546	1	0.461	1	0.498	1
C3	0.691	0.673	0.755	0.659	0.635	0.766
C4	0.622	1	0.588	2	0.658	1
C5	0.766	0.754	0.779	0.030	0.756	0.711
C6	0.585	1	0.549	0.943	0.653	1.001
C7	0.713	1	0.780	0.746	0.641	0.641
C8	0.351	0.316	0.371	0.275	0.340	0.318
C9	0.513	1	0.509	0.443	0.540	0.229
C10	0.686	1.001	0.676	0.616	0.636	1
C11	0.528	1	0.540	2	0.557	2
C12	0.277	1	0.272	1	0.260	1
C13	0.536	0.926	0.536	0.689	0.572	0.739
H1	0.420	1	0.423	1	0.407	1
H2	0.429	1	0.432	1	0.410	1
H3	0.336	1	0.333	1	0.321	1
H4	0.355	1	0.350	1	0.332	1
H5	0.459	1	0.452	1	0.445	1

3) In general, for those ions that did not form molecular fragments in the new simulations (Figure 7.35 (a-c) and Figure 7.36 (a,b)), the scattering patterns are very similar between the two methods. However, the free carbons (i.e. C1, C2, C4, C5, C11, and C12) tend to be slightly slower in the current method (Figure 7.35 (b)).

4) The CF^+ fragments predicted in the new simulations (dark green solid circle) lie in between the respective individual C^+ and F^+ ions predicted by the direct

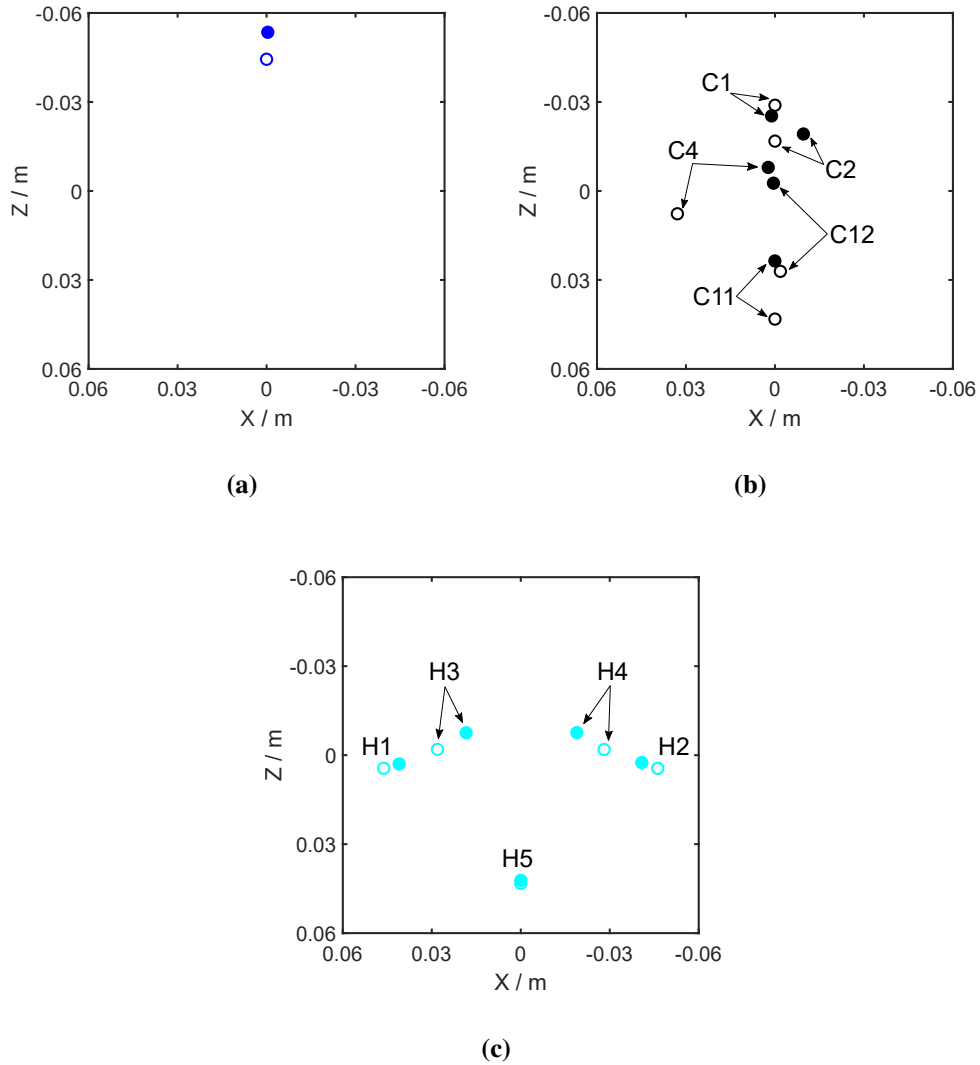


Figure 7.35: Ion images of DBrDFCNBph at t = 2 ps during Coulomb explosion at z = +23 on xz-plane generated from original method (open markers) and current method (filled makers) where identical fragment ions are generated from the same atoms between the two methods. In both original and current methods, the fragment ions are (a) N^+ from N1, (b) C^+ from C1, C2, C4, C11, and C12, and (c) H^+ from H1, H2, H3, H4, and H5.

method (black empty circle and green empty circle) (Figure 7.36 (e,f)). A similar relationship is also observed in the case of the six-carbon molecular fragment (Figure 7.36 (c,d)).

The comparison between the new and earlier simulations implies that attractive forces between atoms continue to be important even for initial charge states as high as +23.

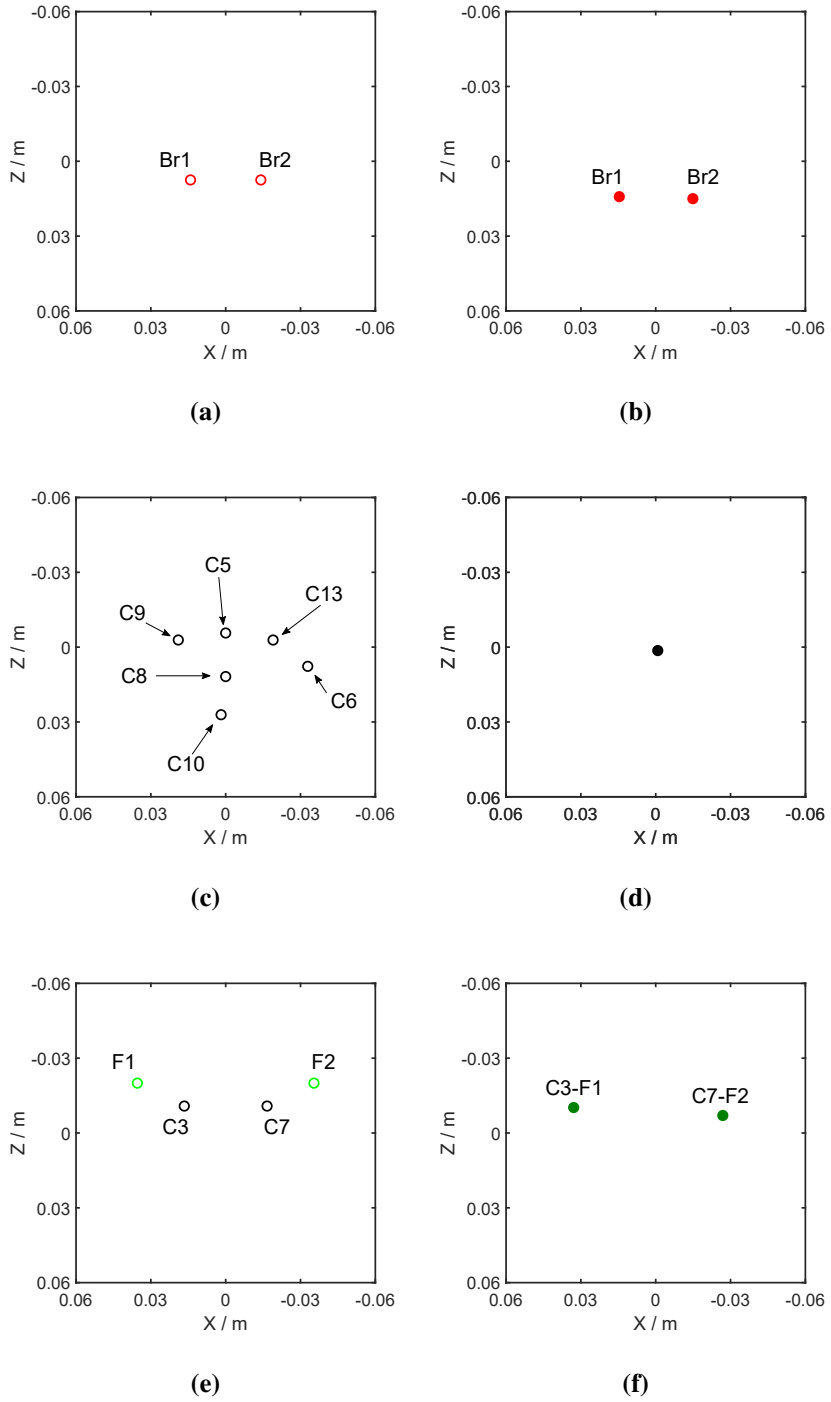


Figure 7.36: Ion images of DBrDFCNBph at t = 2 ps during Coulomb explosion at z = +23 on xz-plane generated from original method (open markers) and current method (filled markers) where different fragment ions are generated from the same atoms between the two methods. In original method, the fragment ions are (a) Br^+ from Br1 and Br2, (c) C^+ from C5, C6, C8, C9, C10, and C13, and (e) C^+ and F^+ from C3, C7, F1, and F2. In current method, the fragment ions are (b) Br^{2+} from Br1 and Br2, (d) ${C_6}^{3+}$ from C5, C6, C8, C9, C10, and C13, and (f) CF^+ from C3, C7, F1, and F2.

We add the caveat that the simulations assumed that the Coulomb exploding parent ion is present in its ground electronic state. If it is formed in higher electronic states this could destabilise the bonding further, leading to more extensive fragmentation. The extent of fragmentation observed in the new simulations can be understood intuitively by inspecting the atomic partial charges within the parent ion as listed in Table 7.11. For example, both Br atoms possess partial charges much higher than the +1 assigned in the earlier simulations, explaining the higher terminal velocities of the Br^+ atomic ions in the new simulations. Similar arguments explain the differences observed for the terminal velocity of the N^+ ion, which has an initial charge of +2.182 within the molecular ion, compared with +1 in the earlier simulations, and the H^+ ions, which have an initial charge much lower than the +1 assumed in the earlier simulations.

7.3.1.3 Covariance-map imaging

To fully utilise the power of Coulomb explosion to probe molecular structures, covariance-map imaging is required. According to Equation (7.1), covariance describes the extent of correlation between two variables.

$$cov(A,B) = \langle (A - \langle A \rangle) * (B - \langle B \rangle) \rangle \tag{7.1}$$

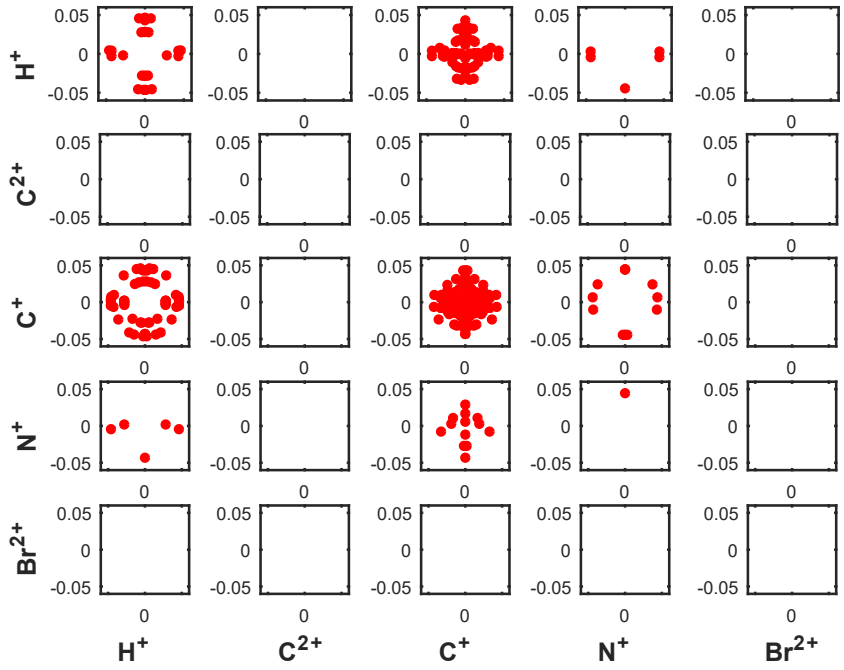
Covariance may be used to measure the correlations between the velocity vectors of various fragment ions after Coulomb explosion. It is necessary to transform the image data from the original coordinate system to a recoil-frame system in which one type of fragment ion is regarded as the "reference" ion, and the covariances between all other partner ions and the reference ion are calculated. The covariance maps are then rotated so that the reference ion velocity vector is pointing up vertically. The resulting maps can then be compared with the covariance-map images obtained by processing the data from the original experiments [12].

Figure 7.37 and Figure 7.38 compare the recoil-frame covariance images obtained from experiment with those obtained from original Coulomb-only simulation method and current simulations at MP2/6-311G(d,p) level, respectively, where the molecular axis is aligned parallel to the image plane (perpendicular to the time-of-flight axis of the experiment). Figure 7.39 and Figure 7.40 perform the same comparison when molecular axis is aligned perpendicular to the image plane (parallel to the time-of-flight axis).

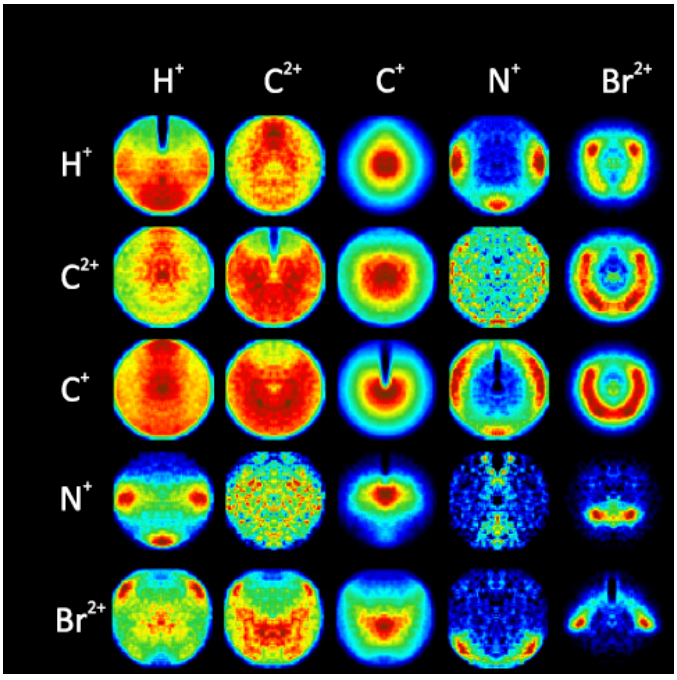
As mentioned in Sections 7.3.1.1 and 7.3.1.2, the main differences between the predictions of the two sets of simulations lie in the behaviour of the carbon atoms, particularly those on the Br-substituted ring, and in the CF^+ molecular fragments predicted by the new simulations. The fate of remaining atoms is similar in both sets of simulations.

The covariance images predicted by the present simulations (Figure 7.38 (a)) with either H^+ or N^+ as the reference ion are in very good agreement with their experimentally measured counterparts for molecules oriented with their principal axis parallel to the image plane (Figure 7.38 (b)). However, we note that the experimental images contain contributions from many different parent ion charge states, whereas the simulations only show products arising from the +23 charge state. In particular, the H^+/H^+, H^+/N^+, and N^+/H^+ covariance images show very good agreement with experiment, and generally also match with the predictions of the previous simulation method. The Br^{2+} and C^{2+} ions predicted by the present method and observed in the experiments are not observable in the earlier simulations. Covariance images with Br^{2+} as the reference ion show reasonably good agreement with experiment. It is difficult to draw conclusions on the performance with respect to the C^+ and C^{2+} ions, given that all 13 carbon ions are in single charge state in original simulations, but only two C^+ and three C^{2+} are formed in current simulations.

For parent molecules in perpendicular alignment, the agreement between simulations (Figure 7.39 (a) and 7.40 (a)) and experiment (Figure 7.39 (b)) is less convincing. We

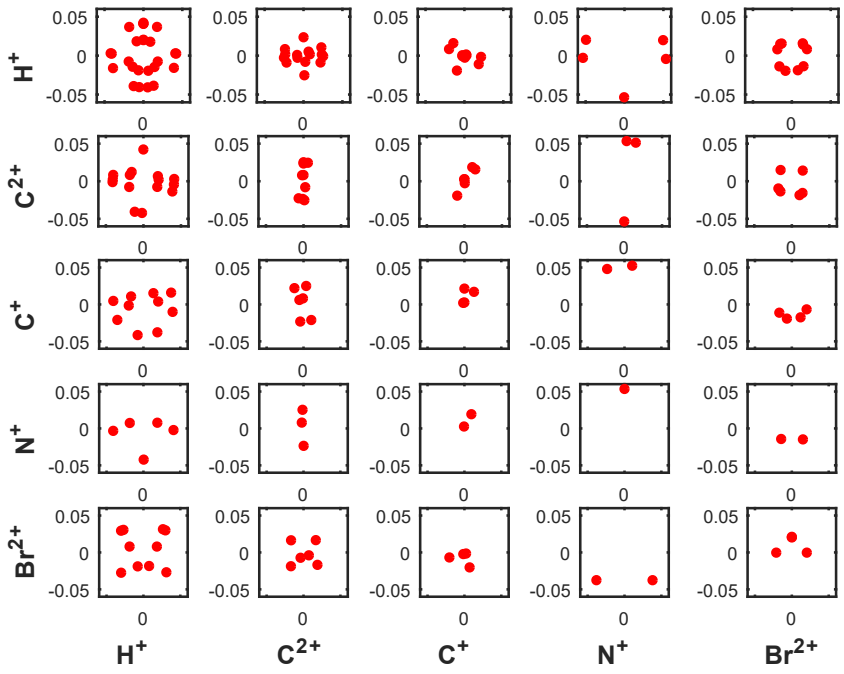


(a)

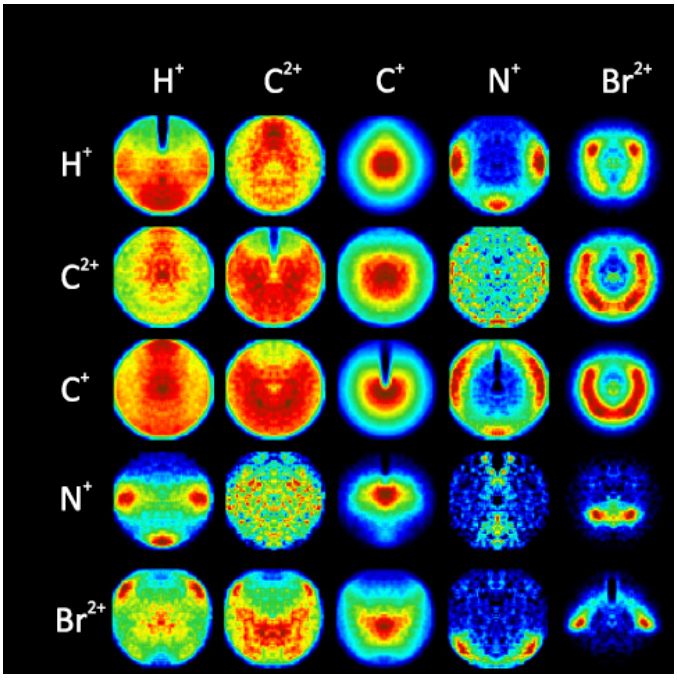


(b)

Figure 7.37: Recoil-frame covariance images in parallel alignment from (a) original simulation method and (b) experimental measurement. Note that reference ions are vertically labelled and plotted ions are horizontally labelled.

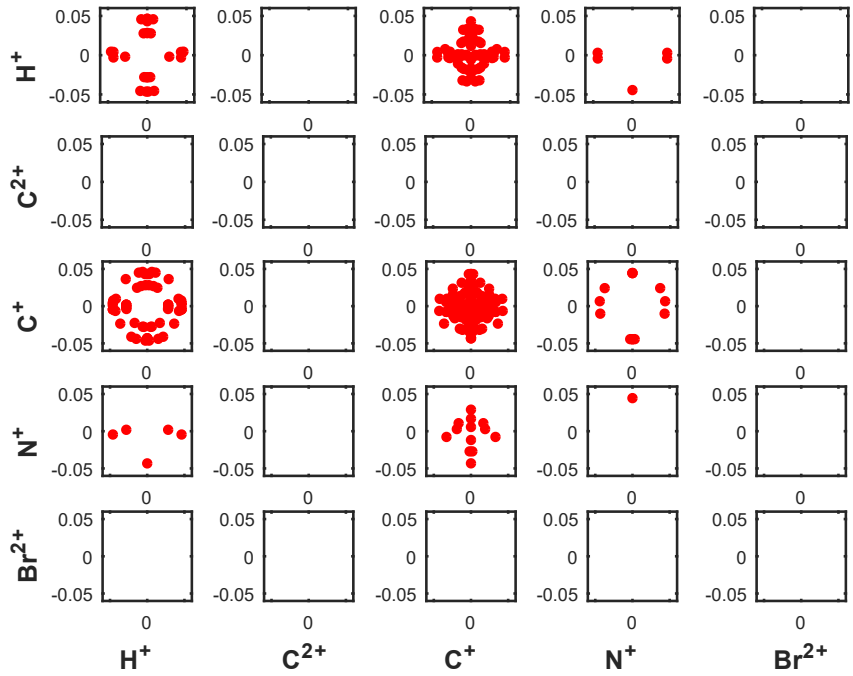


(a)

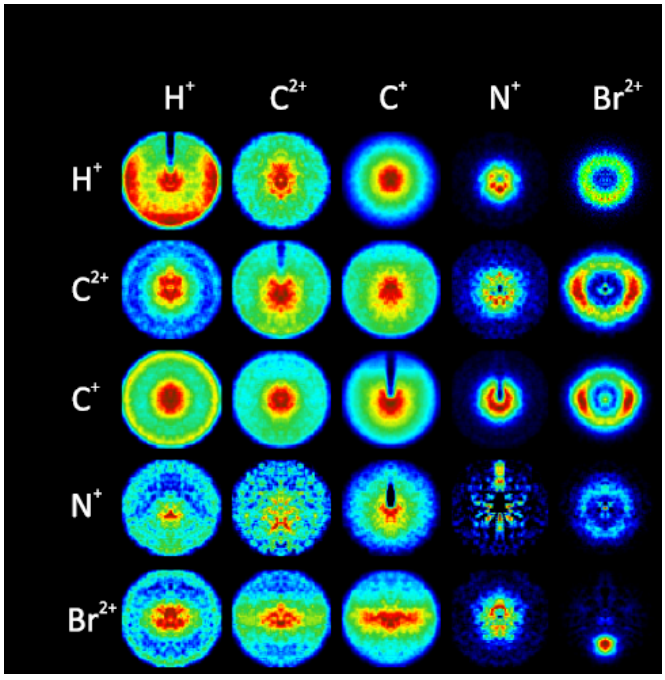


(b)

Figure 7.38: Recoil-frame covariance images in parallel alignment from (a) current simulation method at MP2/6-311G(d,p) and (b) experimental measurement. Note that reference ions are vertically labelled and plotted ions are horizontally labelled.

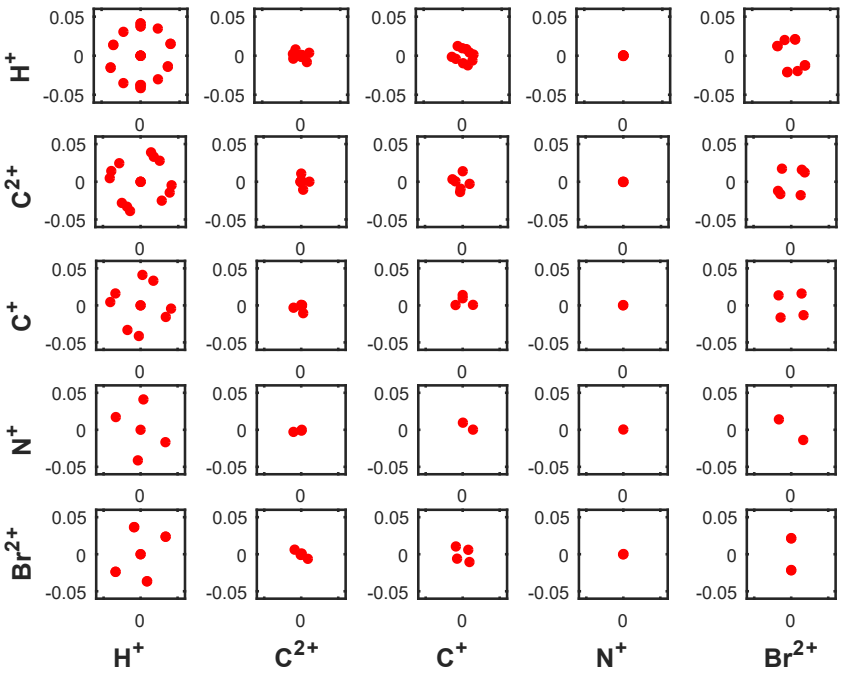


(a)

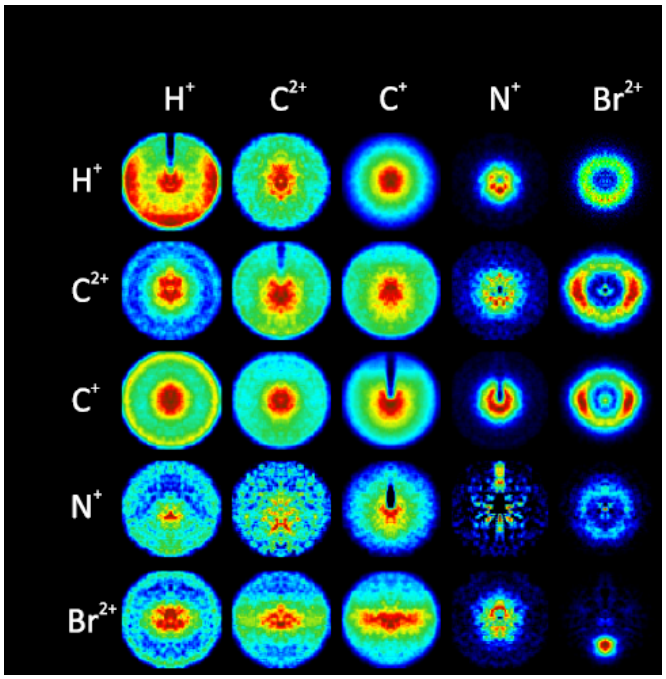


(b)

Figure 7.39: Recoil-frame covariance images in perpendicular alignment from (a) original simulation method and (b) experimental measurement. Note that reference ions are vertically labelled and plotted ions are horizontally labelled.



(a)



(b)

Figure 7.40: Recoil-frame covariance images in perpendicular alignment from (a) current simulation method at MP2/6-311G(d,p) and (b) experimental measurement. Note that reference ions are vertically labelled and plotted ions are horizontally labelled.

hope that this will improve once it becomes possible to perform multiple simulations with appropriately sampled initial conditions.

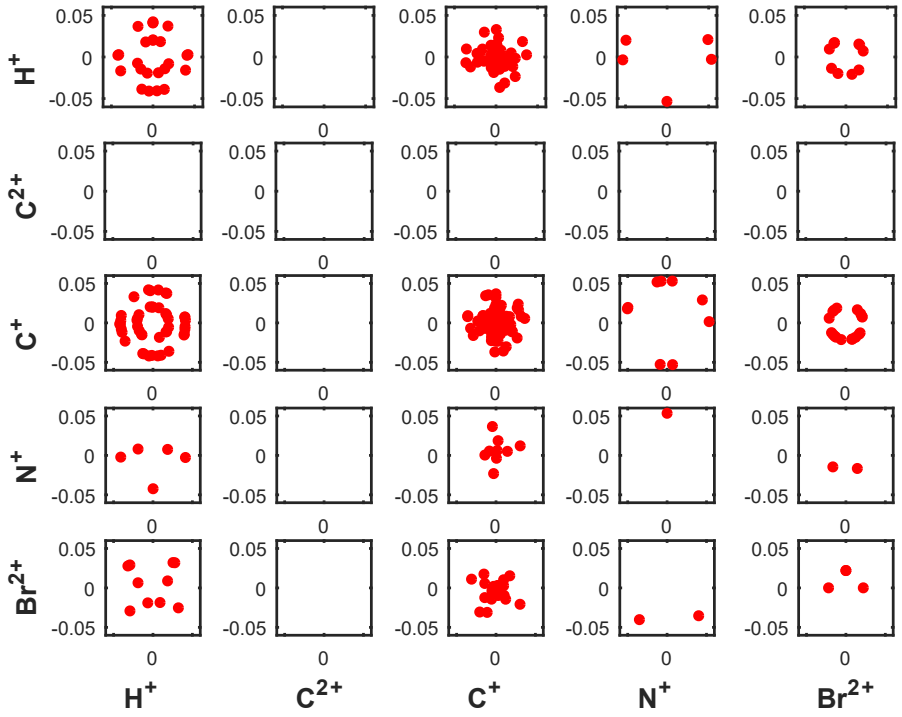
As shown in Table 7.11, the choice of basis set has a significant effect on the partial charges and fate of the carbon atoms. Using the 6-31G(d,p) basis set there are nine C^+ ions predicted, whereas the cc-pVTZ basis set yields five C^+ ions. Figures 7.41 to 7.44 show covariance images simulated using the two basis sets in both parallel and perpendicular molecular orientations.

7.4 Conclusion and future work

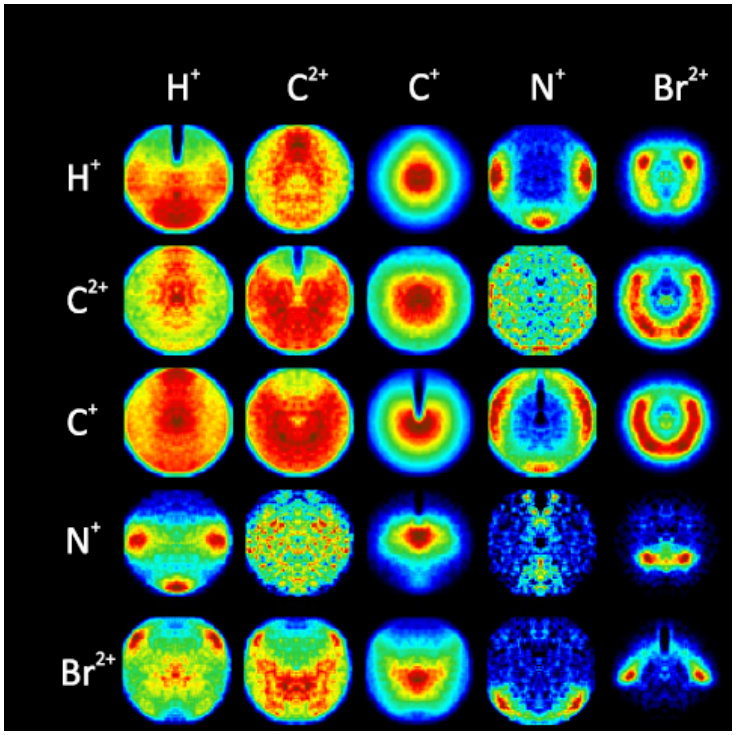
The simulation program developed in Chapter 6 has been tested on a handful of molecules with different chemical characteristics. The overall results confirm that this simulation method is advantageous in the following aspects:

1) It is not only versatile in predicting a wide range of chemical and dynamical outcomes using an *ab initio* approach, but also producing information that is highly self-consistent and shows promising agreement with available experimental data.
2) It is capable of predicting distinctive features of fragment ion formation and bond breakage processes, as well as other outcomes that are not easily measurable in experiments, such as partial charge evolution.
3) It allows for adjusting key input parameters such as level of theory, ODE integration error tolerance, and initial conditions of molecular system.
4) Although the current program is limited to a single molecular system in the electronic ground state, it is possible to extend the applicability at the cost of extra computational resources.

One of the most desirable improvements is to repeat the trajectory simulation for a range of initial conditions sampled by using Monte-Carlo methods. Obviously, this is severely limited by the computational time per one trajectory. Only for very small systems where

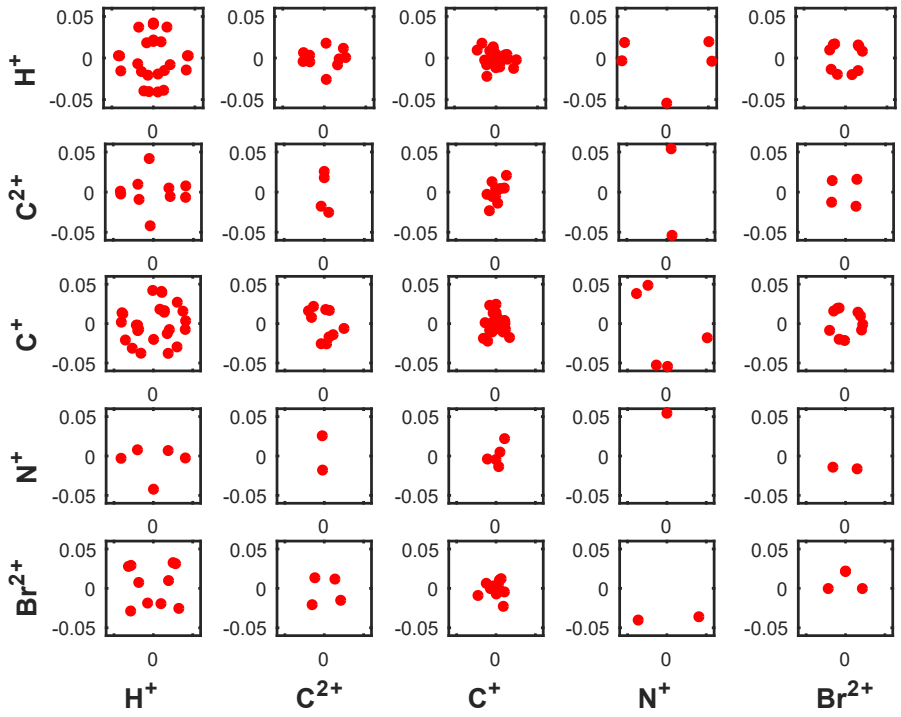


(a)

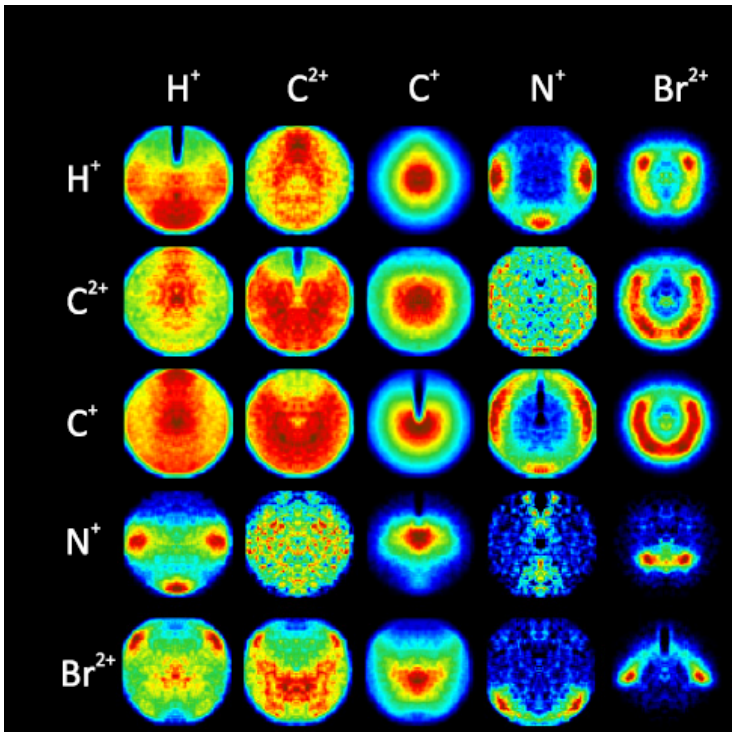


(b)

Figure 7.41: Recoil-frame covariance images in parallel alignment from (a) current simulation method at MP2/6-31G(d,p) and (b) experimental measurement [12]. Note that reference ions are vertically labelled and plotted ions are horizontally labelled.

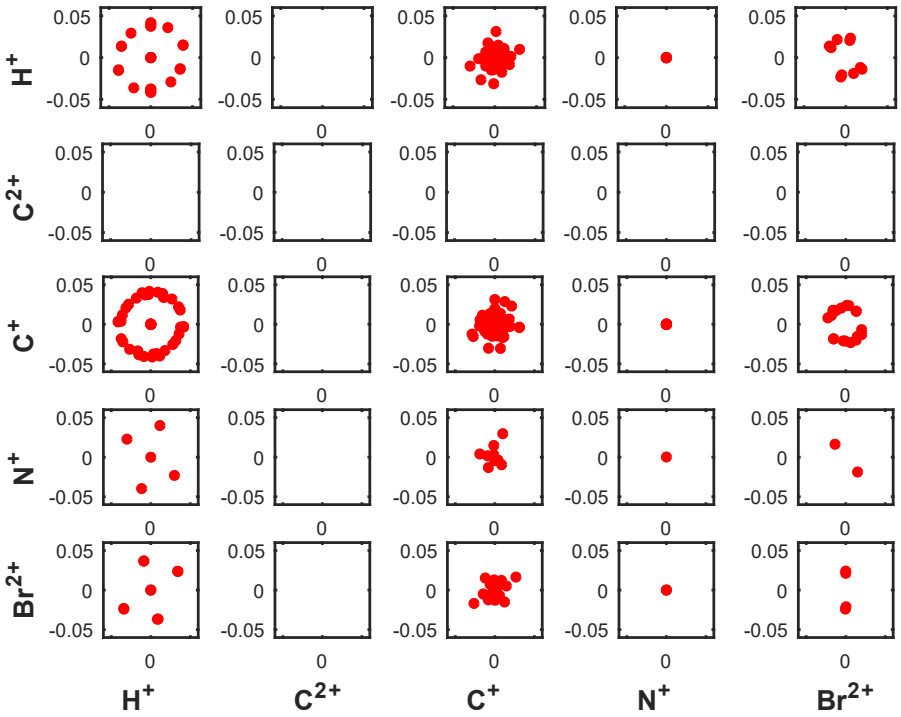


(a)

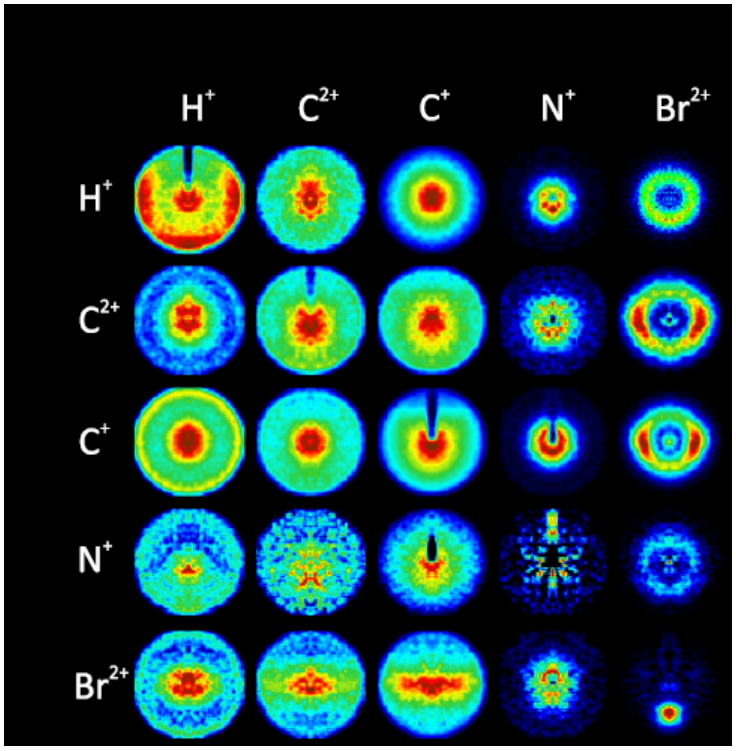


(b)

Figure 7.42: Recoil-frame covariance images in parallel alignment from (a) current simulation method at cc-pVTZ and (b) experimental measurement [12]. Note that reference ions are vertically labelled and plotted ions are horizontally labelled.

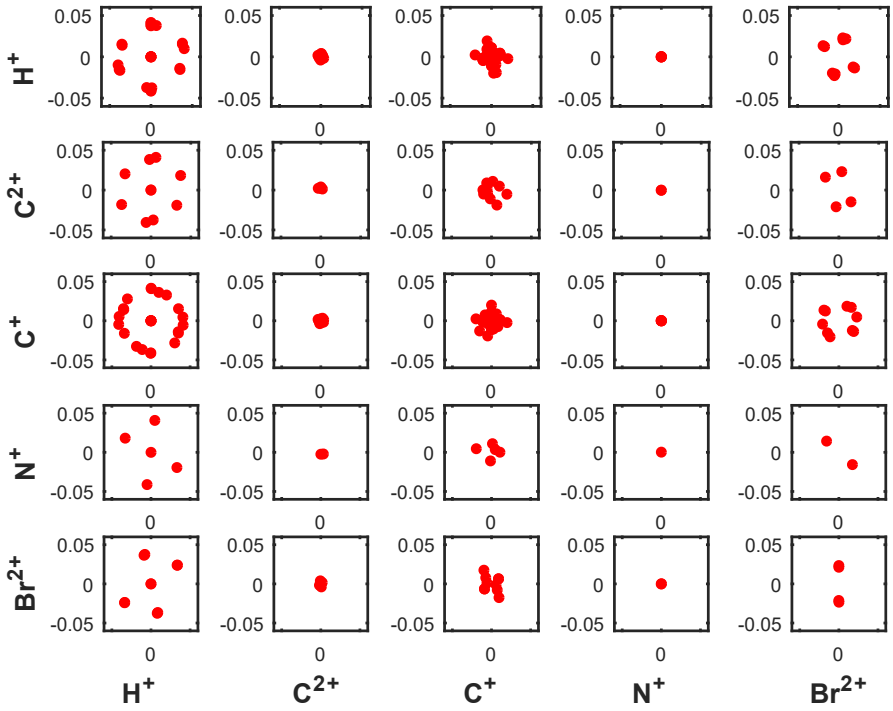


(a)

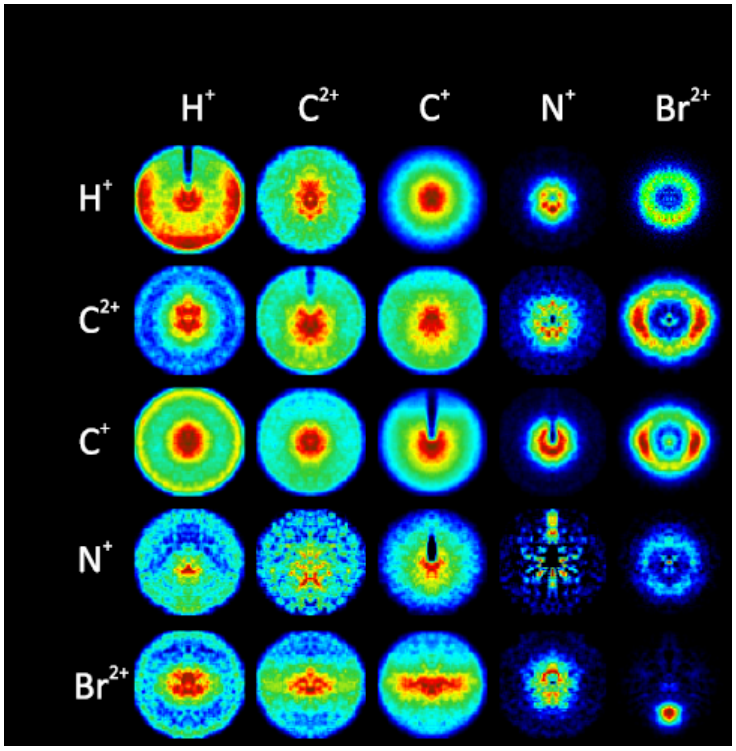


(b)

Figure 7.43: Recoil-frame covariance images in perpendicular alignment from (a) current simulation method at MP2/6-31G(d,p) and (b) experimental measurement [12]. Note that reference ions are vertically labelled and plotted ions are horizontally labelled.



(a)



(b)

Figure 7.44: Recoil-frame covariance images in perpendicular alignment from (a) current simulation method at cc-pVTZ and (b) experimental measurement [12]. Note that reference ions are vertically labelled and plotted ions are horizontally labelled.

a few minutes is needed for one trajectory would this be considered to be technically feasible for a statistically significant total number of trajectories (e.g. >500).

It is certainly necessary to explore the performance of the current program by testing on many more molecular targets of practical interest, and comparing the results with experimental data where available. This will allow key parameters to be characterized for certain types of problem and systems. A key question is how to determine the lowest level of theory needed to achieve acceptable accuracy for a particular molecular system thereby maximising computational efficiency and minimising run time. If the unnecessary computational time can be greatly reduced without compromising the acceptable accuracy needed, more time will be made available for running full-scale simulation of experiments with thousands of trajectories.

One of the eventual aims of the velocity-map imaging experiments is to use the relationship between initial position and final velocity of the atomic fragments of a Coulomb explosion as a method for gaining structural information on gas-phase molecules. The trajectory calculations carried out on various initial charge states of formyl chloride, *cis*-1,2,-dichloroethene, fluoromethane, and chloroiodomethane demonstrate that this can be achieved when the initial charge state is sufficiently high. In these cases, Coulomb repulsion is the dominant force, and there is a clear relationship between the initial atomic positions and final atomic velocities, with further increases in charge leading to little change in the "shapes" of the trajectories, though the magnitudes of the final velocities continue to increase with increasing charge state. In contrast, low charge states often undergo complex fragmentation dynamics, controlled by a mixture of attractive and repulsive forces. Dissociation is often incomplete, and there is no straightforward relationship between initial position and final velocity of the atoms.

For complete dissociation into atoms, it is found that the final atomic charge states are determined purely by the ionization potentials of the atoms, with the system adopting

the charge distribution that minimises its energy.

Overall, the current simulation program is proved to be a powerful, robust, and versatile tool for simulating Coulomb explosion processes of highly charged molecular ions. It is expected that it will be used for promoting the understanding of Coulomb explosion dynamics and will provide theoretical input for relevant experimental work.

References

[1] D. A. Fisher, C. H. Hales, D. L. Filkin, M. K. W. Ko, N. D. Sze, P. S. Connell, D. J. Wuebbles, I. S. A. Isaksen, and F. Stordal. "Model calculations of the relative effects of CFCs and their replacements on stratospheric ozone". In: *Nature* 344 (1990), p. 508.

[2] A. R. Ravishankara, A. A. Turnipseed, N. R. Jensen, S. Barone, M. Mills, C. J. Howard, and S. Solomon. "Do Hydrofluorocarbons Destroy Stratospheric Ozone?" In: *Science* 263.5143 (1994), p. 71.

[3] W. H. Fang and R. Z. Liu. "*Ab initio* studies of dissociation pathways on the ground- and excited-state potential energy surfaces for formyl chloride (HClCO)". In: *The Journal of Chemical Physics* 115.22 (2001), pp. 10431–10437.

[4] S. Anand and H. B. Schlegel. "Unimolecular dissociation of formyl halides HXCO $\rightarrow$ CO + HX (X = F, Cl): An *ab initio* direct classical trajectory study". In: *Journal of Physical Chemistry A* 106.47 (2002), pp. 11623–11629.

[5] M. Mühlhäuser and M. Gruber-Stadler. "*Ab initio* MRD-CI study of excited states of formyl chloride HClCO and photofragmentation along Cl–C cleavage". In: *Chemical Physics* 343.2 (2008), pp. 311–318.

[6] R. Krishnan, J. S. Binkley, R. Seeger, and J. A. Pople. "Self-consistent molecular orbital methods. XX. A basis set for correlated wave functions". In: *The Journal of Chemical Physics* 72.1 (1980), pp. 650–654.

[7] A. D. McLean and G. S. Chandler. "Contracted Gaussian basis sets for molecular calculations. I. Second row atoms, Z=11–18". In: *The Journal of Chemical Physics* 72.10 (1980), pp. 5639–5648.

[8] T. Yatsuhashi, N. Nakashima, and J. Azuma. "Coulomb Explosion of Dichloroethene Geometric Isomers at 1 PW cm^{-2}". In: *The Journal of Physical Chemistry A* 117.7 (2013), pp. 1393–1399.

[9] U. Ablikim, C. Bomme, H. Xiong, E. Savelyev, R. Obaid, B. Kaderiya, S. Augustin, K. Schnorr, I. Dumitriu, T. Osipov, R. Bilodeau, D. Kilcoyne, V. Kumarappan, A. Rudenko, N. Berrah, and D. Rolles. "Identification of absolute geometries of *cis* and *trans* molecular isomers by Coulomb Explosion Imaging". In: *Scientific Reports* 6.38202 (2016), pp. 1–8.

[10] F. Weigend and R. Ahlrichs. "Balanced basis sets of split valence, triple zeta valence and quadruple zeta valence quality for H to Rn: Design and assessment of accuracy". In: *Physical Chemistry Chemical Physics* 7.18 (2005), pp. 3297–3305.

[11] S. G. Lias. *Ionization Energy Evaluation. In: Linstrom, P. J. and Mallard, W. G. (eds.) NIST Chemistry WebBook, NIST Standard Reference Database Number 69*. Gaithersburg, MD, 20899: National Institute of Standards and Technology.

[12] C. S. Slater, S. Blake, M. Brouard, A. Lauer, C. Vallance, C. S. Bohun, L. Christensen, J. H. Nielsen, M. P. Johansson, and H. Stapelfeldt. "Coulomb-explosion imaging using a pixel-imaging mass-spectrometry camera". In: *Physical Review A* 91.5 (2015), p. 053424.

[13] C. S. Slater, S. Blake, M. Brouard, A. Lauer, C. Vallance, J. J. John, R. Turchetta, A. Nomerotski, L. Christensen, J. H. Nielsen, M. P. Johansson, and H. Stapelfeldt. "Covariance imaging experiments using a pixel-imaging mass-spectrometry camera". In: *Physical Review A* 89.1 (2014), p. 011401.

8

Summary and Perspectives

This thesis has demonstrated various approaches to unravelling the quantitative dynamics of ionization processes. The first part of the thesis described experimentally measured and calculated absolute total ionization cross-section data for a variety of interstellar molecules. This was followed by the introduction of a newly developed Coulomb explosion simulation software suite that can be used to help interpret data from velocity-map imaging experiments.

The total ionization cross-section instrument developed in this thesis fully addresses all experimental requirements. These include the achievement of full collection efficiency of both electron and ion currents, accurate measurement of absolute gas sample pressure, and a collision pathlength that is explicitly calibrated against simulation and standard measurements from Rapp and Englander-Golden [1]. This ensures that the absolute cross-sections measured can be considered to be reliable, without requiring normalisation to other data.

Extensive effort was concentrated on optimising various parts of the apparatus in order to attain optimal operational status. The ion optics were designed through SIMION simulations [2]. The optimised electrostatic optics design was combined with high quality,

extremely sensitive, electronics in order to achieve the most accurate measurement. The MKS Type 690A Series Absolute Baratron® pressure transducer is capable of measuring gas pressure with accuracy as high as 0.05% of reading.

The molecules measured in this thesis have long been of interest within astrochemistry community, where the ionization cross-section data are desired [3]. This is the first time that total ionization cross-sections have been measured for these molecules, and the cross-sections demonstrated interesting features, as detailed in Chapter 5.

One of the ways in which the total ionization cross-sections recorded in the present work will be used in future will be to convert relative partial ionization cross-sections recorded on our electron-molecule crossed-beam instrument [4, 5] into absolute partial cross-sections. Crossed-beam experiments will also allow the speed and angular distributions of the dissociative ionization products to be measured, providing further insight into the dynamics of electron ionization. We are currently working on establishing a comprehensive database of electron-ionization data for molecules relevant to astrochemistry and plasma science. This will include total and partial ionization cross-sections, cross-sections predicted using the BEB model [6], and fragment ion velocity distributions where available.

The Coulomb explosion simulations described in Chapters 6 and 7 proved to be able to predict a diverse range of outcomes as a function of the initial molecular geometry and charge. The approach can be adapted for use with any molecule, and the fragmentation products predicted by the simulations were consistent with expectations based on knowledge of relative bond strengths. The software has been rigorously tested on molecules of different structure and sizes to confirm its robustness and versatility. Though there is still a significant amount of work to do in terms of comparing the results of the simulations with data from velocity-map imaging studies of Coulomb explosion processes, preliminary comparisons with a limited amount of experimental data are encouraging. Importantly,

the simulations allow investigation of phenomena such as atomic partial charge evolution and structural evolution during the Coulomb explosion to be investigated, which are not readily amenable to experimental measurement.

Over the course of the work described in this thesis, a great deal of time and effort was devoted to overcoming technical issues associated with implementing the simulations. Now that these issues have been overcome, the code has been developed into a user-friendly executable Linux program with easily adjustable input parameters (See Appendix E), and may in future even be developed into a stand-alone software package with its own graphical user interface (GUI). Developing the approach to allow multi-trajectory simulations based on statistical sampling of a range of initial conditions is a key future goal, and would allow the simulations to provide a much better reflection of the experimental reality. Limitations on computational capacity mean that this is not possible at present, but the ever-increasing CPU power available means that it may well become possible in future.

References

[1] D. Rapp and P. Englander-Golden. “Total Cross Sections for Ionization and Attachment in Gases by Electron Impact. I. Positive Ionization”. In: *The Journal of Chemical Physics* 43.5 (1965), pp. 1464–1479.

[2] D. A. Dahl. “SIMION for the personal computer in reflection”. In: *International Journal of Mass Spectrometry* 200.1–3 (2000), pp. 3–25.

[3] C. N. Shingledecker. “On cosmic rays in astrochemical models”. Ph.D. thesis, University of Virginia. 2018.

[4] J. N. Bull, J. W. L. Lee, and C. Vallance. “Quantification of ions with identical mass-to-charge (m/z) ratios by velocity-map imaging mass spectrometry”. In: *Physical Chemistry Chemical Physics* 15.33 (2013), pp. 13796–13800.

[5] J. N. Bull, J. W. L. Lee, and C. Vallance. “Electron ionization dynamics of N_2 and O_2 molecules: Velocity-map imaging”. In: *Physical Review A* 91.2 (2015), p. 022704.

[6] W. Hwang, Y.-K. Kim, and M. E. Rudd. “New model for electron-impact ionization cross sections of molecules”. In: *Journal of Chemical Physics* 104.8 (1996), pp. 2956–2966.

Appendices

A

Derivation of Beer-Lambert law for describing electron ionization

The electron ionization cross-section can be determined from experimentally measurable variables using the Beer-Lambert law, which relates the attenuation of the incident electron beam through ionizing collisions with the sample gas. A typical experimental setup is shown in Figure A.1. Over a suitably short pathlength increment dl, the attenuation of the electron beam current dI is proportional to the number density n of the sample gas, the pathlength increment dl through the sample gas, and the current of the electron beam before entering this increment), I:

$$\mathrm{d}I = -\sigma n I \mathrm{d}l \tag{A.1}$$

The proportionality constant σ is the total ionization cross-section (assuming that ionization is the dominant process).

We can rearrange Equation A.1 and integrate over the pathlength of the collision cell from 0 to l, and assume n is uniformly distributed over the length l:

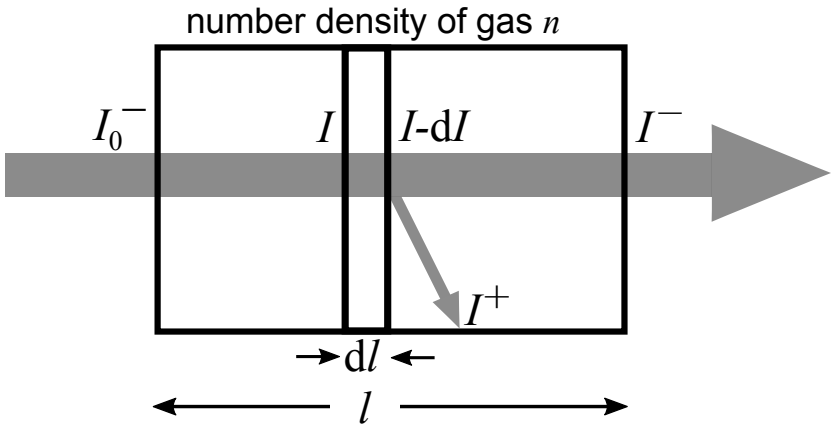


Figure A.1: Schematic conceptual diagram of electron ionization cross-section experiment with terms used in Beer-Lambert law derivation. The infinitesimal pathlength increment dl is shown in the middle.

$$\int_{I_0^-}^{I^-} \frac{\mathrm{d}I}{I} = -\sigma n \int_0^l \mathrm{d}l \tag{A.2}$$

where I_0^- is the initial current of the electron beam before passing through the gas sample, and I^- is the current after passing through the gas sample. Integration of Equation A.2 leads to:

$$\ln \frac{I^-}{I_0^-} = -\sigma n l \tag{A.3}$$

or

$$\frac{I^-}{I_0^-} = \mathrm{e}^{-\sigma n l} \tag{A.4}$$

This is essentially in the form of original Beer-Lambert law.

During an experiment, positive ion current I^+ is generated, which in quantity is equal to the reduced amount of electrons, i.e. $I^- = I_0^- - I^+$. Equation (A.4) can then be re-written as:

$$\frac{I_0^- - I^+}{I_0^-} = \mathrm{e}^{-\sigma n l} \tag{A.5}$$

Since only a very small amount of electrons are lost, i.e. $I^- \approx I_0^-$, we have

$$\frac{I^- - I^+}{I^-} = \mathrm{e}^{-\sigma nl} \tag{A.6}$$

Also, according to Maclaurin series expansions:

$$\mathrm{e}^{-\sigma nl} = \sum_{k=0}^{k} \frac{(-\sigma nl)^k}{k!} = 1 + (-\sigma nl) + \frac{(-\sigma nl)^2}{2!} \cdots \tag{A.7}$$

$-\sigma nl$ is usually a very small quantity (i.e. $\sigma nl \ll 1$). For example, if pressure is 2×10^{-4} Torr and temperature is 293.15 K, according to ideal gas law, the number density n is approximately 1×10^{-5}. This allows the right-hand side of Equation (A.7) to only take the first two terms:

$$\mathrm{e}^{-\sigma nl} \approx 1 - \sigma nl \tag{A.8}$$

By considering Equations (A.6) and (A.8):

$$\frac{I^- - I^+}{I^-} = 1 - \sigma nl \tag{A.9}$$

which leads to

$$1 - \frac{I^+}{I^-} = 1 - \sigma nl \tag{A.10}$$

and

$$\frac{I^+}{I^-} = \sigma nl \tag{A.11}$$

which is Equation (2.26) in Chapter 2.

B

Standard operating procedures of total ionization cross-section measurement

Contents

B.1 Procedures of starting and terminating a measurement 247
B.2 Maintenance considerations 249

B.1 Procedures of starting and terminating a measurement

The LabVIEW program `cross-section.vi` provides the main instrument control interface. A standard measurement consists of the following steps:

1) Check that the Series 203 Granville-Phillips® variable leak valve is fully closed ("16" on the scale). Pump down the sample line for 1 minute and then introduce the sample gas to the sample line.
2) Check to make sure that the background pressure within the instrument is below 1×10^{-7} Torr.

3) After at least 4 hours warm-up time, zero the MKS Type 690A.1 high accuracy Baratron capacitance manometer (refer to manual for instructions on how to do this).
4) After at least 4 hours warm-up time, zero both Keithley model 486 and Model 6487 picoammeters (used to measure the ion and electron currents, respectively).
5) Turn on the multiple channel power supply unit that provides bias potentials to the electrostatic optics within the instrument.
6) Turn on the filament power supply (Aim-TTi Model PL 155). Press "output" and turn up the voltage slightly, then gradually turn up the current to a few hundred mA.
7) Open LabVIEW program `cross-section.vi`.
8) Enter the desired static voltages, range and step size for the electron energy scan, name and path of output files, number of readings (which needs to match the number of files entered), and waiting time. It is recommended to set the first warm-up time to 30 minutes (can only be specified in Block Diagram). Make sure to tick the "Save Data?" box.
9) Check and make sure the program is using the following default settings: MKS Com Address=COM5, VISA Refnum in=GPIB0::2:, Thermoprobe=6.
10) Click the "Run" button from the Toolbar and then click the "Set Static Voltages" button. Check the output panel to make sure the potentials have been set correctly.
11) Click the "Run Experiment" button. Then click the "Pause" button on the Toolbar.
12) Gradually open the Series 203 Granville-Phillips® variable leak valve, while carefully checking the pressure reading from the MKS 670B Signal Conditioner. Try to maintain a stable pressure within the collision cell between 2×10^{-4} Torr and 3×10^{-4} Torr.
13) Gradually turn up the filament power supply to 2.4 A. The current display on Keithley model 486 picoammeter should increase to a few nA.
14) Click the "Pause" button at LabVIEW Toolbar to resume the program.

15) After the pre-set 30 minutes warm-up time, measurement will start. Real-time readings of the collision cell pressure, ion and electron currents, and cell temperature will be plotted, together with the calculated total cross-section data at every electron energy. It is also advisable to check that the output file is indeed created.

To terminate an experiment:

1) Turn off the Series 203 Granville-Phillips® variable leak valve. Do not tighten further than 16 on the scale, as this may damage the valve.
2) Turn down the current on filament power supply to zero, then turn down the voltage to zero.
3) Click "Abort Experiment".
4) Click "Stop" button at the toolbar.
5) Turn off the filament power supply.
6) Turn off the multiple channel power supply unit.
7) Turn off both Keithley model 486 and Model 6487 picoammeters.
8) Evacuate sample line once the measurements have been completed.

B.2 Maintenance considerations

The ion optics within the instrument must be cleaned periodically. Build-up of ion and/or electron burn on the optics manifests as an anomalous spike or peak in the measured cross-sections near 70 eV. When reassembling the system, care must be taken to ensure that the filament is replaced precisely on axis. A number of precautions can be taken to increase the lifetime of the filament and the time interval between consecutive cleaning of the components.

1) Keep the filament current below 2.6 A.
2) Try not to allow the cell pressure to exceed 5×10^{-4} Torr when the filament is turned on. Particular vigilance is required for samples comprising the vapour

pressure above a liquid, due to their tendence to condense and re-evaporate within the system.

3) When adjusting the variable leak valve to set the cell pressure, first turn down the filament power current below 1 A (which should generate no electron beam), and then turn it up to 2.4 A once the cell pressure adjustment is finished. This ensures that even if there is a pressure surge, it is unlikely to damage the filament or to cause contamination of the cell.

C

Deconvolution method of cross-section data

With the current total ionization cross-section experimental apparatus and optimised static potentials, there exists a variation in potential along the axis of the cell, as shown in Figure C.1 based on SIMION simulations performed at an electron energy of 100 eV (as mentioned in Section 4.2.3, it is assumed that the potential along the axis of the cell is independent of electron energy due to the very small aperture on L3). The potential is lowest in the centre of the cell (approximately −7.870 V), and highest at the two ends of the cell (approximately −2.674 V). The slightly asymmetric shape of the potential is due to the different diameters of the apertures in lens elements L3 (1 mm) and L4 (4 mm). At any position along the axis of the cell, electrons from the filament have been accelerated from the nominal filament potential, e.g. −100 V, to a potential between −2.674 V to −7.870 V rather than 0 V. The electron energy at the point of an electron-molecule collision is therefore slightly lower than the nominal electron energy with a constant range of uncertainty. To correct for these overestimation and variation in electron energies, the measured cross-sections are deconvoluted from the potential

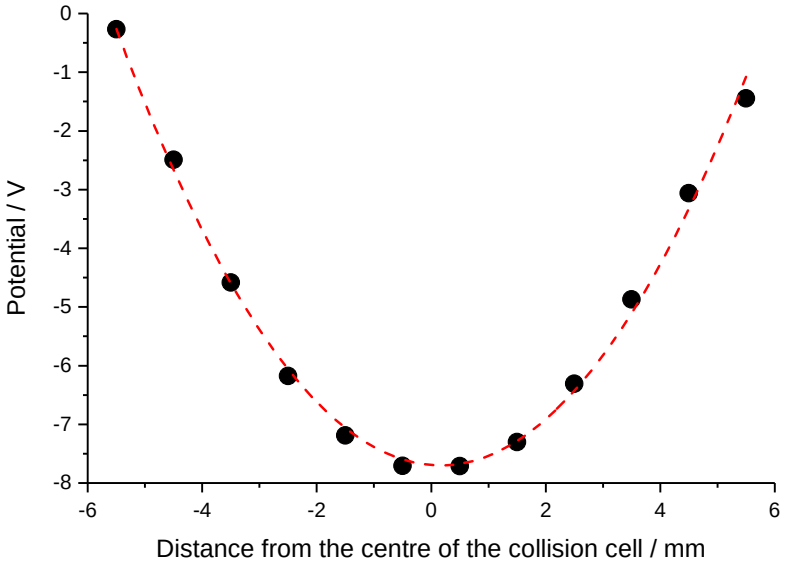


Figure C.1: Potential along the axis of the cell when EE = 100 eV. Dots are potentials simulated by SIMION. Dash line is the fitted polynomial curve with equation $y = 0.2322x^2 - 0.0736x - 7.6931$ ($R^2 = 0.9942$) where x is the distance from the centre of the collision cell (in mm) and y is corresponding potential (in V).

energy function along the collision axis.

As described in Section 2.4.2 and Appendix A, a typical total ionization cross-section experiment can be described by the simplified version of Beer-Lambert law (Equation (2.26)). A cross-section (σ) measured at each nominal electron energy (E_{nom}) is an average over many cross-sections measured at infinitesimal segments along the pathlength of the cell, each recorded at an actual electron energy (E_{act}) determined by the difference between the nominal electron energy and the potential energy within each respective segment. If the total pathlength, l, can be divided into K number of equal and infinitesimal segments, Equation (2.26) still applies for each segment:

$$\frac{I_k^+}{I^-} = \sigma_k n l_k \tag{C.1}$$

where $l_k = l/K$ and σ_k is the resolved cross-section at pathlength segment k where its actual electron energy is determined by the fitted polynomial equation obtained from Figure C.1. I^- and n are the same in all infinitesimal segments.

Equation (C.1) can be rearranged to give:

$$\sigma_k = K\frac{I_k^+}{I^- nl} \tag{C.2}$$

Since $I_1^+ + I_2^+ + I_3^+ + \cdots + I_K^+ = I^+$, summing Equation (C.2) over all K infinitesimal segments of pathlength l:

$$K\frac{I_1^+}{I^- nl} + K\frac{I_2^+}{I^- nl} + K\frac{I_3^+}{I^- nl} + \cdots + K\frac{I_K^+}{I^- nl} = K\frac{I^+}{I^- nl} = K\sigma_{\text{raw}} \tag{C.3}$$

or

$$\sigma_1 + \sigma_2 + \sigma_3 + \cdots + \sigma_K = K\sigma_{\text{raw}} \tag{C.4}$$

where σ_{raw} is the measured cross-section.

By dividing the range of the nominal electron energy over which the experiment measures the cross-section (i.e. from 10 eV to 300 eV) by a pre-specified dividing size into M elements, M equations in the form of Equation (C.4) can be constructed for each nominal electron energy from the 1st to the Mth element of the nominal electron energy array (i.e. from element 10 eV to 300 eV spaced by $(300 - 10)/(M - 1)$):

$$\begin{aligned}
\sigma_{1,1} + \sigma_{2,1} + \sigma_{3,1} + \cdots + \sigma_{K,1} &= K\sigma_{\text{raw},1} \\
\sigma_{1,2} + \sigma_{2,2} + \sigma_{3,2} + \cdots + \sigma_{K,2} &= K\sigma_{\text{raw},2} \\
\sigma_{1,3} + \sigma_{2,3} + \sigma_{3,3} + \cdots + \sigma_{K,3} &= K\sigma_{\text{raw},3} \\
&\cdots \\
\sigma_{1,M} + \sigma_{2,M} + \sigma_{3,M} + \cdots + \sigma_{K,M} &= K\sigma_{\text{raw},M}
\end{aligned} \tag{C.5}$$

Where $\sigma_{k,m}$ is the resolved cross section of the kth segment when the nominal electron energy is the mth value of the array defined in the range from 10 eV to 300 eV. $\sigma_{\text{raw},m}$ is the measured cross-section interpolated at the mth element of the array from 10 eV to 300 eV.

Since the energy of $\sigma_{\text{raw},m}$ is incremented by a constant size, it is expected that many terms on the left-hand side of each equation are common between neighbouring equations, i.e.

the equation describing mth nominal electron energy, compared with equation describing $(m-1)$th nominal electron energy, omits a few terms that describes the lower resolved electron energy and adds a few new terms that describes the higher resolved electron energy on the left-hand side of the equation. Furthermore, by rounding the divided electron energy values to certain decimal places, i.e. 0.01, many terms on the left-hand side within each equation become the same due to the near-symmetric nature of the potential curve as shown in Figure C.1. Therefore, a number N of unique actual electron energy terms can be determined and used in the left-hand side of all of the equations, with corresponding frequency coefficients to account for the number of times each term appears within a given equation. Irrelevant actual electron energy terms within each equation are simply assigned a zero frequency.

Therefore, linear equations (C.5) can be re-written as:

$$\begin{aligned}
a_{1,1}\sigma_1 + a_{2,1}\sigma_2 + a_{3,1}\sigma_3 + \cdots + a_{N,1}\sigma_N &= K\sigma_{\text{raw},1} \\
a_{1,2}\sigma_1 + a_{2,2}\sigma_2 + a_{3,2}\sigma_3 + \cdots + a_{N,2}\sigma_N &= K\sigma_{\text{raw},2} \\
a_{1,3}\sigma_1 + a_{2,3}\sigma_2 + a_{3,3}\sigma_3 + \cdots + a_{N,3}\sigma_N &= K\sigma_{\text{raw},3} \\
&\cdots \\
a_{1,M}\sigma_1 + a_{2,M}\sigma_2 + a_{3,M}\sigma_3 + \cdots + a_{N,M}\sigma_N &= K\sigma_{\text{raw},M}
\end{aligned} \tag{C.6}$$

where $a_{n,m}$ is the frequency of the nth unique actual electron energy term when the nominal electron energy is the mth element of the array from 10 eV to 300 eV, and σ_n is the resolved cross-section at nth unique actual electron energy.

Equations (C.6) can be considered as linear equations in matrix form, $\mathbf{AX} = \mathbf{B}$, where $\mathbf{A}$ is a $M \times N$ matrix representing the frequency coefficients, $\mathbf{X}$ is a $N \times 1$ matrix representing the resolved cross-sections at N unique actual electron energies, and $\mathbf{B}$ is a $M \times 1$ matrix representing the measured cross-sections at the M interpolated nominal electron energies multiply by K. If dividing sizes of pathlength segments (which determines K) and nominal electron energies (which determines M) are carefully chosen so that $N < M$, the linear

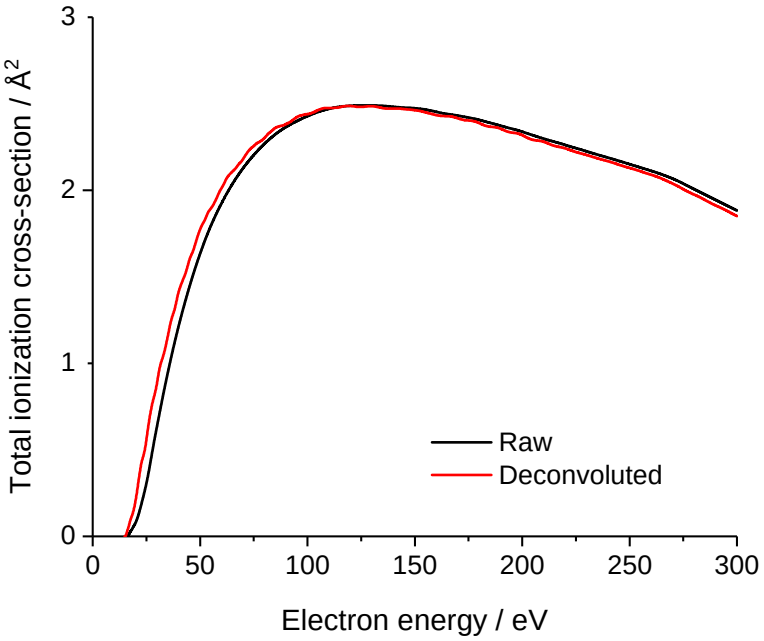


Figure C.2: Raw and deconvoluted data of total ionization cross-section of N_2. Raw data are interpolated at M = 5801 equally divided nominal electron energies, pathlength is divided into K = 1101 equal segments, and deconvoluted data are calculated at N = 2976 unique actual electron energies.

equations (C.6) can be readily solved to obtain resolved cross-sections at all N unique actual electron energies. For example, if K = 1101 (dividing size of pathlength = 0.01 mm) and M = 5801 (dividing size of nominal electron energy = 0.05 eV), N will be 2976, which is smaller than M. The N resolved cross-sections can then be used to interpolate the cross-sections at original nominal electron energies.

Figure C.2 shows an example of this deconvolution process for N_2 data. Since the nominal electron energies are overestimated by a mean value of 5.272 eV, it is expected that the deconvoluted data will be shifted to the left by this amount. However, since this energy difference and range of uncertainty have a far smaller effect on the cross-section in the high electron energy region than in the low electron energy region, the amount of shifting is noticeably larger at low electron energy than high electron energy, as confirmed in Figure C.2.

D

Absolute total ionization cross-section data

Contents

D.1 Interstellar molecules **258**
D.1.1 Acrolein (CH_2CHCHO) 258
D.1.2 Acrylonitrile (CH_2CHCN) 259
D.1.3 Methyl cyanide (CH_3CN) 260
D.1.4 Ethyl cyanide (CH_3CH_2CN) 261
D.1.5 Propyl cyanide ($CH_3CH_2CH_2CN$) 262
D.1.6 Isopropyl cyanide ($(CH_3)_2CHCN$) 263
D.1.7 Ethanethiol (CH_3CH_2SH) 264
D.1.8 Methyl oxirane (C_3H_6O) 265
D.1.9 Benzene (C_6H_6) 266
D.2 Common permanent gas molecules **267**
D.2.1 Nitrogen (N_2) 267
D.2.2 Carbon dioxide (CO_2) 268
D.2.3 Ethylene (C_2H_4) 269
D.2.4 Propene (C_3H_6) 270
D.2.5 Nitrous oxide (N_2O) 271
D.2.6 Tetrafluoromethane (CF_4) 272
D.2.7 Sulfur hexafluoride (SF_6) 273

D.1 Interstellar molecules

D.1.1 Acrolein (CH_2CHCHO)

Table D.1: Absolute total ionization cross-section data of acrolein.

EE / eV	σ / Å^2	SD / Å^2	EE / eV	σ / Å^2	SD / Å^2
14.5	0.753	0.034	153.1	7.825	0.027
19.5	2.145	0.039	158.0	7.789	0.039
24.4	3.274	0.044	163.4	7.743	0.041
29.4	4.132	0.039	168.3	7.695	0.045
34.4	4.872	0.030	172.7	7.652	0.042
39.3	5.498	0.034	178.3	7.594	0.018
44.2	6.025	0.046	183.2	7.537	0.012
49.2	6.450	0.015	188.1	7.472	0.040
54.2	6.815	0.036	193.2	7.406	0.044
59.1	7.105	0.030	198.0	7.341	0.055
64.1	7.357	0.017	203.2	7.278	0.018
69.1	7.564	0.015	207.8	7.220	0.046
74.0	7.723	0.040	212.7	7.164	0.011
78.9	7.836	0.048	217.7	7.113	0.015
83.8	7.919	0.025	222.9	7.052	0.011
88.7	7.965	0.033	227.4	6.978	0.009
93.9	8.000	0.020	232.2	6.870	0.022
98.8	8.019	0.025	237.1	6.761	0.016
103.5	8.046	0.020	242.5	6.663	0.014
108.8	8.060	0.013	247.8	6.600	0.026
113.6	8.059	0.028	251.8	6.567	0.012
118.6	8.041	0.004	257.9	6.523	0.009
123.7	8.022	0.010	262.5	6.474	0.008
128.7	8.007	0.002	267.4	6.406	0.022
133.6	7.985	0.008	272.3	6.338	0.001
138.5	7.955	0.039	277.3	6.271	0.002
143.3	7.911	0.023	282.1	6.208	0.008
148.5	7.866	0.024	286.9	6.141	

D.1.2 Acrylonitrile (CH_2CHCN)

Table D.2: Absolute total ionization cross-section data of acrylonitrile.

EE / eV	σ / Å^2	SD / Å^2	EE / eV	σ / Å^2	SD / Å^2	EE / eV	σ / Å^2	SD / Å^2
11.5	0.004		29.4	3.955	0.022	200.0	6.866	0.010
11.7	0.025		34.4	4.650	0.017	204.9	6.803	0.010
12.0	0.047		39.3	5.245	0.011	210.3	6.729	0.011
12.2	0.075		44.2	5.758	0.010	215.1	6.674	0.009
12.5	0.103		49.1	6.191	0.026	219.5	6.622	0.010
12.7	0.133		54.2	6.559	0.035	225.3	6.552	0.010
13.0	0.166		59.1	6.857	0.022	230.2	6.476	0.006
13.2	0.205		65.9	7.171	0.018	233.6	6.417	0.006
13.5	0.251		69.1	7.289	0.017	237.1	6.366	0.004
13.7	0.303		75.0	7.484	0.004	242.5	6.288	4E-04
14.0	0.365		78.9	7.581	0.053	247.6	6.214	0.004
14.2	0.430		83.8	7.675	0.016	251.8	6.145	
14.5	0.497		88.6	7.731	0.023	257.9	6.052	
14.7	0.565		93.9	7.770	0.022	262.5	5.994	
15.0	0.633		98.8	7.795	0.019	267.4	5.927	
15.2	0.698		103.5	7.801	0.014	272.3	5.844	
15.5	0.770		108.8	7.781	0.013	277.2	5.748	
15.7	0.841		113.6	7.749	0.014	282.1	5.658	
16.0	0.917	0.043	118.5	7.728	0.014	286.9	5.568	
16.2	0.990	0.021	123.7	7.709	0.015			
16.5	1.060	0.021	128.7	7.675	0.010			
16.7	1.127	0.002	133.6	7.640	0.014			
17.0	1.207	0.040	138.5	7.607	0.013			
17.2	1.269	0.029	143.3	7.550	0.012			
17.5	1.340	0.006	148.5	7.473	0.008			
17.7	1.398	0.013	153.1	7.418	0.009			
18.0	1.450	0.018	158.0	7.375	0.017			
18.2	1.492	0.005	163.4	7.318	0.010			
18.5	1.539	0.021	168.3	7.255	0.021			
18.7	1.589	0.031	172.7	7.201	0.018			
19.0	1.639	0.031	178.3	7.138	0.011			
19.2	1.703	0.029	185.3	7.058	0.009			
19.5	1.771	0.015	190.2	6.997	0.008			
24.4	3.087	0.033	194.3	6.947	0.009			

D.1.3 Methyl cyanide (CH_3CN)

Table D.3: Absolute total ionization cross-section data of methyl cyanide.

EE / eV	σ / Å^2	SD / Å^2	EE / eV	σ / Å^2	SD / Å^2
13.5	0.008		148.5	5.967	0.065
14.0	0.103		153.1	5.933	0.048
14.5	0.215	0.006	158.0	5.893	0.099
15.0	0.336	0.008	163.4	5.854	0.051
15.5	0.470	5E-04	168.3	5.818	0.059
16.0	0.617	0.005	172.7	5.784	0.014
16.5	0.742	0.008	178.3	5.721	0.010
17.0	0.847	0.009	183.2	5.669	0.098
17.5	0.939	0.009	188.0	5.604	0.023
24.4	2.347	0.028	193.2	5.545	0.042
29.4	3.105	0.020	198.0	5.495	0.006
34.4	3.722	0.031	203.2	5.461	0.062
39.3	4.233	0.018	207.8	5.415	0.043
44.2	4.651	0.025	212.7	5.361	0.052
49.2	4.992	0.027	217.6	5.317	0.052
54.2	5.268	0.031	222.9	5.269	0.004
59.1	5.482	0.050	227.4	5.227	0.047
64.1	5.685	0.031	232.2	5.169	0.022
69.1	5.844	0.030	237.1	5.119	0.030
74.0	5.981	0.032	242.5	5.058	0.087
78.9	6.067	0.006	247.7	5.019	0.060
83.8	6.128	0.065	251.8	4.987	0.049
88.7	6.151	0.072	257.9	4.927	0.007
93.9	6.163	0.018	262.5	4.872	0.050
98.8	6.179	0.036	267.4	4.813	0.061
103.5	6.192	0.008	272.3	4.758	0.051
108.8	6.191	0.024	277.2	4.690	0.062
113.6	6.159	0.015	282.1	4.626	0.065
118.6	6.146	0.006	286.9	4.557	0.037
123.7	6.133	0.048			
128.7	6.116	0.009			
133.6	6.063	0.153			
138.5	6.023	0.102			
143.3	5.990	0.036			

D.1.4 Ethyl cyanide (CH_3CH_2CN)

Table D.4: Absolute total ionization cross-section data of ethyl cyanide.

EE / eV	σ / Å^2	SD / Å^2	EE / eV	σ / Å^2	SD / Å^2	EE / eV	σ / Å^2	SD / Å^2
10.0	0.051		18.5	1.545	0.007	160.0	8.411	0.037
10.3	0.032		18.8	1.620	0.005	165.0	8.361	0.048
10.5	0.019		19.0	1.706	0.009	170.0	8.312	0.058
10.8	0.012		19.3	1.794	0.007	175.0	8.262	0.048
11.0	0.011		19.5	1.882	0.008	180.0	8.210	0.061
11.3	0.016		19.8	1.968		185.0	8.150	0.035
11.5	0.028		20.0	2.053		190.0	8.073	0.047
11.8	0.045		25.0	3.519	0.016	195.0	7.977	0.045
12.0	0.069		30.0	4.603	0.023	200.0	7.865	0.045
12.3	0.098		35.0	5.388	0.029	205.0	7.743	0.054
12.5	0.134		40.0	5.961	0.036	210.0	7.618	0.044
12.8	0.174	0.006	45.0	6.405	0.018	215.0	7.498	0.046
13.0	0.220	0.003	50.0	6.827	0.040	220.0	7.388	0.050
13.3	0.272	0.003	55.0	7.205	0.044	225.0	7.288	0.039
13.5	0.331	0.007	60.0	7.538	0.060	230.0	7.198	0.052
13.8	0.401	0.006	65.0	7.827	0.045	235.0	7.113	0.040
14.0	0.485	0.007	70.0	8.071	0.053	240.0	7.024	0.056
14.3	0.573	0.009	75.0	8.268	0.057	245.0	6.931	0.045
14.5	0.661	0.006	80.0	8.418	0.051	250.0	6.829	0.043
14.8	0.745	0.010	85.0	8.522	0.047	255.0	6.718	0.052
15.0	0.823	0.010	90.0	8.585	0.062	260.0	6.601	0.036
15.3	0.893	0.009	95.0	8.618	0.045	265.0	6.478	0.056
15.5	0.954	0.013	100.0	8.632	0.065	270.0	6.348	0.052
15.8	1.007	0.009	105.0	8.639	0.048	275.0	6.211	0.044
16.0	1.052	0.008	110.0	8.641	0.056	280.0	6.069	0.059
16.3	1.090	0.008	115.0	8.640	0.056	285.0	5.920	0.048
16.5	1.119	0.009	120.0	8.636	0.044			
16.8	1.155	0.007	125.0	8.628	0.055			
17.0	1.192	0.007	130.0	8.615	0.061			
17.3	1.238	0.008	135.0	8.599	0.043			
17.5	1.281	0.008	140.0	8.582	0.048			
17.8	1.339	0.008	145.0	8.557	0.051			
18.0	1.404	0.010	150.0	8.518	0.061			
18.3	1.467	0.009	155.0	8.466	0.050			

D.1.5 Propyl cyanide ($CH_3CH_2CH_2CN$)

Table D.5: Absolute total ionization cross-section data of propyl cyanide.

EE / eV	σ / Å^2	SD / Å^2	EE / eV	σ / Å^2	SD / Å^2	EE / eV	σ / Å^2	SD / Å^2
12.0	0.061		30.0	5.636	0.016	200.0	11.189	0.022
12.3	0.151		35.0	6.854	0.019	205.0	11.031	0.014
12.5	0.241		40.0	7.930	0.020	210.0	10.868	0.029
12.8	0.331		45.0	8.862	0.014	215.0	10.704	0.019
13.0	0.420		50.0	9.644	0.028	220.0	10.543	0.031
13.3	0.509	0.006	55.0	10.289	0.027	225.0	10.386	0.027
13.5	0.597	0.005	60.0	10.812	0.020	230.0	10.235	0.024
13.8	0.685	0.008	65.0	11.220	0.029	235.0	10.086	0.027
14.0	0.773	0.010	70.0	11.537	0.015	240.0	9.933	0.022
14.3	0.860	0.007	75.0	11.773	0.050	245.0	9.769	0.026
14.5	0.947	0.007	80.0	11.929	0.030	250.0	9.596	0.030
14.8	1.034	0.007	85.0	12.023	0.030	255.0	9.416	0.020
15.0	1.120	0.005	90.0	12.075	0.022	260.0	9.229	0.025
15.3	1.206	0.008	95.0	12.103	0.028	265.0	9.034	0.026
15.5	1.292	0.006	100.0	12.126	0.036	270.0	8.832	0.035
15.8	1.377	0.006	105.0	12.153	0.034	275.0	8.622	0.024
16.0	1.462	0.008	110.0	12.186	0.021	280.0	8.403	0.027
16.3	1.546	0.009	115.0	12.218	0.047	285.0	8.176	0.023
16.5	1.630	0.009	120.0	12.247	0.024			
16.8	1.714	0.008	125.0	12.269	0.027			
17.0	1.797	0.008	130.0	12.281	0.030			
17.3	1.880	0.008	135.0	12.277	0.022			
17.5	1.963	0.005	140.0	12.257	0.019			
17.8	2.045	0.008	145.0	12.222	0.028			
18.0	2.127	0.012	150.0	12.173	0.026			
18.3	2.209	0.006	155.0	12.115	0.022			
18.5	2.290	0.005	160.0	12.048	0.048			
18.8	2.371	0.005	165.0	11.975	0.042			
19.0	2.451	0.003	170.0	11.895	0.025			
19.3	2.531	0.011	175.0	11.807	0.035			
19.5	2.611	0.005	180.0	11.710	0.017			
19.8	2.690	0.009	185.0	11.600	0.041			
20.0	2.769		190.0	11.476	0.038			
25.0	4.274	0.008	195.0	11.338	0.035			

D.1.6 Isopropyl cyanide ($(CH_3)_2CHCN$)

Table D.6: Absolute total ionization cross-section data of isopropyl cyanide.

EE / eV	σ / Å^2	SD / Å^2	EE / eV	σ / Å^2	SD / Å^2	EE / eV	σ / Å^2	SD / Å^2
12.8	0.049		45.0	8.478	0.030	215.0	9.759	0.034
13.0	0.110		50.0	9.040	0.029	220.0	9.600	0.032
13.3	0.173	0.007	55.0	9.549	0.027	225.0	9.461	0.039
13.5	0.238	0.005	60.0	9.955	0.032	230.0	9.330	0.033
13.8	0.305	0.007	65.0	10.310	0.034	235.0	9.213	0.035
14.0	0.374	0.006	70.0	10.615	0.039	240.0	9.107	0.031
14.3	0.444	0.007	75.0	10.872	0.034	245.0	9.007	0.024
14.5	0.515	0.006	80.0	11.082	0.032	250.0	8.919	0.036
14.8	0.589	0.009	85.0	11.243	0.040	255.0	8.842	0.033
15.0	0.664	0.007	90.0	11.351	0.034	260.0	8.775	0.030
15.3	0.740	0.008	95.0	11.408	0.034	265.0	8.718	0.028
15.5	0.819	0.007	100.0	11.433	0.041	270.0	8.672	0.027
15.8	0.899	0.006	105.0	11.440	0.036	275.0	8.636	0.044
16.0	0.980	0.009	110.0	11.441	0.033	280.0	8.610	0.032
16.3	1.063	0.008	115.0	11.443	0.038	285.0	8.595	0.032
16.5	1.148	0.007	120.0	11.447	0.036			
16.8	1.234	0.006	125.0	11.447	0.034			
17.0	1.322	0.006	130.0	11.437	0.037			
17.3	1.411	0.008	135.0	11.409	0.035			
17.5	1.501	0.005	140.0	11.357	0.037			
17.8	1.593	0.005	145.0	11.284	0.034			
18.0	1.687	0.006	150.0	11.193	0.035			
18.3	1.781	0.005	155.0	11.092	0.032			
18.5	1.878	0.005	160.0	10.994	0.043			
18.8	1.975	0.006	165.0	10.908	0.040			
19.0	2.074	0.006	170.0	10.835	0.033			
19.3	2.173	0.006	175.0	10.771	0.029			
19.5	2.271	0.007	180.0	10.707	0.035			
19.8	2.368	0.006	185.0	10.632	0.036			
20.0	2.464		190.0	10.538	0.039			
25.0	4.211	0.009	195.0	10.415	0.035			
30.0	5.651	0.011	200.0	10.267	0.035			
35.0	6.819	0.020	205.0	10.102	0.039			
40.0	7.750	0.020	210.0	9.929	0.032			

D.1.7 Ethanethiol (CH_3CH_2SH)

Table D.7: Absolute total ionization cross-section data of ethanethiol.

EE / eV	σ / Å^2	SD / Å^2	EE / eV	σ / Å^2	SD / Å^2	EE / eV	σ / Å^2	SD / Å^2
9.7	0.001		18.2	3.105	0.013	163.4	9.939	0.069
10.0	0.006		18.5	3.184	0.020	168.3	9.850	0.114
10.2	0.014		18.7	3.263	0.015	172.7	9.792	0.101
10.5	0.029		19.0	3.342	0.017	178.3	9.704	0.088
10.7	0.050		19.2	3.432	0.016	183.2	9.636	0.110
11.0	0.080		19.5	3.521	0.020	188.1	9.548	0.116
11.2	0.119		24.4	5.260	0.083	193.2	9.445	0.102
11.5	0.169		29.4	6.427	0.079	198.0	9.325	0.100
11.7	0.232		34.4	7.362	0.096	203.2	9.201	0.113
12.0	0.297		39.3	8.137	0.071	207.8	9.110	0.076
12.2	0.372		44.2	8.771	0.152	212.7	9.025	0.077
12.5	0.452		49.2	9.261	0.140	217.6	8.959	0.085
12.7	0.538	0.009	54.2	9.665	0.091	222.9	8.866	0.074
13.0	0.629	0.023	59.1	9.977	0.177	227.4	8.794	0.083
13.2	0.725	0.008	64.1	10.236	0.142	232.2	8.706	0.152
13.5	0.829	0.018	69.1	10.408	0.148	237.1	8.626	0.091
13.7	0.940	0.009	74.0	10.541	0.062	242.5	8.530	0.087
14.0	1.058	0.020	78.9	10.618	0.145	247.7	8.443	0.061
14.2	1.183	0.011	83.8	10.691	0.174	251.8	8.366	0.083
14.5	1.311	0.019	88.6	10.741	0.149	257.9	8.253	0.075
14.7	1.442	0.010	93.9	10.790	0.169	262.5	8.165	0.020
15.0	1.575	0.013	98.8	10.775	0.277	267.4	8.074	0.066
15.2	1.709	0.009	103.5	10.718	0.160	272.3	7.972	0.062
15.5	1.844	0.013	108.8	10.651	0.208	277.2	7.858	0.077
15.7	1.981	0.011	113.6	10.610	0.155	282.1	7.748	0.074
16.0	2.118	0.007	118.6	10.565	0.199	286.9	7.635	0.071
16.2	2.247	0.004	123.7	10.474	0.131			
16.5	2.363	0.010	128.7	10.401	0.163			
16.7	2.480	0.007	133.6	10.342	0.018			
17.0	2.598	0.010	138.5	10.314	0.112			
17.2	2.714	0.004	143.3	10.256	0.166			
17.5	2.824	0.013	148.5	10.184	0.152			
17.7	2.926	0.013	153.1	10.109	0.129			
18.0	3.019	0.015	158.0	10.030	0.143			

D.1.8 Methyl oxirane (C_3H_6O)

Table D.8: Absolute total ionization cross-section data of methyl oxirane.

EE / eV	σ / Å^2	SD / Å^2	EE / eV	σ / Å^2	SD / Å^2	EE / eV	σ / Å^2	SD / Å^2
12.0	0.017		78.9	8.810	0.066	247.8	7.665	0.030
12.2	0.058		83.8	8.932	0.015	251.8	7.610	0.009
12.5	0.104		88.7	9.005	0.060	257.9	7.519	0.024
12.7	0.156		93.9	9.074	0.102	262.5	7.436	0.087
13.0	0.212		98.8	9.132	0.025	267.4	7.355	0.044
13.2	0.278	0.010	103.5	9.168	0.088	272.3	7.267	0.059
13.5	0.347	0.008	108.8	9.203	0.066	277.3	7.186	0.057
13.7	0.427	0.016	113.6	9.203	0.198	282.1	7.103	0.054
14.0	0.507	0.013	118.6	9.159	0.210	286.9	7.023	0.025
14.2	0.596	0.009	123.7	9.106	0.189			
14.5	0.685	0.014	128.7	9.093	0.110			
14.7	0.778	0.009	133.6	9.081	0.173			
15.0	0.873	0.008	138.5	9.036	0.078			
15.2	0.971	0.007	143.3	9.003	0.139			
15.5	1.068	0.008	148.5	8.946	0.103			
15.7	1.171	0.015	153.1	8.888	0.131			
16.0	1.274	0.009	158.0	8.825	0.058			
16.2	1.371	0.008	163.4	8.786	0.189			
16.5	1.450	0.005	168.3	8.746	0.146			
16.7	1.541	0.010	172.8	8.690	0.108			
17.0	1.619	0.009	178.3	8.611	0.082			
17.2	1.699	0.006	183.3	8.534	0.046			
17.5	1.774	0.006	188.1	8.473	0.081			
24.4	3.548	0.047	193.2	8.393	0.075			
29.4	4.472	0.040	198.0	8.322	0.081			
34.4	5.311	0.044	203.2	8.251	0.076			
39.3	6.026	0.054	207.8	8.199	0.072			
44.2	6.631	0.051	212.7	8.134	0.073			
49.2	7.137	0.059	217.7	8.056	0.061			
54.2	7.552	0.057	222.9	7.993	0.055			
59.1	7.881	0.017	227.4	7.942	0.059			
64.1	8.178	0.052	232.2	7.886	0.015			
69.1	8.428	0.042	237.1	7.812	0.012			
74.0	8.647	0.098	242.5	7.736	0.014			

D.1.9 Benzene (C_6H_6)

Table D.9: Absolute total ionization cross-section data of benzene.

EE / eV	σ / Å^2	SD / Å^2	EE / eV	σ / Å^2	SD / Å^2
9.5	0.016		158.0	12.600	0.121
14.5	1.383	0.062	163.4	12.496	0.173
19.5	3.734	0.120	168.3	12.413	0.186
24.4	5.455	0.014	172.7	12.342	0.029
29.4	6.846	0.004	178.3	12.245	0.172
34.4	8.094	0.008	183.2	12.146	0.162
39.3	8.959	0.005	188.1	12.040	0.145
44.2	9.906	0.046	193.2	11.916	0.162
49.2	10.540	0.096	198.0	11.788	0.022
54.2	11.071	0.047	203.2	11.651	0.176
59.1	11.526	0.022	207.8	11.529	0.018
64.1	11.933	0.142	212.7	11.411	0.176
69.1	12.280	0.032	217.6	11.298	0.152
74.0	12.564	0.134	222.9	11.177	0.015
78.9	12.788	0.119	227.4	11.071	0.036
83.8	12.955	0.153	232.2	10.953	0.036
88.7	13.075	0.108	237.1	10.838	0.033
93.9	13.154	0.117	242.5	10.712	0.033
98.8	13.190	0.210	247.7	10.592	0.015
103.5	13.202	0.134	251.8	10.504	0.035
108.8	13.197	0.045	257.9	10.386	0.041
113.6	13.180	0.113	262.5	10.309	0.006
118.6	13.156	0.001	267.4	10.233	0.033
123.7	13.128	0.048	272.3	10.158	0.027
128.7	13.091	0.118	277.2	10.075	0.198
133.6	13.044	0.160	282.1	9.987	0.197
138.5	12.981	0.043	286.9	9.885	0.196
143.3	12.898	0.122			
148.5	12.797	0.183			
153.1	12.701	0.079			

D.2 Common permanent gas molecules

D.2.1 Nitrogen (N_2)

Table D.10: Absolute total ionization cross-section data of nitrogen.

EE / eV	σ / Å^2	SD / Å^2	EE / eV	σ / Å^2	SD / Å^2	EE / eV	σ / Å^2	SD / Å^2
15.0	3E-04		98.8	2.438	2E-04	267.4	2.054	0.004
15.2	0.002		103.5	2.455	0.010	272.3	2.025	0.006
15.5	0.007		108.8	2.476	0.006	277.3	1.991	0.004
15.7	0.015		113.6	2.477	0.008	282.1	1.964	0.003
16.0	0.026		118.6	2.487	0.003	286.9	1.932	0.016
16.2	0.036		123.7	2.482	0.001			
16.5	0.045	0.002	128.7	2.486	0.010			
16.7	0.056	0.002	133.6	2.479	0.005			
17.0	0.068	0.002	138.5	2.473	0.005			
17.2	0.080	0.001	143.3	2.471	0.002			
17.5	0.091	0.002	148.5	2.465	0.005			
17.7	0.100	0.003	153.1	2.457	0.007			
18.0	0.110	0.001	158.0	2.441	0.004			
18.2	0.118	0.003	163.4	2.429	0.004			
18.5	0.127	0.003	168.3	2.423	5E-04			
18.7	0.136	0.005	172.8	2.407	0.006			
19.0	0.147	0.003	178.3	2.397	0.003			
19.2	0.160	0.004	183.2	2.372	0.007			
19.5	0.174	0.003	188.1	2.363	0.004			
24.4	0.508	0.005	193.2	2.339	0.002			
29.4	0.848	0.002	198.0	2.328	0.010			
34.4	1.122	0.005	203.2	2.299	0.008			
39.3	1.376	0.010	207.8	2.286	0.011			
44.2	1.561	0.004	212.7	2.267	0.003			
49.2	1.745	0.006	217.6	2.250	0.003			
54.2	1.882	0.005	222.9	2.230	0.002			
59.1	1.994	1E-04	227.4	2.213	0.003			
64.1	2.097	0.009	232.2	2.195	0.003			
69.1	2.165	0.006	237.1	2.177	0.002			
74.0	2.246	0.004	242.5	2.158	0.005			
78.9	2.290	0.008	247.8	2.137	0.006			
83.8	2.347	0.009	251.8	2.123	0.001			
88.7	2.375	0.006	257.9	2.098	0.001			
93.9	2.413	0.009	262.5	2.079	0.005			

D.2.2 Carbon dioxide (CO_2)

Table D.11: Absolute total ionization cross-section data of carbon dioxide.

EE / eV	σ / Å^2	SD / Å^2	EE / eV	σ / Å^2	SD / Å^2
14.5	0.099		163.4	3.726	0.048
19.5	0.370	0.006	168.3	3.709	0.034
24.4	0.804	0.005	172.7	3.692	0.027
29.4	1.268	0.010	178.2	3.669	0.023
34.4	1.688	0.016	183.1	3.647	0.044
39.3	2.004	0.036	188.0	3.623	0.021
44.2	2.265	0.012	193.2	3.597	0.009
49.1	2.499	0.014	198.0	3.571	0.020
54.2	2.723	0.014	203.1	3.543	0.014
59.1	2.906	0.002	207.8	3.516	0.012
64.1	3.070	0.022	212.7	3.487	0.044
69.1	3.208	0.025	217.6	3.458	0.020
74.0	3.294	0.058	222.9	3.426	0.014
78.9	3.372	0.002	227.4	3.399	0.016
83.8	3.457	0.034	232.2	3.369	0.007
88.7	3.533	0.029	237.1	3.339	0.027
93.9	3.590	0.017	242.5	3.306	0.024
98.8	3.632	0.016	247.6	3.275	0.023
103.5	3.656	0.033	251.8	3.251	0.044
108.8	3.689	0.028	257.9	3.216	0.036
113.6	3.712	0.033	262.5	3.190	0.020
118.5	3.755	0.011	267.4	3.163	0.026
123.7	3.778	0.037	272.3	3.138	0.005
128.7	3.781	0.012	277.2	3.113	0.024
133.6	3.781	0.022	282.1	3.091	0.063
138.5	3.778	0.031	286.9	3.070	0.041
143.3	3.773	0.012	291.8	3.050	
148.5	3.765	0.010	297.2	3.030	
153.1	3.755	0.038			
158.0	3.743	0.020			

D.2.3 Ethylene (C_2H_4)

Table D.12: Absolute total ionization cross-section data of ethylene.

EE / eV	σ / Å^2	SD / Å^2	EE / eV	σ / Å^2	SD / Å^2	EE / eV	σ / Å^2	SD / Å^2
10.7	0.002		19.2	1.040	0.014	125.8	5.510	0.067
11.0	0.005		19.5	1.083	0.016	130.6	5.489	0.054
11.2	0.012		19.7	1.127	0.012	135.5	5.469	0.081
11.5	0.021		20.0	1.170	0.019	140.7	5.444	0.091
11.7	0.032		20.2	1.213	0.017	145.5	5.415	0.099
12.0	0.045		20.5	1.256	0.019	150.2	5.379	0.021
12.2	0.060	0.003	20.7	1.298	0.015	155.7	5.328	0.092
12.5	0.077	0.002	21.0	1.340	0.019	160.4	5.277	0.002
12.7	0.097	0.005	21.2	1.381	0.019	165.3	5.225	0.079
13.0	0.118	0.002	21.5	1.421	0.002	170.7	5.171	0.093
13.2	0.141	0.011	21.7	1.461		175.6	5.127	0.100
13.5	0.166	0.012	22.0	1.499		180.5	5.084	0.105
13.7	0.192	0.002	22.2	1.537		185.3	5.044	0.085
14.0	0.220	0.011	22.5	1.574		190.2	5.000	0.001
14.2	0.250	0.014	26.4	2.116	0.026	195.4	4.951	0.031
14.5	0.280	0.012	31.4	3.113	0.038	200.0	4.906	0.062
14.7	0.313	0.014	36.4	3.463	0.051	204.9	4.860	0.101
15.0	0.346	0.012	41.3	4.046	0.066	210.3	4.815	0.096
15.2	0.381	0.004	46.4	4.410	0.074	215.1	4.778	0.079
15.5	0.417	0.009	51.3	4.613	0.026	218.8	4.752	0.079
15.7	0.454	0.012	56.2	4.800	0.061	225.3	4.704	0.087
16.0	0.492	0.017	61.3	4.970	0.013	230.2	4.668	0.056
16.2	0.531	0.003	66.2	5.115	0.031	235.1	4.628	0.046
16.5	0.570	0.001	71.1	5.240	0.053	240.0	4.584	0.081
16.7	0.611	0.017	75.9	5.348	0.017	244.9	4.537	0.066
17.0	0.652	0.001	80.8	5.436	0.006	249.8	4.489	0.006
17.2	0.694	0.019	86.1	5.510	0.117	254.7	4.441	0.062
17.5	0.736	0.016	91.1	5.562	0.086	259.6	4.393	0.037
17.7	0.778	0.020	95.9	5.588	0.097	265.0	4.340	0.069
18.0	0.822	0.018	101.1	5.592	0.115	269.8	4.292	0.046
18.2	0.865	0.001	105.8	5.587	0.078	274.2	4.250	0.012
18.5	0.908	0.005	110.9	5.578	0.045	279.4	4.199	0.044
18.7	0.952	0.020	116.0	5.558	0.026	284.1	4.153	0.022
19.0	0.996	0.028	120.9	5.534	0.088	289.6	4.096	0.059

D.2.4 Propene (C_3H_6)

Table D.13: Absolute total ionization cross-section data of propene.

EE / eV	σ / Å^2	SD / Å^2	EE / eV	σ / Å^2	SD / Å^2	EE / eV	σ / Å^2	SD / Å^2
9.7	1E-04		18.2	1.731	0.014	123.7	8.393	0.065
10.0	0.001		18.5	1.812	0.001	128.7	8.367	0.030
10.2	0.002		18.7	1.894	0.008	133.6	8.352	0.076
10.5	0.005		19.0	1.975	0.001	138.5	8.304	0.063
10.7	0.010		19.2	2.054	0.018	143.3	8.252	0.045
11.0	0.016		19.5	2.127	0.017	148.5	8.190	0.043
11.2	0.025		19.7	2.196	0.003	153.1	8.139	0.015
11.5	0.037		20.0	2.257	0.024	158.0	8.082	0.084
11.7	0.051		20.2	2.314	0.009	163.4	8.000	0.056
12.0	0.070	0.004	20.5	2.368	0.029	168.3	7.934	0.018
12.2	0.092	0.004	20.7	2.427	0.014	172.7	7.862	0.031
12.5	0.119	0.005	21.0	2.485	0.034	178.3	7.798	0.082
12.7	0.150	0.005	21.2	2.559	0.026	183.2	7.723	0.013
13.0	0.187	0.006	21.5	2.638	0.025	188.0	7.665	0.049
13.2	0.229	0.004	24.4	3.477	0.012	193.2	7.579	0.055
13.5	0.276	0.001	29.4	4.445		198.0	7.510	0.030
13.7	0.331	0.006	34.4	5.298	0.038	203.2	7.448	0.003
14.0	0.391	0.005	39.3	5.978	0.058	207.8	7.388	0.075
14.2	0.458	0.003	44.2	6.486	0.042	212.7	7.323	0.003
14.5	0.526	0.009	49.2	6.905	0.090	217.6	7.249	0.026
14.7	0.594	0.009	54.2	7.263	0.012	222.9	7.189	0.019
15.0	0.664	0.009	59.1	7.548	0.038	227.4	7.123	0.045
15.2	0.737	0.001	64.1	7.793	0.077	232.2	7.056	0.017
15.5	0.817	0.005	69.1	7.989	0.004	237.1	6.992	0.040
15.7	0.904	0.007	74.0	8.156	0.041	242.5	6.921	0.028
16.0	0.998	0.005	78.9	8.266	0.057	247.7	6.855	0.049
16.2	1.088	0.009	83.8	8.357		251.8	6.792	0.016
16.5	1.164	0.001	88.7	8.407	0.055	257.9	6.698	0.062
16.7	1.243	0.001	93.9	8.437	0.078	262.5	6.607	0.023
17.0	1.325	0.004	98.8	8.453	0.061	267.4	6.536	0.012
17.2	1.408	0.014	103.5	8.484	0.003	272.3	6.467	0.017
17.5	1.490	0.012	108.8	8.491	0.080	277.2	6.418	0.017
17.7	1.572	0.012	113.6	8.466	0.010	282.1	6.367	0.014
18.0	1.651	0.022	118.5	8.420	0.045	286.9	6.320	0.032

D.2.5 Nitrous oxide (N_2O)

Table D.14: Absolute total ionization cross-section data of nitrous oxide.

EE / eV	σ / Å^2	SD / Å^2	EE / eV	σ / Å^2	SD / Å^2	EE / eV	σ / Å^2	SD / Å^2
13.5	0.003		88.7	3.604	0.006	257.9	3.143	0.042
13.7	0.015	0.001	93.9	3.657	0.039	262.5	3.111	0.003
14.0	0.027	4E-04	98.8	3.661	0.033	267.4	3.079	0.105
14.2	0.045	4E-04	103.5	3.700	0.003	272.3	3.049	0.010
14.5	0.062	0.004	108.8	3.705	0.016	277.2	3.021	0.005
14.7	0.081	0.008	113.6	3.756	0.005	282.1	2.996	0.010
15.0	0.103	1E-04	118.6	3.769	0.012	286.9	2.973	0.066
15.2	0.124	1E-04	123.7	3.796	0.040			
15.5	0.147	0.001	128.7	3.787	0.033			
15.7	0.176	0.005	133.6	3.788	0.012			
16.0	0.203	0.001	138.5	3.796	0.018			
16.2	0.232	0.003	143.3	3.789	0.009			
16.5	0.255	0.002	148.5	3.795	0.044			
16.7	0.281	0.008	153.1	3.780	0.008			
17.0	0.303	0.005	158.0	3.774	0.035			
17.2	0.329	0.002	163.4	3.755	0.047			
17.5	0.348	0.001	168.3	3.748	0.027			
17.7	0.363	0.002	172.7	3.735	0.042			
18.0	0.375	0.003	178.3	3.735	0.029			
18.2	0.384	4E-04	183.2	3.693	0.056			
18.5	0.393	0.002	188.0	3.686	0.041			
24.4	0.984	0.003	193.2	3.618	0.049			
29.4	1.362	0.008	198.0	3.635	0.008			
34.4	1.775	0.004	203.1	3.598	0.040			
39.3	2.060	0.001	207.8	3.556	0.061			
44.2	2.339	2E-04	212.7	3.513	0.050			
49.2	2.597	0.004	217.6	3.469	0.035			
54.2	2.774	0.015	222.9	3.423	0.023			
59.1	2.980	0.001	227.4	3.384	0.047			
64.1	3.102	0.032	232.2	3.343	0.038			
69.1	3.287	0.016	237.1	3.302	0.041			
74.0	3.372	0.011	242.5	3.259	0.040			
78.9	3.483	0.032	247.7	3.218	0.035			
83.8	3.539	0.006	251.8	3.187	0.056			

D.2.6 Tetrafluoromethane (CF_4)

Table D.15: Absolute total ionization cross-section data of tetrafluoromethane.

EE / eV	σ / Å^2	SD / Å^2	EE / eV	σ / Å^2	SD / Å^2
17.0	0.002		123.7	4.854	0.025
17.2	0.009		128.7	4.897	0.025
17.5	0.019		133.6	4.932	0.005
17.7	0.030	0.001	138.5	4.959	0.025
18.0	0.042	0.003	143.3	4.979	0.002
18.2	0.056	1E-04	148.5	4.996	0.007
18.5	0.071	0.005	153.1	5.007	0.004
18.7	0.088	0.001	158.0	5.017	0.001
19.0	0.107	0.002	163.4	5.024	0.068
19.2	0.126	3E-04	168.3	5.028	0.007
19.5	0.146	0.002	172.7	5.029	0.029
20.0	0.185		178.3	5.027	
20.5	0.227		183.2	5.021	0.033
21.0	0.272		188.0	5.013	0.068
21.5	0.316		193.2	5.000	0.001
24.4	0.586	0.003	198.0	4.986	0.013
29.4	1.143	0.004	203.1	4.968	0.032
34.4	1.606	0.018	207.8	4.951	0.017
39.3	2.070		212.7	4.931	0.020
44.2	2.422	0.013	217.6	4.911	0.009
49.2	2.807	0.003	222.9	4.888	0.012
54.2	3.110	0.009	227.4	4.868	0.036
59.1	3.335	0.003	232.2	4.844	0.027
64.1	3.583	0.021	237.1	4.817	0.004
69.1	3.755	0.003	242.5	4.781	0.002
74.0	3.959	0.020	247.7	4.742	0.006
78.9	4.087	0.036	251.8	4.708	0.034
83.8	4.234	0.001	257.9	4.653	0.011
88.7	4.349	0.008	262.5	4.607	0.017
93.9	4.448	0.053	267.4	4.556	0.009
98.8	4.533	0.003	272.3	4.507	0.052
103.5	4.608	0.018	277.2	4.461	0.050
108.8	4.683	0.034	282.1	4.421	4E-04
113.6	4.746	0.005	286.9	4.383	0.084
118.6	4.803	0.014			

D.2.7 Sulfur hexafluoride (SF_6)

Table D.16: Absolute total ionization cross-section data of sulfur hexafluoride.

EE / eV	σ / Å^2	SD / Å^2	EE / eV	σ / Å^2	SD / Å^2	EE / eV	σ / Å^2	SD / Å^2
15.2	0.001		23.7	0.776		138.5	7.413	0.055
15.5	0.005		24.0	0.823		143.3	7.457	0.077
15.7	0.011		24.2	0.868		148.5	7.493	0.060
16.0	0.018		24.4	0.899		153.1	7.517	0.077
16.2	0.028		24.5	0.917		158.0	7.537	0.068
16.5	0.039		24.7	0.957		163.4	7.553	0.065
16.7	0.052	0.002	25.0	1.001		168.3	7.565	0.079
17.0	0.066	0.006	25.2	1.039		172.7	7.573	0.073
17.2	0.081	0.004	25.5	1.080		178.3	7.577	0.075
17.5	0.098	0.005	25.7	1.119		183.2	7.575	0.079
17.7	0.115	0.001	26.0	1.163		188.0	7.567	0.072
18.0	0.134	9E-05	26.2	1.205	0.009	193.2	7.554	0.077
18.2	0.153	0.003	29.4	1.721	0.025	198.0	7.537	0.072
18.5	0.173	0.005	34.4	2.534	0.024	203.1	7.516	0.079
18.7	0.193	0.005	39.3	3.126	0.031	207.8	7.494	0.085
19.0	0.213	0.001	44.2	3.652	0.008	212.7	7.468	0.089
19.2	0.234	0.008	49.2	4.116	0.029	217.6	7.439	0.086
19.5	0.254	0.005	54.2	4.642	0.041	222.9	7.404	0.086
19.7	0.274	0.003	59.1	4.950	0.011	227.4	7.371	0.068
20.0	0.294	0.010	64.1	5.245	0.031	232.2	7.331	0.097
20.2	0.314	0.006	69.1	5.517	0.048	237.1	7.288	0.078
20.5	0.336	0.005	74.0	5.763	0.035	242.5	7.234	0.096
20.7	0.362	0.005	78.9	5.990	0.060	247.7	7.175	0.055
21.0	0.390	0.004	83.8	6.196	0.032	251.8	7.124	0.041
21.2	0.419	0.001	88.7	6.382	0.022	257.9	7.036	0.111
21.5	0.447	0.005	93.9	6.557	0.051	262.5	6.962	0.065
21.7	0.477	0.001	98.8	6.706	0.009	267.4	6.883	0.136
22.0	0.508	0.005	103.5	6.832	0.055	272.3	6.805	0.108
22.2	0.541	0.008	108.8	6.958	0.055	277.2	6.729	0.114
22.5	0.575	2E-04	113.6	7.057	0.064	282.1	6.655	0.115
22.7	0.611	0.003	118.6	7.148	0.075	286.9	6.582	0.105
23.0	0.648	0.003	123.7	7.230	0.058	291.8	6.513	
23.2	0.688	0.007	128.7	7.300	0.068	297.2	6.440	
23.5	0.732	0.004	133.6	7.361	0.058			

E

Coulomb explosion simulation program and standard operating procedures

Contents

E.1 Standard operating procedures 275
E.2 Sample Matlab simulation program (*cis*-1,2-dichloroethene) 276
E.2.1 CES_dichloroethene.m 277
E.2.2 dichloroethene.inp 291
E.2.3 g09commands 291
E.2.4 g09commandf 292
E.2.5 runces 293

E.1 Standard operating procedures

As shown in Figure E.1, operationally, there are six files that needed to be created within the Linux environment in order to perform a simulation. The description and function of these files are listed in Table E.1. Running a simulation requires the following steps (use *cis*-1,2-dichloroethene as an example):

1) Keep `basisset.txt` as an empty file if the basis set is specified in the route

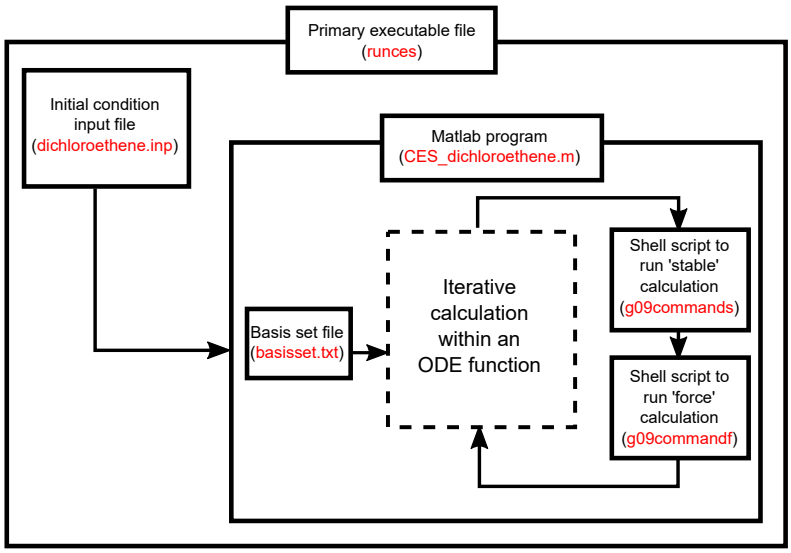


Figure E.1: Functional block diagram showing relationships between the six simulation files. Use *cis*-dichloroethene as a working example.

section of the Gaussian input file (this is generated within the Matlab trajectory simulation program). Otherwise, externally downloaded basis sets should be pasted into `basisset.txt` and the keyword `gen` should be specified in the route section of the Gaussian input file.

2) Create an input file, `dichloroethene.inp`, to contain the required initial information on the molecule.

3) Check and ensure correct setting of parameters in `CES_dichloroethene.m` file such as total trajectory time, ODE integration error tolerance, and output file directory.

4) Check and ensure correct setting of parameters in `runces`, such as requested wall-time, notification e-mail address, and job name.

5) Run `runces` by executing command `qsub runces`.

E.2 Sample Matlab simulation program (*cis*-1,2-dichloroethene)

Context of all files are provided below. For simulating a different molecule, changes need to be made accordingly.

Table E.1: Description of all six files of current Coulomb explosion simulation. Use *cis*-dichloroethene as a working example.

File name	Description
`runces`	Shell script which is the primary and the only executable file. It invokes Matlab program and specifies notification email address, requested walltime, and job name.
`CES_dichloroethene.m`	Matlab program that runs everything about the simulation. The core part of this program is an ODE function, which propagates the trajectory calculation iteratively by invoking Gaussian calculation (i.e. g09commands and g09commandf)
`dichloroethene.inp`	ASCII file containing atomic masses and initial condition of the molecule such as geometry, velocity, and force
`basisset.txt`	ASCII file containing the external basis sets downloaded from https://bse.pnl.gov/bse/portal when keyword gen is specified in route section. If the internal basis set of Gaussian is specified in the route section, this file needs to be kept empty (but not deleted)
`g09commands`	Shell script that performs Gaussian calculation with keyword Stable
`g09commandf`	Shell script that performs Gaussian calculation with keyword Force

E.2.1 CES_dichloroethene.m

```
%=====================================================
% Name:      Coulomb explosion trajectory programme
% System:    Linux - Chemistry Hartree
% molecule: dichloroethene-MP2/6-311G(d,p) Q8m1-run1
% Author:    Weiwei Zhou
% Created:   8 Aug 2018
%=====================================================

function out = CES_dichloroethene()

% delete possible remaining files
if exist('dichloroethene-stable.com','file')==2
  delete('dichloroethene-stable.com');
```

```
end
if exist('dichloroethene-force.com','file')==2
  delete('dichloroethene-force.com');
end
if exist('dichloroethene.inp','file')==6
  delete('dichloroethene.inp');
end
if exist('dichloroethene-stable.log','file')==2
  delete('dichloroethene-stable.log');
end
if exist('dichloroethene-force.log','file')==2
  delete('dichloroethene-force.log');
end
if exist('dichloroethene_alldata.txt','file')==2
  delete('dichloroethene_alldata.txt');
end

%print current working directory
pwd

clear all
format long % set long format

% list of global variables
global Mass;
global nAtoms;
global nrun;
global tfinal;
global MassConv;
global flag_xfs;
global t_xfs;

%======Values of variables and constants============
% Duration of Coulomb explosion / ps
tfinal = 0.5;
%
% conv. factor from amu to kg
MassConv = 1.660539040e-27;
%
% start time, intermediate time when
% data is saved, and final time
t_xfs=[0:0.025:tfinal];
%
% flag when data is saved
flag_xfs=1;
%====================================================

%========= Start to read in input file =============
% The input file has the following format:
%  nAtoms             (first line of file)
%  m1 z1 x1 y1 z1 fx1 fy1 fz1 vx1 vy1 vz1
%  m2 z2 x2 y2 z2 fx2 fy2 fz2 vx2 vy2 vz2
%   ...
%  mn zn xn yn zn fxn fyn fzn vxn vyn vzn
%
```

```
% Note: wz: 18 Dec 2016:
% Atoms need to be in the order of atomic number,
% i.e. from high mass to low mass.
% mass is in g/mol; charge is in units of e;
% x, y, z in angstroms; force is in atomic unit;
% velocity is in whatever unit used during the
% calculation.
%=====================================================

% define position and velocity variables.
r0=zeros(nAtoms,3);
v0=zeros(nAtoms,3);
% wz 24 Apr 2017 add v0.
% note: v0 will be non-zero in resume input files.

fileID=fopen('dichloroethene.inp','r');
nAtoms = fscanf(fileID,'%i',1);

% wz 14 Jun 2015:
% changed AtomProps from 5 to 8 elements (+ 3 vels)
for k=1:nAtoms
  AtomProps = fscanf(fileID,'%f',11);
  Mass(k) = AtomProps(1);
  r0(k,1) = AtomProps(3);
  r0(k,2) = AtomProps(4);
  r0(k,3) = AtomProps(5);
  v0(k,1) = AtomProps(9);
  v0(k,2) = AtomProps(10);
  v0(k,3) = AtomProps(11);
end
fclose(fileID);

% Create a vector that contains a list of initial
% positions for each atom followed by a list of
% initial velocities (initially zero). This will
% be used to initialize the ODE solver.

yinit = zeros(2*3*nAtoms,1);
for n=1:nAtoms
  for l=1:3
    m=3*(n-1)+l;
    yinit(m)=r0(n,l);     %positions / m
  end
end

% for resume file only:
% add initial velocity (non-zero)
for n=1:nAtoms
  for l=1:3
    m=3*nAtoms+3*(n-1)+l;
    yinit(m)=v0(n,l);     %vel
  end
end

%================= Prepare ODE ====================
```

```
% Call ODE solver to generate trajectories from
% Newton's equations (solves for particle vel).
% atomic forces are calculated from Gaussian.
% tspan is the time range to solve for.
% The other parameters are the initial conditions
% read in from the input file above.
%
% wz: Create an external molecule_alldata.txt file
%     to store charge, geometry, vel, force and
%     all other information obtained at each step.
%     First, write in the header only.
%     The order of columns are:
%     Step number
%     Computer system time
%     Traj time (starts from 0)
%     molecule 1: ESP charge (not for heavy atom)
%                 Mulliken charge
%                 Hirshfeld charge
%                 NBO charge
%                 Force, x,y,z (3 columns)
%                 Pos,   x,y,z (3 columns)
%                 Vel,   x,y,z (3 columns)
%     Molecule n: same as above
%     Then:
%     nAtom x nAtom columns of Atom-atom
%     overlap-weighted NAO bond order.
%     nAtom x nAtom columns of Wiberg bond
%     index matrix in the NAO basis.
%     nAtom x nAtom columns of MO bond order.
%     note: remember to update the molecule-spec
%           headers for different molecules.
%=================================================

nrun=0; % serial step number
fileID=fopen('dichloroethene_alldata.txt', 'w');
% write header of output file.
fprintf(fileID,['nrun\tSysTime\tFlyTime\t'...
'Cl1_espQ\tCl1_mQ\tCl1_hQ\tCl1_nQ\tCl1_Fx\tCl1_Fy\
   tCl1_Fz\tCl1_x\tCl1_y\tCl1_z\tCl1_vx\tCl1_vy\tCl1_vz\t
   '...
'Cl2_espQ\tCl2_mQ\tCl2_hQ\tCl2_nQ\tCl2_Fx\tCl2_Fy\
   tCl2_Fz\tCl2_x\tCl2_y\tCl2_z\tCl2_vx\tCl2_vy\tCl2_vz\t
   '...
'C1_espQ\tC1_mQ\tC1_hQ\tC1_nQ\tC1_Fx\tC1_Fy\tC1_Fz\tC1_x
   \tC1_y\tC1_z\tC1_vx\tC1_vy\tC1_vz\t'...
'C2_espQ\tC2_mQ\tC2_hQ\tC2_nQ\tC2_Fx\tC2_Fy\tC2_Fz\tC2_x
   \tC2_y\tC2_z\tC2_vx\tC2_vy\tC2_vz\t'...
'H1_espQ\tH1_mQ\tH1_hQ\tH1_nQ\tH1_Fx\tH1_Fy\tH1_Fz\tH1_x
   \tH1_y\tH1_z\tH1_vx\tH1_vy\tH1_vz\t'...
'H2_espQ\tH2_mQ\tH2_hQ\tH2_nQ\tH2_Fx\tH2_Fy\tH2_Fz\tH2_x
   \tH2_y\tH2_z\tH2_vx\tH2_vy\tH2_vz\t'...
'aaobostarts\r\n']);
fclose(fileID);
```

```
tspan=[0 tfinal]; % total fly time

% different absolute error tol for Pos and Vel
at1=ones(1,3*nAtoms)*1e-4;
at2=ones(1,3*nAtoms)*1e-2;
at=[at1 at2];
at=at';

% same relative error tol for both Pos and Vel
rt = 1e-3;

% define options of odeset based on at and rt above
options=odeset('AbsTol',at,'RelTol',rt,'Refine',1);

%=============== run ODE solver ====================
[t,y]=ode45(@NewtonEquations,tspan,yinit,options);
%===================================================
disp 'ODE finished'

% The vector of solutions, y, contains the atomic
% positions in the first 3*nAtoms elements, and the
% atomic velocities in the last 3*nAtoms elements.

%========== define Newton Equations ================
function dydt = NewtonEquations(t,y)
% Generates a vector of first order DEs for the ODE
% solver to solve. The first 3*nAtoms elements of
% the vector dydt are the particle velocities, and
% the last 3*nAtoms elements are the accelerations.
% In the solution vector, y, the first 3*nAtoms
% elements are the positions, and the last 3*nAtoms
% elements are the velocities.
%===================================================
% list of global variables
global Mass;
global nAtoms;
global nrun;
global tfinal;
global MassConv;
global flag_xfs;
global t_xfs;

% wzsode:
% define nrun as a counter of steps within ODE
nrun=nrun+1;

% First derivatives of positions (i.e. velocities).
for k=1:3*nAtoms
  dydt(k)=y(3*nAtoms+k);
end

% wzsode:
% need to pass y(position) to Gaussian for
% calculation to output Force and Charge (archive
% both).
ypos=zeros(nAtoms, 3);
```

```
for k=1:nAtoms
  ypos(k,1)=y(1+3*(k-1));
  ypos(k,2)=y(2+3*(k-1));
  ypos(k,3)=y(3+3*(k-1));
end;

%========= Gaussian files: Char list ===============
% Define variable atom to store the Char list of
% atom symbols
% Char list needs to:
%  be in the order of decreasing atomic weight
%  have length==2 for all atoms, e.g. 'C ' not 'C'
%  be updated for different molecules
%===================================================
atom=['Cl';'Cl';'C ';'C ';'H ';'H '];

%============ Gaussian files: input =================
% wz: Write Gaussian input file from Matlab, by
%     using yfinal (latest geometry from ODE).
%     Needs to be updated for different molecules
%     and different Gaussian approach/parameters.
%     same for force.com.
%===================================================
fileID=fopen('dichloroethene-stable.com','w');
fprintf(fileID,'%15s\r\n', '%nprocshared=16');
fprintf(fileID,'%8s\r\n', '%mem=8gb');
fprintf(fileID,'%23s\r\n', '%Chk=dichloroethene.chk');

% first step
if nrun==1
  fprintf(fileID,'%89s\r\n', '#p UHF/6-311G(d,p) stable=
     opt Guess=mix SCF(YQC,novaracc,noincfock,conver=6)
     geom=nocrowd');
end

% all other steps
if nrun~=1
  fprintf(fileID,'%96s\r\n', '#p UHF/6-311G(d,p) stable=
     opt Guess=(mix,read) SCF(YQC,novaracc,noincfock,
     conver=6) geom=nocrowd');
end

fprintf(fileID,'%0s\r\n', '');
fprintf(fileID,'%15s\r\n', 'UHF/6-311G(d,p)');
fprintf(fileID,'%0s\r\n', '');
fprintf(fileID,'%3s\r\n', '8 1');

for k=1:nAtoms
  fprintf(fileID,'%1c',[atom(k),atom(nAtoms+k)] );
  fprintf(fileID,'   %12.8f',ypos(k,1));
  fprintf(fileID,'   %12.8f',ypos(k,2));
  fprintf(fileID,'   %12.8f\r\n',ypos(k,3));
end;
fprintf(fileID,'%0s\r\n', '');
status = fclose(fileID);
```

```
% 2017-09-30:
% Open basisset.txt, to get number of lines.
fid = fopen('basisset.txt','r');
allText = textscan(fid,'%s','delimiter','\n');
numberOfLines = length(allText{1});
fclose(fid);

% 2017-09-30:
% Open stable.com file, ready for appending,
% then write in each line of basisset.txt.
fileID=fopen('dichloroethene-stable.com', 'a');
fid=fopen('basisset.txt','r');
for eln=1:numberOfLines
fprintf(fileID, fgetl(fid));
fprintf(fileID,'%0s\r\n', '');
end
fclose(fid);
fprintf(fileID,'%0s\r\n', '');
fprintf(fileID,'%0s\r\n', '');
fprintf(fileID,'%0s\r\n', '');
fprintf(fileID,'%0s\r\n', '');
fprintf(fileID,'%0s\r\n', '');
fprintf(fileID,'%0s\r\n', '');
fclose(fileID);

% wz: write a DOS batch file that contains plink
% command to execute g09sub in Linux, and then copy
% dichloroethene-stable.log from Linux to local
% directory
commands='g09commands';
% commands; note: needs to be changed for either
% ARC or hartree system.
unix(commands);

% wz: Write Gaussian input file which performed
%     FORCE calculation based on chk file from
%     dichloroethene-stabe.com
fileID=fopen('dichloroethene-force.com','w');
fprintf(fileID,'%15s\r\n', '%nprocshared=16');
fprintf(fileID,'%8s\r\n', '%mem=8gb');
fprintf(fileID,'%14s\r\n', '%Chk=dichloroethene.chk');

fprintf(fileID,'%125s\r\n', '#p UMP2/6-311G(d,p) pop=(MK
   ,NBORead,Hirshfeld) iop(6/76=8) FORCE Guess=read SCF(
   YQC,novaracc,noincfock,conver=6) geom=nocrowd');

fprintf(fileID,'%0s\r\n', '');
fprintf(fileID,'%16s\r\n', 'UMP2/6-311G(d,p)');
fprintf(fileID,'%0s\r\n', '');
fprintf(fileID,'%3s\r\n', '8 1');

for k=1:nAtoms
  fprintf(fileID,'%1c',[atom(k),atom(nAtoms+k)] );
```

```
  fprintf(fileID,'   %12.8f',ypos(k,1));
  fprintf(fileID,'   %12.8f',ypos(k,2));
  fprintf(fileID,'   %12.8f\r\n',ypos(k,3));
end;
fprintf(fileID,'%0s\r\n', '');
status = fclose(fileID);

% 2017-09-30:
% Open basisset.txt, to get number of lines.
fid=fopen('basisset.txt','r');
allText=textscan(fid,'%s','delimiter','\n');
numberOfLines=length(allText{1});
fclose(fid);

% 2017-09-30:
% Open force.com file, ready for appending, then
% write in each line of basisset.txt.
fileID = fopen('dichloroethene-force.com', 'a');
fid = fopen('basisset.txt','r');
for eln=1:numberOfLines
  fprintf(fileID, fgetl(fid));
  fprintf(fileID,'%0s\r\n', '');
end
fclose(fid);
fprintf(fileID,'%0s\r\n', '');
fprintf(fileID,'%0s\r\n', '');
fprintf(fileID,'%16s\r\n', '$nbo bndidx $end');
fprintf(fileID,'%0s\r\n', '');
fprintf(fileID,'%0s\r\n', '');
fprintf(fileID,'%0s\r\n', '');
fprintf(fileID,'%0s\r\n', '');
fprintf(fileID,'%0s\r\n', '');
fclose(fileID);

% commandf; note: needs to be changed for either
% ARC or hartree system.
commandf='g09commandf';
unix(commandf);

%=====================================================
% wz: Open dichloroethene.log, extract charges
% information and store them into an array called
% chargeline.
% Note: This section is critical. Make sure that
% correct values from the log file are extracted.
% It needs to be checked for each different
% molecule. Also make sure that the correct energy
% value is extracted depending on whether HF, DFT,
% or post-HF methods is used.
%=====================================================

% Extract ESP charges.
% 26 Jul 2017, wz updated for ARC
fid = fopen('dichloroethene-force.log','r');
```

```
allText = textscan(fid,'%s','delimiter','\n');
numberOfLines = length(allText{1});
fclose(fid);
% extract gaussian charge
fid = fopen('dichloroethene-force.log','r');
head=' ESP charges:';
if (fid < 0)
  printf('Error:could not open file\n') ;
  else
  for eln=1:numberOfLines
    line=fgetl(fid);
    if (isequal(line, head))
      capline=line;
      break;
    end
  end
  chargeline=zeros(1,nAtoms);
  fseek(fid,27,0);
  chargeline(1,1)=str2num(fgetl(fid));
%fgetl(fid)
  for l=2:nAtoms
    fseek(fid,12,0);
    chargeline(1,l)=str2num(fgetl(fid));
%fgetl(fid)
%chargeline
  end
end
fclose(fid);

% wz: 11 March 2017, extract Mulliken Charge.
% 26 Jul 2017, wz updated for ARC.
fid = fopen('dichloroethene-force.log','r');
head=' Mulliken charges and spin densities:';
if (fid < 0)
  fprintf('Error:could not open file\n') ;
  else
  for eln=1:numberOfLines
    line=fgetl(fid);
    if (isequal(line, head))
      capline=line;
    break;
    end
  end
  m_chargeline=zeros(1,nAtoms);
  fseek(fid,38,0);
  m_chargeline_raw=fgetl(fid);
  m_chargeline(1,1)=str2num(m_chargeline_raw(1:12));
  for l=2:nAtoms
    fseek(fid,10,0);
    m_chargeline_raw=fgetl(fid);
    m_chargeline(1,l)=str2num(m_chargeline_raw(1:12));
  end
end
fclose(fid);
```

```
% extract Hirsfeld charges.
% 26 Jul 2017, wz updated for ARC
fid = fopen('dichloroethene-force.log','r');
head='               Q-H        S-H        Dx          Dy
          Dz        Q-CM5   ';
if (fid < 0)
  fprintf('Error:could not open file\n') ;
  else
  for eln=1:numberOfLines
    line=fgetl(fid);
    if (isequal(line, head))
      capline=line;
      break;
    end
  end
  h_chargeline=zeros(1,nAtoms);
  for l=1:nAtoms
    fseek(fid,10,0);
    h_chargeline_raw=fgetl(fid);
    h_chargeline(1,l)=str2num(h_chargeline_raw(1:11));
  end
end
fclose(fid);

% extract NBO natural charges
fid = fopen('dichloroethene-force.log','r');
head='    Atom  No    Charge         Core      Valence
     Rydberg      Total';
if (fid < 0)
  fprintf('Error:could not open file\n') ;
  else
  for eln=1:numberOfLines
    line=fgetl(fid);
    if (isequal(line, head))
      capline=line;
      break;
    end
  end
  n_chargeline=zeros(1,nAtoms);
  fseek(fid,86,0);
  n_chargeline_raw=fgetl(fid);
  n_chargeline(1,1)=str2num(n_chargeline_raw(1:11));
  for l=2:nAtoms
    fseek(fid,13,0);
    n_chargeline_raw=fgetl(fid);
    n_chargeline(1,l)=str2num(n_chargeline_raw(1:11));
  end
end
fclose(fid);

% extract NBO atom-atom overlap bond order
fid = fopen('dichloroethene-force.log','r');
head=' Atom-atom overlap-weighted NAO bond order:
                                        ';
if (fid < 0)
```

```
  fprintf('Error:could not open file\n') ;
  else
  for eln=1:numberOfLines
    line=fgetl(fid);
    if (isequal(line, head))
      capline=line;
      break;
    end
  end
  n_aaobo=zeros(nAtoms,nAtoms);
  fseek(fid,121,0);
  n_aaobo_raw=fgetl(fid);
  n_aaobo(1,1:6)=str2num(n_aaobo_raw);
  for l=2:nAtoms
    fseek(fid,8,0);
    n_aaobo(l,1:6)=str2num(fgetl(fid));
  end
end
fclose(fid);

% extract Wiberg bond index matrix in the NAO basis
fid = fopen('dichloroethene-force.log','r');
head=' Wiberg bond index matrix in the NAO basis:
                                          ';
if (fid < 0)
  fprintf('Error:could not open file\n') ;
  else
  for eln=1:numberOfLines
    line=fgetl(fid);
    if (isequal(line, head))
      capline=line;
      break;
    end
  end
  n_wbim=zeros(nAtoms,nAtoms);

  fseek(fid,121,0);
  n_wbim_raw=fgetl(fid);
  n_wbim(1,1:6)=str2num(n_wbim_raw);
  for l=2:nAtoms
    fseek(fid,8,0);
    n_wbim(l,1:6)=str2num(fgetl(fid));
  end
end
fclose(fid);

% extract MO bond order
fid = fopen('dichloroethene-force.log','r');
head=' MO bond order:

   ';
if (fid < 0)
  fprintf('Error:could not open file\n') ;
  else
  for eln=1:numberOfLines
    line=fgetl(fid);
```

```
    if (isequal(line, head))
      capline=line;
      break;
    end
  end
  n_mobo=zeros(nAtoms,nAtoms);

  fseek(fid,121,0);
  n_mobo_raw=fgetl(fid);
  n_mobo(1,1:6)=str2num(n_mobo_raw);
  for l=2:nAtoms
    fseek(fid,8,0);
    n_mobo(l,1:6)=str2num(fgetl(fid));
  end
end
fclose(fid);

% wz 11Jun2015, extract gaussian force
fid = fopen('dichloroethene-force.log','r');
head=' Center     Atomic                     Forces (
   Hartrees/Bohr)';
if (fid < 0)
  printf('Error:could not open file\n') ;
  else
  for eln=1:numberOfLines
    line=fgetl(fid);
    if (isequal(line, head))
      capline=line;
      break;
    end
  end
  forceline=zeros(nAtoms,3);
  fseek(fid,156,0);

  forceraw=fgetl(fid);
%forceraw
  forceline(1,1)=str2num(forceraw(1:15));
  forceline(1,2)=str2num(forceraw(16:30));
  forceline(1,3)=str2num(forceraw(31:45));
%forceline(1,:)

  for l=2:nAtoms
    fseek(fid,23,0);
    forceraw=fgetl(fid);
%forceraw
    forceline(l,1)=str2num(forceraw(1:15));
    forceline(l,2)=str2num(forceraw(16:30));
    forceline(l,3)=str2num(forceraw(31:45));
%forceline
  end
end
fclose(fid);

% extract total energy.
% 26 Jul 2017, wz updated for ARC.
```

```
% uncorrected HF energy
fid = fopen('dichloroethene-force.log','r');
head=' SCF Done:  E(UHF) =';
if (fid < 0)
  fprintf('Error:could not open file\n') ;
  else
  for eln=1:numberOfLines
    line=fgetl(fid);
    if ( length(line)>20 && isequal(line(1:20), head)
         )
      capline=line;
      break;
    end
  end
  SCF=0.000000000;
  SCF_raw=capline;
  if eln~=numberOfLines
    SCF=str2num(SCF_raw(21:36));
  end
  if eln==numberOfLines
    SCF=0.0;
  end
end
fclose(fid);

% Extract total MP2 SCF energy
fid = fopen('dichloroethene-force.log','r');
head='EUMP2 =';
if (fid < 0)
  fprintf('Error:could not open file\n') ;
  else
  for eln=1:numberOfLines
    line=fgetl(fid);
    if ( length(line)>34 && isequal(line(28:34), head)
         )
      capline=line;
      break;
    end
  end
  SCFMP2=0.000000000;
  SCFMP2_raw=capline;
  if eln~=numberOfLines
    SCFMP2=str2num(SCFMP2_raw(35:59));
  end
  if eln==numberOfLines
    SCFMP2=0.0;
  end
end
fclose(fid);

% wzsode:
% write all data to alldata.txt in each step
% note:
% retain the same order as per that of the header
fileID=fopen('dichloroethene_alldata.txt', 'a');
```

```
fprintf(fileID,'%6d\t%20s\t%12.6e\t',nrun,datestr(now),t
   );
for k=1:nAtoms
  fprintf(fileID,'%12.6f\t%12.6f\t%12.6f\t%12.6f\t%15.9f
     \t%15.9f\t%15.9f\t%15.8f\t%15.8f\t%15.8f\t%15.8f\t
     %15.8f\t%15.8f\t',chargeline(1,k), m_chargeline(1,k)
     ,h_chargeline(1,k),n_chargeline(1,k),forceline(k,1),
     forceline(k,2),forceline(k,3),ypos(k,1),ypos(k,2),
     ypos(k,3),dydt(1,(k-1)*3+1),dydt(1,(k-1)*3+2),dydt
     (1,(k-1)*3+3));
end
for k=1:nAtoms
  for j=1:nAtoms
    fprintf(fileID,'%12.6f\t',n_aaobo(k,j));
  end
end
for k=1:nAtoms
  for j=1:nAtoms
    fprintf(fileID,'%12.6f\t',n_wbim(k,j));
  end
end
for k=1:nAtoms
  for j=1:nAtoms
    fprintf(fileID,'%12.6f\t',n_mobo(k,j));
  end
end
fprintf(fileID,'%16.8f\t',SCF);

% note: please check the molecule-spec force.log
% file to identify/update the number of digits for
% SCF and SCFMP2
fprintf(fileID,'%18.10f\t',SCFMP2);
fprintf(fileID,'\r\n');
fclose(fileID);

% wz 2017-02-26, print current fly time in .o file
t

% note: change it for different molecule and/or
% different charge/multiplicity states.
rootpath='/home/hartree2/cv/exet3684/CES/DR/
   dichloroethene-MP2-chk/cis/vert/Q8-m1/output';

% note:
% change the molecule name for different molecules.
for i=2:(size(t_xfs,2)-1)
  if t>=t_xfs(i) & t<t_xfs(i+1) & flag_xfs~=i
    foldername=fullfile(rootpath,sprintf('time-%.3f',
       t_xfs(i)*1));
%note: need to make sure %.xf is consistent with the
   minimum t_xfs
    mkdir(foldername);
    unix( sprintf('cp dichloroethene*.chk ''%s''',
       foldername) );
```

```
    unix( sprintf('cp dichloroethene*.log ''%s''',
       foldername) );
    unix( sprintf('cp dichloroethene*.com ''%s''',
       foldername) );
    unix( sprintf('cp dichloroethene_alldata.txt ''%s
       ''', foldername) );
    flag_xfs=i;
    break;
  end
end

% First derivatives of vel. (i.e. accelerations)
for n = 1:nAtoms
  for l=1:3
    dydt(3*nAtoms+3*(n-1)+l) = ((forceline(n,l)
       *8.23872336e-8)/(MassConv*Mass(n)))*1e-14;
%Newton's equations (dv/dt = F/m)
  end
end

dydt=dydt';

%============= End of programme ====================
```

E.2.2 dichloroethene.inp

```
6
35    4.688975     0.00     1.649204    -0.450742     0.00
       1.049846972    -0.755746788     0.00     0.00     0.00
35    4.688975     0.00    -1.649204    -0.450742     0.00
   -1.049846972    -0.755746788     0.00     0.00     0.00
12    1.231391     0.00    -0.664341     0.961687     0.00
   -0.124004669     0.152548902     0.00     0.00     0.00
12    1.231391     0.00     0.664341     0.961687     0.00
       0.124004669     0.152548902     0.00     0.00     0.00
1     1.079634     0.00    -1.208384     1.892485     0.00
   -0.379469193     0.603197886     0.00     0.00     0.00
1     1.079634     0.00     1.208384     1.892485     0.00
       0.379469193     0.603197886     0.00     0.00     0.00
```

E.2.3 g09commands

```
#!/bin/csh
#$ -S /bin/csh
#$ -cwd
#$ -pe smp 16
source /usr/local/gaussian/scripts/g09.login
```

```
#echo start to remove temp files
#echo remove chk b
#rm -f dichloroethene.chk
#echo remove chk e
#echo remove csh b
rm -f dichloroethene-stable.csh
#echo remove csh e
#echo remove log b
rm -f dichloroethene-stable.log
#echo remove log e
#echo remove inp b
rm -f *.inp
#echo remove inp e
#echo remove d2e b
rm -f *.d2e
#echo remove d2e e
#echo remove int b
rm -f *.int
#echo remove int e
#echo remove rwf b
rm -f *.rwf
#echo remove rwf e
#echo remove scr b
rm -f *.scr
#echo remove scr e
#echo finish removing temp files
#
#echo start to backup chk file
rm -f dichloroethene_bk.chk
cp dichloroethene.chk dichloroethene_bk.chk
#echo finish backup chk file
#echo Start to run Gaussian 1st time
g09   <dichloroethene-stable.com >&dichloroethene-stable
   .log
#echo Finish Gaussian 1st time
#echo About to exit g09command
exit
```

E.2.4 g09commandf

```
#!/bin/csh
#$ -S /bin/csh
#$ -cwd
#$ -pe smp 16
source /usr/local/gaussian/scripts/g09.login
#echo start to remove temp files
#echo remove csh b
rm -f dichloroethene-force.csh
#echo remove csh e
#echo remove log b
rm -f dichloroethene-force.log
#echo remove log e
#echo remove inp b
```

```
rm -f *.inp
#echo remove inp e
#echo remove d2e b
rm -f *.d2e
#echo remove d2e e
#echo remove int b
rm -f *.int
#echo remove int e
#echo remove rwf b
rm -f *.rwf
#echo remove rwf e
#echo remove scr b
rm -f *.scr
#echo remove scr e
#echo finish removing temp files
#
#echo start to backup chk file
rm -f dichloroethene_bk.chk
cp dichloroethene.chk dichloroethene_bk.chk
#echo finish backup chk file
#echo Start to run Gaussian 1st time
g09   <dichloroethene-force.com >&dichloroethene-force.
   log
#echo Finish Gaussian 1st time
#echo About to exit g09command
exit
```

E.2.5 runces

```
#!/bin/csh
#$ -cwd
#$ -pe smp 16
#$ -l s_rt=1:00:00
#$ -N dichloroethene-MP2-cis-Q8-m1-vert
#$ -m bea
#$ -M firstname.lastname@chem.ox.ac.uk

module load matlab/2015b

mkdir -p output

SCR=$TMPDIR
ORIG=‘pwd‘
mkdir -p $SCR

cp CES_dichloroethene.m $SCR
cp dichloroethene.inp $SCR
cp g09commands $SCR
cp g09commandf $SCR
cp basisset.txt $SCR

cd $SCR
```

```
matlab -nodisplay -nosplash -r "CES_dichloroethene()"

echo about to copy log via runces
\cp dichloroethene*.log $ORIG
\cp dichloroethene*.com $ORIG

echo about to copy alldata via runces
\cp dichloroethene_alldata.txt $ORIG
\cp *.chk $ORIG

echo about to leave runces
cd $ORIG
```